Deformation Prediction and Autonomous Path Planning for Robot-Assisted Endovascular Interventions

Li, Z.

DOI
10.4233/uuid:9d3d7180-d021-4067-b14c-05bec9bf5756

Publication date
2023

Document Version
Final published version

Citation (APA)
Li, Z. (2023). *Deformation Prediction and Autonomous Path Planning for Robot-Assisted Endovascular Interventions*. [Dissertation (TU Delft), Delft University of Technology]. https://doi.org/10.4233/uuid:9d3d7180-d021-4067-b14c-05bec9bf5756

DEFORMATION PREDICTION AND AUTONOMOUS PATH PLANNING FOR ROBOT-ASSISTED ENDOVASCULAR INTERVENTIONS

DEFORMATION PREDICTION AND AUTONOMOUS PATH PLANNING FOR ROBOT-ASSISTED ENDOVASCULAR INTERVENTIONS

Dissertation

for the purpose of obtaining the degree of doctor
at the Delft University of Technology,
by the authority of the Rector Magnificus, prof.dr.ir. T.H.J.J. van der Hagen,
chair of the Board for Doctorates,
to be defended publicly on
Friday 15 December 2023 at 10:00 o'clock

by

Zhen LI

Master of Science, Technology and Health, Specialism Advanced Robotics,
École Centrale de Nantes, France,
Master of Science in Engineering, Specialism Automatic Control and Robotics,
Warsaw University of Technology, Poland,
born in Henan, China.

This dissertation has been approved by the promotors.

Composition of the doctoral committee:

Rector Magnificus,	chairperson
Prof. dr. J. Dankelman,	Delft University of Technology, promotor
Dr. E. De Momi,	Politecnico di Milano, promotor
Independent members:	
Prof. dr. ir. J.C.F. de Winter,	Delft University of Technology
Prof. dr. P. Valdastri,	University of Leeds, United Kingdom
Dr. E. Votta,	Politecnico di Milano, Italy
Dr. L.S. De Mattos,	Italian Institute of Technology, Italy
Prof. dr. ir. P. Breedveld,	Delft University of Technology, reserve member
Other member:	
Dr. E. Vander Poorten,	KU Leuven, Belgium

Dr. E. Vander Poorten of KU Leuven has made a significant contribution to the completion of this dissertation.

The doctoral research has been carried out in the context of an agreement for double degree PhD program between Delft University of Technology, the Netherlands and Politecnico di Milano, Italy.

This work was supported by the ATLAS project. This project has received funding from the European Union's Horizon 2020 research and innovation programme under the Marie Sklodowska-Curie grant agreement No 813782.

Keywords: Path planning, Medical robots, Augmented reality

Printed by: Gildeprint

ISBN 978-94-6384-520-5

An electronic version of this dissertation is available at
`http://repository.tudelft.nl/`

Boldly hypothesize, meticulously validate.
Researchers in this spirit will embark on a transformative journey,
unraveling the enigmatic aspects of their research topics.

Zhen Li

CONTENTS

SUMMARY

Endovascular interventions, as emerging medical therapies, utilize blood vessels as conduits to access anatomically challenging regions deep within the body. Within endovascular interventions, one of the prominent challenges involves maneuvering the instrument tip by coordinating insertion, retraction, and torque actions at the proximal end of the instrument. This intricate task is hindered by the presence of a complex mapping between input actions and resulting motion, rendering precise control and accurate targeting of the desired area difficult. Thanks to the introduction of robotic assistance and the steerability of robotic catheters, the complexity of endovascular interventions has been mitigated.

The integration of steerable catheters and navigation guidance has the potential to reduce the level of expertise required for endovascular interventions. By leveraging autonomous navigation, path-related complications, such as perforation, embolization, and dissection, arising from excessive interaction forces between interventional tools and the vessels, can be effectively addressed and potentially reduced. Within the context of robotic catheters navigating through narrow, delicate, and deformable vessels, path planning presents significant challenges, particularly under complex operating conditions, stringent safety constraints, and the inherent limitations on catheter steering capability. Furthermore, the intricate interplay between the steerable catheter and vessel walls, coupled with the deformable nature of the vessels, intensifies the complexity of achieving reliable and real-time path planning, rendering it a hard problem to solve.

This dissertation aims to develop a safe, accurate, and efficient path planner for steerable robotic catheters. Firstly, this dissertation provides a systematic literature analysis of path planning techniques, collating the findings from the most significant research contributions in the field employing the PRISMA method. In the first part of this dissertation, a novel path planning approach named BFS-GA is proposed, which effectively adheres to the robot curvature constraint while keeping the catheter's path as close to the vasculature's centerline as possible. This path planner is capable of swiftly calculating obstacle-free trajectories that conform to the patient's vasculature, while incorporating the inherent limitations of the catheter such as maximum curvature.

A major challenge during autonomous navigation in endovascular interventions is the complexity of operating in a deformable but constrained workspace with an instrument. To address this, two methods are proposed in the second part of this dissertation to provide a realistic and dynamic environment for path planning. Specifically, a realistic, auto-adaptive, and visually plausible simulator is developed. This simulator has the capability to accurately predict the interplay between catheters and vessel walls. Additionally, it accounts for the deformable nature of the vessels induced by the cyclic heartbeat motion. In addition, a novel deformable model-to-image registration framework is designed to reconstruct comprehensive intra-operative vessel structures from medical imaging data, while accurately accounting for deformations.

Given the dynamic vascular environments generated as above, a robust path planner named C-GAIL for steerable catheters is proposed in the third part of this dissertation. This path planner ensures higher precision and robustness by accounting for both the deformable properties of vessels and the catheter's steering capabilities. The *in-vitro* experiments demonstrate that the path generated by the proposed C-GAIL path planner aligns better with the actual steering capability of robotic catheters. Thereafter, the dissertation presents an in-depth exploration of path planning assistance utilizing various interactive modalities based on augmented reality. Three interactive control modalities for steering robotic catheters are introduced, and their impact on human-in-the-loop robot-assisted cardiac catheterization is investigated. The path guidance is facilitated by the previously discussed C-GAIL path planning method. A user study is conducted, which demonstrates the feasibility of harnessing the capabilities of a gaming joystick for catheter teleoperation and the practicality of utilizing a head-mounted display to receive 3D visual feedback.

SAMENVATTING

Endovasculaire interventies, als opkomende medische therapieën, gebruiken bloedvaten als doorvoerkanalen om anatomisch uitdagende gebieden diep in het lichaam te bereiken. Binnen endovasculaire interventies is een van de belangrijkste uitdagingen het manoeuvreren van de punt van het instrument door middel van coördinatie van inbrengen, terugtrekken en draaiacties aan het proximale uiteinde van het instrument. Deze complexe taak wordt bemoeilijkt door de aanwezigheid van een complexe koppeling tussen invoeracties en resulterende beweging, waardoor het lastig wordt om precieze controle en nauwkeurige targeting van het gewenste gebied te bereiken. De introductie van robotondersteuning en de bestuurbaarheid van robotische katheters heeft bijgedragen aan het verminderen van de complexiteit van endovasculaire interventies.

De integratie van bestuurbare katheters en navigatiebegeleiding heeft het potentieel om het vereiste expertiseniveau voor endovasculaire interventies te verlagen. Door gebruik te maken van autonavigatie kunnen path-gerelateerde complicaties, zoals perforatie, embolisatie en dissectie, veroorzaakt door overmatige interactiekrachten tussen interventiegereedschappen en bloedvaten, effectief worden aangepakt en mogelijk verminderd. Binnen de context van robotische katheters die door smalle, delicate en vervormbare bloedvaten navigeren, brengt padplanning aanzienlijke uitdagingen met zich mee, met name onder complexe werkomstandigheden, strikte veiligheidsbeperkingen en de inherente beperkingen van de katheterstuurcapaciteit. Bovendien versterkt de complexe interactie tussen de bestuurbare katheter en de bloedvatwanden, in combinatie met de vervormbare aard van de bloedvaten, de complexiteit van het realiseren van betrouwbare en real-time padplanning, wat het tot een uitdagend probleem maakt om op te lossen.

Dit proefschrift heeft als doel een veilige, nauwkeurige en efficiënte padplanner te ontwikkelen voor bestuurbare robotische katheters. Dit proefschrift begint met een systematische literatuuranalyse van padplanningstechnieken, waarin de bevindingen van de belangrijkste onderzoeksbijdragen in dit veld worden verzameld met behulp van de PRISMA-methode. In het eerste deel van dit proefschrift wordt een nieuwe benadering voor padplanning, genaamd BFS-GA, voorgesteld, die effectief voldoet aan de buigingsrestrictie van de robot terwijl het pad van de katheter zo dicht mogelijk bij de middellijn van het vaatstelsel wordt gehouden. Deze padplanner kan snel vrije van obstakels trajecten berekenen die in overeenstemming zijn met de vasculatuur van de patiënt, terwijl de inherente beperkingen van de katheter, zoals maximale kromming, worden meegenomen.

Een grote uitdaging tijdens autonavigatie bij endovasculaire interventies is de complexiteit van het werken in een vervormbare maar beperkte werkruimte met een instrument. Om dit aan te pakken worden in het tweede deel van dit proefschrift twee methoden voorgesteld om een realistische en dynamische omgeving te bieden voor padplanning. Specifiek wordt een realistische, auto-adaptieve en visueel aannemelijke simulator ontwikkeld. Deze simulator heeft het vermogen om de wisselwerking tussen katheters en vaatwanden nauwkeurig te voorspellen. Bovendien houdt het rekening met de vervormbare aard van de vaten veroorzaakt door de cyclische hartslagbeweging. Daarnaast is een nieuw vervormbaar model-naar-afbeelding registratiekader ontworpen om uitgebreide intra-operatieve vaatstructuren te reconstrueren uit medische beeldgegevens, terwijl deze nauwkeurig rekening houdt met vervormingen.

In het licht van de dynamische vaatomgevingen, zoals eerder beschreven, introduceert het derde deel van dit proefschrift een robuuste padplanner genaamd C-GAIL voor bestuurbare katheters. Deze padplanner zorgt voor hogere precisie en robuustheid door zowel de vervormbare eigenschappen van bloedvaten als de stuurmogelijkheden van de katheter mee te nemen. De *in-vitro* experimenten tonen aan dat het pad gegenereerd door de voorgestelde C-GAIL padplanner beter overeenkomt met de daadwerkelijke stuurmogelijkheden van robotische katheters. Vervolgens presenteert de dissertatie een diepgaande verkenning van hulp bij padplanning met gebruik van diverse interactieve modaliteiten gebaseerd op augmented reality. Er worden drie interactieve besturingsmodaliteiten voor het sturen van robotische katheters geïntroduceerd, en hun impact op mens-in-de-lus robot-ondersteunde hartkatheterisatie wordt onderzocht. De padbegeleiding wordt vergemakkelijkt door de eerder besproken C-GAIL padplanningmethode. Een gebruikersstudie toont aan dat het haalbaar is om de mogelijkheden van een game-joystick te benutten voor katheter-teleoperatie en dat het praktisch is om een head-mounted display te gebruiken voor 3D visuele feedback.

SOMMARIO

Gli interventi endovascolari, come terapie mediche emergenti, utilizzano i vasi sanguigni come condotti per accedere a regioni anatomicamente complesse all'interno del corpo. In tali interventi, una delle principali sfide è la manovra della punta dello strumento coordinando le azioni di inserimento, ritrazione e torsione all'estremità prossimale dello strumento. Questa complessa operazione è resa più difficile dalla presenza di una correlazione complessa tra le azioni di input e il movimento risultante, rendendo difficile il controllo preciso e il puntamento accurato dell'area desiderata. Grazie all'introduzione dell'assistenza robotica e alla manovrabilità dei cateteri robotici, la complessità degli interventi endovascolari è stata mitigata.

L'integrazione di cateteri manovrabili e orientamenti di navigazione ha il potenziale per ridurre il livello di competenza richiesta per gli interventi endovascolari. Sfruttando la navigazione autonoma, le complicanze legate al percorso, come la perforazione, l'embolizzazione e la dissezione, derivanti dalle forze di interazione eccessive tra gli strumenti interventistici e i vasi sanguigni, possono essere affrontate in modo efficace e potenzialmente ridotte. Nel contesto dei cateteri robotici che si muovono attraverso vasi sanguigni stretti, delicati e deformabili, la pianificazione del percorso presenta significative sfide, in particolare in condizioni operative complesse, stringenti vincoli di sicurezza e le limitazioni intrinseche della capacità di manovra del catetere. Inoltre, l'interazione complessa tra il catetere manovrabile e le pareti dei vasi sanguigni, unita alla natura deformabile dei vasi stessi, intensifica la complessità nel raggiungere una pianificazione del percorso affidabile e in tempo reale, rendendo il problema difficile da risolvere.

Questa dissertazione si propone di sviluppare un pianificatore di percorso sicuro, accurato ed efficiente per cateteri robotici manovrabili. Innanzitutto, la tesi fornisce un'analisi sistematica della letteratura sulle tecniche di pianificazione del percorso, raccogliendo i risultati delle più significative ricerche nel campo utilizzando il metodo PRISMA. Nella prima parte di questa tesi, viene proposto un nuovo approccio alla pianificazione del percorso chiamato BFS-GA, che rispetta efficacemente il vincolo di curvatura del robot, mantenendo il percorso del catetere il più vicino possibile alla linea centrale del sistema vascolare. Questo pianificatore del percorso è in grado di calcolare rapidamente percorsi privi di ostacoli che si adattano alla vascolarizzazione del paziente, considerando le limitazioni intrinseche del catetere, quali la massima curvatura.

Una delle principali sfide durante la navigazione autonoma negli interventi endovascolari è la complessità di operare in uno spazio di lavoro deformabile ma vincolato con uno strumento. Per affrontare ciò, nella seconda parte di questa dissertazione sono proposti due metodi per creare un ambiente realistico e dinamico utile alla pianificazione del percorso. Specificamente, viene sviluppato un simulatore realistico, auto-adattivo e visivamente plausibile. Questo simulatore ha la capacità di prevedere accuratamente l'interazione tra cateteri e pareti dei vasi. Inoltre, tiene conto della natura deformabile dei vasi causata dal movimento ciclico del battito cardiaco. In aggiunta, viene progettato un nuovo framework di registrazione deformabile da modello a immagine per ricostruire strutture vascolari intra-operatorie complete dai dati di imaging medico, considerando accuratamente le deformazioni.

Dato l'ambiente vascolare dinamico descritto in precedenza, nella terza parte di questa dissertazione viene proposto un robusto pianificatore di percorso chiamato C-GAIL per cateteri sterzabili. Questo pianificatore di percorso assicura una maggiore precisione e robustezza tenendo conto sia delle proprietà deformabili dei vasi sanguigni che delle capacità di manovra del catetere. Gli esperimenti *in-vitro* dimostrano che il percorso generato dal pianificatore C-GAIL si allinea meglio con la reale capacità di manovra dei cateteri robotici. Successivamente, la dissertazione presenta un'esplorazione approfondita dell'assistenza alla pianificazione del percorso utilizzando varie modalità interattive basate sulla realtà aumentata. Vengono introdotte tre modalità di controllo interattivo per manovrare cateteri robotici, e viene indagato il loro impatto sulla cateterizzazione cardiaca assistita da robot con interazione umana. La guida del percorso è facilitata dal metodo di pianificazione C-GAIL precedentemente discusso. Viene condotto uno studio utente che dimostra la fattibilità di sfruttare le capacità di un joystick da gioco per la teleoperazione del catetere e la praticità di utilizzare un display montato sulla testa per ricevere un feedback visivo tridimensionale.

Parole chiave: Pianificazione del percorso, Robot medici, Progettazione del simulatore, Realtà aumentata

1

INTRODUCTION

The important thing is not to stop questioning.

Albert Einstein

The scientific mind does not so much provide the right answers
as ask the right questions.

Claude Lévi-Strauss

The main objective of this dissertation is to develop autonomous path planning techniques for robot-assisted endovascular interventions conducted in tortuous and deformable environments. The introduction chapter of this dissertation offers a comprehensive clinical background and elucidates the motivations behind this research endeavor. It begins by highlighting the prevailing challenges in endovascular interventions and underscores the indispensability of autonomous path planning in their execution. The chapter specifically delves into pre-operative path planning and robust path planning within deformable environments, the central focus of this thesis, accentuating key unresolved issues within the field. The research objectives are then outlined, followed by a succinct summary of the subsequent chapters' organization.

Parts of this chapter have been published as:
Ameya Pore*, **Zhen Li***, Diego Dall'Alba, Albert Hernansanz, Elena De Momi, Arianna Menciassi, Alicia Casals Gelpí, Jenny Dankelman, Paolo Fiorini, and Emmanuel Vander Poorten. "Autonomous Navigation for Robot-Assisted Intraluminal and Endovascular Procedures: A Systematic Review". In: *IEEE Transactions on Robotics* 39.4 (2023), pp. 2529–2548. DOI: `10.1109/TRO.2023.3269384`. (Ameya Pore and Zhen Li contributed equally to this manuscript. Corresponding author: Zhen Li.)

1.1. CLINICAL BACKGROUND

Endovascular interventions are a growing field in medical therapy, offering a minimally invasive approach to accessing complex anatomical regions deep within the body. To enable these procedures, the use of flexible instruments with snake-like characteristics is essential, as they can navigate through the intricate endovascular anatomy with ease [1]. Typically, cardiologists introduce a guidewire through a small incision in the groin, arm, or neck during endovascular interventions. This guidewire acts as a stable pathway, guiding the catheter to the desired target location. It is worth noting that endovascular interventions have significantly improved patient outcomes, leading to reductions in blood loss, post-operative trauma, wound infections, and overall recovery time [2].

In the field of endovascular interventions, there are two significant challenges associated with controlling catheters and guidewires. The first challenge involves navigating the instruments based on two-dimensional (2D) fluoroscopy images, requiring a precise understanding of the three-dimensional (3D) anatomy projected onto a 2D plane [3, 4]. The second challenge in endovascular interventions involves the intricate maneuvering of the instrument tip, which is achieved by coordinating actions such as insertion, retraction, and torque applied at the proximal end of the catheter and guidewire. This task is inherently complex due to the non-linear relationship between the input actions and the resulting motion of the instrument tip. This non-linearity is an intrinsic characteristic of the physical and mechanical properties of these flexible instruments as they navigate through the vascular system's complex and variable anatomy. Such characteristics impose significant cognitive and physical demands on clinicians, necessitating a substantial learning curve to achieve proficiency in manipulating these highly dexterous instruments effectively [5]. Furthermore, operating within deformable and constrained anatomical pathways introduces additional risks, as friction and collisions between the instruments and vascular walls can lead to potentially dangerous outcomes. Predicting instrument behavior, particularly in situations where direct visualization of the local anatomy is unavailable, poses a substantial challenge.

The navigation challenges encountered in endovascular interventions have prompted the development of robotic systems to improve the current landscape. Robotic assistance, involving instrumentation, imaging, and navigation, has significantly advanced the field of endovascular procedures. These robotic platforms allow for precise control of the catheter tip, enhancing stability during operations. As a result, teleoperated robotic catheterization systems have gained considerable attention due to their numerous advantages, including reduced radiation exposure, increased precision, elimination of tremors, and improved operator comfort.

Endovascular interventions have witnessed remarkable advancements in robotic technology, leading to significant developments in the field. The CorPath™ GRX system from Corindus (Waltham, USA) is a notable example, offering guided robotic control that allows clinicians to navigate endovascular tools using a joystick interface. Hansen Medical's Sensei™ X and Magellan platforms, although no longer commercially available, have played a crucial role in the evolution of robotic systems for endovascular interventions, with J&J Robotics (New Brunswick, USA) acquiring them. The Monarch platform by Auris Health (Redwood, USA), focused on bronchoscopy, incorporates certain elements from these technologies. Catheter Robotics Inc.'s Amigo™ platform and Robocath's R-One™ platform employ mechanical mechanisms to enable steering of standard catheters in 3 Degrees-of-Freedom (DoFs) through an intuitive remote controller designed to mimic the standard catheter handle. On the other hand, the Niobe™ system by Stereotaxis (St. Louis, USA) utilizes remote magnetic navigation, employing a magnetic field to guide the catheter tip. Tip deflection is controlled by adjusting the orientation of external magnets through a mouse or joystick at the workstation. These robotic systems have demonstrated exceptional capabilities in intravascular navigation.

Despite the incorporation of robotic assistance, the challenges posed by the complexity of procedures in endovascular interventions remain unresolved to a significant extent [6]. These challenges stem from factors such as the non-intuitive mapping between user and robot motions, inherent limitations on tool dexterity, and insufficient shape sensing capabilities, all of which contribute to a lack of situational awareness [7]. There is a growing consensus that automation can play a pivotal role in reducing clinicians' workload while enhancing overall procedural outcomes [6, 7, 8]. The integration of steerable catheters and navigation guidance holds promise in reducing the level of expertise required for percutaneous treatments [9].

One noteworthy area where the utilization of navigation assistance can have a significant impact is in the mitigation of path-related complications, including perforation, embolization, and dissection, which can arise from excessive interaction forces between interventional tools and blood vessels. By harnessing autonomous navigation capabilities, these complications can be potentially addressed and minimized. Furthermore, the growing demand for endovascular interventions, coupled with a limited number of experts in the field [10], highlights the significance of autonomous navigation. Such advancements would position clinicians in a supervisory role, requiring minimal and sporadic intervention. This transition allows clinicians to focus on high-level decision-making rather than being immersed in low-level execution, resulting in improved efficiency and optimal resource allocation.

In the quest to enable autonomous navigation in endovascular interventions, a crucial aspect involves the implementation of path planning techniques [11]. Path planning encompasses the process of determining an optimal trajectory that connects an initial configuration to a desired goal configuration while ensuring a collision-free workspace. When considering the specific context of robotic catheters maneuvering through narrow, delicate, and deformable vessels, path planning poses significant challenges. These challenges are further compounded by complex operating conditions, stringent safety constraints, and the inherent limitations on catheter steering capability. Moreover, the intricate interplay between the steerable catheter and the vessel walls, combined with the deformable nature of the vessels, amplifies the complexity of achieving reliable and real-time path planning. Consequently, there is a demand for robust path planning approaches that effectively tackle these constraints and uncertainties.

1.2. RESEARCH OBJECTIVES

This research project aims to develop a safe, accurate, and efficient path planner for steerable robotic catheters. The primary objectives driving the PhD research can be summarized as follows, aiming to advance the field of robotic catheter navigation and path planning:

- (O1) to devise an expeditious path planner capable of swiftly calculating trajectories free of obstacles (such as plaque or calcium) that conform to the patient's vasculature, while incorporating the inherent limitations of the catheter such as maximum curvature;

- (O2) to develop a simulator with the ability to accurately predict the interplay between catheters and vessel walls, as well as account for the deformable nature of the vessels;

- (O3) to reconstruct comprehensive intra-operative vessel tree structures from medical imaging data, while accurately accounting for deformations;

- (O4) to develop an enhanced path planner tailored for steerable catheters, which ensures higher precision and robustness by accounting for both the deformable properties of vessels and the catheter's steering capabilities.

1.3. THESIS ORGANIZATION

The structure of this thesis, along with the interconnections between each chapter, is depicted in Figure 1.1. A comprehensive overview of the contents within each part and chapter is provided below.

In Chapter 1, a thorough clinical context is presented, shedding light on the underlying motivations that drive this research endeavor. The intricate challenges faced in the realm of endovascular interventions are explored, emphasizing the crucial role of autonomous path planning in overcoming these obstacles. Special attention is given to pre-operative path planning and the development of robust path planning methodologies tailored for deformable environments.

Chapter 2 provides an overview of path planning techniques and categorizes them according to the displayed Level of Autonomy (LoA). A systematic literature analysis is carried out using the PRISMA method to summarise the results of the most relevant work. For each retained work, the clinical aim, the level of autonomy, the adopted path planning method, and the type of validation conducted are investigated. The limitations of the corresponding path planning methods are further identified, along with directions to improve the robustness of the algorithms, enabling adaptation to a dynamic intraluminal environment.

Chapter 2 is partially based on the following publication:

[12] Ameya Pore*, **Zhen Li***, Diego Dall'Alba, Albert Hernansanz, Elena De Momi, Arianna Menciassi, Alicia Casals Gelpí, Jenny Dankelman, Paolo Fiorini, and Emmanuel Vander Poorten. "Autonomous Navigation for Robot-Assisted Intraluminal and Endovascular Procedures: A Systematic Review". In: *IEEE Transactions on Robotics* 39.4 (2023), pp. 2529–2548. DOI: `10.1109/TRO.2023.3269384`. (Ameya Pore and Zhen Li contributed equally to this manuscript. Corresponding author: Zhen Li.)

The main research studies of this dissertation are composed of three parts: pre-operative path planning, vessels deformation prediction, and path planning in deformable environments. Each part will be introduced in detail as follows.

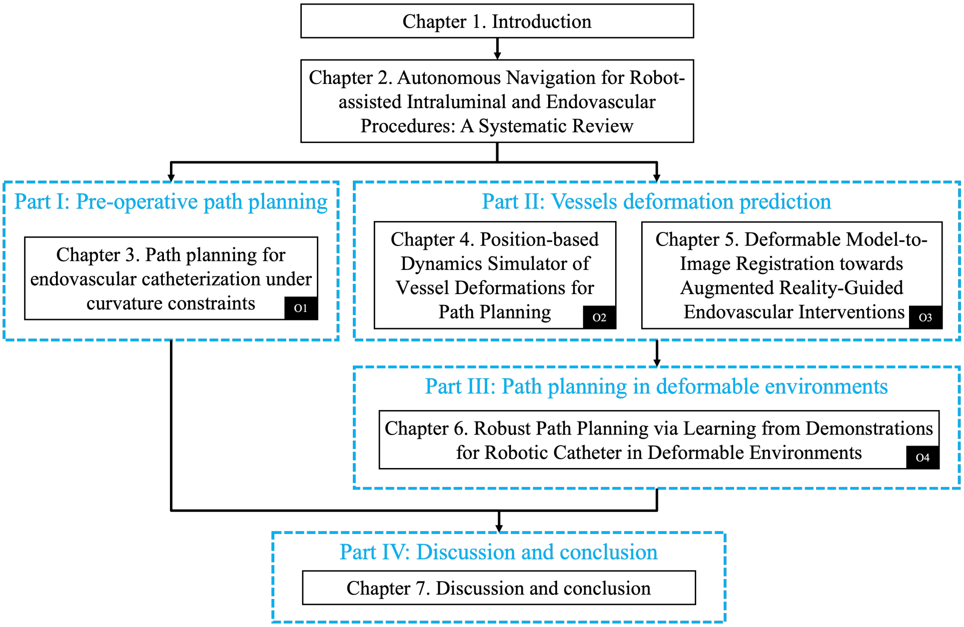

Figure 1.1: Structure of the thesis. Arrows indicate read-before relations.

Part I: Pre-operative path planning
Current state-of-the-art methods frequently overlook the constraint of catheter curvature and do not consistently achieve a low computational time which is essential for real-time path replanning. The acceptable computation time should be appropriately determined based on several key factors: the frequency of catheter tip tracking, the frequency of vision sensing feedback, and the controller's operating frequency. This part of the dissertation proposes a fast two-phase path planning approach specifically designed to address these challenges while accommodating the robot curvature constraint.

Chapter 3 is dedicated to fulfilling objective O1. A novel path planning approach called BFS-GA is introduced, which effectively adheres to the robot curvature constraint while keeping the catheter's path as close to the centerlines as possible. The high efficiency of the method is demonstrated through extensive experimentation in both 2D and 3D scenarios. The results highlight the planner's capability to satisfy the robot curvature constraint while maintaining low computational time costs when compared to sampling-based methods. The presented work is particularly suitable for clinical procedures that require compatibility with curvature constraints while optimizing specific criteria. Additionally, it finds applicability in scenarios involving curvature-constrained robots navigating through narrow passages.

Chapter 3 is partially based on the following publication:

[13] **Zhen Li**, Jenny Dankelman, and Elena De Momi. "Path planning for endovascular catheterization under curvature constraints via two-phase searching approach". In: *International Journal of Computer Assisted Radiology and Surgery* 16.4 (2021),

pp. 619–627. DOI: `10.1007/s11548-021-02328-x`

Part II: Vessels deformation prediction

A major challenge during autonomous navigation in endovascular interventions is the complexity of operating in a deformable but constrained workspace with an instrument. To address this, the simulation of deformations provides a cost-effective training platform for path planning, as explored in Chapter 4. Additionally, Chapter 5 focuses on intra-operative model reconstruction from medical images while considering deformations, offering a realistic and dynamic environment for path planning.

Chapter 4 is dedicated to fulfilling objective O2. Within this chapter, a realistic, auto-adaptive, and visually plausible simulator is developed. This simulator can accurately predict the global deformation of vessels induced by the contact of a robotic catheter and the cyclic motion corresponding to the heartbeat. Extensive *in-vitro* experiments are conducted and compared with *in-silico* results. The evaluation of end-user experiences is presented through quantitative performance metrics and a 5-Point Likert Scale questionnaire. The real-time and accurate performance of the simulator renders this framework suitable for creating a dynamic environment conducive to the training of path planning for robotic catheters.

Chapter 4 is partially based on the following publication:

[14] **Zhen Li**, Enrico Manzionna, Giovanni Monizzi, Angelo Mastrangelo, Maria Elisabetta Mancini, Daniele Andreini, Jenny Dankelman, and Elena De Momi. "Position-based dynamics simulator of vessel deformations for path planning in robotic endovascular catheterization". In: *Medical Engineering & Physics* 110 (2022), p. 103920. DOI: `10.1016/j.medengphy.2022.103920`

Chapter 5 is dedicated to fulfilling objective O3. Within this chapter, a novel deformable model-to-image registration framework is introduced, leveraging deep learning techniques specifically tailored for augmented reality-guided endovascular catheterization. The registration accuracy is validated in both 2D and 3D scenarios. For the 2D validation, a dataset comprising nine patients is utilized, while for the 3D validation, a dataset obtained from the previously mentioned intervention simulator is employed. This study successfully demonstrates the feasibility and accuracy of the proposed weakly-supervised deformable model-to-image registration framework. The results highlight its potential to provide intra-operative 3D imaging as valuable intervention assistance in dynamic vascular environments.

Chapter 5 is partially based on the following publications:

[15] **Zhen Li**, Maria Elisabetta Mancini, Giovanni Monizzi, Daniele Andreini, Giancarlo Ferrigno, Jenny Dankelman, and Elena De Momi. "Model-to-Image Registration via Deep Learning towards Image-Guided Endovascular Interventions". In: *2021 International Symposium on Medical Robotics (ISMR)*. 2021, pp. 1–6. DOI: `10.1109/ISMR48346.2021.9661511`

[16] **Zhen Li**, Letizia Contini, Alessandro Ippoliti, Elena Bastianelli, Federico De Marco, Jenny Dankelman, and Elena De Momi. "Deformable Model-to-Image Registration towards Augmented Reality-Guided Endovascular Interventions". 2023. (Under Review)

Part III: Path planning in deformable environments

Navigation within tortuous and deformable vessels using catheters with limited steering capabilities necessitates the development of reliable path planning techniques. Existing state-of-the-art path planners fail to fully consider the deformable nature of the environment, making real-time and dependable path planning a challenging task due to the complex interaction between the steerable catheter and vessel walls.

Chapter 6 is dedicated to addressing objective O4. Within this chapter, a robust path planner named Curriculum Generative Adversarial Imitation Learning (C-GAIL) is proposed, based on a Learning from Demonstrations (LfD) approach to enhance risk management. This framework aims to reduce the uncertainty associated with vessel deformation, thereby minimizing tracking errors. By accounting for the interaction between steerable catheters and vessel walls, as well as the deformable properties of the vessels, the proposed path planning framework demonstrates superior performance in managing uncertainty and achieving lower tracking errors, as validated through both *in-silico* and *in-vitro* experiments. Thereafter, Chapter 6 introduces an in-depth exploration of path planning assistance utilizing various interactive modalities. This chapter introduces three interactive control modalities for steering robotic catheters and investigates their impact on human-in-the-loop robot-assisted cardiac catheterization. The path guidance is facilitated by the previously discussed path planning technique. An *in-vitro* user study was conducted to compare the effectiveness of different interactive modalities. The findings of the study demonstrate the feasibility of employing the proposed path planning technique as guidance in different interactive modalities.

Chapter 6 is partially based on the following publication:

[17] **Zhen Li**, Chiara Lambranzi, Di Wu, Alice Segato, Federico De Marco, Emmanuel Vander Poorten, Jenny Dankelman, and Elena De Momi. “Robust Path Planning via Learning from Demonstrations for Robotic Catheters in Deformable Environments”. 2023. (Under Review)

[18] Di Wu*, **Zhen Li***, Mohammad Hasan Dad Ansari, Xuan Thao Ha, Mouloud Ourak, Jenny Dankelman, Arianna Menciassi, Elena De Momi, and Emmanuel Vander Poorten. “Comparative Analysis of Interactive Modalities for Intuitive Endovascular Interventions”. 2023. (Under Review. Di Wu and Zhen Li contributed equally to this manuscript. Corresponding author: Zhen Li.)

Part IV: Conclusion

Lastly, Chapter 7 presents the concluding remarks, summarizing the main contributions of this thesis and emphasizing potential avenues for future research. Furthermore, a comprehensive list of articles published by the author during her doctoral studies, including those not covered in this dissertation, can be found at the end of this thesis, providing a comprehensive overview of the author’s scholarly output.

BIBLIOGRAPHY

[1] Jenna Seetohul and Mahmood Shafiee. “Snake Robots for Surgical Applications: A Review”. In: *Robotics* 11.3 (2022), p. 57. DOI: `10.3390/robotics11030057`.

[2] Tomas da Veiga, James H Chandler, Peter Lloyd, Giovanni Pittiglio, Nathan J Wilkinson, Ali K Hoshiar, Russell A Harris, and Pietro Valdastri. “Challenges of continuum robots in clinical context: A review”. In: *Progress in Biomedical Engineering* 2.3 (2020). DOI: `10.1088/2516-1091/ab9f41`.

[3] Hedyeh Rafii-Tari, Christopher J Payne, and Guang-Zhong Yang. “Current and emerging robot-assisted endovascular catheterization technologies: a review”. In: *Annals of biomedical engineering* 42.4 (2014), pp. 697–715. DOI: `10.1007/s10439-013-0946-8`.

[4] Johannes Bonatti, George Vetrovec, Celia Riga, Oussama Wazni, and Petr Stadler. “Robotic technology in cardiovascular medicine”. In: *Nature Reviews Cardiology* 11.5 (2014), p. 266. DOI: `10.1038/nrcardio.2014.23`.

[5] Nabil Simaan, Rashid M Yasin, and Long Wang. “Medical technologies and challenges of robot-assisted minimally invasive intervention and diagnostics”. In: *Annual Review of Control, Robotics, and Autonomous Systems* 1 (2018), pp. 465–490. DOI: `10.1146/annurev-control-060117-104956`.

[6] Paolo Fiorini, Ken Y Goldberg, Yunhui Liu, and Russell H Taylor. “Concepts and Trends in Autonomy for Robot-Assisted Surgery”. In: *Proceedings of the IEEE* 110.7 (2022), pp. 993–1011. DOI: `10.1109/JPROC.2022.3176828`.

[7] Aleks Attanasio, Bruno Scaglioni, Elena De Momi, Paolo Fiorini, and Pietro Valdastri. “Autonomy in Surgical Robotics”. In: *Annual Review of Control, Robotics, and Autonomous Systems* 4 (2020). DOI: `10.1146/annurev-control-062420-090543`.

[8] Tamás Haidegger. “Autonomy for surgical robots: Concepts and paradigms”. In: *IEEE Transactions on Medical Robotics and Bionics* 1.2 (2019), pp. 65–76. DOI: `10.1109/TMRB.2019.2913282`.

[9] Costanza Culmone, Semih Fatih Yikilmaz, Fabian Trauzettel, and Paul Breedveld. “Follow-The-Leader Mechanisms in Medical Devices: A Review on Scientific and Patent Literature”. In: *IEEE Reviews in Biomedical Engineering* (2021). DOI: `10.1109/RBME.2021.3113395`.

[10] Rachel Hargest. “Five thousand years of minimal access surgery: 1990–present: organisational issues and the rise of the robots”. In: *Journal of the Royal Society of Medicine* 114.2 (2021), pp. 69–76. DOI: `10.1177/0141076820967907`.

[11] BK Patle, Anish Pandey, DRK Parhi, A Jagadeesh, et al. "A review: On path planning strategies for navigation of mobile robot". In: *Defence Technology* 15.4 (2019), pp. 582–606. DOI: `10.1016/j.dt.2019.04.011`.

[12] Ameya Pore, Zhen Li, Diego Dall'Alba, Albert Hernansanz, Elena De Momi, Arianna Menciassi, Alicia Casals Gelpí, Jenny Dankelman, Paolo Fiorini, and Emmanuel Vander Poorten. "Autonomous Navigation for Robot-Assisted Intraluminal and Endovascular Procedures: A Systematic Review". In: *IEEE Transactions on Robotics* 39.4 (2023), pp. 2529–2548. DOI: `10.1109/TRO.2023.3269384`.

[13] Zhen Li, Jenny Dankelman, and Elena De Momi. "Path planning for endovascular catheterization under curvature constraints via two-phase searching approach". In: *International Journal of Computer Assisted Radiology and Surgery* 16.4 (2021), pp. 619–627. DOI: `10.1007/s11548-021-02328-x`.

[14] Zhen Li, Enrico Manzionna, Giovanni Monizzi, Angelo Mastrangelo, Maria Elisabetta Mancini, Daniele Andreini, Jenny Dankelman, and Elena De Momi. "Position-based dynamics simulator of vessel deformations for path planning in robotic endovascular catheterization". In: *Medical Engineering & Physics* 110 (2022), p. 103920. DOI: `10.1016/j.medengphy.2022.103920`.

[15] Zhen Li, Maria Elisabetta Mancini, Giovanni Monizzi, Daniele Andreini, Giancarlo Ferrigno, Jenny Dankelman, and Elena De Momi. "Model-to-Image Registration via Deep Learning towards Image-Guided Endovascular Interventions". In: *2021 International Symposium on Medical Robotics (ISMR)*. 2021, pp. 1–6. DOI: `10.1109/ISMR48346.2021.9661511`.

[16] Zhen Li, Letizia Contini, Alessandro Ippoliti, Elena Bastianelli, Federico De Marco, Jenny Dankelman, and Elena De Momi. "Deformable Model-to-Image Registration towards Augmented Reality-Guided Endovascular Interventions". 2023. (Under Review).

[17] Zhen Li, Chiara Lambranzi, Di Wu, Alice Segato, Federico De Marco, Emmanuel Vander Poorten, Jenny Dankelman, and Elena De Momi. "Robust Path Planning via Learning from Demonstrations for Robotic Catheters in Deformable Environments". 2023. (Under Review).

[18] Di Wu, Zhen Li, Mohammad Hasan Dad Ansari, Xuan Thao Ha, Mouloud Ourak, Jenny Dankelman, Arianna Menciassi, Elena De Momi, and Emmanuel Vander Poorten. "Comparative Analysis of Interactive Modalities for Intuitive Endovascular Interventions". 2023. (Under Review).

2

AUTONOMOUS NAVIGATION FOR ROBOT-ASSISTED INTRALUMINAL AND ENDOVASCULAR PROCEDURES: A SYSTEMATIC REVIEW

This chapter presents a comprehensive overview of path planning techniques and organizes them based on their demonstrated Level of Autonomy (LoA). To summarize the findings from relevant studies, a systematic literature analysis is conducted using the PRISMA method. The selected works are examined to determine their clinical objectives, the degree of autonomy, the path planning approach employed, and the validation methods employed. The limitations of these path planning methods are also identified, and strategies are proposed to enhance their robustness, thus enabling adaptation to dynamic tubular environments. Looking ahead, the field of navigation is expected to witness increased autonomy, empowering clinicians with improved precision control and reduced workload, while maintaining their active involvement in the decision-making process.

Parts of this chapter have been published in:
Ameya Pore*, **Zhen Li***, Diego Dall'Alba, Albert Hernansanz, Elena De Momi, Arianna Menciassi, Alicia Casals Gelpí, Jenny Dankelman, Paolo Fiorini, and Emmanuel Vander Poorten. "Autonomous Navigation for Robot-Assisted Intraluminal and Endovascular Procedures: A Systematic Review". In: *IEEE Transactions on Robotics* 39.4 (2023), pp. 2529–2548. DOI: `10.1109/TRO.2023.3269384`. (Ameya Pore and Zhen Li contributed equally to this manuscript. Corresponding author: Zhen Li.)

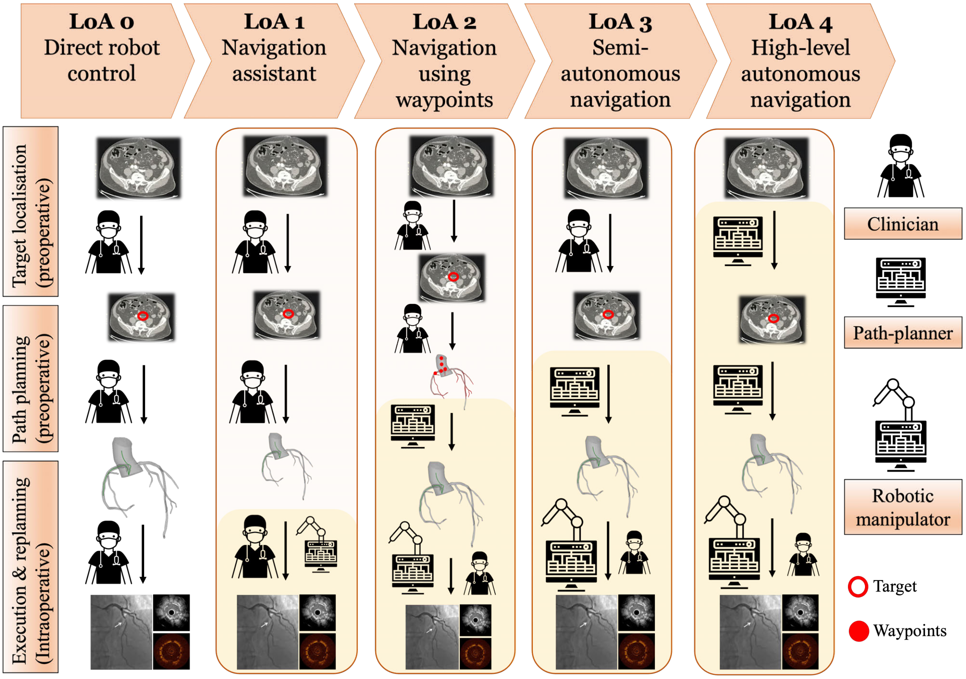

Figure 2.1: Case study examining the LoA for endovascular navigation. The case study is visually depicted as follows: (Row 1) Target localization using preoperative images. The identified target is represented by a red circle. (Row 2) Preoperative path planning. The path representation within the vessels is depicted with a yellow line. (Row 3) Intraoperative motion execution and path planning, along with visualization of intraoperative fluoroscopy. From left to right, LoA0 to LoA4 are presented, respectively. Each level indicates the agent responsible for performing each cognitive function. The agent can refer to a human operator, path planning system, or robotic manipulator. In cases where two agents are involved, the supervisor agent is depicted on the right side, while the main agent executing the actions is on the left side, with its icon displayed larger.

2.1. SYSTEMATIC REVIEW

Path planning has been extensively studied in the field of navigation since the 1980s, supporting a wide range of applications including robotic manipulators and mobile platforms in both indoor and outdoor industrial settings. During the path planning process, various robot characteristics are taken into account to determine a feasible path solution. These characteristics include the geometrical dimensions of the robot to avoid collisions and the kinematic constraints that ensure the robot's movement capabilities are respected. The robot kinematics describes the relationship between the configuration space and the task space [1]. The configuration space, denoted as $\mathscr{C}$, encompasses all possible robot configurations, while the task space, denoted as $\mathscr{T}$, represents the workspace that the robot can reach for each specific configuration $\mathbf{q}$. The general expression for robot kinematics can be described as follows:

$$\mathscr{T} = f(\mathbf{q}) \quad \mathbf{q} \in \mathscr{C} \tag{2.1}$$

Path planning plays a crucial role in autonomous Intraluminal Procedures and Endovascular Interventions (IPEI) robotic systems, even when faced with complex operating conditions and stringent safety constraints. Path planning methods are categorized into four sub-groups, adapted from the general taxonomy of path planning in robots as presented in [2]: node-based, sampling-based, optimization-based, and learning-based techniques.

Node-based (or graph-based) algorithms employ a graph-searching strategy using a tree structure. Sampling-based algorithms construct a tree structure based on random samples in the configuration space, enabling the discovery of collision-free paths that align with the robot's motion capabilities. Optimization-based algorithms formulate the path planning problem as a mathematical optimization problem, aiming to minimize or maximize an objective function subject to constraints. These algorithms employ solvers to obtain the optimal solution. Learning-based methods leverage Markov decision processes to learn goal-directed policies based on reward functions.

To conduct a comprehensive analysis of path planning developments in IPEI, a systematic review was carried out using the PRISMA methodology [3]. The review encompassed works published from 2005 to July 2022. The search terms were selected to broadly encompass the concept of "path planning for intervention". They were combined using logical operators AND and OR, enabling a thorough coverage of a wide search space. Each search query incorporated a blend of research topic, application scenario, and clinical device, such as "planning AND *vascular AND catheter". After exploring all possible combinations, the approach resulted in 520 entries. For detailed information on the search terms, methodology, and selection criteria, refer to [4]. The initial literature search identified 11,404 references. Through the application of the Prisma flow diagram, 10,833 references were excluded after the title check, followed by an additional 515 references after the abstract check. Nine references were manually included due to various reasons that prevented their coverage in the search results. This process resulted in a final list of 65 references.

The outcomes of the studies were classified based on several criteria, including the targeted procedure, LoA (see Figure 2.1), path planning method, validation techniques, and the dynamics of the environment. Figure 2.1 presents a case study examining the LoA for endovascular navigation. The entire navigation task is divided into three cognitive functions: target localization using preoperative imaging, preoperative path planning, and intraoperative motion execution and path planning. For more details, please refer to our study [4].

The path planning methods were further categorized into subgroups, as illustrated in Figure 2.2, to facilitate a detailed analysis. The evolution of path planning approaches is depicted in Figure 2.3. Up to 2016, the predominant focus in studies was on implementing node-based and sampling-based algorithms. However, in recent years, there has been a shift towards learning-based methods, facilitated by the exponential increase in computational resources. A summary of the state-of-the-art in IPEI path planning publications is presented in Table 2.1. Additionally, Table 2.1 indicates that certain studies involved intraoperative path replanning in dynamic environments, as denoted in the last column.

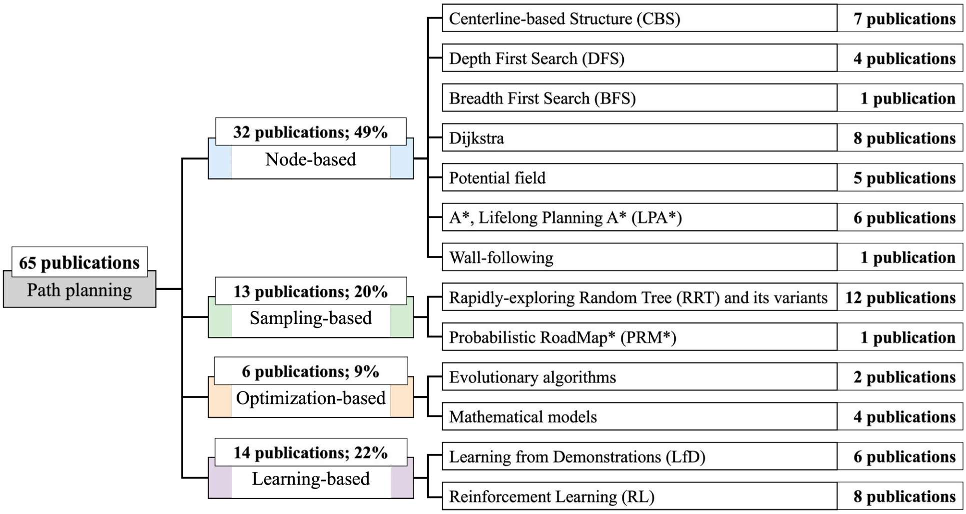

Figure 2.2: Classification of IPEI path planning methods for continuum robots found in the literature.

2.1.1. NODE-BASED ALGORITHMS

Node-based algorithms utilize an information structure to represent the environment map and are frequently employed in navigation assistance [2]. Table 2.1 presents a compilation of various path planning studies for IPEI that utilize node-based methods. The algorithms depicted in Figure 2.2 include Centerline-based Structure (CBS), Depth First Search (DFS), Breadth First Search (BFS), Dijkstra, potential field, A*, Lifelong Planning A* (LPA*), and wall-following.

Centerline-based Structure Geiger *et al.* [5] employ a methodology for bronchoscopy planning that involves extracting the 3D skeleton by computing the skeleton of the segmented structure. The resulting skeleton is then transformed into a hierarchical tree

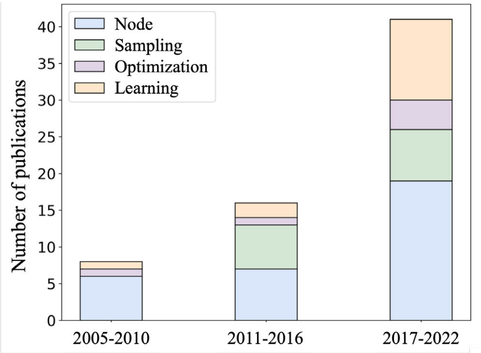

Figure 2.3: Chronological development of path planning approaches.

model consisting of interconnected branches.

S'anchez *et al.* [6] utilize the fast marching method to obtain the skeleton of the bronchial anatomy. The skeleton branching points are then defined as a binary tree (B-tree). In their study, a path is derived by traversing the B-tree nodes, and a geometry likelihood map is employed to match the current exploration to the preoperative path.

Khare *et al.* [7] represent airway centerlines as discrete sets of airway branches, which serve as natural pathways for navigation through the airway tree. Their method automatically derives a navigation plan from each target Region of Interest (ROI) associated airway route. The navigation plan adheres to the rotate-flex-advance paradigm learned by physicians during their training. This rotate-flex-advance paradigm involves initially rotating the device through wrist-twisting either clockwise or counterclockwise, followed by articulating, achieved by thumb flexion on the control lever to adjust the device's tip upwards or downwards, and concluding with translational movements, which include advancing or retracting the device [7, 8]. This navigation approach is evaluated in both phantom and human studies.

Wang *et al.* [9] develop a navigation information tree based on the centerline of the vasculature for catheterization. The authors assume a rigid vascular system and utilize the tree structure to identify the nearest node during intraoperative navigation. Experimental validation is performed on a resin vessel phantom. Another study proposes a method for extracting the centerline of 3D vasculature using a Voronoi diagram [10]. The centerlines are considered as minimal action paths on the Voronoi diagrams within the vascular model surface. The results demonstrate the effectiveness of this approach in extracting the centerlines of the vessel model.

Zheng *et al.* [11] present a two-step approach for bronchoscopy navigation. Firstly, they employ a parallel thinning algorithm to extract the preoperative 3D skeleton. Secondly, a graph matching method is used to establish correspondence between the 3D preoperative skeleton and the 2D intraoperative skeleton extracted from fluoroscopic images. However, the proposed graph matching technique is sensitive to topology variations and transformations in the sagittal and transverse planes. In a recent study on transnasal exploration, Yudong *et al.* [12] propose a central path extraction algorithm based on pre-planning for the roaming area.

However, a common limitation of the existing literature on this topic is the focus on constructing an information structure, while neglecting the exploration of paths within the information structure [5, 6, 7, 9, 10, 11]. Although tree structures are built, the autonomous generation of path solutions through graph search strategies remains unexplored. This gap in the methodology can lead to uncertainties in the path solution, especially when multiple viable paths to the target exist.

Depth First Search Several studies have employed DFS as a method to explore tree structures or graphs in the context of endobronchial ultrasound bronchoscopes and endovascular interventions.

Zang *et al.* [13, 14] implemented a route search strategy using DFS for an integrated endobronchial ultrasound bronchoscope. They explored a graph by expanding the most promising node along the depth. Similarly, Gibbs *et al.* [15] utilized DFS as a first phase search to view sites, followed by a second search focused on ROI localization, and a final refinement to adjust the viewing directions of the bronchoscope. Huang *et al.* [16] also developed a DFS approach for endovascular interventions. In their work, instead of considering path length as node weights in the typical DFS approach, they defined the node weights as an experience value set by doctors.

It is important to note that the search time and the resulting planned path can significantly vary depending on the order of nodes within the same graph layer. Although DFS can search for a feasible path by exploring the graph along the depth, it does not guarantee that the first path found is the optimal path.

Breadth First Search The BFS algorithm was utilized in Fischer *et al.* [17] to find a path for a magnetically-actuated catheter, specifically along vascular centerline points towards a target. However, the BFS algorithm may require significantly more time to find a solution in complex vascular environments with multiple branches.

Dijkstra In Schafer *et al.* [18], a graph structure based on vasculature's centerlines is designed using a volume growing and a wavefront technique. The optimal path is determined using the shortest path algorithms from Dijkstra. However, it is important to note that Schafer *et al.* make the assumption that the centerline points are provided as an ordered set, which can be a strict assumption. Additionally, they only report on scenarios with a single lumen and no branches, which does not fully reflect the advantages of the Dijkstra algorithm. Similarly, Egger *et al.* [19] present a similar method, but in a backward direction. They determine an initial path using Dijkstra, where users define the initial and destination points. The initial path is then aligned with the blood vessel, resulting in the vasculature's centerline. However, this methodology is not fully autonomous and involves manually tuned parameters.

Another approach, presented in Liu *et al.* [20], involves extracting the centerline and placing a series of guiding circular workspaces along the navigation path that are perpendicular to the path. These circular planes collectively form a safe cylindrical path from the start to the target. The Dijkstra algorithm is implemented in several works to find the minimal cumulative cost set of voxels within the airway tree for bronchoscope navigation [21, 22] and to find the shortest path along the vessel's centerline [23, 24, 25].

Compared to DFS, the Dijkstra algorithm keeps track of and checks the cost until it reaches the target, increasing the likelihood of obtaining a better solution. However, it should be noted that these studies still primarily focus on tracking anatomical centerlines, which can be challenging to precisely follow and may not always be desirable. Aligning the instrument tip with the centerline can result in excessive forces at more proximal points along the instrument's body where contact with the anatomy occurs.

Potential field In the work by Rosell *et al.* [26], a potential field is computed over grids based on the L1 distance to obstacles for bronchoscopy path planning. Wavefront propagation is used to search for a path, taking into account geometry and kinematic constraints to select the best motion based on a cost function. Yang *et al.* [27] extract centerlines using a distance field method and then establish and navigate a tree structure. However, it is important to note that the authors only considered the curvature constraint at 180° turns along vasculature's centerlines and assumed that all path points have the same Y coordinate.

Martin *et al.* [28] employ a potential field approach by defining an attractive force from the endoluminal image center mass to the colon center mass. They reconstruct a linear translation between the colon center mass and the image center, considering it as the linear motion of the colonoscope tip. This work is validated in both synthetic colon and pig colon (*in-vivo*) settings. Zhang *et al.* [29] follow a similar approach, using a robotic endoscope platform to bring surgical instruments to the target site. Girerd *et al.* [30] utilize a 3D point cloud representation of a tubular structure and compute a repulsive force to ensure that the concentric tube needle tip remains inside the contour.

The potential field method has an advantage in local planning by keeping the center of the image close to the center of the lumen or vessel cross-section. However, it primarily considers short-term benefits during local planning and may encounter difficulties in achieving global optimality during global path planning, potentially getting stuck in a local minimum.

A* and Lifelong Planning A* He *et al.* [31] compute and optimize endoscopic paths using the A* algorithm. The effectiveness of the preoperatively planned path is verified through an automatic virtual nasal endoscopy browsing experiment. Ciobirca *et al.* [32] search for the shortest airway paths through voxels of a bronchus model using the A* algorithm, suggesting that this method could potentially improve the diagnostic success rate with a system for tracking the bronchoscope during a real procedure. However, this claim has not been validated yet.

Some studies propose path planning methods for CTRs in brain surgery. The authors of these studies build a nearest-neighbor graph and utilize the LPA* algorithm for efficient replanning to optimize the insertion pose [33, 34]. Compared to A*, LPA* [35] can reuse information from previous searches to accelerate future ones. Ravigopal *et al.* [36] propose a modified hybrid A* algorithm to navigate a tendon-actuated coaxially aligned steerable guidewire robot along a pre-computed path in 2D vasculature phantoms under C-arm fluoroscopic guidance. Huang *et al.* [37] demonstrate colon navigation using a real-time heuristic searching method called Learning real-time A* (LRTA*). LRTA* with a designed directional heuristic evaluation shows efficient performance in colon exploration compared to BFS and DFS. Directional biasing avoids the need for unnecessary searches by constraining the next state based on local trends.

A* and LPA* algorithms utilize a heuristic method to approximate the cost of the cheapest path from the current node to the target. This strategy directs their exploration through the graph, prioritizing the most likely paths. Typically, this heuristic is represented by the Euclidean distance between the current node and the target. Additionally, it can encompass costs associated with the robot's functional abilities, like the expense incurred from altering the curvature radius [36]. A* is commonly used for static environments, while LPA* can adapt to changes in the environment. They converge quickly while ensuring optimality by considering both the cost from the start and the cost to the goal. However, their execution performance depends on the accuracy of the heuristic information. If inaccurate heuristic information is employed, searching in non-optimal directions can severely impact their performance.

Wall-following In the study by Fagogenis *et al.* [38], a wall-following algorithm is used to assist catheter navigation. They employ haptic vision to accomplish wall-following inside the blood-filled heart for a catheter. The wall-following algorithm can be considered an efficient navigation approach when there are few feasible routes to reach the target state. However, the solution provided by a wall-following algorithm does not guarantee optimality when multiple options exist.

2.1.2. SAMPLING-BASED ALGORITHMS

As evident from the references listed in Table 2.1, various studies in the field of path planning for IPEI utilize sampling-based methods. Illustrated in Figure 2.2, these methods include algorithms based onRapidly-exploring Random Tree (RRT) and its variants, as well as Probabilistic RoadMap* (PRM*).

Rapidly-exploring Random Tree and its variants Several studies have conducted comparisons among various algorithms based on RRT in the context of virtual bronchoscopy simulation. These algorithms include RRT, RRT-Connect, dynamic-domain RRT, and RRT-Connect with dynamic-domain [39, 40]. The results indicate that RRT-Connect with Dynamic Domain is the optimal method, as it requires the minimum number of samples and computation time to find a solution path. Fellmann *et al.* use a collision-free path generated by RRT as a baseline in their work [41]. They then apply and evaluate different trajectory generation strategies. In narrow and straight nasal passages, the synchronous point-to-point strategy is found to be the most effective. However, as the distance between intermediate configurations increases, this strategy may become infeasible. Kuntz *et al.* introduce a three-step planning approach using an RRT-based algorithm for a novel transoral lung system that includes a bronchoscope, a CTR, and a bevel-tip needle [42]. Their approach takes into account the needle steering capability during path planning and demonstrates the motion planner's ability to adhere to a maximum needle steering curvature. The time required to find a motion plan depends significantly on the steering capability and the target location.

The research conducted by Guo *et al.* [43] introduces an enhanced version of the Rapidly-exploring RRT algorithm for cerebrovascular intervention. In their study, they optimize the expansion direction of the random tree by considering a trade-off between the newly sampled node and the target. This approach aims to improve the convergence speed of the algorithm, even in scenarios where catheter constraints are not taken into account.

The approach introduced by Alterovitz *et al.* [44] presents a modified version of the Rapidly-exploring RoadMap (RRM) method. Similar to the RRT, the RRM algorithm explores the configuration space to find a path. However, the RRM method includes an additional step that refines the explored space by adding edges to the current roadmap. This refinement process aims to find higher-quality paths within the explored space. The method is initially proposed for planning in tubular environments with protrusions, such as bronchial tubes in lung procedures.

The RRM method has been further developed and enhanced in subsequent studies. Torres *et al.* [45] improve the RRM method by incorporating more accurate mechanics-based models. They apply this enhanced method in skull base surgery scenarios, where the planner successfully avoids bone, critical blood vessels, and healthy brain tissue while reaching the skull base tumor. In a later work [46], Torres *et al.* propose a modified Rapidly-exploring Random Graph (RRG) method that computes motion plans at interactive rates. This modification improves the computation cost and allows for replanning when the robot tip position changes. However, it should be noted that generating such a roadmap still requires a significant amount of computation. As a result, while the method performs well in static environments, its effectiveness in deformable lumens may be limited.

Fauser *et al.* utilize the formulation of bi-directional RRT (or bi-RRT) (RRT-connect), previously introduced by them, to address a common path planning challenge in which instruments must adhere to curvature-constrained trajectories. This approach is discussed in their earlier work [47] and is employed to solve the problem in [48]. In a subsequent study [49], the RRT-connect algorithm is implemented for path planning of a catheter in a 3D static aorta model. The algorithm ensures that the catheter follows a trajectory with a maximum allowable curvature of $0.1\,\mathrm{mm}^{-1}$. In an extension of their research, Fauser *et al.* propose path replanning from various robot positions along the initial path, starting from the descending aorta and leading to the left ventricle [50].

Probabilistic RoadMap* Kuntz *et al.* present an approach that combines the PRM* method with local optimization to plan motions in a point cloud representation of a nasal cavity anatomy [51]. It should be noted that this approach has a limitation: the anatomy model is updated only within the visible region of the endoscope, neglecting deformations in the remaining anatomy. This planning method can be applicable for intraoperative planning in cases where tissue deformation is insignificant. However, if significant deformations are expected, the overall model's deformations need to be accounted for in advance.

2.1.3. OPTIMIZATION-BASED ALGORITHM

Path planning can be framed as an optimization problem and addressed using numerical solvers [52]. These solvers can be customized to incorporate considerations of robotic kinematics.

Mathematical model Lyons *et al.* [53] propose an optimization-based planning algorithm for Concentric Tube Robots (CTRs) with five tubes, aiming to optimize the insertion length and orientation angle of each tube. The authors formulate the path planning problem as a non-linear constrained optimization problem. To simplify the problem, they incorporate the constraint into the objective function, resulting in a series of unconstrained optimization problems. The optimal solution is then obtained using the Limited-memory Broyden-Fletcher-Goldfarb-Shanno (L-BFGS) algorithm [54] and Armijo's Rule [55]. In their work, the robot kinematics are modeled using a physically-based simulation that incorporates beam mechanics. The evaluation of this method is conducted through simulation on a patient's lung anatomy. However, it is important to note that the computation time required by the proposed approach is relatively high, which limits its practical applicability in real-time scenarios. Additionally, the authors manually define the skeleton and assume rigid body behavior, which may restrict the generalizability of their findings.

Qi *et al.* [56] propose an Inverse Kinematics (IK) path planning method for continuum robots, formulated as an optimization problem based on the backbone curve method. This technique aims to minimize the distance to the vasculature's centerline under kinematic constraints at each step independently. However, it should be noted that this approach does not consider long-term cumulative costs or the influence of past and future phases. Consequently, the optimality of the IK solution achieved in this manner may not be globally optimal.

Guo *et al.* [57] utilized directional modeling of a teleoperated catheter and proposed a hybrid evaluation function to determine the optimal trajectory. In their work, wall-hit experiments were conducted to compare the obstacle avoidance response time with and without path planning. However, it is worth noting that the optimal solution was obtained through exhaustive enumeration, which can be computationally expensive. Abah *et al.* [58] approached path planning as a nonlinear least-squares problem, aiming to minimize the passive deflection of the steerable catheter. They achieved this by closely matching the shape of the steerable segment to the cerebrovascular's centerline. However, it should be acknowledged that the centerline may not necessarily represent the optimal reference route for steerable catheters.

Evolutionary algorithms An enhanced Ant Colony Optimization (ACO) method is introduced for optimal vascular path planning, considering factors such as catheter diameter, vascular length, diameter, as well as curvature and torsion [59]. The computation time associated with this method ranged from 2 s to 30 s, with an average of 12.32 s. However, the high computation time restricts its practical application in real-time scenarios. Li *et al.* [60] proposed a rapid path planning approach under the constraint of steerable catheter curvature using a local Genetic Algorithm (GA) optimization. The reported results demonstrate the planner's ability to satisfy the curvature constraint of the robot while maintaining a low computation time cost.

2.1.4. LEARNING-BASED ALGORITHMS

Learning-based techniques offer a promising solution for real-time path planning, leveraging statistical tools like artificial neural networks, Hidden Markov models (HMMs), and dynamical models to establish mappings between perceptual and behavioral spaces. In the context of this article, two sub-fields of learning methods have been identified: LfD and Reinforcement Learning (RL) approaches.

Learning from Demonstrations Rafii-Tari *et al.* introduced a collaborative human-robot system for catheterization, where the procedure is decomposed into catheter movement primitives modeled using HMMs and learned through LfD [61]. Additionally, a higher-level HMM is employed to sequence these motion primitives. In another work by the same authors, they presented a semi-automated navigation approach, where guidewire manipulation is controlled manually while catheter motion is automated using a Gaussian Mixture Model (GMM) based on temporally aligned phase data from demonstrations [62]. Chi *et al.* extended this work by incorporating subject-specific anatomical information from preoperative image data to account for variability among type I aortic arches [63]. The learning process in all these methods involved expectation maximization for maximum-likelihood estimation of model parameters. In a different study, a LfD method based on Dynamical Movement Primitives (DMPs) was employed to avoid undesired contact between the catheter tip and the vessel wall [64]. DMPs serve as compact representations of motion primitives defined by dynamic system equations [65]. The proposed robotic catheterization platform utilized DMPs trained from human demonstrations to generate motion trajectories, adapting to various flow simulations, vascular models, and catheterization tasks. Building upon their previous work, Chi *et al.* further improved the RL component by incorporating a model-free Generative Adversarial Imitation Learning (GAIL) loss that learns from multiple expert demonstrations [66]. This enhancement enabled the catheterization policies to adapt to real-world setups and successfully replicate the task despite uncertainties in simulated parameters such as blood flow and tissue-tool interaction. Another study by Zhao *et al.* proposed a Generative Adversarial Network (GAN) framework that combines Convolutional Neural Network (CNN) and Long Short Term Memory (LSTM) networks to estimate suitable manipulation actions for catheterization [67]. The Deep Neural Network (DNN) in this framework was trained using expert demonstration data and evaluated using a phantom and a grayscale camera simulating X-ray imaging.

Reinforcement Learning Trovato *et al.* developed a hardware system for a robot colonic endoscope, where classic RL algorithms such as State-Action-Reward-State-Action (SARSA) and Q-learning were used to control the propulsion voltage for forward and backward motion [68]. In recent years, Deep Reinforcement Learning (DRL) algorithms, which leverage DNNs to learn directly from high-dimensional and unstructured state inputs with minimal feature engineering, have become the state-of-the-art in RL [69]. Behr *et al.* [70], Karstensen *et al.* [71], and Meng *et al.* [72] proposed closed-loop control systems based on DRL. These systems utilize the kinematic coordinates of the guidewire tip and manipulator as inputs and generate continuous actions for rotation and translation in each degree of freedom. The translation capability was demonstrated in ex-vivo veins of a porcine liver in the work by Karstensen *et al.* [73]. To further enhance closed-loop control, You *et al.* [74] and Kweon *et al.* [75] introduced DRL-based automation of catheter control, incorporating image inputs in addition to the kinematic information. The authors trained a policy in a simulator and successfully transferred it to a real robotic system. Real robotic experiments utilized tip position data from an electromagnetic sensor, which was sent to the simulator to emulate the virtual image input.

Pore *et al.* introduced a deep visuomotor control approach for transanal interventional procedures, where endoscopic images were mapped to control signals [76]. The study demonstrated efficient colon navigation in various in-silico colon models and outperformed human experts in terms of overall trajectory properties. Tracheotomy is another area where applications of DRL have emerged. Athiniotis *et al.* utilized a snake-like clinical robot for autonomous navigation through the airway [77]. Their work employed a navigation policy based on Deep Q-Network (DQN), utilizing images from a monocular camera mounted on the robot's tip. The system serves as an assistive device for medical personnel, facilitating endoscopic intubation with minimal human intervention.

Table 2.1: Summary of path planning methods for IPEI navigation

Ref.	Procedure	Method	Robot	Kinematics	Validation	Environment
Level 1: Navigation assistant						
Node-based:						
[5] Geiger 2005	Transoral	CBS	Bronchoscope	N	in-silico (3D pulmonary vessels)	Static
[18] Schafer 2007	Endovascular	Dijkstra	Guidewire	N	in-vitro (3D cardiovascular)	Static
[19] Egger 2007	Endovascular	Dijkstra	Catheter	N	in-silico (3D aorta)	Static
[21] Gibbs 2007	Transoral	Dijkstra	Bronchoscope	N	in-silico (3D bronchus)	Static
[22] Gibbs 2008	Transoral	Dijkstra	Bronchoscope	N	in-silico (3D bronchus)	Static
[20] Liu 2010	Endovascular	Dijkstra	Catheter	N	in-vitro (3D aorta)	Static
[9] Wang 2011	Endovascular	CBS	Catheter	N	in-vitro (3D resin vessel)	Static
[16] Huang 2011	Endovascular	DFS	Guidewire	N	in-silico (3D aorta)	Static
[26] Rosell 2012	Transoral	Potential field	Bronchoscope	Y	in-silico (3D tracheobronchial)	Static
[15] Gibbs 2013	Transoral	DFS	Bronchoscope	Y	in-vivo (3D bronchus)	Dynamic
[10] Yang 2014	Endovascular	CBS	Guidewire	N	in-silico (3D aorta)	Static
[7] Khare 2015	Transoral	CBS	Bronchoscope	Y	in-vivo (3D bronchus)	Dynamic
[6] Sánchez 2016	Transoral	CBS	Bronchoscope	N	in-silico (3D bronchus)	Static
[11] Zheng 2018	Endovascular	CBS	Catheter	N	in-vitro (3D aorta)	Dynamic
[32] Ciobirca 2018	Transoral	A*	Bronchoscope	N	in-silico (3D bronchus)	Static
[33] Niyaz 2018	Transnasal	LPA*	Concentric tube robot	Y	in-silico (3D nasal cavity)	Static
[34] Niyaz 2019	Transnasal	LPA*	Concentric tube robot	Y	in-silico (3D nasal cavity)	Static
[13] Zang 2019	Transoral	DFS	Bronchoscope	Y	in-vivo (3D bronchus)	Dynamic
[27] Yang 2019	Transurethral	Potential field	Ureteroscope	Y	in-silico (3D ureter)	Static
[38] Fagogenis 2019	Endovascular	wall-following	Concentric tube robot	Y	in-vivo (3D cardiovascular)	Dynamic
[31] He 2020	Transnasal	A*	Endoscope	N	in-silico (3D nasal cavity)	Static
[14] Zang 2021	Transoral	DFS	Bronchoscope	Y	in-vivo (3D bronchus)	Static
[37] Huang 2021	Transanal	LRPA*	Colonoscope	Y	in-vitro (2D colon)	Dynamic
[12] Wang 2021	Transnasal	CBS	Endoscope	N	in-silico (3D nasal cavity)	Static
[36] Ravigopal 2021	Endovascular	Hybrid A*	Robotic guidewire	Y	in-vitro (2D vessel)	Static
sampling-based:						
[44] Alterovitz 2011	Transoral	RRM	Concentric tube robot	Y	in-silico (3D bronchus)	Static
[45] Torres 2011	Transnasal	RRM	Concentric tube robot	Y	in-silico (3D nasal cavity)	Static
[78] Torres 2012	Transoral	RRM	Concentric tube robot	Y	in-silico (3D bronchus)	Static
[46] Torres 2014	Transnasal	RRG	Concentric tube robot	Y	in-silico (3D nasal cavity)	Static
[41] Fellmann 2015	Transnasal	RRT	Concentric tube robot	Y	in-silico (3D nasal cavity)	Static
[42] Kuntz 2015	Transoral	RRT	Steerable needle	Y	in-silico (3D bronchus)	Static
[39] Aguilar 2017	Transoral	bi-RRT	Bronchoscope	Y	in-silico (3D bronchus)	Static
[40] Aguilar 2017	Transoral	bi-RRT	Bronchoscope	Y	in-silico (3D bronchus)	Static
[48] Fauser 2018	Endovascular	bi-RRT	Catheter	Y	in-silico (3D vena cava)	Static
[49] Fauser 2019a	Endovascular	bi-RRT	Steerable guidewire	Y	in-silico (3D aorta)	Static
[50] Fauser 2019b	Endovascular	bi-RRT	Steerable guidewire	Y	in-silico (3D aorta)	Static
[51] Kuntz 2019	Transnasal	PRM*	Concentric tube robot	Y	in-silico (3D nasal cavity)	Dynamic
[43] Guo 2021	Endovascular	RRT	Catheter	N	in-silico (cerebrovascular)	Static
Optimization-based:						
[53] Lyons 2010	Transoral endotracheal	Mathematical model	Concentric tube robot	Y	in-silico (3D bronchus)	Static
[59] Gao 2015	Endovascular	ACO	Catheter	Y	in-silico (3D lower limb arteries)	Static
[56] Qi 2019	Endovascular	Mathematical model	Continuum robot	Y	in-vitro (blood vessels)	Static
[60] Li 2021	Endovascular	GA	Catheter	Y	in-silico (3D aorta and coronaries)	Static
[57] Guo 2021	Endovascular	Mathematical model	Catheter	Y	in-silico, in-vitro (3D vessel model)	Static
[58] Abah 2021	Endovascular	Mathematical model	Catheter	Y	in-vitro (3D cerebrovascular)	Static
Learning-based:						
[67] Zhao 2022	Endovascular	LfD using GAN	Guidewire	N	in-vitro (3D vessel model)	Static
[72] Meng 2021	Endovascular	RL	Catheter	N	in-silico (3D aorta)	Static
Level 2: Navigation using waypoints						
Learning-based:						
[68] Trovato 2010	Transanal	RL	Fibre optic endoscope	N	ex-vivo (3D swine colon)	Dynamic
[62] Rafii-Tari 2013	Endovascular	LfD using GMM	Catheter	N	in-vitro (3D aorta)	Static

Continued on next page

Table 2.1 – *Continued from previous page*

Ref.	Procedure	Method	Robot	Kinematics	Validation	Environment
[61] Rafii-Tari 2014	Endovascular	LfD using H+HMM	Catheter	Y	in-vitro (3D aorta)	Static
[64] Chi 2018a	Endovascular	LfD using DMPs	Catheter	Y	in-vitro (3D aorta)	Dynamic
[63] Chi 2018b	Endovascular	LfD using GMMs	Catheter	N	in-vitro (3D aorta)	Static
[66] Chi 2020	Endovascular	LfD using GAIL	Catheter	N	in-vitro (3D aorta)	Static
Level 3: Semi-autonomous navigation						
Node-based:						
[23] Qian 2019	Endovascular	Dijkstra	Guidewire	N	in-vitro (3D femoral arteries, aorta)	Static
[30] Girerd 2020	Transnasal	Potential field	Concentric tube robot	Y	in-silico (3D nasal cavity), in-vitro (origami tunnel)	Static
[28] Martin 2020	Transanal	Potential field	Endoscope	N	in-vivo (3D colon)	Dynamic
[29] Zhang 2020	Transanal	Potential field	Endoscope	Y	in-vitro (2D colon model)	Dynamic
[25] Cho 2021	Endovascular	Dijkstra	Guidewire	N	in-vitro (2D vessel)	Static
[17] Fischer 2022	Endovascular	BFS	Catheter	N	in-vitro (2D vessel)	Static
[24] Schegg 2022	Endovascular	Dijkstra	Guidewire	N	in-silico (3D coronary arteries)	Static
Learning-based:						
[74] You 2019	Endovascular	RL	Catheter	N	in-vitro (3D heart)	Static
[70] Behr 2019	Endovascular	RL	Catheter	N	in-vitro (2D vessel)	Static
[71] Karstensen 2020	Endovascular	RL	Catheter	N	in-vitro (2D vessel)	Static
[75] Kweon 2021	Endovascular	RL	Guidewire	N	in-vitro (2D coronary artery)	Static
[76] Pore 2022	Transanal	RL	Endoscope	N	in-silico (3D colon)	Dynamic
[73] Karstensen 2022	Endovascular	RL	Guidewire	N	ex-vivo (2D venous system)	Dynamic

2.2. LIMITATIONS OF PRESENT PATH PLANNING METHODS

Path planning plays a critical role in facilitating autonomous navigation, but certain limitations impede its widespread applicability in IPEI procedures. This section aims to address and discuss the limitations associated with the aforementioned path planning methods.

Node-based Node-based algorithms employ searching strategies based on specific cost functions, ensuring the optimality and completeness of the obtained solutions. However, these algorithms exhibit several shortcomings:

(i) Inadequate Consideration of Robot Capability: Node-based algorithms often overlook the incorporation of robot kinematic constraints during path planning.

(ii) Neglect of Sensing Uncertainty: The uncertainty associated with sensing is rarely taken into account, limiting the robustness of these methods.

(iii) Limited Application to Rigid Environments: The proposed node-based methods primarily focus on rigid environments, disregarding tissue deformations that may occur during procedures.

(iv) Dependency on Accurate Anatomical Graph Structures: Node-based algorithms heavily rely on precise reconstructions of anatomical environments in the preoperative phase to construct the necessary data structures and facilitate efficient search operations. This requirement further restricts their usability.

These limitations hinder the practical application of node-based algorithms for autonomous real-time navigation in real-life conditions, despite their theoretical viability. Addressing these challenges is crucial to enhance their effectiveness and enable their successful deployment in autonomous systems.

Sampling and Optimization-based Approaches The utilization of sampling and optimization approaches offers the advantage of considering robot-specific characteristics. However, these methods encounter significant performance limitations associated with the robot model. Furthermore, when applied to continuum soft robots, as discussed in [79], modeling methods and incorporating soft constraints for obstacle collision pose ongoing challenges that are currently under investigation. Sampling-based approaches present the advantage of reduced computation time compared to optimization approaches. However, they do not guarantee optimal solutions, as their inherent property of random sampling results in "probabilistic" completeness. In other words, the feasibility of finding a path solution is not always assured. Existing optimization-based methods, primarily utilized in static environments for preoperative path planning, suffer from time-consuming computations. For instance, the average computation time can be as long as 12.32 s, as noted in [59]. To maximize the benefits of these approaches, hybrid methods that integrate multiple techniques could be employed, capitalizing on their respective strengths.

Learning-based Approaches The application of learning-based methods in robotics has experienced significant growth. However, the current challenges associated with these approaches restrict their universal use in clinical scenarios, as highlighted in [80].

Safety is a major concern in learning-based methods [81]. The utilization of Deep Neural Networks (DNNs) introduces the potential for unpredictable behavior when encountering unseen data beyond the training regime. Therefore, ensuring that the decisions made by DNN never lead to safety violations is of utmost importance [82, 83].

Furthermore, learning-based methods based on DNN necessitate a substantial amount of training data due to their inherent complexity, involving a large number of parameters and learning optimization [84]. Consequently, efficient acquisition, storage, annotation, and querying of massive amounts of data become essential [85]. However, in the surgical domain, obtaining high-quality diverse information is a rarity [86]. To address data limitations, various groups have proposed shared standards for device integration, data acquisition systems, and scalable infrastructure for data transmission, such as the CONDOR (Connected Optimized Network and Data in Operating Rooms) project (https://condor-h2020.eu/) and OR black box [87]. The use of simulators has become increasingly prevalent as a solution to address the issue of data scarcity. These simulators offer a controlled and data-rich environment for training and experimentation. However, a significant challenge arises when attempting to apply the insights and policies learned within these simulators to real-world scenarios. This challenge is commonly referred to as the “sim-to-real" reality gap. The crux of the issue lies in the discrepancies between the simulated environment and the real world, often due to differences in modeling and environmental variables [88, 89]. As a result, policies that are effective in a simulated setting may not perform as expected when deployed in actual conditions. Addressing this “sim-to-real" gap is crucial for the successful implementation of simulator-trained models in practical scenarios.

It is worth noting that model-free Deep Reinforcement Learning (DRL) has gained popularity in learning goal-directed behaviors and demonstrated promising success in controlled robotic environments [80]. Commonly used algorithms include PPO (Proximal Policy Optimization) [90] and SAC (Soft Actor-Critic) [91]. However, model-free DRL exhibits several limitations. Firstly, the design of an implicit reward function necessitates domain knowledge of the environment’s dynamics, which can be highly complex for deformable objects and tissues [80, 92, 93]. Secondly, sensitivity to hyperparameters and under-optimized parameters can significantly impact performance, requiring significant time investment in hyperparameter tuning. Thirdly, learning from high-dimensional inputs like images poses challenges compared to low-dimensional state features such as robot kinematic data and often encounters generalization problems due to the high capacity of DNNs [80]. Finally, continuum robots, such as endoscopes, introduce additional dimensionality to the action space due to their complex architectures and high number of Degrees of Freedom (DoFs), unlike industrial robots [94]. Certain algorithmic difficulties are associated with restricted policy search.

LfD is a popular approach for acquiring human gestures within the realm of imitation learning [95]. Nevertheless, LfD methods face a notable limitation: they necessitate a substantial number of demonstrations for effective training, which proves impractical in clinical settings due to time constraints, resource limitations, and ethical considerations. Additionally, LfD primarily allows the robot to perform at the level demonstrated by humans, as significant deviations from the demonstrated data can result in unstable policy learning [96].

2.3. FUTURE DIRECTIONS

Navigation is one of the crucial interventional phases of an IPEI procedure. The need for automation in IPEI navigation will increasingly support the adoption of novel path planning techniques capable of working in unstructured and dynamic luminal environments. This section describes the improvements in path planning algorithms that have been applied in other robotics domains and can be extended to IPEI. Moreover, robot navigation relies on robot design and its sensing capabilities. Therefore, the essential robotics capabilities that are yet to be developed to enable navigation systems with a higher level of autonomy, such as Level of Autonomy 4 (LoA 4), are discussed.

Path planning for continuum robots presents a complex challenge due to the existence of numerous configurations and multiple internal DoFs that must be coordinated to achieve purposeful motion [94, 97]. Among the 65 publications reviewed, 32 focus on path planning for the robot without considering its kinematics, as outlined in Table 2.1. It is imperative for future studies to prioritize incorporating robotic constraints into active path planning. Additionally, in order to navigate through deformable environments, replanning is required based on sensory information. The objective of replanning is to minimize navigation errors measured by predefined metrics. Hence, computational efficiency in path planning becomes crucial for real-time scenarios.

Exploring novel studies on path planning for steerable needles in neurosurgery can provide inspiration for IPEI applications, as these studies consider curvature constraints of robotic needles. Liu *et al.* propose the use of parallel path exploration in their Adaptive Fractal Trees (AFT) method for a programmable bevel-tip steerable needle [98]. This approach utilizes fractal theory and Graphics Processing Units (GPUs) architecture to parallelize the planning process, thereby improving computational performance and enabling online replanning, as demonstrated in simulated 3D liver needle insertions. Subsequently, an Adaptive Hermite Fractal Tree (AHFT) is introduced, combining AFT with optimized geometric Hermite curves to satisfy heading and targeting curvature constraints in path planning [99]. Although originally developed and tested for preoperative neurosurgery, AHFT is well-suited for GPU parallelization to facilitate rapid replanning.

Hybrid approaches have the potential to leverage the strengths of individual methods and overcome their limitations. Learning-based approaches, for instance, can be combined with other techniques to enhance performance. Wang *et al.* propose a hybrid approach that combines RL and RRT algorithms for path planning in narrow passages [100]. This method enhances the ability to explore local space while ensuring efficient global path planning. Other authors have also presented hybrid path planning methods for IPEI navigation. For instance, Meng *et al.* propose a hybrid method that utilizes BFS and GA for micro-robot navigation in blood vessels of rat livers, aiming to minimize energy consumption [101].

Optimization-based methods have gained significant attention as a means to obtain optimal preoperative plans while considering complex constraints. Granna *et al.* implement Particle Swarm Optimization (PSO) for a concentric tube robotic system in neurosurgery [102]. Micro-robot path planning in rigid arteries under a minimum effort criterion utilizes Dynamic Programming [103]. However, the reduction of search space for constrained optimization problems is crucial for intraoperative path planning. Howell *et al.* propose an augmented Lagrangian trajectory optimizer solver that addresses general nonlinear state and input constraints, offering fast convergence and numerical robustness [104]. The application of an efficient optimization solver with reduced search space holds potential for intraoperative planning in IPEI scenarios.

As illustrated in Figure 2.3, recent research has witnessed a shift towards learning-based approaches, which have demonstrated promising success. Ensuring provable behavior using DNN remains an open problem, and it is essential to incorporate safety constraints to automate IPEI navigation tasks and prevent hazardous actions. Some studies propose safe RL frameworks that utilize barrier functions to restrict robot actuation within a safe workspace [105, 81], with behavior formally verified to ensure safety [82, 83]. Large policy updates in gradient-based optimization can lead to unsafe robot behavior. To mitigate this issue, the policy update can be constrained within a trust region, promoting monotonic improvement in policy performance. Some works employ f-divergence methods, such as KL-divergence, to restrict the policy search from being overly greedy [90]. To tackle issues like high costs, environmental interaction risks, and data inefficiency in current DRL methods, recent research has shifted focus to offline RL, which learns exclusively from static datasets of previously collected experiences [106].

Commonly used model-free RL techniques often overlook the dynamics of the environment [107]. However, complexities such as pulsatile flow within the vasculature or nonlinear behavior of instruments pose challenges for implementing model-free algorithms and necessitate problem simplification. Consequently, the future trend may involve the adoption of model-based approaches in endoluminal or endovascular environments [108]. Model-based approaches are sample-efficient and require less training data [109]. Hierarchical RL is an untapped field for addressing long navigation tasks, as it subdivides the interventional phase into steps and applies specific policies to each step, adapting to their specific requirements. The entire navigation task of IPEI can be divided and incrementally learned [110]. Recently, curriculum learning has been proposed to facilitate learning in increasingly complex environments [111].

2.4. CONCLUSION

Navigation is a pivotal element in the success of IPEI procedures, demanding exceptional levels of dexterity and proficiency in interventional techniques. The incorporation of autonomous navigation systems stands to revolutionize IPEI procedures by streamlining operational processes. This advancement enables interventionists to shift their focus from the complexities of instrument manipulation to the critical medical aspects of the procedure. This chapter conducts a thorough systematic review of various path planning techniques currently employed in IPEI navigation. This review is crucial as it sheds light on the capabilities and constraints of existing methodologies. One key aspect of this chapter is its focus on identifying and addressing the limitations of current methods. Addressing these limitations is essential for enhancing the autonomy of existing robotic systems. Improvements in autonomy are envisaged in areas such as enhanced path planning approaches and the augmentation of robotic functions, including more sophisticated actuation and precise proprioception modeling. The adoption of autonomous navigation in IPEI promises to broaden the accessibility of these advanced medical procedures to a wider patient demographic.

BIBLIOGRAPHY

[1] Bruno Siciliano, Oussama Khatib, and Torsten Kröger. *Springer handbook of robotics*. Vol. 200. Springer, 2008. DOI: `10.1007/978-3-319-32552-1`.

[2] Liang Yang, Juntong Qi, Dalei Song, Jizhong Xiao, Jianda Han, and Yong Xia. "Survey of robot 3D path planning algorithms". In: *Journal of Control Science and Engineering* (2016). DOI: `10.1155/2016/7426913`.

[3] Matthew J Page, Joanne E McKenzie, Patrick M Bossuyt, Isabelle Boutron, Tammy C Hoffmann, Cynthia D Mulrow, Larissa Shamseer, Jennifer M Tetzlaff, Elie A Akl, Sue E Brennan, et al. "The PRISMA 2020 statement: an updated guideline for reporting systematic reviews". In: *Bmj* 372 (2021). DOI: `10.1016/j.ijsu.2021.105906`.

[4] Ameya Pore, Zhen Li, Diego Dall'Alba, Albert Hernansanz, Elena De Momi, Arianna Menciassi, Alicia Casals Gelpí, Jenny Dankelman, Paolo Fiorini, and Emmanuel Vander Poorten. "Autonomous Navigation for Robot-Assisted Intraluminal and Endovascular Procedures: A Systematic Review". In: *IEEE Transactions on Robotics* 39.4 (2023), pp. 2529–2548. DOI: `10.1109/TRO.2023.3269384`.

[5] Bernhard Geiger, Atilla P. Kiraly, David P. Naidich, and Carol L. Novak. "Virtual bronchoscopy of peripheral nodules using arteries as surrogate pathways". In: *Medical Imaging 2005: Physiology, Function, and Structure from Medical Images*. Ed. by Amir A. Amini and Armando Manduca. SPIE, 2005. DOI: `10.1117/12.595734`.

[6] Carles Sánchez, Marta Diez-Ferrer, Jorge Bernal, F. Javier Sánchez, Antoni Rosell, and Debora Gil. "Navigation Path Retrieval from Videobronchoscopy Using Bronchial Branches". In: *Clinical Image-Based Procedures. Translational Research in Medical Imaging*. Springer International Publishing, 2016, pp. 62–70. DOI: `10.1007/978-3-319-31808-0_8`.

[7] Rahul Khare, Rebecca Bascom, and William E Higgins. "Hands-free system for bronchoscopy planning and guidance". In: *IEEE Transactions on Biomedical Engineering* 62.12 (2015), pp. 2794–2811. DOI: `10.1109/TBME.2015.2401514`.

[8] SM Nadeem. "Fiberoptic bronchoscopy: the technique". In: *educational material from Committee for European Education in Anesthesiology.[Online]* (2009).

[9] Junchen Wang, Takashi Ohya, Hongen Liao, Ichiro Sakuma, Tianmiao Wang, Iwai Tohnai, and Toshinori Iwai. "Intravascular catheter navigation using path planning and virtual visual feedback for oral cancer treatment". In: *The International Journal of Medical Robotics and Computer Assisted Surgery* 7.2 (2011), pp. 214–224. DOI: `10.1002/rcs.392`.

[10] Fan Yang, Zeng-Guang Hou, Shao-Hua Mi, Gui-Bin Bian, and Xiao-Liang Xie. “Centerlines extraction for lumen model of human vasculature for computer-aided simulation of intravascular procedures”. In: *Proceeding of the 11th World Congress on Intelligent Control and Automation*. IEEE. 2014, pp. 970–975. DOI: `10.1109/WCICA.2014.7052847`.

[11] Jian-Qing Zheng, Xiao-Yun Zhou, Celia Riga, and Guang-Zhong Yang. “Towards 3d path planning from a single 2d fluoroscopic image for robot assisted fenestrated endovascular aortic repair”. In: *International Conference on Robotics and Automation (ICRA)*. IEEE. 2019, pp. 8747–8753. DOI: `10.1109/ICRA.2019.8793918`.

[12] WANG Yudong, HAN Jing, PAN Junjun, WANG Jing, CAO Yi, ZHU Li, and LUO Yanlin. “Rapid Path Extraction and Three-Dimensional Roaming of the Virtual Endonasal Endoscope”. In: *Chinese Journal of Electronics* 30.3 (2021), pp. 397–405. DOI: `10.1049/cje.2021.03.002`.

[13] Xiaonan Zang, Jason D Gibbs, Ronnarit Cheirsilp, Patrick D Byrnes, Jennifer Toth, Rebecca Bascom, and William E Higgins. “Optimal route planning for image-guided EBUS bronchoscopy”. In: *Computers in biology and medicine* 112 (2019), p. 103361. DOI: `10.1016/j.compbiomed.2019.103361`.

[14] Xiaonan Zang, Ronnarit Cheirsilp, Patrick D Byrnes, Trevor K Kuhlengel, Catherine Abendroth, Thomas Allen, Rickhesvar Mahraj, Jennifer Toth, Rebecca Bascom, and William E Higgins. “Image-guided EBUS bronchoscopy system for lung-cancer staging”. In: *Informatics in medicine unlocked* 25 (2021), p. 100665.

[15] Jason D Gibbs, Michael W Graham, Rebecca Bascom, Duane C Cornish, Rahul Khare, and William E Higgins. “Optimal procedure planning and guidance system for peripheral bronchoscopy”. In: *IEEE Transactions on Biomedical Engineering* 61.3 (2013), pp. 638–657.

[16] Dongjin Huang, Wen Tang, Youdong Ding, Taoruan Wan, and Yimin Chen. “An Interactive 3D Preoperative Planning and Training System for Minimally Invasive Vascular Surgery”. In: *2011 12th International Conference on Computer-Aided Design and Computer Graphics*. 2011, pp. 443–449. DOI: `10.1109/CAD/Graphics.2011.40`.

[17] Cedric Fischer, Quentin Boehler, and Bradley J Nelson. “Using Magnetic Fields to Navigate and Simultaneously Localize Catheters in Endoluminal Environments”. In: *IEEE Robotics and Automation Letters* (2022).

[18] Sebastian Schafer, Vikas Singh, Kenneth R. Hoffmann, Peter B. Noël, and Jinhui Xu. “Planning image-guided endovascular interventions: guidewire simulation using shortest path algorithms”. In: *Medical Imaging: Visualization and Image-Guided Procedures*. SPIE, 2007.

[19] J. Egger, Z. Mostarkic, S. Grosskopf, and B. Freisleben. “A Fast Vessel Centerline Extraction Algorithm for Catheter Simulation”. In: *Twentieth IEEE International Symposium on Computer-Based Medical Systems (CBMS’07)*. 2007, pp. 177–182.

[20] H Liu, YL Fu, YY Zhou, HX Li, ZG Liang, and SG Wang. "An in vitro investigation of image-guided steerable catheter navigation". In: *Proceedings of the Institution of Mechanical Engineers, Part H: Journal of Engineering in Medicine* 224.8 (2010), pp. 945–954.

[21] Jason D Gibbs and William E Higgins. "3D path planning and extension for endoscopic guidance". In: *Medical Imaging: Visualization and Image-Guided Procedures*. International Society for Optics and Photonics. 2007.

[22] Jason D Gibbs, Michael W Graham, Kun-Chang Yu, and William E Higgins. "Integrated system for planning peripheral bronchoscopic procedures". In: *Medical Imaging: Physiology, Function, and Structure from Medical Images*. International Society for Optics and Photonics. 2008.

[23] Hanxin Qian, Xiaofeng Lin, Zonghan Wu, Quan Zeng, Chichi Li, Yi Pang, Cheng Wang, and Shoujun Zhou. "Towards Rebuild The Interventionist's Intra-Operative Natural Behavior: A Fully Sensorized Endovascular Robotic System Design". In: *2019 International Conference on Medical Imaging Physics and Engineering (ICMIPE)*. 2019, pp. 1–7. DOI: `10.1109/ICMIPE47306.2019.9098198`.

[24] Pierre Schegg, Jérémie Dequidt, Eulalie Coevoet, Edouard Leurent, Rémi Sabatier, Philippe Preux, and Christian Duriez. "Automated Planning for Robotic Guidewire Navigation in the Coronary Arteries". In: *2022 IEEE 5th International Conference on Soft Robotics (RoboSoft)*. IEEE. 2022, pp. 239–246. DOI: `10.1109/RoboSoft54090.2022.9762096`.

[25] Yongjun Cho, Jae-Hyeon Park, Jaesoon Choi, and Dong Eui Chang. "Image processing based autonomous guidewire navigation in percutaneous coronary intervention". In: *2021 IEEE International Conference on Consumer Electronics-Asia (ICCE-Asia)*. IEEE. 2021, pp. 1–6. DOI: `10.1109/ICCE-Asia53811.2021.9641975`.

[26] Jan Rosell, Alexander Pérez, Paolo Cabras, and Antoni Rosell. "Motion planning for the virtual bronchoscopy". In: *2012 IEEE International Conference on Robotics and Automation*. IEEE. 2012, pp. 2932–2937.

[27] Fan Yang, Yu Dai, Jianxun Zhang, Huijiao Sun, Liang Cui, Xiaotao Yin, Xiaofeng Gao, and Ling Li. "Path planning of flexible ureteroscope based on CT Image". In: *2019 Chinese Control Conference (CCC)*. IEEE. 2019, pp. 4667–4672. DOI: `10.23919/ChiCC.2019.8865196`.

[28] James W Martin, Bruno Scaglioni, Joseph C Norton, Venkataraman Subramanian, Alberto Arezzo, Keith L Obstein, and Pietro Valdastri. "Enabling the future of colonoscopy with intelligent and autonomous magnetic manipulation". In: *Nature Machine Intelligence* 2.10 (2020), pp. 595–606.

[29] Qi Zhang, J Micah Prendergast, Gregory A Formosa, Mitchell J Fulton, and Mark E Rentschler. "Enabling Autonomous Colonoscopy Intervention Using a Robotic Endoscope Platform". In: *IEEE Transactions on Biomedical Engineering* 68.6 (2020), pp. 1957–1968.

[30] Cedric Girerd, Andrey V Kudryavtsev, Patrick Rougeot, Pierre Renaud, Kanty Rabenorosoa, and Brahim Tamadazte. “SLAM-based follow-the-leader deployment of concentric tube robots”. In: *IEEE Robotics and Automation Letters* 5.2 (2020), pp. 548–555.

[31] Yucheng He, Peng Zhang, Xiaozhi Qi, Baoliang Zhao, Shibo Li, and Ying Hu. “Endoscopic Path Planning in Robot-Assisted Endoscopic Nasal Surgery”. In: *IEEE Access* PP (Jan. 2020), pp. 1–1. DOI: `10.1109/ACCESS.2020.2967474`.

[32] C Ciobirca, T Lango, G Gruionu, Håkon Olav Leira, LG Gruionu, and SD Pastrama. “A new procedure for automatic path planning in bronchoscopy”. In: *Materials Today: Proceedings* 5.13 (2018), pp. 26513–26518.

[33] Sherdil Niyaz, Alan Kuntz, Oren Salzman, Ron Alterovitz, and Siddhartha Srinivasa. “Following Surgical Trajectories with Concentric Tube Robots via Nearest-Neighbor Graphs”. In: *Int. Symp. Experimental Robotics (ISER)*. 2018.

[34] Sherdil Niyaz, Alan Kuntz, Oren Salzman, Ron Alterovitz, and Siddhartha S Srinivasa. “Optimizing Motion-Planning Problem Setup via Bounded Evaluation with Application to Following Surgical Trajectories”. In: *IEEE/RSJ International Conference on Intelligent Robots and Systems (IROS)*. IEEE. 2019, pp. 1355–1362.

[35] Nathan Koenig and Andrew Howard. “Design and use paradigms for gazebo, an open-source multi-robot simulator”. In: *IEEE/RSJ International Conference on Intelligent Robots and Systems (IROS)(IEEE Cat. No. 04CH37566)*. Vol. 3. IEEE. 2004, pp. 2149–2154.

[36] Sharan R Ravigopal, Timothy A Brumfiel, and Jaydev P Desai. “Automated Motion Control of the COAST Robotic Guidewire under Fluoroscopic Guidance”. In: *2021 International Symposium on Medical Robotics (ISMR)*. IEEE. 2021, pp. 1–7. DOI: `10.1109/ISMR48346.2021.9661508`.

[37] Hao-En Huang, Sheng-Yang Yen, Chia-Feng Chu, Fat-Moon Suk, Gi-Shih Lien, and Chih-Wen Liu. “Autonomous navigation of a magnetic colonoscope using force sensing and a heuristic search algorithm”. In: *Scientific reports* 11.1 (2021), pp. 1–15.

[38] G Fagogenis, M Mencattelli, Z Machaidze, B Rosa, K Price, F Wu, V Weixler, M Saeed, JE Mayer, and PE Dupont. “Autonomous robotic intracardiac catheter navigation using haptic vision”. In: *Science robotics* 4.29 (2019). DOI: `10.1126/scirobotics.aaw1977`.

[39] Wilbert G Aguilar, Vanessa Abad, Hugo Ruiz, Jenner Aguilar, and Fabián Aguilar-Castillo. “RRT-based path planning for virtual bronchoscopy simulator”. In: *International Conference on Augmented Reality, Virtual Reality and Computer Graphics*. Springer. 2017, pp. 155–165.

[40] Wilbert G Aguilar, Vanessa Abad, Hugo Ruiz, Jenner Aguilar, and Fabián Aguilar-Castillo. “Virtual bronchoscopy motion planner”. In: *IEEE XXIV International Conference on Electronics, Electrical Engineering and Computing (INTERCON)*. IEEE. 2017, pp. 1–4.

[41] Carolin Fellmann and Jessica Burgner-Kahrs. “Implications of trajectory generation strategies for tubular continuum robots”. In: *IEEE/RSJ International Conference on Intelligent Robots and Systems (IROS)*. IEEE. 2015, pp. 202–208.

[42] Alan Kuntz, Luis G Torres, Richard H Feins, Robert J Webster, and Ron Alterovitz. “Motion planning for a three-stage multilumen transoral lung access system”. In: *IEEE/RSJ International Conference on Intelligent Robots and Systems (IROS)*. IEEE. 2015, pp. 3255–3261.

[43] Jian Guo, Yue Sun, and Shuxiang Guo. “A Training System for Vascular Interventional Surgeons based on Local Path Planning”. In: *2021 IEEE International Conference on Mechatronics and Automation (ICMA)*. IEEE. 2021, pp. 1328–1333. DOI: `10.1109/ICMA52036.2021.9512808`.

[44] Ron Alterovitz, Sachin Patil, and Anna Derbakova. “Rapidly-exploring roadmaps: Weighing exploration vs. refinement in optimal motion planning”. In: *2011 IEEE International Conference on Robotics and Automation*. IEEE. 2011, pp. 3706–3712.

[45] Luis G. Torres and Ron Alterovitz. “Motion Planning for Concentric Tube Robots Using Mechanics-based Models”. In: *IEEE/RSJ International Conference on Intelligent Robots and Systems*. 2011.

[46] Luis G Torres, Cenk Baykal, and Ron Alterovitz. “Interactive-rate motion planning for concentric tube robots”. In: *IEEE International Conference on Robotics and Automation (ICRA)*. IEEE. 2014, pp. 1915–1921.

[47] Johannes Fauser, Georgios Sakas, and Anirban Mukhopadhyay. “Planning nonlinear access paths for temporal bone surgery”. In: *International journal of computer assisted radiology and surgery* 13.5 (2018), pp. 637–646. DOI: `10.1007/s11548-018-1712-z`.

[48] Johannes Fauser, Igor Stenin, Julia Kristin, Thomas Klenzner, Jörg Schipper, Dieter Fellner, and Anirban Mukhopadhyay. “Generalized trajectory planning for nonlinear interventions”. In: *OR 2.0 Context-Aware Operating Theaters, Computer Assisted Robotic Endoscopy, Clinical Image-Based Procedures, and Skin Image Analysis*. Springer, 2018, pp. 46–53. DOI: `10.1007/978-3-030-01201-4_6`.

[49] Johannes Fauser, Igor Stenin, Julia Kristin, Thomas Klenzner, Jörg Schipper, and Anirban Mukhopadhyay. “Optimizing clearance of bézier spline trajectories for minimally-invasive surgery”. In: *International Conference on Medical Image Computing and Computer-Assisted Intervention*. Springer. 2019, pp. 20–28. DOI: `10.1007/978-3-030-32254-0_3`.

[50] Johannes Fauser, Romol Chadda, Yannik Goergen, Markus Hessinger, Paul Motzki, Igor Stenin, Julia Kristin, Thomas Klenzner, Jörg Schipper, Stefan Seelecke, et al. “Planning for flexible surgical robots via Bézier spline translation”. In: *IEEE Robotics and Automation Letters* 4.4 (2019), pp. 3270–3277. DOI: `10.1109/LRA.2019.2926221`.

[51] Alan Kuntz, Mengyu Fu, and Ron Alterovitz. “Planning high-quality motions for concentric tube robots in point clouds via parallel sampling and optimization”. In: *IEEE/RSJ International Conference on Intelligent Robots and Systems (IROS)*. IEEE. 2019, pp. 2205–2212. DOI: `10.1109/IROS40897.2019.8968172`.

[52] Purushothaman Raja and Sivagurunathan Pugazhenthi. “Optimal path planning of mobile robots: A review”. In: *International journal of physical sciences* 7.9 (2012), pp. 1314–1320.

[53] Lisa A Lyons, Robert J Webster, and Ron Alterovitz. “Planning active cannula configurations through tubular anatomy”. In: *IEEE international conference on robotics and automation*. IEEE. 2010, pp. 2082–2087.

[54] Dong C Liu and Jorge Nocedal. “On the limited memory BFGS method for large scale optimization”. In: *Mathematical programming* 45.1 (1989), pp. 503–528.

[55] Mokhtar S Bazaraa, Hanif D Sherali, and Chitharanjan M Shetty. *Nonlinear programming: theory and algorithms*. John Wiley & Sons, 2013.

[56] Fei Qi, Feng Ju, Dongming Bai, Yaoyao Wang, and Bai Chen. “Kinematic analysis and navigation method of a cable-driven continuum robot used for minimally invasive surgery”. In: *The International Journal of Medical Robotics and Computer Assisted Surgery* (2019), e2007. DOI: `10.1002/rcs.2007`.

[57] Jian Guo, Han Zhao, and Shuxiang Guo. “Design A Novel of Path Planning Method for The Vascular Interventional Surgery Robot based on DWA Model”. In: *2021 IEEE International Conference on Mechatronics and Automation (ICMA)*. IEEE. 2021, pp. 1322–1327.

[58] Colette Abah, Rohan Chitale, and Nabil Simaan. “Image-Guided Optimization of Robotic Catheters for Patient-Specific Endovascular Intervention”. In: *2021 International Symposium on Medical Robotics (ISMR)*. IEEE. 2021, pp. 1–8.

[59] Ming-ke Gao, Yi-min Chen, Quan Liu, Chen Huang, Ze-yu Li, and Dian-hua Zhang. “Three-dimensional path planning and guidance of leg vascular based on improved ant colony algorithm in augmented reality”. In: *Journal of medical systems* 39.11 (2015), p. 133. DOI: `10.1007/s10916-015-0315-2`.

[60] Zhen Li, Jenny Dankelman, and Elena De Momi. “Path planning for endovascular catheterization under curvature constraints via two-phase searching approach”. In: *International Journal of Computer Assisted Radiology and Surgery* 16.4 (2021), pp. 619–627. DOI: `10.1007/s11548-021-02328-x`.

[61] Hedyeh Rafii-Tari, Jindong Liu, Christopher J Payne, Colin Bicknell, and Guang-Zhong Yang. “Hierarchical HMM based learning of navigation primitives for cooperative robotic endovascular catheterization”. In: *International Conference on Medical Image Computing and Computer-Assisted Intervention*. Springer. 2014, pp. 496–503. DOI: `10.1007/978-3-319-10404-1_62`.

[62] Hedyeh Rafii-Tari, Jindong Liu, Su-Lin Lee, Colin Bicknell, and Guang-Zhong Yang. “Learning-Based Modeling of Endovascular Navigation for Collaborative Robotic Catheterization”. In: *Advanced Information Systems Engineering*. Springer Berlin Heidelberg, 2013, pp. 369–377. DOI: `10.1007/978-3-642-40763-5_46`.

[63] Wenqiang Chi, Jindong Liu, Hedyeh Rafii-Tari, Celia Riga, Colin Bicknell, and Guang-Zhong Yang. “Learning-based endovascular navigation through the use of non-rigid registration for collaborative robotic catheterization”. In: *International Journal of Computer Assisted Radiology and Surgery* 13.6 (Apr. 2018), pp. 855–864. DOI: `10.1007/s11548-018-1743-5`.

[64] Wenqiang Chi, Jindong Liu, Mohamed EMK Abdelaziz, Giulio Dagnino, Celia Riga, Colin Bicknell, and Guang-Zhong Yang. “Trajectory Optimization of Robot-Assisted Endovascular Catheterization with Reinforcement Learning”. In: *IEEE/RSJ International Conference on Intelligent Robots and Systems (IROS)*. IEEE, Oct. 2018. DOI: `10.1109/IROS.2018.8593421`.

[65] Matteo Saveriano, Fares J Abu-Dakka, Aljaz Kramberger, and Luka Peternel. “Dynamic movement primitives in robotics: A tutorial survey”. In: *arXiv preprint arXiv:2102.03861* (2021).

[66] Wenqiang Chi, Giulio Dagnino, Trevor Kwok, Anh Nguyen, Dennis Kundrat, Mohamed E. M. K. Abdelaziz, Celia Riga, Colin Bicknell, and Guang-Zhong Yang. “Collaborative robot-assisted endovascular catheterization with generative adversarial imitation learning”. In: *IEEE International Conference on Robotics and Automation (ICRA)*. IEEE, June 2020. DOI: `10.1109/ICRA40945.2020.9196912`.

[67] Yan Zhao, Yuxin Wang, Jianhua Zhang, Xinke Liu, Youxiang Li, Shuxiang Guo, Xu Yang, and Shunming Hong. “Surgical GAN: Towards Real-time Path Planning for Passive Flexible Tools in Endovascular Surgeries”. In: *Neurocomputing* (2022). DOI: `10.1016/j.neucom.2022.05.044`.

[68] Gabriele Trovato, M Shikanai, Genya Ukawa, J Kinoshita, N Murai, JW Lee, Hiroyuki Ishii, Atsuo Takanishi, Kazuo Tanoue, Satoshi Ieiri, et al. “Development of a colon endoscope robot that adjusts its locomotion through the use of reinforcement learning”. In: *International journal of computer assisted radiology and surgery* 5.4 (2010), pp. 317–325.

[69] Volodymyr Mnih, Koray Kavukcuoglu, David Silver, Andrei A Rusu, Joel Veness, Marc G Bellemare, Alex Graves, Martin Riedmiller, Andreas K Fidjeland, Georg Ostrovski, et al. “Human-level control through deep reinforcement learning”. In: *Nature* 518.7540 (2015), pp. 529–533.

[70] Tobias Behr, Tim Philipp Pusch, Marius Siegfarth, Dominik Hüsener, Tobias Mörschel, and Lennart Karstensen. “Deep Reinforcement Learning for the Navigation of Neurovascular Catheters”. In: *Current Directions in Biomedical Engineering* 5.1 (2019), pp. 5–8. DOI: `10.1515/cdbme-2019-0002`.

[71] Lennart Karstensen, Tobias Behr, Tim Philipp Pusch, Franziska Mathis-Ullrich, and Jan Stallkamp. “Autonomous guidewire navigation in a two dimensional vascular phantom”. In: *Current Directions in Biomedical Engineering* 6.1 (2020). DOI: `10.1515/cdbme-2020-0007`.

[72] Fanxu Meng, Shuxiang Guo, Wei Zhou, and Zhengyang Chen. “Evaluation of a Reinforcement Learning Algorithm for Vascular Intervention Surgery”. In: *2021 IEEE International Conference on Mechatronics and Automation (ICMA)*. IEEE. 2021, pp. 1033–1037. DOI: `10.1109/ICMA52036.2021.9512675`.

[73] Lennart Karstensen, Jacqueline Ritter, Johannes Hatzl, Torben Pätz, Jens Langejürgen, Christian Uhl, and Franziska Mathis-Ullrich. "Learning-based autonomous vascular guidewire navigation without human demonstration in the venous system of a porcine liver". In: *International Journal of Computer Assisted Radiology and Surgery* (2022), pp. 1–8. DOI: `10.1007/s11548-022-02646-8`.

[74] Hyeonseok You, EunKyung Bae, Youngjin Moon, Jihoon Kweon, and Jaesoon Choi. "Automatic control of cardiac ablation catheter with deep reinforcement learning method". In: *Journal of Mechanical Science and Technology* 33.11 (2019), pp. 5415–5423. DOI: `10.1007/s12206-019-1036-0`.

[75] Jihoon Kweon, Kyunghwan Kim, Chaehyuk Lee, Hwi Kwon, Jinwoo Park, Kyoseok Song, Young In Kim, Jeeone Park, Inwook Back, Jae-Hyung Roh, et al. "Deep reinforcement learning for guidewire navigation in coronary artery phantom". In: *IEEE Access* 9 (2021), pp. 166409–166422. DOI: `10.1109/ACCESS.2021.3135277`.

[76] Ameya Pore, Martina Finocchiaro, Diego Dall'Alba, Albert Hernansanz, Gastone Ciuti, Alberto Arezzo, Arianna Menciassi, Alicia Casals, and Paolo Fiorini. "Colonoscopy Navigation using End-to-End Deep Visuomotor Control: A User Study". In: *arXiv preprint arXiv:2206.15086* (2022).

[77] S Athiniotis, RA Srivatsan, and H Choset. "Deep Q Reinforcement Learning for Autonomous Navigation of Surgical Snake Robot in Confined Spaces". In: *The Hamlyn Symposium on Medical Robotics*. 2019.

[78] Luis G Torres, Robert J Webster, and Ron Alterovitz. "Task-oriented design of concentric tube robots using mechanics-based models". In: *IEEE/RSJ International Conference on Intelligent Robots and Systems*. IEEE. 2012, pp. 4449–4455.

[79] Tomas da Veiga, James H Chandler, Peter Lloyd, Giovanni Pittiglio, Nathan J Wilkinson, Ali K Hoshiar, Russell A Harris, and Pietro Valdastri. "Challenges of continuum robots in clinical context: A review". In: *Progress in Biomedical Engineering* 2.3 (2020). DOI: `10.1088/2516-1091/ab9f41`.

[80] Julian Ibarz, Jie Tan, Chelsea Finn, Mrinal Kalakrishnan, Peter Pastor, and Sergey Levine. "How to train your robot with deep reinforcement learning: lessons we have learned". In: *The International Journal of Robotics Research* 40.4-5 (2021), pp. 698–721.

[81] Javier García and Fernando Fernández. "A comprehensive survey on safe reinforcement learning". In: *Journal of Machine Learning Research* 16.1 (2015), pp. 1437–1480.

[82] Ameya Pore, Davide Corsi, Enrico Marchesini, Diego Dall'Alba, Alicia Casals, Alessandro Farinelli, and Paolo Fiorini. "Safe Reinforcement Learning using Formal Verification for Tissue Retraction in Autonomous Robotic-Assisted Surgery". In: *2021 IEEE/RSJ International Conference on Intelligent Robots and Systems (IROS)*. IEEE. 2021, pp. 4025–4031.

[83] Davide Corsi, Luca Marzari, Ameya Pore, Alessandro Farinelli, Alicia Casals, Paolo Fiorini, and Diego Dall'Alba. "Constrained Reinforcement Learning and Formal Verification for Safe Colonoscopy Navigation". In: *arXiv preprint arXiv:2303.03207* (2023).

[84] Yann LeCun, Yoshua Bengio, and Geoffrey Hinton. “Deep learning”. In: *nature* 521.7553 (2015), pp. 436–444.

[85] David C Birkhoff, Anne Sophie HM van Dalen, and Marlies P Schijven. “A review on the current applications of artificial intelligence in the operating room”. In: *Surgical innovation* 28.5 (2021), pp. 611–619.

[86] Lauren R Kennedy-Metz, Pietro Mascagni, Antonio Torralba, Roger D Dias, Pietro Perona, Julie A Shah, Nicolas Padoy, and Marco A Zenati. “Computer Vision in the Operating Room: Opportunities and Caveats”. In: *IEEE transactions on medical robotics and bionics* 3.1 (2020), pp. 2–10.

[87] Mitchell G Goldenberg, James Jung, and Teodor P Grantcharov. “Using data to enhance performance and improve quality and safety in surgery”. In: *JAMA surgery* 152.10 (2017), pp. 972–973.

[88] Andrei A Rusu, Matej Večerík, Thomas Rothörl, Nicolas Heess, Razvan Pascanu, and Raia Hadsell. “Sim-to-real robot learning from pixels with progressive nets”. In: *Conference on robot learning*. PMLR. 2017, pp. 262–270.

[89] Paul Maria Scheikl, Eleonora Tagliabue, Balázs Gyenes, Martin Wagner, Diego Dall’Alba, Paolo Fiorini, and Franziska Mathis-Ullrich. “Sim-to-real transfer for visual reinforcement learning of deformable object manipulation for robot-assisted surgery”. In: *IEEE Robotics and Automation Letters* 8.2 (2022), pp. 560–567.

[90] John Schulman, Filip Wolski, Prafulla Dhariwal, Alec Radford, and Oleg Klimov. “Proximal policy optimization algorithms”. In: *arXiv preprint arXiv:1707.06347* (2017). URL: `https://arxiv.org/abs/1707.06347`.

[91] Tuomas Haarnoja, Aurick Zhou, Kristian Hartikainen, George Tucker, Sehoon Ha, Jie Tan, Vikash Kumar, Henry Zhu, Abhishek Gupta, Pieter Abbeel, et al. “Soft actor-critic algorithms and applications”. In: *arXiv preprint arXiv:1812.05905* (2018).

[92] Xingyu Lin, Yufei Wang, Jake Olkin, and David Held. “Softgym: Benchmarking deep reinforcement learning for deformable object manipulation”. In: *arXiv preprint arXiv:2011.07215* (2020).

[93] Zhen Li, Enrico Manzionna, Giovanni Monizzi, Angelo Mastrangelo, Maria Elisabetta Mancini, Daniele Andreini, Jenny Dankelman, and Elena De Momi. “Position-based dynamics simulator of vessel deformations for path planning in robotic endovascular catheterization”. In: *Medical Engineering & Physics* 110 (2022), p. 103920. DOI: `10.1016/j.medengphy.2022.103920`.

[94] Pierre Dupont, Nabil Simaan, Howie Choset, and Caleb Rucker. “Continuum Robots for Medical Interventions”. In: *Proceedings of the IEEE* (2022).

[95] Ameya Pore, Eleonora Tagliabue, Marco Piccinelli, Diego Dall’Alba, Alicia Casals, and Paolo Fiorini. “Learning from demonstrations for autonomous soft-tissue retraction”. In: *2021 International Symposium on Medical Robotics (ISMR)*. IEEE. 2021, pp. 1–7. DOI: `10.1109/ISMR48346.2021.9661514`.

[96] Seyed Kamyar Seyed Ghasemipour, Richard Zemel, and Shixiang Gu. “A divergence minimization perspective on imitation learning methods”. In: *Conference on Robot Learning*. PMLR. 2020, pp. 1259–1277.

[97] Jessica Burgner-Kahrs, D Caleb Rucker, and Howie Choset. “Continuum robots for medical applications: A survey”. In: *IEEE Transactions on Robotics* 31.6 (2015), pp. 1261–1280.

[98] Fangde Liu, Arnau Garriga-Casanovas, Riccardo Secoli, and Ferdinando Rodriguez y Baena. “Fast and adaptive fractal tree-based path planning for programmable bevel tip steerable needles”. In: *IEEE Robotics and Automation Letters* 1.2 (2016), pp. 601–608.

[99] Marlene Pinzi, Stefano Galvan, and Ferdinando Rodriguez y Baena. “The Adaptive Hermite Fractal Tree (AHFT): a novel surgical 3D path planning approach with curvature and heading constraints”. In: *International journal of computer assisted radiology and surgery* 14.4 (2019), pp. 659–670. DOI: `10.1007/s11548-019-01923-3`.

[100] Wei Wang, Lei Zuo, and Xin Xu. “A learning-based multi-RRT approach for robot path planning in narrow passages”. In: *Journal of Intelligent & Robotic Systems* 90.1-2 (2018), pp. 81–100.

[101] Ke Meng, Yuanjun Jia, Hao Yang, Fuzhou Niu, Yong Wang, and Dong Sun. “Motion Planning and Robust Control for the Endovascular Navigation of a Microrobot”. In: *IEEE Transactions on Industrial Informatics* (2019). DOI: `10.1109/TII.2019.2950052`.

[102] Josephine Granna, Arya Nabavi, and Jessica Burgner-Kahrs. “Computer-assisted planning for a concentric tube robotic system in neurosurgery”. In: *International journal of computer assisted radiology and surgery* 14.2 (2019), pp. 335–344.

[103] Mohammad Javad Pourmanda and Mojtaba Sharifib. “Navigation and control of endovascular helical swimming microrobot using dynamic programing and adaptive sliding mode strategy”. In: *Control Systems Design of Bio-Robotics and Bio-Mechatronics with Advanced Applications* (2019), p. 201.

[104] Taylor A Howell, Brian E Jackson, and Zachary Manchester. “ALTRO: A fast solver for constrained trajectory optimization”. In: *IEEE/RSJ International Conference on Intelligent Robots and Systems (IROS)*. IEEE. 2019, pp. 7674–7679.

[105] Richard Cheng, Gábor Orosz, Richard M Murray, and Joel W Burdick. “End-to-end safe reinforcement learning through barrier functions for safety-critical continuous control tasks”. In: *Proceedings of the AAAI Conference on Artificial Intelligence*. Vol. 33. 01. 2019, pp. 3387–3395.

[106] Rafael Figueiredo Prudencio, Marcos ROA Maximo, and Esther Luna Colombini. “A Survey on Offline Reinforcement Learning: Taxonomy, Review, and Open Problems”. In: *arXiv preprint arXiv:2203.01387* (2022).

[107] Xuanke You, Yixiao Zhang, Xiaotong Chen, Xinghua Liu, Zhanchi Wang, Hao Jiang, and Xiaoping Chen. “Model-free control for soft manipulators based on reinforcement learning”. In: *IEEE/RSJ International Conference on Intelligent Robots and Systems (IROS)*. IEEE. 2017, pp. 2909–2915.

[108] Thomas George Thuruthel, Egidio Falotico, Federico Renda, and Cecilia Laschi. “Model-based reinforcement learning for closed-loop dynamic control of soft robotic manipulators”. In: *IEEE Transactions on Robotics* 35.1 (2018), pp. 124–134.

[109] Junjia Liu, Jiaying Shou, Zhuang Fu, Hangfei Zhou, Rongli Xie, Jun Zhang, Jian Fei, and Yanna Zhao. “Efficient reinforcement learning control for continuum robots based on Inexplicit Prior Knowledge”. In: *arXiv preprint arXiv:2002.11573* (2020).

[110] Ameya Pore and Gerardo Aragon-Camarasa. “On Simple Reactive Neural Networks for Behaviour-Based Reinforcement Learning”. In: *2020 IEEE International Conference on Robotics and Automation (ICRA)* (2020).

[111] Yoshua Bengio, Jérôme Louradour, Ronan Collobert, and Jason Weston. “Curriculum learning”. In: *Proceedings of the 26th annual international conference on machine learning*. 2009, pp. 41–48.

I

PRE-OPERATIVE PATH PLANNING

3

PATH PLANNING FOR ENDOVASCULAR CATHETERIZATION UNDER CURVATURE CONSTRAINTS

Planning a safe path for steerable catheters is one of the major challenges of endovascular catheterization. State-of-the-art methods rarely consider the catheter curvature constraint and reduced computation time of path planning which guarantees the possibility to re-plan the path during the actual operation. In this chapter, a fast two-phase path planning approach under the robot curvature constraint is proposed. Firstly, the vascular structure is extracted and represented by vascular centerlines and corresponding vascular radii. Then, the path is searched along the vascular centerline using Breadth First Search (BFS) strategy and locally optimized via the Genetic Algorithm (GA) to satisfy the robot curvature constraint. This approach (BFS-GA) is able to respect the robot curvature constraint while keeping it close to the centerlines as much as possible. The optimization search space can also be reduced, and parallel optimization techniques can be applied to decrease the computation time. The method's high efficiency is demonstrated in both two-dimensional and three-dimensional space scenarios. The results showed the planner's ability to satisfy the robot curvature constraint while keeping a low computation time cost compared with sampling-based methods. Path replanning in femoral arteries can reach an updating frequency at 6.4 ± 2.3*Hz. The presented work is suited for surgical procedures demanding satisfying curvature constraints while optimizing specified criteria. It is also applicable for curvature-constrained robots in narrow passages.*

This chapter is available as:
Zhen Li, Jenny Dankelman, and Elena De Momi. "Path planning for endovascular catheterization under curvature constraints via two-phase searching approach". In: *International Journal of Computer Assisted Radiology and Surgery* 16.4 (2021), pp. 619–627. DOI: `10.1007/s11548-021-02328-x`.

3.1. INTRODUCTION

Percutaneous Coronary Intervention (PCI) is used to widen stenotic and occluded blood vessels by pushing the plaque aside and placing a stent nearby to restore and maintain blood circulation. For example, in Figure 3.1, a catheter is inserted from a femoral artery and targeting the occlusion site.

Tool and navigation guidance can lower the skill requirements for percutaneous treatment. Nowadays, steerable catheters have been developed via mechanical, magnetic, and fluidic actuation principles. Steerable catheters have different bending capabilities exhibiting a minimum bending radius. The minimum bending radius found in literature lies between 8.13mm and 171mm [1].

Path planning is one of the major challenges of endovascular catheterization. Vascular centerlines were seen as a reference trajectory, and centerline extraction has aroused the interest of researchers. A graph matching method is proposed to establish the correspondence between the 3D pre-operative and 2D intra-operative skeletons extracting from fluoroscopic images, and then the two skeletons are registered by skeleton deformation [2]. Nevertheless, the path planning approach which merely follows centerlines might be infeasible when the path curvature exceeds catheter bending capability. For example, if the robot is attempting to follow the centerlines (like in [2]), the minimum bending radius is less than 1mm at the bifurcation (Figure 3.1B), which exceeds the robot bending capability 13.1mm [3] and makes the robot fail to follow.

A performant path planner should provide a reliable path within the catheter's capability. Sampling-based methods such as extended Probabilistic RoadMap (PRM) [4] and RRT-connect [5] are able to plan the path in configuration space. These methods have been coupled with the Dubins path and Bézier spline to generate curvature-bounded paths. AFT [6] takes advantage of the fractal theory and the architecture of GPUs paralleling the planning process. It has a higher success rate than RRTs, as demonstrated for needle insertions in a complex environment [6]. However, the success rate of RRTs or AFT is not always ensured.

To overcome the drawbacks mentioned above, a compromise between following the

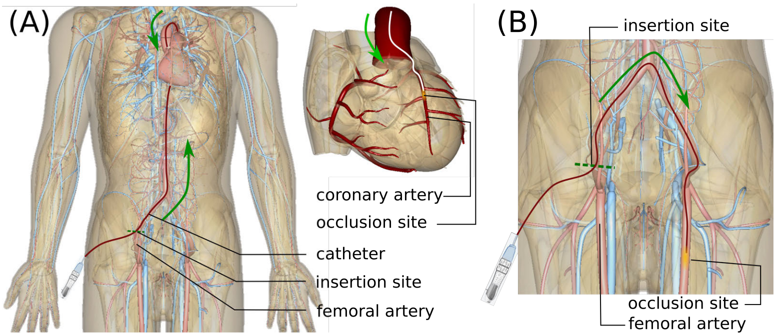

Figure 3.1: Clinical background (A) Coronary endovascular procedure (B) Femoral endovascular procedure (The anatomy models are made using BodyParts3D, ©2008 The Database Center for Life Science licensed under CC Attribution-Share Alike 2.1 Japan).

vascular centerlines and satisfying the curvature constraint is needed. An approach was implemented that involves gradually reducing the arch height of the path away from the vascular centerline until it meets the curvature constraint [7]. An enhanced ACO method is introduced for optimal vascular path planning, considering factors such as catheter diameter, vascular length, diameter, as well as curvature and torsion [8]. The computation time associated with this method ranged from 2 s to 30 s, with an average of 12.32 s. Also, in [9], a backbone curve method was implemented to optimize the path under kinematic constraint for a cable-driven continuum robot in a cardiovascular system. Nevertheless, this work considers the constrained optimization problem along the overall path without reducing the optimization search space.

More importantly, reducing computation time would help path planners to be applied in path replanning. Intra-operatively, planned paths might be infeasible or less accurate due to environment deformations and sensing uncertainties. The work in [10] quantified the displacement of arteries during endovascular catheterization: the aortic bifurcation was mostly displaced in a cranial direction with the median cranio-caudal dislocation of 6.7 mm (min 2.1, max 12.3). Considering that the high computation time of 12.3 s [8] can barely make the path adapted to the deformation, the need for real-time path planning with low computation time is highlighted. In practical applications, the optimal frequency for replanning is determined by several key factors: the tracking frequency of the catheter tip position, the frequency of vision sensing feedback, and the operational frequency of the controller. It is essential for the path planner to function at a frequency that not only effectively utilizes the latest data from the sensing modules but also delivers instructions to the controller in a timely manner. For instance, the frequency of the electromagnetic tracking system (Aurora) is reported to be 40 Hz [11], while the frequency for intra-operative model reconstruction stands at 1.25 Hz [2], and the controller operates at a frequency of 10 Hz [12]. The controller's operational frequency of 10 Hz naturally serves as the practical ceiling for the path planner's frequency. Path planning at a frequency exceeding that of the controller's operational capacity offers minimal additional benefit. Therefore, a pragmatic strategy involves setting the path planner's frequency at or slightly above the 10 Hz mark of the controller. This ensures that the path planner remains responsive to control commands and incorporates the most current high-frequency sensor data effectively.

In this chapter, a fast two-phase path planning approach is proposed, considering the robot curvature and time constraints.

3.2. METHODOLOGY

The proposed approach is a two-phase searching framework (see the pipeline in Figure 3.2). The inputs of the path planner are the centerline points $\boldsymbol{p_i}$ and their minimum distances to the vascular walls r_i, where i is the running index (detailed in Sec 3.2.1). Globally, a cubic B-spline curve $\boldsymbol{a_s}$ is found along the vascular centerlines from a user-defined initial point $\boldsymbol{p_0}$ to a goal point $\boldsymbol{p_G}$ (detailed in Sec 3.2.2). Locally, the aforementioned curve is optimized to satisfy the catheter curvature constraint. The final output curve $\boldsymbol{a_f}$ is the curve with locally optimized curve segments (detailed in Sec 3.2.3).

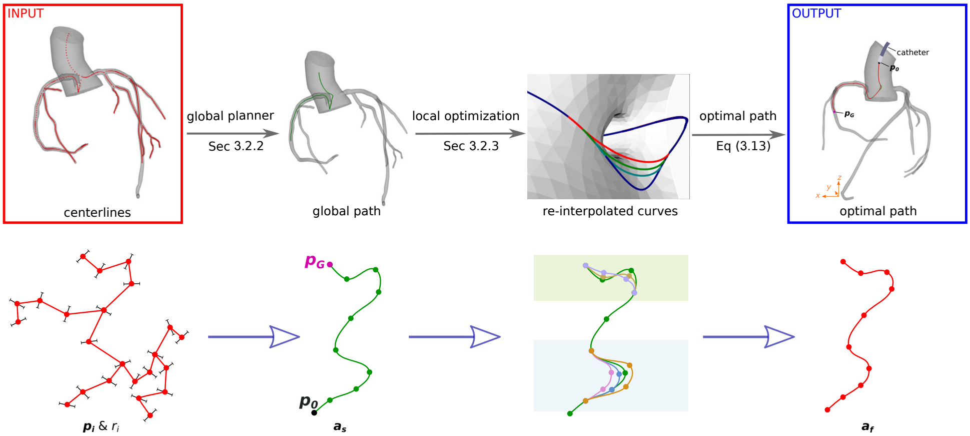

Figure 3.2: Pipeline for the proposed path planning approach: given centerlines and radii, the global planner computes a tentative curve, then the local planner optimizes the curve to satisfy the catheter curvature constraint.

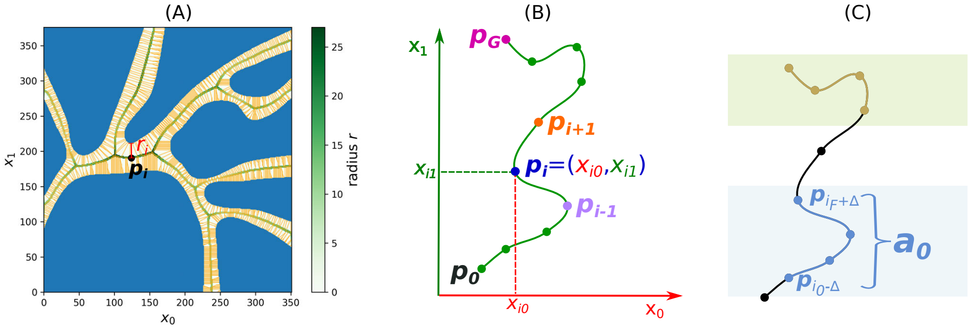

Figure 3.3: The schematic view of: (A) Voronoi regions to extract centerlines and radii, where Voronoi vertices, Voronoi edges, and centerlines are blue, yellow, and green, respectively. (B) Example of path points definition (C) Example of curve segments to be optimized.

3.2.1. CENTERLINE EXTRACTION

Our approach employs the method demonstrated in [13], which treats the centerlines as the minimal action paths linking Voronoi vertices inside the model surface. By solving a nonlinear hyperbolic equation (Eikonal equation) followed by an ordinary differential equation, the approach [13] provides the minimal action paths points $\boldsymbol{p_i}$ that locally maximize their minimum distances r_i to the boundary of the surface. The Vascular Modeling Toolkit (VMTK) library based on [13] was used to automatically extract $\boldsymbol{p_i}$ and r_i. For example, Figure 3.3A shows the Voronoi regions with Voronoi vertices (blue), Voronoi edges (yellow), and extracted centerline points (green).

3.2.2. GLOBAL PLANNER

From the global planner, a tentative curve from an initial point $\boldsymbol{p_0}$ to a goal point $\boldsymbol{p_G}$ inside blood vessels is obtained (see Figure 3.3B). Each waypoint is presented in the N-dimensional Cartesian coordinate system ($N = 2$ or 3).

$$\boldsymbol{p_i} = [x_{i0}, x_{i1}, \cdots, x_{i(N-1)}] \quad i = 0, \cdots, G \tag{3.1}$$

The initial point $\boldsymbol{p_0}$ is regarded as the exploration tree root. The BFS strategy starts at the tree root and explores the k-nearest neighbor centerline nodes at the present depth prior to moving on to the nodes at the next depth level. It stops when the goal point is visited. Thus a list of centerline points from $\boldsymbol{p_0}$ to $\boldsymbol{p_G}$ is obtained by navigating through the BFS tree.

The list of points is smoothed via cubic B-spline interpolation and a tentative B-spline curve $\boldsymbol{a_s}$ is then obtained. Given a knot sequence $t_0, \cdots, t_G$, B-splines with degree $M = 3$ can be defined by the Cox–de Boor recursion formula as (3.2), where w is the parametric space of the B-spline.

$$\begin{aligned} {}^{0}\boldsymbol{p_i}(w) &= \begin{cases} 1 & t_i \le w < t_{i+1} \\ 0 & \text{otherwise} \end{cases} \\ {}^{M}\boldsymbol{p_i}(w) &= \frac{w - t_i}{t_{i+M} - t_i}\, {}^{M-1}\boldsymbol{p_i}(w) + \frac{t_{i+M+1} - w}{t_{i+M+1} - t_{i+1}}\, {}^{M-1}\boldsymbol{p_{i+1}}(w) \end{aligned} \qquad i = 0, \cdots, G \tag{3.2}$$

3.2.3. LOCAL PLANNER

The curvature s_i at $\boldsymbol{p_i}$ along the B-spline interpolated curve is defined as (3.3) in a generic form. Specifying $N = 3$, the expression is simplified as (3.4).

$$s_i = \frac{\sqrt{\frac{1}{2}\sum_{j=0}^{N-1}\sum_{k=0}^{N-1}(\dot{x}_{ij}\ddot{x}_{ik} - \dot{x}_{ik}\ddot{x}_{ij})^2}}{(\sum_{j=0}^{N-1}\dot{x}_{ij}^2)^{\frac{3}{2}}} \qquad i = 0, \cdots, G \tag{3.3}$$

$$s_i = \frac{\sqrt{(\dot{x}_{i0}\ddot{x}_{i1} - \dot{x}_{i1}\ddot{x}_{i0})^2 + (\dot{x}_{i0}\ddot{x}_{i2} - \dot{x}_{i2}\ddot{x}_{i0})^2 + (\dot{x}_{i1}\ddot{x}_{i2} - \dot{x}_{i2}\ddot{x}_{i1})^2}}{(\dot{x}_{i0}^2 + \dot{x}_{i1}^2 + \dot{x}_{i2}^2)^{\frac{3}{2}}} \tag{3.4}$$

The curvature constraint is expressed as (3.5), and S is the allowed maximal curvature value depending on robot kinematic constraints.

$$s_i \le S \text{ for } i = 0, \cdots, G \tag{3.5}$$

It is evaluated for the tentative curve $\boldsymbol{a_s}$ first. If the constraint is satisfied, $\boldsymbol{a_s}$ will be the final path without further optimization. Otherwise, local optimization will be applied. The curve to be optimized $\boldsymbol{a}_0$ is defined by the curvature at path points, as outlined in (3.6).

$$\begin{gathered} \text{If } s_i > S \text{ for } i = i_0, \cdots, i_F \\ \text{Then } \boldsymbol{a}_0 = [\boldsymbol{p}_{i_0-\Delta}, \cdots, \boldsymbol{p}_{i_F+\Delta}] \end{gathered} \tag{3.6}$$

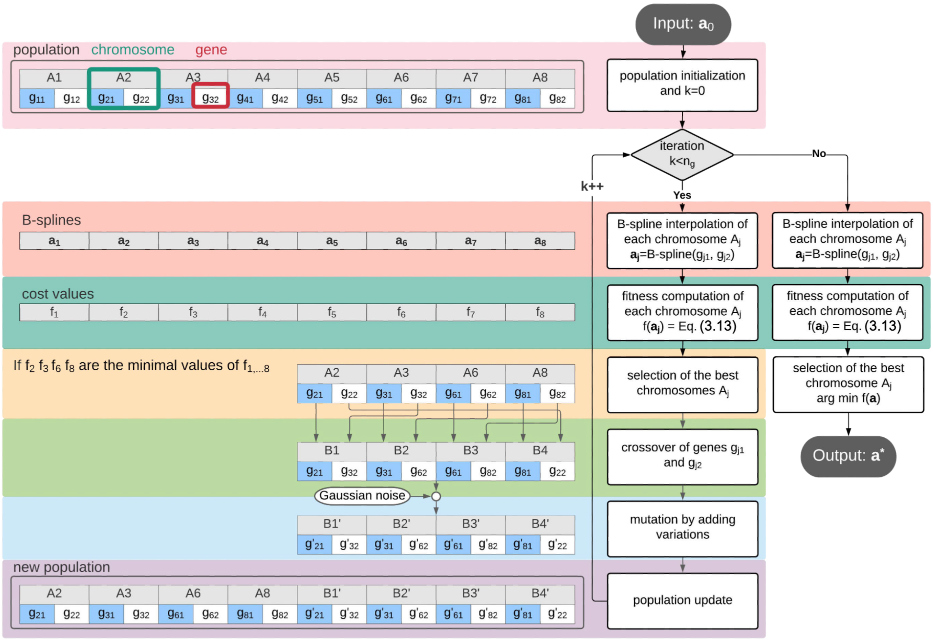

Figure 3.4: Schematics of the genetic algorithm procedure for local optimization.

where $\boldsymbol{a}_0$ is the curve segment exceeding robot bending capability and it is represented by a list of waypoints (see Figure 3.3C). The variable Δ represents a user-defined marginal capacity allocated for local optimization, set at a value like 5% of the total number of path points. This margin is instrumental in facilitating the seamless connection between the local curve $\boldsymbol{a}_0$ and the global curve.

GA finds the optimal re-interpolated curve segment. In Figure 3.4, there are 8 chromosomes making up the initial population. Each chromosome $A_j(j = 1\cdots 8)$ is composed of 2 genes, which are the parameters determining the re-interpolated B-spline curve $\boldsymbol{a}_j$. Specifically, the gene g_{j1} is the number of points that are assigned with weight 0 when performing B-spline fitting; the gene g_{j2} is the smoothness value that affects the trade-off between smoothness and displacement during spline fitting, and it is the upper border of the error sum of displacement squares. Then the fitness f_j is computed for each re-interpolated curve segment according to a cost function. Next, the best re-interpolated curves are selected for mating. For example, there are 4 chromosomes selected for mating in Figure 3.4. Then the crossover and mutation of genes are performed so that the population is updated. During mutation, a Gaussian distributed noise $\Delta g_j \sim \mathcal{N}(\mu, \sigma^2)$ is added to the genes. Finally, the optimal curve segment is selected from the population after n_g iterations.

The cost function is designed to find the optimal path by a trade-off between the distance to vascular walls, path length, and curvature. The constrained optimization problem is formulated as

$$\begin{aligned} \min f(\boldsymbol{a}) &= w_1 g_d(\boldsymbol{a}) + w_2 g_s(\boldsymbol{a}) + w_3 g_l(\boldsymbol{a}) \\ \text{s.t. } s_i &\le S \text{ for } i = i_0 - \Delta, \cdots, i_F + \Delta \\ d_i &\le r_i \text{ for } i = i_0 - \Delta, \cdots, i_F + \Delta \end{aligned} \tag{3.7}$$

where $g_d(\boldsymbol{a})$ is the mean value of normalized distances to the centerlines, $g_s(\boldsymbol{a})$ is the mean value of normalized curvatures, and $g_l(\boldsymbol{a})$ is the normalized path length.

The mean value of the normalized distances to the centerlines $g_d(\boldsymbol{a})$ is

$$g_d(\boldsymbol{a}) = \mathrm{mean}\,(d_c/r) \tag{3.8}$$

$$d_{ci} = \min_{j=0,\cdots,G} ||\boldsymbol{p_j^0} - \boldsymbol{p_i}|| \quad i = i_0 - \Delta, \cdots, i_F + \Delta \tag{3.9}$$

where d_c is the distance from B-spline curve $\boldsymbol{a}$ to the centerline. At the i-th index, d_{ci} is computed by the minimum value of Euclidean distance from the new point $\boldsymbol{p_i}$ to centerline points $\boldsymbol{p_j^0}$.

The mean value of normalized curvatures $g_s(\boldsymbol{a})$ is formulated as

$$g_s(\boldsymbol{a}) = \mathrm{mean}(s)/S \tag{3.10}$$

The normalized path length $g_l(\boldsymbol{a})$ is presented as (3.11), where the length $l(\boldsymbol{a})$ is a cumulative sum of the distance between adjacent points. In specific medical procedures, such as catheterizations and endoscopies, the path length is a critical consideration. Opting for shorter paths can lead to reduced procedural duration, which may in turn decrease the likelihood of patient discomfort and lower the risk of complications. However, it is important to note that in certain scenarios, the variability in path length may be inherently limited due to anatomical constraints. Nonetheless, strategically shorter paths could be beneficial in minimizing tissue damage and avoiding critical structures, such as plaques. Conversely, longer paths in these procedures would increase wear and tear on instruments, such as catheters. This is particularly pertinent in catheterizations, where the instruments are required to navigate through narrow and convoluted paths. Additionally, extensive bending or manipulation of these instruments could adversely affect their structural integrity.

$$g_l(\boldsymbol{a}) = l(\boldsymbol{a})/l(\boldsymbol{a_0}) \tag{3.11}$$

$$l(\boldsymbol{a}) = \sum_{i_0-\Delta}^{i_F+\Delta} ||\boldsymbol{p_{i+1}} - \boldsymbol{p_i}|| \tag{3.12}$$

Moreover, there are two constraints in (3.7): the curvature constraint and the collision avoidance constraint. In the context of the collision avoidance constraint, ensuring that the distance to the centerline remains smaller than the vascular radius (specifically, the minimum distance to the vascular walls, denoted as r_i) guarantees that the point is positioned within the blood vessels. Since the path points are already refined in the B-spline interpolation in (3.2), the collision avoidance constraint is checked merely for the path points to reduce computational cost.

The constrained optimization problem (3.7) is converted to an unconstrained one via moving constraints to the objective function as

$$\begin{aligned}\min f(\boldsymbol{a}) &= w_1 g_d(\boldsymbol{a}) + w_2 g_s(\boldsymbol{a}) + w_3 g_l(\boldsymbol{a}) \\ &\quad + w_4 \max\{0, s - S\} + w_5 \max\{0, d_c - r\}\end{aligned} \tag{3.13}$$

Here, in order to satisfy the hard constraints (curvature constraint and collision avoidance), the weights assigned to the cost function should have a significant difference between w_4, w_5 and others, for example, $w_1 = 1, w_2 = 1, w_3 = 1, w_4 = 1000, w_5 = 1000$. When the hard constraints are satisfied, the last two elements are 0. Otherwise, a large number will be added to the cost function value $f(\boldsymbol{a})$, indicating that the corresponding solution $\boldsymbol{a}$ will not be selected since the procedure intends to find the minimum cost value. After n_g iterations, if the optimal cost value is greater than a reasonable threshold (such as 1000), which means the constraints are not fully satisfied, there is no feasible solution until now. To look for new solutions within the time limit, the number of iterations n_g will be increased. If the time limit is reached and there is still no feasible solution found, the path planner fails to find a path respecting all constraints.

There may be several portions of the tentative curve exceeding the allowed maximum curvature. In that case, each portion is assigned to an individual local planning thread. Multiple threads are carried on in parallel, instead of being conducted in serial to reduce computation time. After all the threads are done, the final path $\boldsymbol{a_f}$ under curvature constraint is obtained.

3.2.4. EVALUATION METRICS

Multiple criteria are chosen for performance evaluation. The time cost t is the time spent on path planning in a single trial from start to finish. The path length (3.12) is one of the essential components to evaluate the path optimality, and it is normalized by dividing it by the shortest distance from the initial point to the goal point. The curvature (3.3) is used to evaluate the bending extent of a curve.

The minimum distance to vascular walls at point $\boldsymbol{p_i}$ can be obtained by the subtraction of two elements: the vascular radius r_i and the distance to vascular centerline d_{ci} given in (3.9). The distance to the vascular wall represents a safety margin ensuring collision avoidance between the catheter tip and the vascular wall. To prevent physical harm such as scratching to soft tissues if the catheter comes in contact with vascular walls, the distance to the vascular wall should not be less than the outer radius of the catheter.

The success rate is defined as the fraction or percentage of success among a number of attempts as $\delta = n_s/n$, where n_s is the successful times to find a path and n is the number of attempts. For the proposed two-phase searching approach in this chapter, a feasible path solution can be found as long as there is a feasible solution between the initial and goal points.

3.2.5. EXPERIMENTAL SETUP

This work targets endovascular procedures such as PCI, Endovascular Aortic Repair (EVAR), Transcatheter Aortic Valve Implantation (TAVI), and iliac recanalization. The datasets include models such as the coronary artery, aorta, femoral artery, peripheral arterial, etc, to evaluate and validate the approach. The datasets are classified into 4 groups, including 2D ($G1$, $G2$) and 3D ($G3$, $G4$) space scenarios.

The dataset $G1$ contains 2D images describing femoral arteries (pixel resolution of 220×294 and spacing of 0.68mm). The dataset $G2$ includes 2D images describing lower limb arteries (pixel resolution of 2822×1539 and spacing of 0.37mm). The dataset $G3$ includes several 3D mesh models: (i) A model which takes patient specific Computed Tomography (CT) images as inputs, typically in a $512 \times 512 \times 737$ voxel dimension with a voxel spacing of $0.6445 \times 0.6445 \times 0.8$mm; (ii) A model which takes patient specific Magnetic Resonance Imaging (MRI) images as inputs, typically in a $512 \times 64 \times 512$ voxel dimension with a voxel spacing of $0.7813 \times 2.0 \times 0.7813$mm; (iii) An embeddable model of the lower limb made from anatomical parts, with the physical dimension of $852 \times 116 \times 169$mm; (iv) A mesh model of a single femoral artery with a physical dimension of $37 \times 88 \times 450$mm. The dataset $G4$ includes a 3D mesh model describing coronary arteries in a physical dimension of $102 \times 89 \times 101$mm. Table 3.1 provides other information of the datasets, among which the tortuosity is used to measure the arc-chord ratio of vascular structure.

The inputs of the path planner are obtained as follows. First, the centerline is extracted using the VMTK module on the platform 3DSlicer. Second, Gaussian distributed noise $\Delta \boldsymbol{p}_{0,G} \sim \mathcal{N}(\mu = 0, \sigma = 10)$ is added to the initial and goal points in each trail to increase data variability. Third, without loss of generality, the path planner is designed in a generic form which takes the robot's specification S as an input. The experiments are carried out on a computer equipped with an Intel (R) Core (TM) i5-8250U CPU @ 1.60GHz 1.80GHz processor and 8GB RAM.

The proposed approach is compared with sampling-based methods RRT and RRT* [18]. Compared with the basic RRT and RRT* [19], the extended ones [18] take random samples on centerlines instead of randomly sampling inside the vascular model. The parameter specification is given as follows: the maximum number of samples to take before timing out is 4048, the probability of checking for a connection to the goal is 0.1, and the number of nearby branches to rewire is 32.

3.2.6. STATISTICAL ANALYSIS

The statistically significant difference between the proposed method and others will be evaluated via the Kruskal-Wallis test in this work. It is a non-parametric test that does not assume a normal distribution of populations. The null hypothesis is that there is no significant difference between solutions using different methods. If the significance level $\alpha = 0.05$, the null hypothesis is accepted as having $p > 0.05$. If $p < 0.05$, the null

Table 3.1: The datasets description and related parameters of experiments.

dataset	*subjects*	*tortuosity*	*source*	S (mm^{-1})	*trials*
G1	5	2.365 ± 0.100	-	0.08	250
G2	3	1.067 ± 0.015	[14]	0.10	150
G3	4	1.075 ± 0.045	[15],[16], [17]	0.08	200
G4	1	1.501 ± 0.120	[15]	0.20	100

Table 3.2: The performance comparison regarding to success rate.

Method	*G1*	*G2*	*G3*	*G4*
RRT [18]	0.980	0.760	0.890	0.910
*RRT** [18]	0.988	0.740	0.890	0.950
BFS-GA	1	1	1	1

hypothesis is rejected, which demonstrates that there is a significant difference between the proposed method with others.

3.3. RESULTS AND DISCUSSION

The proposed approach is performed on our datasets and compared with sampling-based methods. Figure 3.5A shows that with respect to computation time, the proposed method has a smaller median and variance. In specific scenarios, where the blood vessels are slender and narrow, collision checking and avoidance of RRT series could take more time than continuous sampling along the vascular centerlines. More importantly, to save time, the approach optimizes curve segments in the local planner rather than considering the curvature constraint in overall path planning. This is because, in most cases, the curvature limitation would be respected except for some sharp turns along the centerlines. Therefore, the proposed method takes less computation time. Reducing computation time would help the path planner to be applied in path replanning. For example, the time cost on $G1$ is 191 ± 102ms and the path replanning can achieve an updating frequency at 6.4 ± 2.3Hz. Compared with serial thread processing in the proposed local planner, the speed of parallel thread processing improves noticeably. For instance, the time is reduced by 41% ($p < 0.05$) when processing two threads in parallel on the dataset $G4$.

For path length, Figure 3.5B shows that the proposed method has a smaller median value, while the variance is similar to the results of other methods. The random sampling property of RRT series leads to path points locating not always on vascular centerlines. Floating around the centerlines results in paths that can not be ensured to be the shortest ones. To avoid this drawback, the proposed method adopts a BFS strategy within the vascular tree, ensuring the path solution is the shortest one. Moreover, the local planner pushes the path points in the same direction away from the centerlines, avoiding bi-directional floating around the centerlines that increases path length.

Figure 3.5C shows that the proposed method increases the distance to vascular walls by keeping close to centerlines. It resulted not only from the sampling property analyzed in the previous paragraph, but also from the specified optimization criteria in the local planner. Figure 3.5D demonstrates that the curvature constraint is satisfied using the proposed method and the curvature median value is decreased. Specifically, the curvature constraint is respected in the local planner. The median value is also decreased by avoiding bi-directional floating around the centerline.

Table 3.2 shows that the success rate of the method proposed in this study is higher. As long as a feasible path exists, the proposed method is able to find it by navigating through the tree and optimize it locally. RRT series can not ensure a path could be found

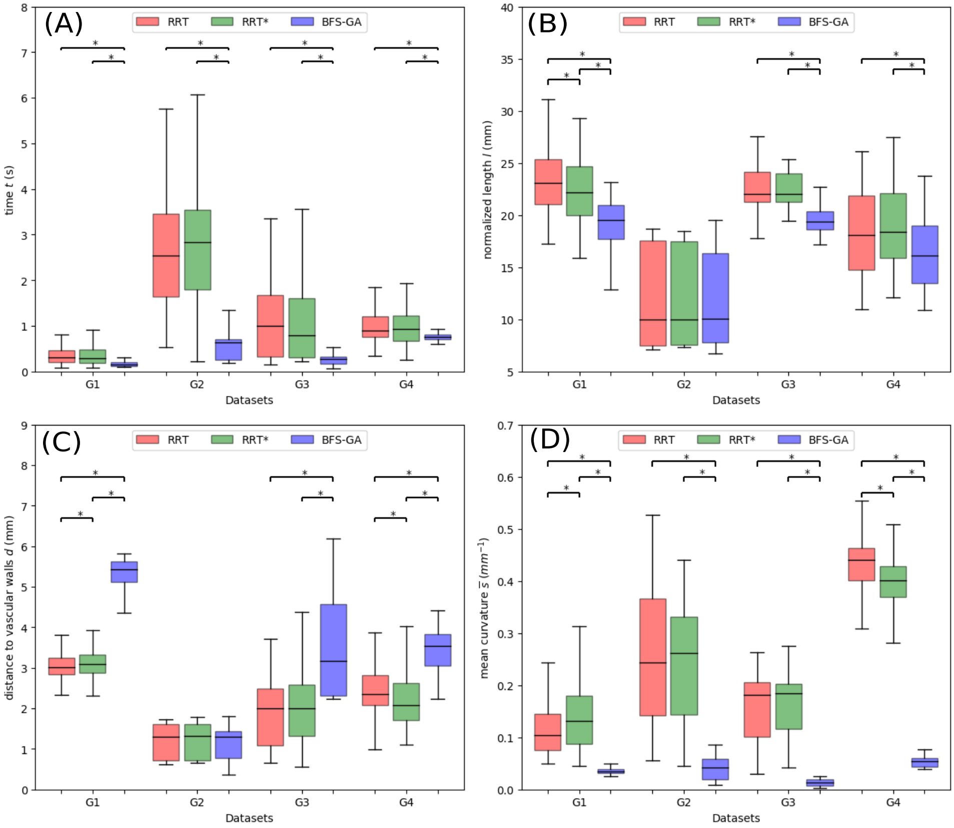

Figure 3.5: The performance comparison between the proposed method and sampling-based methods [18] according to (A) time cost, (B) path length, (C) distance to vascular walls, and (D) curvature. ($*, p < 0.05$ using Kruskal-Wallis test).

in a specific trail due to its incompleteness.

In short, the results show that the proposed method achieves a higher efficiency and better performance. It is further applicable for path planning in narrow passages for curvature-constrained robots.

To validate the effectiveness of the proposed path planner, it was integrated with a robotic catheter system and subjected to testing in an *in-vitro* experimental setup. A demonstration of the integrated system can be found in the accompanying materials provided by ATLAS [20]. This validation process aimed to assess the planner's performance and ensure its suitability for real-world applications in endovascular interventions.

3.4. CONCLUSION

In this chapter, a fast two-phase path planning approach, named BFS-GA, is proposed for endovascular catheterization. Vascular centerlines were seen as a reference trajectory assisting catheterization in literature. State-of-the-art methods rarely consider the catheter curvature constraint. The presented approach is able to respect robot curvature constraints while keeping it close to the centerlines as much as possible. Moreover, researchers in the literature considered merely the constrained optimization problem along the overall path without reducing search space. In this work, the optimization problem is formulated and solved for specific portions of the path, with parallel optimization employed to reduce the computation time. The limit is that it could lose accuracy in intra-operative interventions resulting from vasculature deformations and sensing uncertainties. Future works will concentrate on developing an accurate intra-operative path planner. A real-time path replanning algorithm based on a pre-operative path should also be proposed. Such an algorithm should consider additional factors like the unpredictable deformation of environments and the uncertainties of model sensing (e.g., the tip position and vascular model).

BIBLIOGRAPHY

[1] Tomas da Veiga, James H Chandler, Peter Lloyd, Giovanni Pittiglio, Nathan J Wilkinson, Ali K Hoshiar, Russell A Harris, and Pietro Valdastri. “Challenges of continuum robots in clinical context: A review”. In: *Progress in Biomedical Engineering* 2.3 (2020). DOI: `10.1088/2516-1091/ab9f41`.

[2] Jian-Qing Zheng, Xiao-Yun Zhou, Celia Riga, and Guang-Zhong Yang. “Towards 3D Path Planning from a Single 2D Fluoroscopic Image for Robot Assisted Fenestrated Endovascular Aortic Repair”. In: *2019 International Conference on Robotics and Automation (ICRA)*. 2019, pp. 8747–8753. DOI: `10.1109/ICRA.2019.8793918`.

[3] Awaz Ali, Aimee Sakes, Ewout A Arkenbout, Paul Henselmans, Remi van Starkenburg, Tamas Szili-Torok, and Paul Breedveld. “Catheter steering in interventional cardiology: Mechanical analysis and novel solution”. In: *Proceedings of the Institution of Mechanical Engineers, Part H: Journal of Engineering in Medicine* 233.12 (2019), pp. 1207–1218. DOI: `10.1177/2F0954411919877709`.

[4] Alan Kuntz, Mengyu Fu, and Ron Alterovitz. “Planning high-quality motions for concentric tube robots in point clouds via parallel sampling and optimization”. In: *IEEE/RSJ International Conference on Intelligent Robots and Systems (IROS)*. IEEE. 2019, pp. 2205–2212. DOI: `10.1109/IROS40897.2019.8968172`.

[5] Johannes Fauser, Romol Chadda, Yannik Goergen, Markus Hessinger, Paul Motzki, Igor Stenin, Julia Kristin, Thomas Klenzner, Jörg Schipper, Stefan Seelecke, et al. “Planning for flexible surgical robots via Bézier spline translation”. In: *IEEE Robotics and Automation Letters* 4.4 (2019), pp. 3270–3277. DOI: `10.1109/LRA.2019.2926221`.

[6] Marlene Pinzi, Stefano Galvan, and Ferdinando Rodriguez y Baena. “The Adaptive Hermite Fractal Tree (AHFT): a novel surgical 3D path planning approach with curvature and heading constraints”. In: *International journal of computer assisted radiology and surgery* 14.4 (2019), pp. 659–670. DOI: `10.1007/s11548-019-01923-3`.

[7] Fan Yang, Yu Dai, Jianxun Zhang, Huijiao Sun, Liang Cui, Xiaotao Yin, Xiaofeng Gao, and Ling Li. “Path planning of flexible ureteroscope based on CT Image”. In: *2019 Chinese Control Conference (CCC)*. IEEE. 2019, pp. 4667–4672. DOI: `10.23919/ChiCC.2019.8865196`.

[8] Ming-ke Gao, Yi-min Chen, Quan Liu, Chen Huang, Ze-yu Li, and Dian-hua Zhang. “Three-dimensional path planning and guidance of leg vascular based on improved ant colony algorithm in augmented reality”. In: *Journal of medical systems* 39.11 (2015), p. 133. DOI: `10.1007/s10916-015-0315-2`.

[9] Fei Qi, Feng Ju, Dongming Bai, Yaoyao Wang, and Bai Chen. "Kinematic analysis and navigation method of a cable-driven continuum robot used for minimally invasive surgery". In: *The International Journal of Medical Robotics and Computer Assisted Surgery* (2019), e2007. DOI: `10.1002/rcs.2007`.

[10] Giasemi Koutouzi, Marcus Pfister, Katharina Breininger, Mikael Hellström, Håkan Roos, and Mårten Falkenberg. "Iliac artery deformation during EVAR". In: *Vascular* 27.5 (2019), pp. 511–517. DOI: `10.1177/1708538119840565`.

[11] Erik Nypan, Geir Arne Tangen, Frode Manstad-Hulaas, and Reidar Brekken. "Vessel-based rigid registration for endovascular therapy of the abdominal aorta". In: *Minimally Invasive Therapy & Allied Technologies* 28.2 (2019), pp. 127–133. DOI: `10.1080/13645706.2019.1575240`.

[12] Jakub Sikorski, Alper Denasi, Giuseppe Bucchi, Stefano Scheggi, and Sarthak Misra. "Vision-based 3-D control of magnetically actuated catheter using BigMag—An array of mobile electromagnetic coils". In: *IEEE/ASME Transactions on Mechatronics* 24.2 (2019), pp. 505–516. DOI: `10.1109/TMECH.2019.2893166`.

[13] Luca Antiga, Bogdan Ene-Iordache, and Andrea Remuzzi. "Computational geometry for patient-specific reconstruction and meshing of blood vessels from MR and CT angiography". In: *IEEE transactions on medical imaging* 22.5 (2003), pp. 674–684. DOI: `10.1109/TMI.2003.812261`.

[14] Pierangela Bruno, Paolo Zaffino, Salvatore Scaramuzzino, Salvatore De Rosa, Ciro Indolfi, Francesco Calimeri, and Maria Francesca Spadea. "Using cnns for designing and implementing an automatic vascular segmentation method of biomedical images". In: *International Conference of the Italian Association for Artificial Intelligence*. Springer. 2018, pp. 60–70. DOI: `10.1007/978-3-030-03840-3_5`.

[15] Adam Updegrove, Nathan M Wilson, Jameson Merkow, Hongzhi Lan, Alison L Marsden, and Shawn C Shadden. "SimVascular: an open source pipeline for cardiovascular simulation". In: *Annals of biomedical engineering* 45.3 (2017), pp. 525–541. DOI: `10.1007/s10439-016-1762-8`.

[16] K Okubo. "BodyParts3D". In: *BodyParts3D, by The Database Center for Life Science* (2015). Available online: `http://lifesciencedb.jp/bp3d/`(accessed on 10 July 2015).

[17] Monika Colombo, Marco Bologna, Marc Garbey, Scott Berceli, Yong He, Josè Felix Rodriguez Matas, Francesco Migliavacca, and Claudio Chiastra. "Computing patient-specific hemodynamics in stented femoral artery models obtained from computed tomography using a validated 3D reconstruction method". In: *Medical Engineering & Physics* 75 (2020), pp. 23–35. DOI: `10.1016/j.medengphy.2019.10.005`.

[18] Zhen Li, Alice Segato, Alberto Favaro, Jenny Dankelman, and Elena De Momi. "A Heuristic-Sliding-Window-based RRT Path Planning for Endovascular Catheterization". In: *Proceedings of the 7th Congress of the National Group of Bioengineering (GNB)*. Pàtron editore. 2020. Available online: `https://atlas-itn.eu/wp-content/uploads/2020/12/GNB2020_ZhenLi.pdf`.

[19] Steven M LaValle. *Planning algorithms.* Cambridge university press, 2006. Available online: `http://planning.cs.uiuc.edu/`.

[20] ATLAS. *ATLAS: Deliverable D2.4 - Demonstration of exteroceptive skills of soft robots.* 2021. URL: `https://atlas-itn.eu/wp-content/uploads/2021/11/Delivarable2.4_video.mp4` (visited on 11/01/2021).

II

VESSELS DEFORMATION PREDICTION

4

POSITION-BASED DYNAMICS SIMULATOR OF VESSEL DEFORMATIONS FOR PATH PLANNING

A major challenge during autonomous navigation in endovascular interventions is the complexity of operating in a deformable but constrained workspace with an instrument. Simulation of deformations for it can provide a cost-effective training platform for path planning. The aim of this chapter is to develop a realistic, auto-adaptive, and visually plausible simulator to predict vessels' global deformation induced by the robotic catheter's contact and cyclic heartbeat motion. Based on a Position-based Dynamics (PBD) approach for vessel modeling, the Particle Swarm Optimization (PSO) algorithm is employed for an auto-adaptive calibration of PBD deformation parameters and of the vessel's movement due to a heartbeat. In-vitro experiments were conducted and compared with in-silico results. The end-user evaluation results were reported through quantitative performance metrics and a 5-Point Likert Scale questionnaire. Compared with literature, this simulator has an error of 0.23±0.13% for deformation and 0.30±0.85mm for the aortic root displacement. In-vitro experiments show an error of 1.35±1.38mm for deformation prediction. The end-user evaluation results show that novices are more accustomed to using joystick controllers, and cardiologists are more satisfied with the visual authenticity. The real-time and accurate performance of the simulator make this framework suitable for creating a dynamic environment for autonomous navigation of robotic catheters.

This chapter is available as:
Zhen Li, Enrico Manzionna, Giovanni Monizzi, Angelo Mastrangelo, Maria Elisabetta Mancini, Daniele Andreini, Jenny Dankelman, and Elena De Momi. "Position-based dynamics simulator of vessel deformations for path planning in robotic endovascular catheterization". In: *Medical Engineering & Physics* 110 (2022), p. 103920. DOI: `10.1016/j.medengphy.2022.103920`.

4.1. INTRODUCTION

Vascular disease is a common, abnormal condition of blood vessels, and it can be severe. Narrowed or obstructed arteries, typically due to atherosclerosis, affect blood circulation. PCI is a reliable and valid procedure for patients with symptomatic coronary stenosis. Based on patient characteristics, different access sites can be selected. Among them, radial access is recommended (Class I, Level A) as the standard approach due to its fewer vascular complications compared with the transfemoral approach [1].

Intra-operative path planning and control for a robotic catheter will increase the level of autonomy in medical robotics [2]. Vessel deformations in these procedures can be very high. The displacement of vessels due to the collision of the catheter with the aortic wall was quantified in [3, 4, 5]: the aortic bifurcation was mostly displaced in a cranial direction with the median craniocaudal dislocation of 6.7 mm (min 2.1 mm, max 12.3 mm). A displacement at the aortic bifurcation of (1.4 ± 1.1) mm was reported due to the passing of a stiff guidewire [6]. This deformation of vessels makes robotic catheterization very challenging and will require training. For training, a virtual endovascular catheterization system that simulates the characteristics of percutaneous devices and the vasculature can provide a cost-effective and safe training environment for robotic catheter manipulation compared with phantoms, *ex-vivo* or *in-vivo* experiments. Moreover, important intra-operative data can be collected (e.g., the catheter tip trajectory) and post-processed to gain valuable insight for improving the outcome and developing autonomous interventions [7]. Peral-Boiza *et al.* [8] presented a virtual reality training platform involving the progress of a flexible endoscope with a steerable tip into a virtual rigid vascular phantom. Hao *et al.* [9] proposed a personalized cardiovascular intervention simulation system that can simulate the complex interactions between vessels and tipped guidewires.

To model and simulate intra-operative vessel deformations, different prediction approaches were developed using Mass-Spring Model (MSM) [10], Finite-Element Method (FEM) [6], and Position-Based Dynamics (PBD) [11]. Compared with the first two methods, PBD is more suitable for real-time simulations because it does not need a complex mesh generation [11, 12, 13]. Although PBD is not as accurate as other methods, its high efficiency and close match to real deformations have been reported [14, 15]. However, PBD parameters do not have physical meanings, and thus they should be properly tuned.

Different modeling methods for catheters and guidewires are studied. PBD and shape matching approaches were applied for endoscope modeling [8]. FEM, MSM [16], and rigid multibody links [17] were also developed for catheters and guidewires [18]. Concerning the steerable tip, Cosserat rod [19], elastic rod [9], constant-curvature [20], and rigid-link [21] were extensively exploited as modeling approaches of steerable devices. While the Cosserat rod provides an exact solution to the static equilibrium of the device, the computational complexity and cost become high when extending the modeling to dynamics. On the other hand, the rigid-link modeling approach is well-established, but the number of variables increases dramatically when a realistic model is of interest. Constant curvature modeling may constitute a valuable trade-off between the Cosserat rod's complications and assumptions of rigid-link models [22].

Current research extensively explores various aspects such as vessel deformations due to device contact, the impact of heartbeat motion on vessel movement, and the steerability of robotic catheters. However, a comprehensive modeling and simulation approach that integrates all these elements within a single framework has not been reported in existing literature. This work distinguishes itself with three major contributions compared to existing studies: (1) It models the deformations of vessels due to device contact as global distributions, in contrast to the localized deformation approach using an individual bounding box, as demonstrated in the work of Ye *et al.* [11]; (2) It incorporates vessel movement induced by heartbeat motion; and (3) It employs a more universal and autonomous method for calibrating patient-specific parameters.

4.2. MATERIALS AND METHODS

4.2.1. MODELING METHOD OF VASCULATURE

Mimicking intra-operative deformations is essential for providing a dynamic environment in robotic system simulation. To achieve this goal, a vasculature deformation framework is proposed, as depicted in Figure 4.1 (top left). This framework illustrates the workflow of a patient-specific vessel mesh model extracted from Computed Tomography Angiography (CTA) images and deformed via the PBD approach. A series of optimization processes were performed to calibrate our modeling and simulation framework. To simulate the deformable properties of the aorta accurately, the vasculature PBD parameters were calibrated using PSO based on the data reported in the reference [11]. The vessel's movement due to a heartbeat was also calibrated through PSO according to the cyclic movement of the aortic annulus [23].

The data collection followed the ethical protocol approved by the Centro Cardiologico Monzino (CCM) under the assigned code of *02_21 PA*. The CTA images are from a patient with cardiac disease. The simulation environment was developed in *Unity* 2020.3.7 using *NVIDIA FleX* on a workstation equipped with an Intel Core i9-9900KF CPU @3.60GHz processor, 32GB RAM, NVIDIA GeForce GTX 1660 GPU with CUDA 11.0. The time step of the simulation was set as 0.02 s.

VASCULATURE RECONSTRUCTION

First, a vessel mesh model was extracted from CTA images. Pre-operative CTA images were acquired following the typical Multidetector Computed Tomography (MDCT) scan strategies: cardiac Electrocardiogram (ECG)-synchronized CTA of the aortic root and heart followed by a non-ECG-synchronized helical CTA of the thorax, abdomen and pelvis. Respiratory motion is also a common artifact seen in cardiac CT [24]. There are novel studies regarding motion correction under a free-breathing acquisition mode [25, 26]. In this study, a breath-holding method was employed for CT scan acquisition, and the respiratory motion was assumed to be negligible. The image data were acquired with a voxel size of 0.789 × 0.789 × 0.625 mm and a voxel number of 512 × 512 × 832.

Semi-automatic segmentation of the vessels and 3D mesh model reconstruction were performed using the *AW server* (GE Healthcare), followed by a manual refinement process. The 3D models with embedded lesions were exported under the support of the *3D suite* (GE Healthcare). After that, to better represent the aortic geometry and avoid undesired section distortion, a constant thickness of 1 mm was constructed for the aorta and a thickness of 0.55 mm for the coronaries using *Meshmixer* (Autodesk, Inc., CA, US),

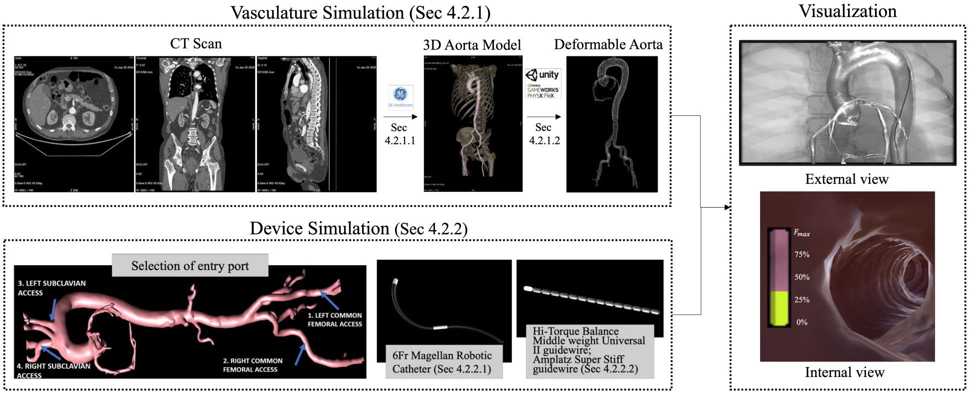

Figure 4.1: Overview of the proposed modeling and simulation system, presenting the workflow from the extraction of the patient-specific deformable vessel mesh model (top left, Sec 4.2.1) and the device simulation procedure (bottom left, Sec 4.2.2) to the visualization of the simulated training environment (right).

considering that the thickness of aorta is between 0.97 mm and 1.99 mm [27] and the thickness of coronaries is between 0.55 mm and 1 mm [28]. Post-processing was applied using *MeshLab* (ISTI - CNR) [29] by applying a simplification of the mesh with the quadratic edge collapse decimation with a default quality threshold of 0.3 and the target number of faces of 7000. Finally, smoothing was carried out using a Taubin smoothing technique [30] with scaling factors $\lambda = 0.5$, $\mu = -0.53$ and 10 smoothing steps.

POSITION-BASED DYNAMICS (PBD) APPROACH

As first proposed by Müller *et al.* [31], the PBD approach discretizes an object into a particle system composed of a set of particles. Then it computes the time evolution of the system by directly updating particles positions, subject to a set of equality and inequality constraints. The type of constraints among particles can influence the system's behavior. For generating deformations of objects, a multi-cluster shape matching constraint [32] is considered. Specifically, the particle system is represented as a set of clusters, and the clusters can overlap. Since one particle can belong to multiple clusters, the final position correction is obtained by averaging all goal positions of the belonging clusters.

The PBD approach implementation is based on the simulation library *NVIDIA FleX*. A realistic elastic behavior is obtained by appropriately selecting cluster-related parameters: cluster spacing (s_c, the distance between adjacent clusters), cluster radius (r_c, the radius of each cluster region) and cluster stiffness ($t_c \in [0,1]$, the extent to which adjacent cluster are constrained to each other). The cluster spacing and radius would influence the overlapping of adjacent clusters and the particles' goal positions.

The other PBD parameters keep their values fixed across all the simulations (See Table 4.1). The particle spacing and particle radius are set in accordance with the following rules: the number of particles that discretizes the whole aorta should be less than 10000, which is the maximum allowable number in *NVIDIA FleX*, and the particle spacing should be less than the two times of particle radius to maintain connectivity. The solid rest and collision distance were set to 2.5 mm respecting the particle radius. Fur-

Table 4.1: PBD parameters kept constant for all simulations.

Category	Parameter	Value
FleX Container	Particle Radius	3.0 mm
	Solid Rest	2.5 mm
	Particle Friction	0.1
	Collision Distance	2.5 mm
FleX Soft Asset	Particle Spacing	2.1 mm
	Surface Sampling	6.0
FleX Soft Skinning	Skinning Falloff	100
	Skinning Max Distance	20

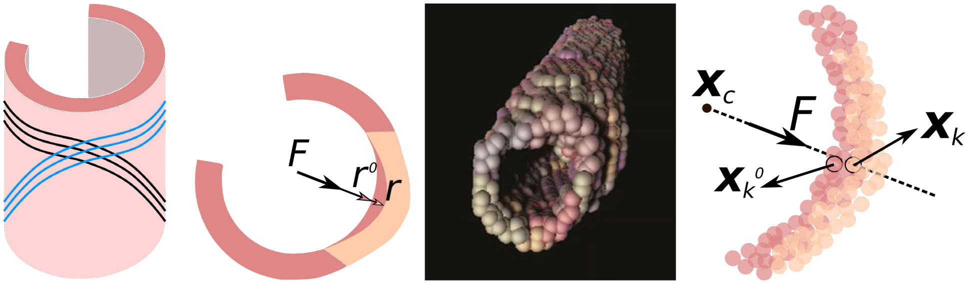

(A) (B) (C) (D)

Figure 4.2: Overview of the steps to obtain the strain: (A) Based on the simplified geometry of fibers, (B) an external force ($\boldsymbol{F}$) is applied in the radial direction (B) on the vasculature particle system. (D) Then the change of radius (r^0, r) is converted from the particle position ($\boldsymbol{x}_k^0, \boldsymbol{x}_k$).

thermore, the flex soft skinning was determined for proper mesh rendering. In the simulation, fixed constraints were applied as boundary conditions, eliminating all movement degrees of freedom for particles in selected regions. These regions include the distal extremities of the internal and external iliac arteries, the supra-aortic vessels, and the coronary arteries.

VASCULATURE PBD CALIBRATION

In this study, the stress-strain curve from [11] is used for calibration. Ye *et al.* [11] presented a geometric vessels model and recorded a sequence of the forces acting on the vertex in the inner wall and the subsequent displacement. A stress-strain curve ($\sigma - \epsilon$) was obtained, which depicts the biomechanics properties appropriately as reported [11]. In order to obtain the stress-strain curve from the virtual system, an assumption is made for simplicity.

Assumption 1: It is assumed that the vessels can be considered as a composition of two main families of fibers, which are axially symmetric to each other (Figure 4.2A). Two fibers yield the same contribution along the circumferential direction.

Therefore, the whole fiber's stretching is directly linked to the extension in the circumferential direction. The displacements along the circumference can be associated with the elongation or shortening of the vessels' internal radius (Figure 4.2B). An external force ($\boldsymbol{F}$) is applied on the vasculature in the radial direction and the change of radius (initial radius r^0, deformed radius r) is computed from the particle position. Specifically, an external distributed force ($\boldsymbol{F}$) is applied on the vasculature particle system over a surface with an area of A in the radial direction (Figure 4.2C). At a specific mark (i.e., the k-th particle), its position is deformed from $\boldsymbol{x}_k^0$ to $\boldsymbol{x}_k$ in a three-dimensional space (Figure 4.2D). Thus the internal radius is estimated by computing the distance from the particle to the center of the cross-section of vessels $\boldsymbol{x}_C$:

$$r^0 = ||\boldsymbol{x}_k^0 - \boldsymbol{x}_C|| \tag{4.1}$$

$$r = ||\boldsymbol{x}_k - \boldsymbol{x}_C|| \tag{4.2}$$

Therefore, the stress-strain curve is computed by:

$$\sigma = ||\boldsymbol{F}||/A \tag{4.3}$$

$$\epsilon = (r - r^0)/r^0 \tag{4.4}$$

The PSO approach [33] is employed to optimize the PBD cluster parameters (s_c, r_c, t_c) by minimizing the Root Mean Square Error (RMSE) (e_v) compared with the reference stress-strain curve:

$$\min_{s_c, r_c, t_c} e_v \quad \text{with } e_v = \sqrt{\frac{\sum_{m=1}^{M}(\hat{\epsilon}_m - \epsilon_m)^2}{M}} \tag{4.5}$$

where $\hat{\epsilon}_m$ is the mth strain of the reference stress-strain curve and ϵ_m is the mth strain of the simulated strain stress curve with m that spans from 0 to M, where M is the total number of samples.

The PSO algorithm considers each solution as a particle of a swarm that moves through the search space to find an optimal position. Each particle has a position $\boldsymbol{\chi}_i = (x_i^1, x_i^2, ..., x_i^N)$ and a velocity $\boldsymbol{v}_i = (v_i^1, v_i^2, ..., v_i^N)$ in an N-dimensional configuration space, where i denotes the ith particle and N represents the dimension of the configuration or number of unknown variables. During every iteration, each particle is updated by following two "best" values: the position vector of the local optimal solution ("cognitive" item) this particle has achieved so far and the global optimal position ("social" item), obtained so far, by any particle in the population according to:

$$\begin{aligned} \boldsymbol{v}_i^k &= w\boldsymbol{v}_i^k + c_1 u_1({}^*p_i^k - \boldsymbol{\chi}_i^k) + c_2 u_2({}^*g^k - \boldsymbol{\chi}_i^k) \\ \boldsymbol{\chi}_i^{k+1} &= \boldsymbol{\chi}_i^k + \boldsymbol{v}_i^{k+1} \end{aligned} \tag{4.6}$$

where $\boldsymbol{v}_i^k$ is the velocity of the ith particle at the kth iteration, and $\boldsymbol{\chi}_i^k$ is the current position of the ith particle at the kth iteration. c_1, c_2 are positive constants, and u_1, u_2 are two random variables with a uniform distribution between 0 and 1. In this equation, w is the inertia weight which shows the effect of the previous velocity vector on the new vector, ${}^*p$ is the local optimal and ${}^*g$ is the global one. The hyperparameters of the PSO algorithm were set as $c_1 = 0.5$, $c_2 = 0.3$ and $w = 0.3$.

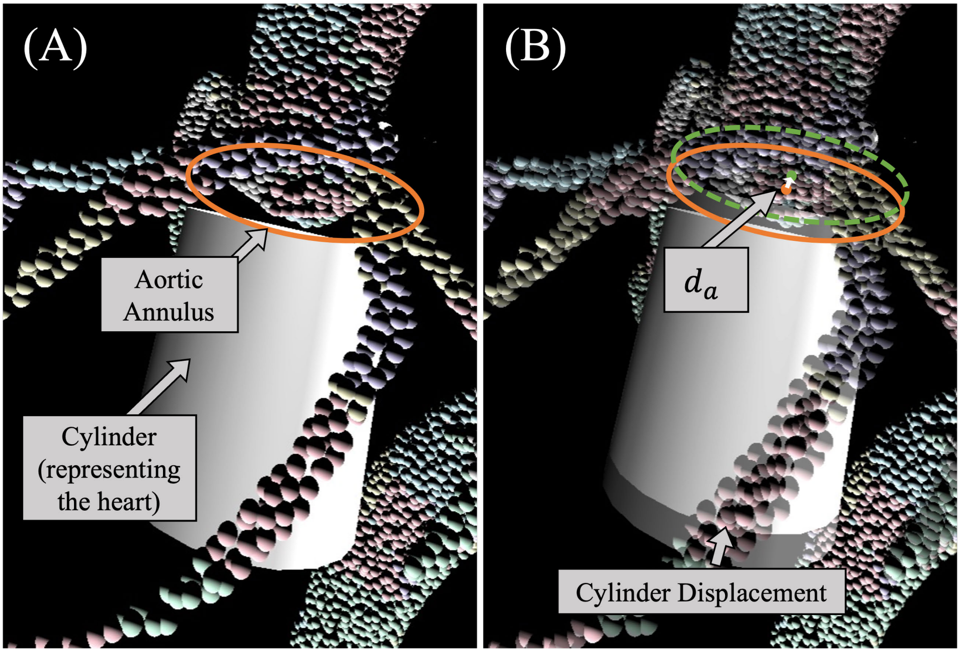

Figure 4.3: Simulation scheme for heartbeat movement: a colliding cylinder representing the heart applies an external force on the aortic root, and causes annulus displacement d_a between two subsequent time steps (A) and (B).

The reference curve with a range of [0, 0.58] MPa [11] was sampled with a constant interval of 0.02 MPa stress. Those values were given as an external force to the aortic wall using (4.3) and the corresponding strains were computed with (4.4). Once the stress-strain curve was obtained, its RMSE e_v was computed relative to the reference and regarded as the particle penalty. At this point, the PSO algorithm tries to reduce the penalty by updating the particles of the swarm (i.e., cluster parameters in this case) in the following iteration. Since PSO does not use the gradient of the objective function, it does not need to be differentiable. Moreover, PSO can evolve into more complicated and customized problems.

HEARTBEAT MOVEMENT AND CALIBRATION

To mimic the vessel movement due to a heartbeat, a time-varying external force $f(t)$ is applied on the aortic root through a colliding cylinder representing the heart (See Figure 4.3). Using the optimal PBD parameters obtained from the vasculature calibration, the heartbeat calibration process looks for the optimal external forces that generate the heartbeat movement. The displacement of the cylinder was tuned with respect to the referred cyclic movement of the aortic annulus [23].

The annulus displacement d_a is defined as the longitudinal displacement of the particles on the aortic annulus.

$$d_a(t) = z_a(t) - z_a^0 \tag{4.7}$$

where $z_a(t)$ is the average longitudinal position of the particles sampling the aortic annulus at the current time and z_a^0 is that position in the rest state (i.e., at the initial time). The PSO is employed to optimize these values by minimizing the RMSE e_a between the simulated and real aortic annulus displacement d_a with respect to the time t.

$$\min_{f(0)\cdots f(T_f)} e_a \quad \text{with } e_a = \sqrt{\frac{\sum_{t=0}^{T_f}(\hat{d}_a(t) - d_a(t))^2}{T_f}} \tag{4.8}$$

where $\hat{d}_a(t)$ is the annulus displacement of the reference curve at time t and $d_a(t)$ is the simulated annulus displacement at time t with t that spans from 0 to T_f, where T_f is the total number of samples for heartbeat calibration.

FORCE BAR VISUALIZATION

To provide visual feedback of the collision force when the device tip collides with the vessel wall, an absolute collision force is obtained along the entire device shaft via Newton's Second Law of Motion, and a ratio between the force and the maximum force was computed [34]. The maximum force represents the highest level of force that a user can apply, beyond which safety may be compromised. For example, the maximum force is set as 0.8 N in femoral arteries, 0.8 N in the aorta, 0.6 N in coronaries, and 0.8 N in subclavian arteries [34].

Only when the device tip collides with the vessel wall, the contact force is considered, and the contact force is considered along the entire device shaft. This assumption was made because end-user interviews revealed that the cardiologists focus more on the device tip for safety reasons. A mean filtering method is applied to force computation. Therefore the force is sometimes non-zero in the force bar visualization when the tip does not seem to be in contact.

4.2.2. MODELING METHOD OF DEVICES

STEERABLE CATHETER

Steerable catheters have one or more bendable segments to help navigate into the coronary ostium. Each steerable segment has three controllable movements: bending, rotating and advancing. Constant curvature modeling may constitute a valuable trade-off between the Cosserat rod's complications and the assumptions of rigid-link models [22].

The constant-curvature modeling method considers a continuum device as a set of finite curved links. These links are represented by a set of arc parameters, converted into analytical frame transformations. For each steerable segment, its shape is assumed as an arc with constant curvature κ at different bending angles, arc center at C, and a total length of l. Figure 4.4A illustrates the segment base frame $\mathscr{F}_b$ convention chosen, considering z-axis tangent to the base of the segment. The configuration space is defined by arc parameters: the rotation angle around z-axis $\phi \in [0, 2\pi]$, the arc length $s \in [0, l]$, and the arc curvature κ which entails the segment bending angle $\beta = \kappa s$.

Given the configuration space (κ, ϕ, s), the transformation ${}^b\boldsymbol{T}_i$ is performed from the segment base frame $\mathscr{F}_b$ to frame $\mathscr{F}_i$ at any point ($\boldsymbol{p}_i = [x, y, z]^T, i \in [0, G]$) along the arc,

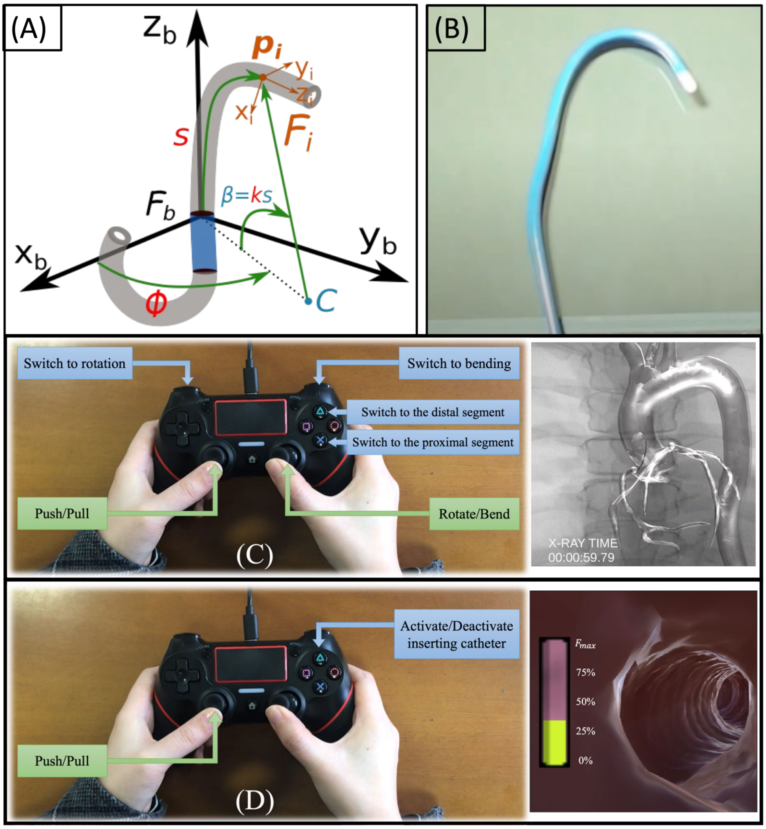

Figure 4.4: (A) Parameterization of the steerable segment modeling: ϕ denotes the arc rotation angle around z-axis, s is the arc length at $\boldsymbol{p}_i$, and κ is the arc curvature. C denotes the arc center. (B) Megellan robotic catheter. The joystick controller settings for (C) steerable catheter and (D) flexible guidewire. The GUI includes a fluoroscopy view with operation time, and an internal view with visual feedback of collision force.

according to the employed D-H table parameterization approach [35]. Then the position $\boldsymbol{p}_i$ in the global frame $\mathscr{F}_0$ can be expressed as:

$$[\boldsymbol{p}_i^T \quad 1]^T = \boldsymbol{T}_b \cdot {}^b\boldsymbol{T}_i \cdot {}^i\boldsymbol{p}_i \text{ with } {}^i\boldsymbol{p}_i = [0,0,0,1]^T \tag{4.9}$$

where $\boldsymbol{T}_b$ denotes the transformation matrix from the global frame $\mathscr{F}_0$ to the segment based reference frame $\mathscr{F}_b$, and ${}^i\boldsymbol{p}_i$ denotes the origin of $\mathscr{F}_i$ (i.e., $\boldsymbol{p}_i$) expressed in $\mathscr{F}_i$.

This transformation allows the mapping from the arc parameters space to the task space ($\boldsymbol{p}_i$). By emerging all steerable segments connected with a rigid link, the robotic catheter can reach multiple points in 3-D space and realize the typical catheterization movements performed in a clinical environment, namely, push/pull, bend, and rotate.

As a proof of concept, the 6Fr Magellan Robotic Catheter (Hansen Medical, USA) model (Figure 4.4B) is built with the following specification: distal bending segment length of 30 mm, proximal bending segment length of 25 mm, guide articulation angle of 140° for distal bend and 60° for the proximal bend. Based on the specified parameters, the maximum curvature is calculated to be 0.08 rad/mm for the distal segment and 0.04 rad/mm for the proximal segment.

FLEXIBLE GUIDEWIRE

A flexible guidewire advances through vessels to reach the target position and provides a rough reference path for catheters. The flexible guidewire modeling employs the MSM-based method [16]. For the modeling implementation in *Unity*, the guidewire consists of a set of capsules linked together with a configurable joint component that are linear springs along the longitudinal direction of the guidewire with a certain stiffness K_s.

Two flexible guidewire models were provided as a user choice. The softer coronary guidewire model was built referring to the Hi-Torque Balance Middleweight Universal II guidewire (Abbot, Illinois, USA) [17] with the following specifications: an internal diameter D_{int} of 0.014 inches (0.356mm), and a bending stiffness K_b of 75 Nmm^2. The stiffer femoral guidewire model was built referring to the Amplatz Super Stiff (Boston Scientific, Massachusetts, USA) [36] with the following specifications: an internal diameter D_{int} of 0.035 inches (0.889mm), and a bending stiffness K_b of 1850 Nmm^2.

Therefore, the moment of inertia I is derived as

$$I = \pi D_{int}^4 / 64 \tag{4.10}$$

and the Young Modulus E is expressed as

$$E = K_b / I \tag{4.11}$$

To the end, the stiffness K_s can be then computed as

$$K_s = E A_s / L \tag{4.12}$$

where K_s is the stiffness of the spring, E is the Young Modulus (which is 8.5 GPa for Hi-Torque, and 60 GPa for Amplatz), A_s is the cross section of the spring and L is the distance between the joints.

In order to mimic the follow-the-wire movement of the catheter-guidewire pair and provide a more realistic visual authenticity, during the advancement of the guidewire, a flexible catheter with a bigger diameter and with referenced mechanical properties as in [37] can be inserted following the guidewire. The combined system (i.e., catheter over a guidewire) is more rigid since the stiffness of the spring is computed as a combination of those two objects:

$$\begin{aligned} K &= K_{gu} + K_{ca} \\ K_{ca} &= \pi E_{ca} (D_{ec}^2 - D_{ic}^2) / 4 \end{aligned} \tag{4.13}$$

where K, K_{gu}, K_{ca} is the stiffness of the resulting system, the guidewire, and the reference catheter. E_{ca} is the Young modulus of the reference catheter, D_{ec}, D_{ic} is the external and internal diameter of the reference catheter. Moreover, the mechanical property of the catheter [37] is specified as E_{ca} of 85.5 GPa, D_{ec} of 2.96 mm, and D_{ic} of 2.51 mm.

GUIDING CONTROLLER FOR DEVICES

The guiding system of devices is a CHEREEKI controller (Figure 4.4C-D) by which the user can move the guidewire and the robotic catheter in a push-pull configuration, and bend-rotate at the distal/proximal segments of the robotic catheter. The Graphical User Interface (GUI) provides a fluoroscopy view, an internal view, visual feedback of collision force, and operation time (Figure 4.4). The users can select starting sites and devices according to their preferences.

4.2.3. *In-vitro* SETUP

In-vitro experiments were conducted for the deformed model validation. The displacement obtained during catheter contacts simulated on our PBD model (*in-silico*) was compared with those obtained on the aortic phantom (*in-vitro*).

The *in-vitro* experimental setup is presented in Figure 4.5. Experiments were performed in a transparent, deformable silicone aortic phantom (Materialise NV, Leuven, Belgium) [38, 39]. This phantom is a dedicated synthetic testbed developed by the EU-funded project CASCADE. The silicon model fabrication includes segmentation of CT data, 3D printing of patient-specific shells and vacuum casting of the silicon model. The realistic mechanical properties of the deformable phantom were verified through uniaxial tensile tests. See [38, 39] for more details. The phantom was placed on a 3D-printed support designed to preserve the anatomical vascular orientation. A polyethylene tube, with an outer diameter of 5 mm and stiffness of 0.245 GPa [40], was used as a catheter to push it against the aortic wall to validate phantom deformation alone. An Electromagnetic (EM) sensor (Northern Digital Inc., Waterloo, Canada) was embedded at the tip of the catheter to track its position. The setup also includes the second EM sensor attached to the surface of the phantom, Aurora EM field generator, and an external camera for filming the experiments. The PBD model in the simulator with fixed particles marked in orange is also shown in Figure 4.5.

The vessel deformation obtained *in-vitro* is defined as the displacement d_{em} of the EM sensor attached to the surface of the phantom. It indicates the ground-truth deformation.

$$d_{em} = ||\boldsymbol{x}_{em} - \boldsymbol{x}^0_{em}|| \tag{4.14}$$

where $\boldsymbol{x}^0_{em}$ is the initial position of the EM sensor attached to the surface of the phantom, and $\boldsymbol{x}_{em}$ is the current position.

The vessel deformation obtained *in-silico* is presented as the displacement d_k of the particle in the PBD model, which aligns with the position of the second EM sensor attached to the surface of the phantom. This displacement indicates the simulated vessel deformation. To identify the corresponding particle in the PBD model, a registration procedure is employed, utilizing the Singular Value Decomposition (SVD) method, as outlined by Arun et al. [41].

$$d_k = ||\boldsymbol{x}_k - \boldsymbol{x}^0_k|| \tag{4.15}$$

where the particle position is deformed from $\boldsymbol{x}^0_k$ to $\boldsymbol{x}_k$ in a three-dimensional space.

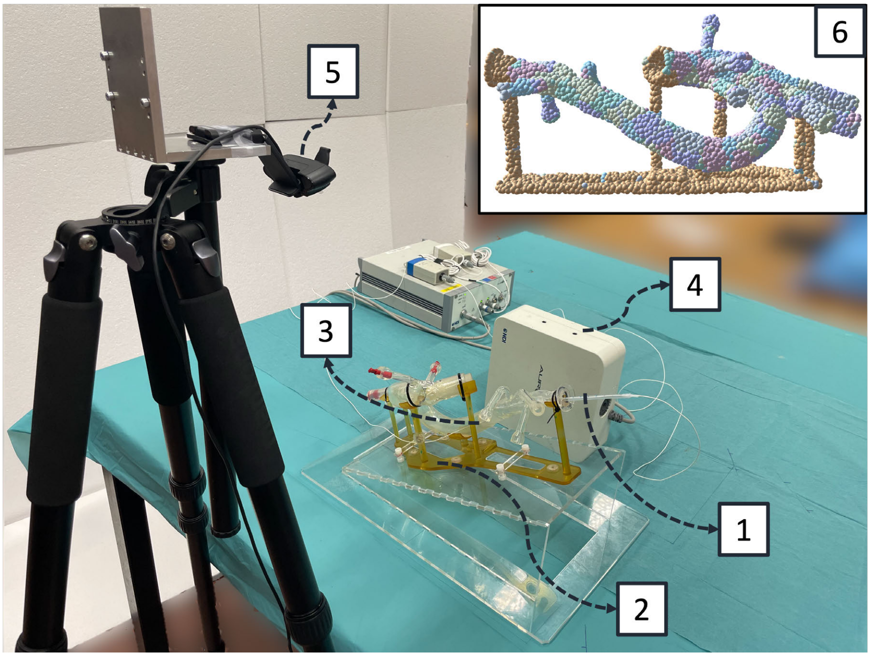

Figure 4.5: The *in-vitro* experimental setup: 1) a catheter with EM sensor embedded at the tip 2) an aortic phantom with support 3) the second EM sensor attached to the surface of the phantom 4) Aurora EM field generator 5) an external camera for filming the experiments 6) The PBD model in the simulator with fixed particles marked in orange.

4.2.4. END-USER VALIDATION PROTOCOL

The validity and visual authenticity of the virtual system were evaluated by cardiologists from CCM, IRCCS, Milan, Italy. The users are composed of ten experts (medical doctors from CCM, experience level 6.4±4.9 years, including two coauthors GM and AM) and ten novices (six medical doctors from CCM, experience level < 1 year, and four bioengineers). The users were asked to test the usability of the simulator by performing specific operation tasks of PCI (Figure 4.6).

For each operation task, their performance matrices are recorded. For evaluating user skills playing with the simulator, two parameters are proposed as performance matrices: playtime (if larger, it means a longer time of exposure to X-rays and a higher risk of infection for the patient), accumulated collision during the whole path (if larger, it means a higher risk of vascular rupture due to contact with the device).

The users did not have any previous training on the simulator and they had two chances to perform the task: the first one to learn how to use the simulator and the second one to record their scores.

Afterwards, the users were asked to fill out a questionnaire to help improve the simulator development. The questionnaire stated 11 questions, and for each question, the users can insert their level of agreement, according to the 5-Point Likert Scale.

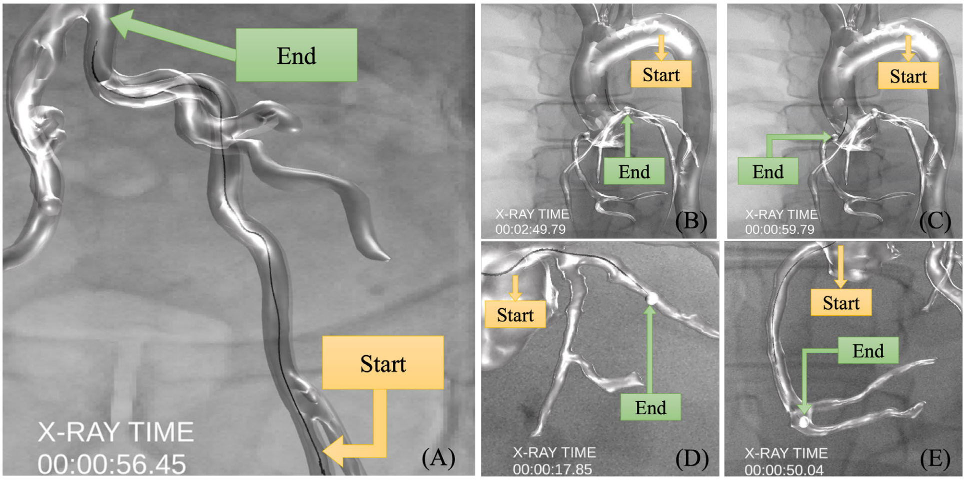

Figure 4.6: The operation tasks: (A) To advance the guidewire from femoral arteries to the abdominal aorta; (B) To advance the robotic catheter from the aortic arch to the left coronary ostium or (C) the right one; (D, E) To advance the guidewire from the coronaries ostium to the target position in the coronaries. A simulated demo of intervention tasks is made available: `https://youtu.be/jdfQeZnBLhs`

4.3. RESULTS

4.3.1. CALIBRATION RESULTS

VASCULATURE PBD CALIBRATION

To obtain the optimal cluster parameters, an external stress was applied perpendicular to the vessel wall with the range of $[0, 0.58]$MPa and the displacement of the particles lying on the vessel wall in the radial direction was measured based on *Assumption 1* as shown in Figure 4.2. Compared with the reference curve [11], the RMSE (4.5) was computed and minimized during the automatic PSO calibration process. The optimal cluster parameters were: $[s_c, r_c, t_c]$ =[8 mm, 12 mm, 0.8] with a RMSE of 0.26% while the mean error and standard deviation are 0.23±0.13%. The optimal stress-strain curve is shown in Figure 4.7A.

HEARTBEAT CALIBRATION

The objective of heartbeat calibration is to automatically adjust the relevant parameters in the simulator to mimic the annulus displacement in [23]. The reference curve [23] is the averaged annulus displacement from 60 patients with aortic stenosis. It is referred to as the ground truth in calibration. The relevant parameters are the displacement of the virtual heart causing the displacement of the annulus. The PSO approach optimizes these parameters by minimizing the RMSE between the simulated and real aortic annulus displacement. Figure 4.7B presents the displacement of the virtual heart, the annulus displacement from literature, and the simulated annulus displacement after calibration, in three cardiac cycles in a time range of $[0, 2.68]$s. The simulated annulus displacement is shown in Figure 4.7B with a RMSE (4.8) of 0.90 mm while the mean error and standard deviation are 0.30±0.85mm. The mean absolute error and the standard deviation of the

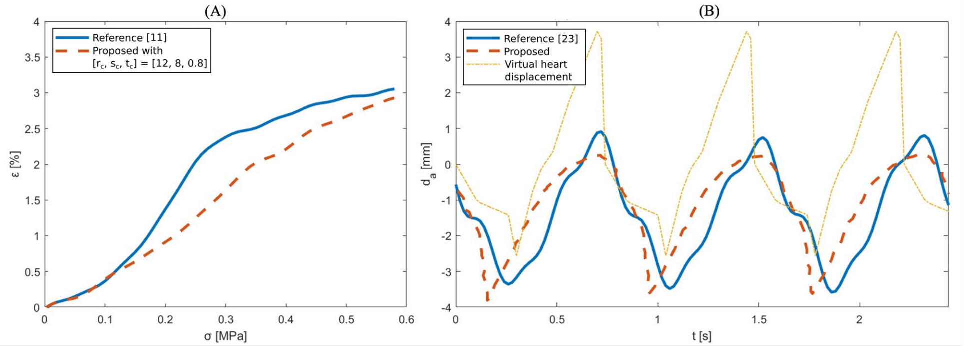

Figure 4.7: Quantitative comparison results between simulator performance and literature: (A) The vessels stress-strain curve ($\sigma - \epsilon$) from literature (blue) and from the optimal case after calibration using PSO algorithm (red). (B) The annulus displacement (d_a) along time t from literature (blue) and from the optimal simulated case after calibration using PSO algorithm (red). The displacement of the colliding cylinder representing the heart (as defined in Figure 4.3) is presented in yellow.

absolute error are 0.64±0.63mm. The median, 90th percentile, and maximum absolute error are 0.31mm, 1.67mm, and 2.44mm, respectively. The simulated annulus displacement has smoother but in-phase positive peaks and sharper anticipated negative peaks. However, the curve frequency was not altered. Therefore, it can mimic the heartbeat movement at a similar frequency, even if the peaks are not the same. The peaks represent the maximum displacement of the annulus plane during cardiac cycles. If the maximum displacement is more of interest, such as the longitudinal displacement of the aortic annulus [42], the objective function of heartbeat calibration can be changed to minimize the error at peaks between the curves.

4.3.2. *In-vitro* VALIDATION

In-vitro experiments were conducted for the deformed model validation. The displacement obtained during ten different catheter contacts simulated on our PBD model (*in-silico*) was compared with those obtained on the aortic phantom (*in-vitro*).

Figure 4.8 shows the comparison results of vessel deformation obtained in two ways: *in-vitro* and *in-silico*. The mean error and standard deviation are 1.35±1.38mm. The RMSE is 1.93mm. The mean absolute error and the standard deviation of the absolute error are 1.46±1.27mm. The median, 90th percentile, and maximum absolute error are 1.13mm, 3.44mm, and 5.66mm, respectively. The Pearson correlation coefficient between the two curves is 0.83, which indicates a strong positive correlation between the in-silico and in-vitro displacement. It verifies the comparability between the proposed PBD deformed model and the silicone aortic phantom. It also reveals the possibility of further ex-vivo, in-vivo, and patient-specific model validation. One of the error sources can be the inaccurate rigid registration between EM space and simulator space. This inaccuracy leads to a less accurate alignment between the second EM sensor and its corresponding particle within the PBD model. Due to this misalignment, another particle might be identified in the PBD model, resulting in varying displacements. Consequently, the displacement measurements of the particle, used to indicate vessel deformation, are

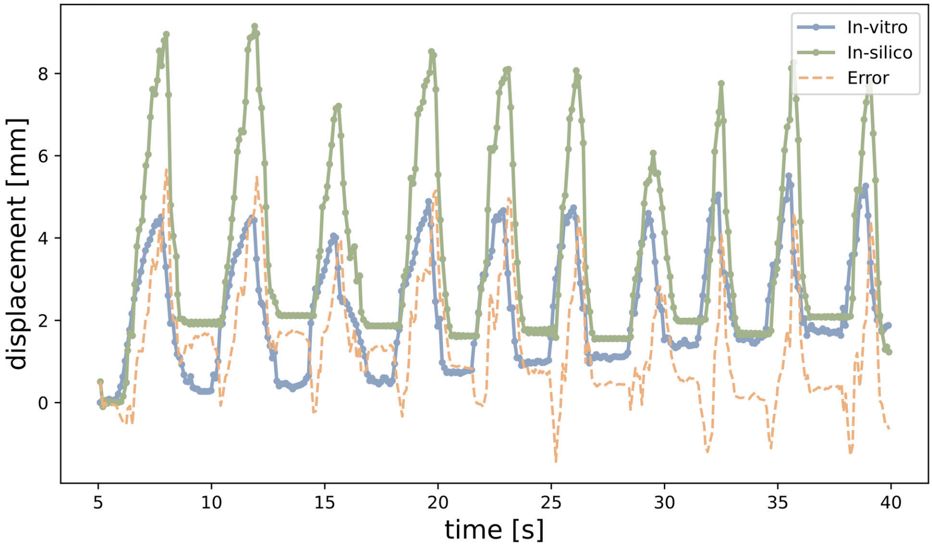

Figure 4.8: The comparison of displacement obtained during ten different catheter contacts simulated on our PBD model (d_{em}, *in-silico*, green) and the one obtained on the aortic phantom (d_k, *in-vitro*, blue). Their difference is marked in orange. The video comparison is made available: `https://youtu.be/2p20Y2-YID8`

subject to inaccuracies. In this work, a traditional registration method, SVD [41], is performed. More accurate registration methods will help reduce deformation prediction errors.

4.3.3. END-USER VALIDATION

As shown by Table 4.2, the performance difference between novices and experts shows that novices are more accustomed to using joystick controllers instead of manual operation. Experts spent more time performing task A, i.e., to advance the guidewire from femoral arteries to the abdominal aorta, and task C, i.e., to advance the robotic catheter from the aortic arch to the right coronary ostium. Meanwhile, the experts presented less collision in task C. The comparison results for other tasks do not show statistically significant differences.

The questionnaire results in Figure 4.9 show that experts have a higher appraisal of the system, whereas novices are more adaptable to novel technologies, such as joystick controllers and simulated internal views. The experts have more diverse opinions on Q6. Two cardiologists rated ‘1’, one cardiologist with three years of experience, and one with six years of experience. The proposed simulator is intended to use as a training platform for robotic catheters [43, 44, 45]. Currently, conventional procedures use flexible catheters without robotic assistance. Cardiologists are more customized to use conventional catheters. Therefore, robot assistance affected the scores on the training capability of the proposed simulator. Scores on other criteria can verify this inference as well. The cardiologists rated higher on Q1 and Q2 and relatively lower on Q3. It shows that the

Table 4.2: Performance comparison of ten novices and ten experts after performing specific operation tasks of PCI, including the operation time of each task and the accumulated collision during the whole task.

Device	**Task**	**User**	**Playtime [s]** (Mean±SD)	**Collision [N]** (Mean±SD)
guidewire	CFA - abdominal aorta	Experts	89.8±38.7 ↕ ★	13.2±14.7
	(Figure 4.6A)	Novices	64.0±25.3	7.3±4.7
	left coronaries angioplasty	Experts	77.8±5.0	3.8±1.7
	(Figure 4.6D)	Novices	75.6±1.2	3.5±1.7
	right coronaries angioplasty	Experts	71.3±17.0	14.7±11.3
	(Figure 4.6E)	Novices	68.4±25.5	12.9±6.9
robotic catheter	left coronaries cannulation	Experts	187.8±156.0	5.8±7.8
	(Figure 4.6B)	Novices	109.1±60.2	2.9±2.6
	right coronaries cannulation	Experts	171.1±111.2 ↕ ★	5.0±8.0
	(Figure 4.6C)	Novices	83.9±46.1	15.2±42.1

★, $p < 0.05$ Kruskal-Wallis test for statistical significance analysis

cardiologists are satisfied with the visual authenticity of the intervention process and the deformable property of the vessels. Those are essential factors in a robotic catheter simulation platform.

Constructive feedback on future improvements was provided by cardiologists as well. The coronary guidewire could be modeled with a preshaped nitinol tip with the capability of rotating, which would let it engage different branches of the coronaries. In addition to the heartbeat motion, the respiration motion could be included as well. As for the visual feedback of collision force, haptic feedback, such as the vibration of the joystick, would be more intuitive. Augmented reality would provide more visually plausible training.

4.4. Discussion

4.4.1. Findings

An important finding of the questionnaire analysis reveals a higher preference for the internal view of vessels among novice clinicians compared to expert cardiologists. This preference suggests that an internal view of vessels may offer greater benefits to clinicians with less experience in the field. The internal view of the vessels can be reconstructed from IntraVascular UltraSound (IVUS) images [46]. The internal view is very useful because cardiologists can only see the structures in 2D in reality without having information about a collision with structures inside vessels. Despite the absence of such a feature in the traditional procedure, it would be helpful to have a real-time 3D view of

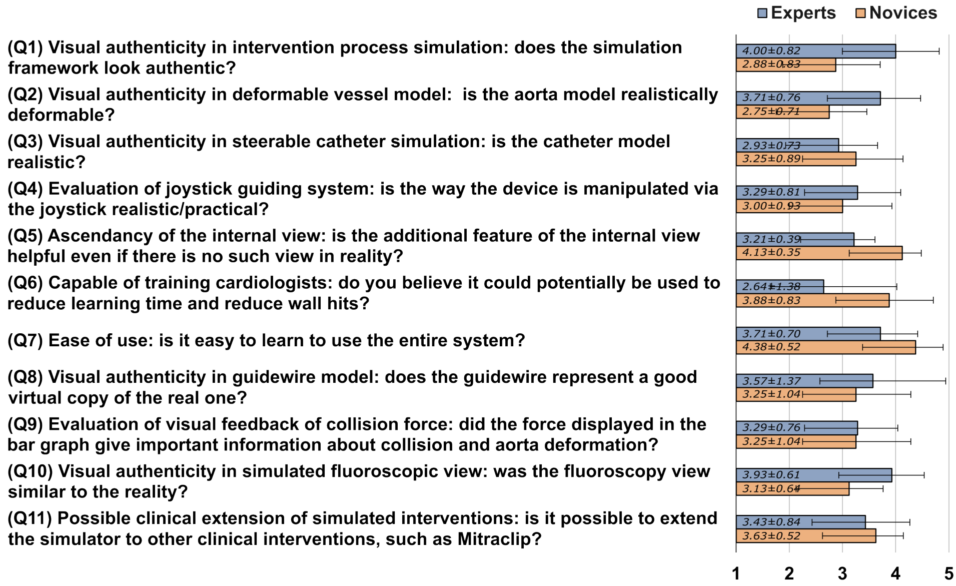

Figure 4.9: The validity evaluation results of ten novices and ten experts, where Q1-Q11 are the evaluation criteria specified in the questionnaire and 1-5 correspond to the level of agreement: 1-Strongly disagree; 2-Disagree; 3-Neither agree nor disagree; 4-Agree; 5-Strongly agree.

the anatomy, the plaques, and device advancement. What is used in reality is the IVUS view (with a diagnosing catheter) that could be helpful to know about the anatomy and plaques etc., but it is not aligned with the advancement of the balloon/stent catheter because the IVUS view and the intervention treatment are not in the same phase. Despite the absence of such an internal view in the treatment process, the goal is to provide the cardiologists with another perspective that will accelerate the process as they can view the interactions from different views.

4.4.2. POSSIBILITY OF GENERALIZATION

The deformed model is reconstructed from CTA images of a patient with cardiac disease. It is patient-specific and can be employed for aorta models of other patients. Heartbeat variability can be achieved as long as a reference curve is given for calibration, such as the reference curve [23].

Even though the 6Fr Magellan Robotic Catheter and two specific guidewires were used as a proof-of-concept, it can be extended to other catheters and guidewires. This simulator can be utilized to optimize the design of robotic catheters, such as maximum bending extent, steerable tip length, and diameter. Those parameters are adjustable in the proposed simulator. It can also be used for autonomous path planning and control in a simulated, cluttered environment.

4.4.3. LIMITATIONS AND PERSPECTIVES

The joystick control approach is different from the traditional way to advance devices. Therefore cardiologists expertized in traditional interventions may perform worse than game players. Existing robotic systems mostly use joystick and workstation as the controller input, such as CorPath™ GRX (Corindus), Niobe™ (Stereotaxis) and R-One™ (Robocath). In [47], a device controller is developed that mimics a standard catheter handle, has vibrotactile feedback, and is easy to use by cardiologists. However, joystick controllers with vibrotactile feedback are relatively easy to use and low in cost [14]. Long-term-following experiments can be carried out to investigate a proper controller and its training effectiveness.

More operation tasks that reveal expert experience will be carried out in end-user validation. Positioning and inflating a balloon or stent catheter at the occlusion site can be developed as an operational task. This proof-of-concept is presented at the link[1]. However, accurate simulation of the mechanical properties of the occlusions and stents requires thorough investigation in the future. The accuracy of stent alignment at the target site can be selected as a performance matrix. Moreover, the user's choice of access route can be assessed to ensure the safety of needle insertion.

Traditional fluoroscopy imaging does not provide enough information for cardiologists, such as depth. Augmented Reality (AR) could be integrated for more visually plausible training [48]. Deformable vessels with AR provide 3D visualization to help guide and locate the instrument more intuitively. Clinical studies in [49] highlight the need for intra-operative 3D visualization to help develop safer interventions. Several commercial systems, such as EnSite NavX (St.Jude), Carto (Biosense Webster), and LocaLisa (Medtronic), develop AR techniques as an alternative to classical imaging techniques.

4.5. CONCLUSION

This chapter presents a realistic, auto-adaptive, and visually plausible simulator for endovascular catheterization procedures. The proposed workflow implements the modeling and simulation of intervention devices and a deformable aorta that could create a dynamic environment for intra-operative path planning and control in robotic endovascular catheterization, which will be presented in future works. Compared with literature, some novel properties of the proposed simulator are highlighted, such as a simulated movement of the vessels caused by the heartbeat and an autonomous calibration using the PSO algorithm. The reported results of *in-vitro* validation show that this simulator framework can be applied to different datasets and represents a good surrogate for the modelization of deformation.

ETHICAL APPROVAL

The data collection followed the ethical protocol approved by Centro Cardiologico Monzino under the assigned code of *02_21 PA*.

---

[1] `https://youtu.be/lqN4Uw4HZz8`

BIBLIOGRAPHY

[1] Franz-Josef Neumann, Miguel Sousa-Uva, Anders Ahlsson, Fernando Alfonso, Adrian P Banning, Umberto Benedetto, Robert A Byrne, Jean-Philippe Collet, Volkmar Falk, Stuart J Head, et al. "2018 ESC/EACTS Guidelines on myocardial revascularization". In: *European heart journal* 40.2 (2019), pp. 87–165. DOI: `10.1093/eurheartj/ehy394`.

[2] Aleks Attanasio, Bruno Scaglioni, Elena De Momi, Paolo Fiorini, and Pietro Valdastri. "Autonomy in surgical robotics". In: *Annual Review of Control, Robotics, and Autonomous Systems* 4 (2021), pp. 651–679. DOI: `10.1146/annurev-control-062420-090543`.

[3] Giasemi Koutouzi, Marcus Pfister, Katharina Breininger, Mikael Hellström, Håkan Roos, and Mårten Falkenberg. "Iliac artery deformation during EVAR". In: *Vascular* 27.5 (2019), pp. 511–517. DOI: `10.1177/1708538119840565`.

[4] Blandine Maurel, Adrien Hertault, Teresa Martin Gonzalez, Jonathan Sobocinski, Marielle Le Roux, Jessica Delaplace, Richard Azzaoui, Marco Midulla, and Stéphan Haulon. "Evaluation of visceral artery displacement by endograft delivery system insertion". In: *Journal of Endovascular Therapy* 21.2 (2014), pp. 339–347. DOI: `10.1583/13-4471MR.1`.

[5] Laura Cercenelli, Barbara Bortolani, Guido Tiberi, Chiara Mascoli, Ivan Corazza, Mauro Gargiulo, and Emanuela Marcelli. "Characterization of vessel deformations during EVAR: a preliminary retrospective analysis to improve fidelity of endovascular simulators". In: *Journal of Surgical Education* 75.4 (2018), pp. 1096–1105. DOI: `10.1016/j.jsurg.2017.10.013`.

[6] Adrien Kaladji, Aurélien Dumenil, Miguel Castro, Alain Cardon, Jean-Pierre Becquemin, Benyebka Bou-Saïd, Antoine Lucas, and Pascal Haigron. "Prediction of deformations during endovascular aortic aneurysm repair using finite element simulation". In: *Computerized medical imaging and graphics* 37.2 (2013), pp. 142–149. DOI: `10.1016/j.compmedimag.2013.03.002`.

[7] Zhen Li, Jenny Dankelman, and Elena De Momi. "Path planning for endovascular catheterization under curvature constraints via two-phase searching approach". In: *International Journal of Computer Assisted Radiology and Surgery* 16.4 (2021), pp. 619–627. DOI: `10.1007/s11548-021-02328-x`.

[8] Maria Peral-Boiza, Teresa Gomez-Fernandez, Patricia Sanchez-Gonzalez, Borja Rodriguez-Vila, Enrique J Gómez, and Álvaro Gutiérrez. "Position Based Model of a Flexible Ureterorenoscope in a Virtual Reality Training Platform for a Minimally Invasive Surgical Robot". In: *IEEE Access* 7 (2019), pp. 177414–177426. DOI: `10.1109/ACCESS.2019.2957857`.

[9] Aimin Hao, Jiahao Cui, Shuai Li, and Qinping Zhao. “Personalized cardiovascular intervention simulation system”. In: *Virtual Reality & Intelligent Hardware* 2.2 (2020), pp. 104–118. DOI: `10.1016/j.vrih.2020.04.001`.

[10] Shuxiang Guo, Mohan Qu, Baofeng Gao, and Jin Guo. “Deformation of the catheter and 3D blood vessel model for a VR-based catheter system”. In: *IEEE International Conference on Mechatronics and Automation*. 2013, pp. 861–866. DOI: `10.1109/ICMA.2013.6618028`.

[11] Xiufen Ye, Jianguo Zhang, Peng Li, Tian Wang, and Shuxiang Guo. “A fast and stable vascular deformation scheme for interventional surgery training system”. In: *Biomedical engineering online* 15.1 (2016), pp. 1–14. DOI: `10.1186/s12938-016-0148-3`.

[12] Eleonora Tagliabue, Diego Dall’Alba, Enrico Magnabosco, Chiara Tenga, Igor Peterlík, and Paolo Fiorini. “Position-based modeling of lesion displacement in Ultrasound guided breast biopsy”. In: *International journal of computer assisted radiology and surgery* 14.8 (2019), pp. 1329–1339. DOI: `10.1007/s11548-019-01997-z`.

[13] Eleonora Tagliabue, Ameya Pore, Diego Dall’Alba, Enrico Magnabosco, Marco Piccinelli, and Paolo Fiorini. “Soft tissue simulation environment to learn manipulation tasks in autonomous robotic surgery”. In: *2020 IEEE/RSJ International Conference on Intelligent Robots and Systems (IROS)*. 2020, pp. 3261–3266. DOI: `10.1109/IROS45743.2020.9341710`.

[14] Alice Segato, Chiara Di Vece, Sara Zucchelli, Marco Di Marzo, Thomas Wendler, Mohammad Farid Azampour, Stefano Galvan, Riccardo Secoli, and Elena De Momi. “Position-Based Dynamics Simulator of Brain Deformations for Path Planning and Intra-Operative Control in Keyhole Neurosurgery”. In: *IEEE Robotics and Automation Letters* 6.3 (2021), pp. 6061–6067. DOI: `10.1109/LRA.2021.3090016`.

[15] Alice Segato, Marco Di Marzo, Sara Zucchelli, Stefano Galvan, Riccardo Secoli, and Elena De Momi. “Inverse reinforcement learning intra-operative path planning for steerable needle”. In: *IEEE Transactions on Biomedical Engineering* 69.6 (2021), pp. 1995–2005. DOI: `10.1109/TBME.2021.3133075`.

[16] Giuseppe Turini, Sara Condino, Umberto Fontana, Roberta Piazza, John E Howard, Simona Celi, Vincenzo Positano, Mauro Ferrari, and Vincenzo Ferrari. “Software framework for vr-enabled transcatheter valve implantation in unity”. In: *International Conference on Augmented Reality, Virtual Reality and Computer Graphics*. 2019, pp. 376–384. DOI: `10.1007/978-3-030-25965-5_28`.

[17] Hoda Sharei, Jeroen Kieft, Kazuto Takashima, Norihiro Hayashida, John J van den Dobbelsteen, and Jenny Dankelman. “A Rigid Multibody Model to Study the Translational Motion of Guidewires Based on Their Mechanical Properties”. In: *Journal of Computational and Nonlinear Dynamics* 14.10 (2019). DOI: `10.1115/1.4043618`.

[18] Hoda Sharei, Tanja Alderliesten, John J van den Dobbelsteen, and Jenny Dankelman. “Navigation of guidewires and catheters in the body during intervention procedures: a review of computer-based models”. In: *Journal of Medical Imaging* 5.1 (2018), p. 010902. DOI: `10.1117/1.JMI.5.1.010902`.

[19] John Till, Vincent Aloi, and Caleb Rucker. “Real-time dynamics of soft and continuum robots based on Cosserat rod models”. In: *The International Journal of Robotics Research* 38.6 (2019), pp. 723–746. DOI: `10.1177/0278364919842269`.

[20] Cosimo Della Santina, Antonio Bicchi, and Daniela Rus. “On an improved state parametrization for soft robots with piecewise constant curvature and its use in model based control”. In: *IEEE Robotics and Automation Letters* 5.2 (2020), pp. 1001–1008. DOI: `10.1109/LRA.2020.2967269`.

[21] Roy J Roesthuis and Sarthak Misra. “Steering of multisegment continuum manipulators using rigid-link modeling and FBG-based shape sensing”. In: *IEEE transactions on robotics* 32.2 (2016), pp. 372–382. DOI: `10.1109/TRO.2016.2527047`.

[22] Tomas da Veiga, James H Chandler, Peter Lloyd, Giovanni Pittiglio, Nathan J Wilkinson, Ali K Hoshiar, Russell A Harris, and Pietro Valdastri. “Challenges of continuum robots in clinical context: A review”. In: *Progress in Biomedical Engineering* 2.3 (2020). DOI: `10.1088/2516-1091/ab9f41`.

[23] Hiromi Nakai, Masaaki Takeuchi, Hidetoshi Yoshitani, Kyoko Kaku, Nobuhiko Haruki, and Yutaka Otsuji. “Pitfalls of anatomical aortic valve area measurements using two-dimensional transoesophageal echocardiography and the potential of three-dimensional transoesophageal echocardiography”. In: *European Journal of Echocardiography* 11.4 (2010), pp. 369–376. DOI: `10.1093/ejechocard/jep220`.

[24] Kevin Kalisz, Ji Buethe, Sachin S Saboo, Suhny Abbara, Sandra Halliburton, and Prabhakar Rajiah. “Artifacts at cardiac CT: physics and solutions”. In: *Radiographics* 36.7 (2016), pp. 2064–2083. DOI: `10.1148/rg.2016160079`.

[25] Zhuo Liu, Zhuolu Zhang, Nan Hong, Lei Chen, Chengfu Cao, Jian Liu, and Ye Sun. “Diagnostic performance of free-breathing coronary computed tomography angiography without heart rate control using 16-cm z-coverage CT with motion-correction algorithm”. In: *Journal of cardiovascular computed tomography* 13.2 (2019), pp. 113–117. DOI: `10.1016/j.jcct.2019.01.005`.

[26] Junfu Liang, Ying Sun, Ziqing Ye, Yanchun Sun, Lei Xu, Zhen Zhou, Brian Thomsen, Jianying Li, Zhonghua Sun, and Zhanming Fan. “Second-generation motion correction algorithm improves diagnostic accuracy of single-beat coronary CT angiography in patients with increased heart rate”. In: *European radiology* 29.8 (2019), pp. 4215–4227. DOI: `10.1007/s00330-018-5929-6`.

[27] Birger Mensel, Alexander Quadrat, Tobias Schneider, Jens-Peter Kühn, Marcus Dörr, Henry Völzke, Wolfgang Lieb, Katrin Hegenscheid, and Roberto Lorbeer. “MRI-based determination of reference values of thoracic aortic wall thickness in a general population”. In: *European radiology* 24.9 (2014), pp. 2038–2044. DOI: `10.1007/s00330-014-3188-8`.

[28] Zahi A Fayad, Valentin Fuster, John T Fallon, Timothy Jayasundera, Stephen G Worthley, Gerard Helft, J Gilberto Aguinaldo, Juan J Badimon, and Samin K Sharma. “Noninvasive in vivo human coronary artery lumen and wall imaging using black-blood magnetic resonance imaging”. In: *Circulation* 102.5 (2000), pp. 506–510. DOI: `10.1161/01.cir.102.5.506`.

[29] Paolo Cignoni, Marco Callieri, Massimiliano Corsini, Matteo Dellepiane, Fabio Ganovelli, Guido Ranzuglia, et al. “Meshlab: an open-source mesh processing tool.” In: *Eurographics Italian chapter conference*. Vol. 2008. 2008, pp. 129–136. DOI: `10.2312/LocalChapterEvents/ItalChap/ItalianChapConf2008/129-136`.

[30] Gabriel Taubin. “Curve and surface smoothing without shrinkage”. In: *IEEE international conference on computer vision*. 1995, pp. 852–857. DOI: `10.1109/ICCV.1995.466848`.

[31] Matthias Müller, Bruno Heidelberger, Marcus Hennix, and John Ratcliff. “Position based dynamics”. In: *Journal of Visual Communication and Image Representation* 18.2 (2007), pp. 109–118. DOI: `10.1016/j.jvcir.2007.01.005`.

[32] Matthias Müller, Bruno Heidelberger, Matthias Teschner, and Markus Gross. “Meshless deformations based on shape matching”. In: *ACM transactions on graphics (TOG)* 24.3 (2005), pp. 471–478. DOI: `10.1145/1073204.1073216`.

[33] Majid Jaberipour, Esmaile Khorram, and Behrooz Karimi. “Particle swarm algorithm for solving systems of nonlinear equations”. In: *Computers & Mathematics with Applications* 62.2 (2011), pp. 566–576. DOI: `10.1016/j.camwa.2011.05.031`.

[34] Hedyeh Rafii-Tari, Celia V Riga, Christopher J Payne, Mohamad S Hamady, Nicholas JW Cheshire, Colin D Bicknell, and Guang-Zhong Yang. “Reducing contact forces in the arch and supra-aortic vessels using the Magellan robot”. In: *Journal of vascular surgery* 64.5 (2016), pp. 1422–1432. DOI: `10.1016/j.jvs.2015.06.215`.

[35] Robert J Webster III and Bryan A Jones. “Design and kinematic modeling of constant curvature continuum robots: A review”. In: *The International Journal of Robotics Research* 29.13 (2010), pp. 1661–1683. DOI: `10.1177/0278364910368147`.

[36] Gareth J Harrison, Thien V How, S Rao Vallabhaneni, John A Brennan, Robert K Fisher, Jagjeeth B Naik, and Richard G McWilliams. “Guidewire stiffness: what’s in a name?” In: *Journal of Endovascular Therapy* 18.6 (2011), pp. 797–801. DOI: `10.1583/11-3592.1`.

[37] Jason Carey, Derek Emery, and Philippe McCracken. “Buckling test as a new approach to testing flexural rigidities of angiographic catheters”. In: *Journal of Biomedical Materials Research Part B: Applied Biomaterials* 76.1 (2006), pp. 211–218. DOI: `10.1002/jbm.b.30358`.

[38] Emmanuel Vander Poorten, P Tran, Alain Devreker, Caspar Gruijthuijsen, Sergio Portoles-Diez, Gabrijel Smoljkic, Vule Strbac, Nele Famaey, Dominiek Reynaerts, Jos Vander Sloten, et al. “Cognitive autonomous catheters operating in dynamic environments”. In: *Journal of Medical Robotics Research* 1.03 (2016), p. 1640011. DOI: `10.1142/S2424905X16400110`.

[39] Maryna Kvasnytsia, Nele Famaey, Michal Böhm, and Eva Verhoelst. “Patient specific vascular benchtop models for development and validation of medical devices for minimally invasive procedures”. In: *Journal of Medical Robotics Research* 1.03 (2016), p. 1640008. DOI: `10.1142/S2424905X16400080`.

[40] Omnexus. *Flexural Modulus Values of Several Plastics.* 2022. URL: `https://omnexus.specialchem.com/polymer-properties/properties/stiffness` (visited on 09/13/2022).

[41] K. S. Arun, T. S. Huang, and S. D. Blostein. “Least-Squares Fitting of Two 3-D Point Sets”. In: *IEEE Transactions on Pattern Analysis and Machine Intelligence* PAMI-9.5 (1987), pp. 698–700. DOI: `10.1109/TPAMI.1987.4767965`.

[42] Tomasz Plonek, Mikolaj Berezowski, Jacek Kurcz, Przemyslaw Podgorski, Marek Sąsiadek, Bartosz Rylski, Andrzej Mysiak, and Marek Jasinski. “The evaluation of the aortic annulus displacement during cardiac cycle using magnetic resonance imaging”. In: *BMC Cardiovascular Disorders* 18.1 (2018), pp. 1–6. DOI: `10.1186/s12872-018-0891-4`.

[43] Mohammad Hasan Dad Ansari, Beatriz Farola Barata, Fabian Trauzettel, Zhen Li, Di Wu, Diego DallÁlba, Gianni Borghesan, Mouloud Ourak, Veronica Iacovacci, Selene Tognarelli, Jenny Dankelman, Elena De Momi, Paul Breedveld, Paolo Fiorini, Jos Vander Sloten, Arianna Menciassi, and Emmanuel Vander Poorten. “Proof-of-Concept Medical Robotic Platform for Endovascular Catheterization”. In: *Proceedings of the 11th Conference on New Technologies for Computer and Robot Assisted Surgery (CRAS)*. 2022, pp. 66–67. Available online: `https://atlas-itn.eu/wp-content/uploads/2022/05/CRAS2022_ATLAS_C3.pdf`.

[44] Di Wu, Yao Zhang, Mouloud Ourak, Kenan Niu, Jenny Dankelman, and Emmanuel Vander Poorten. “Hysteresis modeling of robotic catheters based on long short-term memory network for improved environment reconstruction”. In: *IEEE Robotics and Automation Letters* 6.2 (2021), pp. 2106–2113. DOI: `10.1109/LRA.2021.3061069`.

[45] Di Wu, Xuan Thao Ha, Yao Zhang, Mouloud Ourak, Gianni Borghesan, Kenan Niu, Fabian Trauzettel, Jenny Dankelman, Arianna Menciassi, and Emmanuel Vander Poorten. “Deep-Learning-Based Compliant Motion Control of a Pneumatically-Driven Robotic Catheter”. In: *IEEE Robotics and Automation Letters* 7.4 (2022), pp. 8853–8860. DOI: `10.1109/LRA.2022.3186497`.

[46] Beatriz Farola Barata, Phuong Toan Tran, Gianni Borghesan, Keir McCutcheon, Diego Dall’Alba, Paolo Fiorini, Jos Vander Sloten, and Emmanuel Vander Poorten. “IVUS-Based Local Vessel Estimation for Robotic Intravascular Navigation”. In: *IEEE Robotics and Automation Letters* 6.4 (2021), pp. 8102–8109. DOI: `10.1109/LRA.2021.3102307`.

[47] Laura Cercenelli, Barbara Bortolani, and Emanuela Marcelli. “CathROB: A highly compact and versatile remote catheter navigation system”. In: *Applied Bionics and Biomechanics* 2017 (2017). DOI: `10.1155/2017/2712453`.

[48] Rosanna M Viglialoro, Nicola Esposito, Sara Condino, Fabrizio Cutolo, Simone Guadagni, Marco Gesi, Mauro Ferrari, and Vincenzo Ferrari. “Augmented reality to improve surgical simulation: Lessons learned towards the design of a hybrid laparoscopic simulator for cholecystectomy”. In: *IEEE Transactions on Biomedical Engineering* 66.7 (2018), pp. 2091–2104. DOI: `10.1109/TBME.2018.2883816`.

[49] Christian Butter, Hidehiro Kaneko, Grit Tambor, Masahiko Hara, Michael Neuss, and Frank Hoelschermann. “Clinical utility of intraprocedural three-dimensional integrated image guided transcatheter aortic valve implantation using novel automated computed tomography software: A single-center preliminary experience”. In: *Catheterization and Cardiovascular Interventions* 93.4 (2019), pp. 722–728. DOI: `10.1002/ccd.27920`.

5

DEFORMABLE MODEL-TO-IMAGE REGISTRATION TOWARDS AUGMENTED REALITY-GUIDED ENDOVASCULAR INTERVENTIONS

Existing image registration methods face difficulties in accurately incorporating tissue deformations compared to the pre-operative 3D model, particularly in a weakly-supervised manner. Additionally, reconstructing deformations from 2D to 3D space and presenting this intra-operative model visually to clinicians poses further complexities. To address these challenges, this study introduces a novel deformable model-to-image registration framework using deep learning. Furthermore, this research proposes a visualization method through augmented reality to provide guidance for endovascular interventions. This study utilized image data collected from 9 patients who underwent Transcatheter Aortic Valve Implantation (TAVI) procedures. The registration results in 2D indicate that the proposed deformable model-to-image registration framework achieves a Modified Dice Similarity Coefficient (MDSC) value of 0.55 ± 0.04 *and a Penalization of Deformations in Spare Space (PDSS) value of* 3.77 ± 0.09. *Additionally, the accuracy of registration in 3D was evaluated using a dataset obtained from an intervention simulator, resulting in a Mean Absolute Error (MAE) of* 1.51 ± 1.02 *mm within the region of interest. Overall, the study validates the feasibility and accuracy of the proposed weakly-supervised deformable model-to-image registration framework, demonstrating its potential to provide intra-operative 3D imaging as intervention assistance in dynamic vascular environments.*

This chapter is available as:
Zhen Li, Letizia Contini, Alessandro Ippoliti, Elena Bastianelli, Federico De Marco, Jenny Dankelman, and Elena De Momi. “Deformable Model-to-Image Registration towards Augmented Reality-Guided Endovascular Interventions”. 2023. (Under Review).

5.1. INTRODUCTION

The rising demand for minimally invasive procedures has expedited the acceptance and implementation of endovascular interventions [1]. Endovascular interventions utilize the vascular system to access anatomical regions deep within the body. For example, TAVI procedure, a percutaneous cardiological intervention, facilitates the implantation of a miniaturized biological valve prosthesis into the aortic root. This minimally invasive approach is designed to address aortic valve pathologies, specifically aortic stenosis and steno-insufficiency [2].

During endovascular interventions, image-based guidance plays a crucial role in providing clinicians and robotics systems with valuable insights into the dynamic vascular environment [3, 4]. However, conventional 2D images commonly used for intervention guidance, such as 2D X-ray fluoroscopy and Digital Subtraction Angiography (DSA), are often deemed insufficient by cardiologists due to limited information and the absence of depth perception. Consequently, there is a growing demand among cardiologists for intra-operative 3D imaging [5]. By fusing 3D pre-operative data with 2D intra-operative images, complex clinical procedures can benefit from enhanced visualization of concealed structures and a more comprehensive anatomical model [6, 7, 8]. The necessity for introducing a deformable model-to-image registration approach stems from various physiological factors such as heartbeat, respiration, patient movement, and instrument insertion, all of which can induce vascular deformations and adversely impact registration accuracy [9].

Existing image registration methods to reconstruct vascular deformations can be broadly categorized into optimization-based methods, which rely on iterative optimization processes, and learning-based methods that leverage neural networks. Zhang *et al.* [11] proposed a method to reconstruct a deformed intra-operative 3D aortic model using a pre-operative 3D model and intra-operative fluoroscopy images. They formulated the deformation estimation process as a non-linear optimization problem based on the deformation graph approach, utilizing the comparison between pre-operative model projection contours and intra-operative segmented aortic shape contours. However, optimization-based methods often suffer from high computational complexity [12, 13]. Haskins *et al.* [13] conducted a survey on learning-based methods and highlighted a significant limitation: most studies in the literature rely on landmarks or manually annotated features, making them severely constrained by the laborious task of generating datasets. In another study by Guan *et al.* [14], a Multi-Channel Convolutional Neural Network (MCNN) was employed to achieve favorable registration results, demonstrating average errors of approximately 0.3 mm. This approach, however, necessitates the definition of a mathematical model for periodic deformation, which is only feasible when a complete dataset representing all phases of the periodic movement is available. This requirement implies the need for a long exposure time and significant amounts of contrast media. Overall, existing image registration methods encounter challenges in effectively handling tissue deformations in a weakly-supervised manner and accurately reconstructing deformations from 2D to 3D space.

AR visualization has been widely acknowledged in numerous studies for its ability to offer crucial advantages during clinical procedures. These benefits include providing valuable insights into the physiology of deformable organs and enabling clinicians

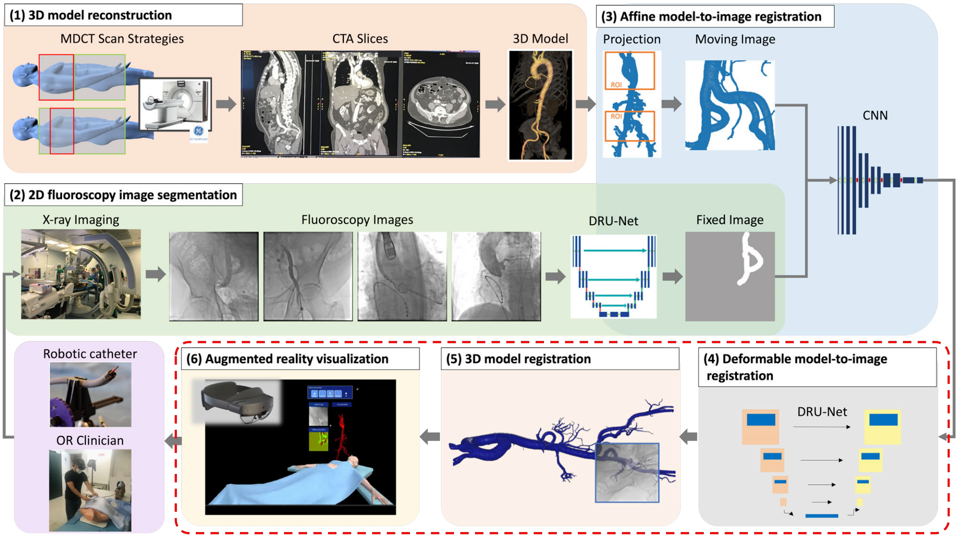

Figure 5.1: The architecture of the proposed framework consists of multiple modules: 1) reconstruction of a pre-operative 3D aortic model from CTA slices; 2) autonomous segmentation of vessels from intra-operative fluoroscopy images using a DRU-Net; 3) generation of 2D ROI projections and registration with segmented images using a hybrid approach incorporating a CNN and 4) DRU-Net model to estimate the registration matrix and deformation fields, respectively; 5) application of these parameters to deform the pre-operative 3D model; 6) visualization of the deformed 3D model alongside the intra-operative fluoroscopy image using an AR HMD (Microsoft HoloLens 2®). The red dashed box highlights the extensions introduced in comparison to our previous work [10].

to integrate information from multiple sources seamlessly, all while maintaining a clear line of sight with the patient in the operating room [15, 16, 17]. These advantages are particularly significant in the context of minimally invasive interventions, where direct visual observation is inherently limited [18]. Moreover, several studies have highlighted the positive outcomes achieved through the integration of AR technologies with robot-assisted medical platforms, as evidenced by user-centric and ergonomic evaluation criteria [19, 20, 21].

To overcome the aforementioned challenges, this study presents a novel deformable model-to-image registration framework using deep learning, specifically tailored for augmented reality-guided endovascular catheterization. Building upon our previous work [10], which proposed an affine model-to-image registration approach using a CNN to align segmented fluoroscopy images with a pre-operative 3D model reconstructed from CTA scans, this study extends the registration pipeline. A phase for deformation prediction and reconstruction is introduced, along with the incorporation of immersive AR visualization using the Microsoft HoloLens 2® augmented reality device. The main contributions of this research can be summarized as follows:

- proposal of an accurate deep learning-based deformable model-to-image registration framework for predicting and reconstructing deformations from 2D images onto the pre-operative 3D model, using a Deep Residual U-Net (DRU-Net) model with a customized loss function to adequately capture the registration accuracy;

- development of an immersive visualization method for intra-operative 3D models using the AR Head-Mounted Display (HMD);
- validation of the registration accuracy both in 2D using a dataset comprising nine patients and in 3D using a dataset obtained from an intervention simulator.

The chapter is organized as follows: Section 5.2 provides an overview of the proposed deformable model-to-image registration framework. Section 5.3 explains the experimental design and the performance metrics employed to evaluate the accuracy of the results. Section 5.4 showcases the results, accompanied by a relevant discussion. Finally, Section 5.5 concludes the chapter and outlines future directions for research.

5.2. MATERIALS AND METHODS

The proposed deformable model-to-image registration framework is illustrated in Figure 5.1, which comprises six modules:

1. **3D model reconstruction**: semi-automatic reconstruction of the patient's 3D model from pre-operative CTA images obtained using one of two typical MDCT scan strategies [22]. The first strategy involves an ECG-synchronized CTA of the aortic root and heart, followed by a non-ECG-synchronized helical CTA of the thorax, abdomen, and pelvis. The second strategy comprises an ECG-synchronized CTA of the thorax, succeeded by a non-ECG-synchronized helical CTA of the abdomen and pelvis;
2. **2D fluoroscopy image segmentation**: acquisition of intra-operative fluoroscopy images, followed by automatic segmentation using a DRU-Net. The segmentation results in the generation of binary images, as described in [10]. These fluoroscopic images predominantly focus on two main Field-of-View (FoV) during interventions: the entry site, typically the femoral arteries, and the target site, generally the aortic root. These fluoroscopy images are typically captured at key stages of the intervention: firstly, following the insertion of the needle into the femoral arteries; secondly, prior to the inflation of the balloon catheter; and finally, subsequent to the placement of the stent at the aortic root;
3. **Affine model-to-image registration**: conversion of the model-to-image registration problem into an image-to-image registration problem by projecting a 2D view of the ROI of the 3D model corresponding to the fluoroscopy image. Two distinct types of ROI are utilized: the entry site, which encompasses the femoral arteries, and the target site, identified as the aortic root. An affine registration matrix is estimated using CNN to align the ROI projection with the segmented image [10];

Extensions in comparison to our previous work [10]:

4. **Deformable model-to-image registration**: estimation of the deformation field describing the vessel deformation between the ROI projection and the segmented image using a DRU-Net model;

Table 5.1: Number of fluoroscopy image frames extracted from each patient.

Patient No.	1	2	3	4	5	6	7	8	9
Age	84	85	82	85	85	75	75	79	80
Sex	M	F	F	M	F	M	M	F	M
Images	38	15	14	21	38	24	30	24	23

Table 5.2: Image dataset subdivision in training, validation and testing sets.

Phase	**Dataset**	**Patient**	**Images**
General Training ($W1$)	Training	1-7	180
	Validation	8	24
	Testing	9	15
Patient-specific Retraining ($W2$)	Training	9	6
	Validation	9	2
	Testing	9	15

5. **3D model registration**: application of the 2D affine registration matrix and deformation field obtained from the previous modules to the 3D model using a Free Form Deformation (FFD) algorithm [23];

6. **Augmented reality visualization**: visualization of the deformed 3D model, along with the fluoroscopy image and deformation field, using the Microsoft HoloLens 2® augmented reality device.

Our contribution to this extended framework introduced in comparison to the previous work [10] is depicted by the red dashed box in Figure 5.1, including the model deformation prediction using a DRU-Net and the reconstruction of deformations onto the pre-operative 3D model. Furthermore, the visualization phase is enhanced by integration with augmented reality. Detailed descriptions of these extensions will be provided in the subsequent subsections.

5.2.1. IMAGE DATASET

For this study, a dataset was collected from 9 patients who underwent TAVI procedures at the CCM in Milan, Italy. The data collection process adhered to the ethical protocol approved by the CCM under the assigned code of *02_21 PA*.

During the procedure, a collection of fluoroscopy images was obtained for each patient. The number of frames extracted varied according to the details presented in Table 5.1. Prior to analysis, all images utilized in this study were resized to dimensions of 256×256. Subsequently, these images were segmented and aligned with the corresponding pre-operative 3D model via the previously proposed affine registration method [10].

To estimate deformations using a DRU-Net model, the dataset was divided into training, validation, and testing sets, as depicted in Table 5.2. Notably, two distinct training phases were introduced: ($W1$) the initial phase involved standard training procedures to obtain a well-trained model, while ($W2$) the subsequent phase focused on rapid re-

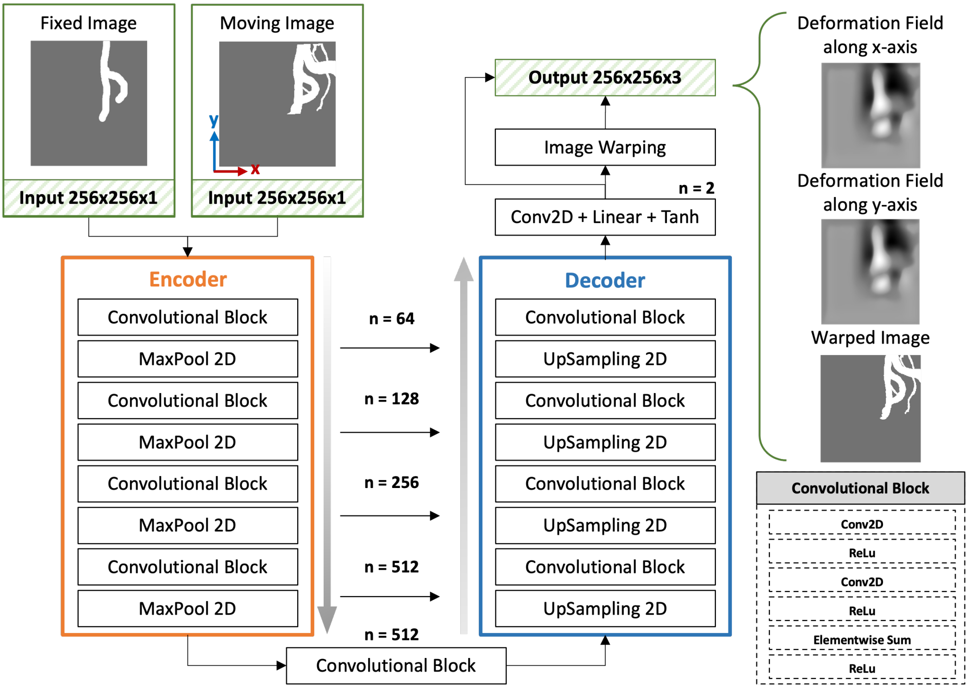

Figure 5.2: The sketch of the DRU-Net architecture for deformable model-to-image registration: given a segmented fixed image and an affine registered moving image as inputs, the DRU-Net network produces a warped image and predicts the deformation fields along the *x* and *y* axes.

training utilizing intra-operative images obtained during the procedure for the specific patient. This personalized fine-tuning phase is proposed to enhance registration accuracy in patient-specific scenarios.

5.2.2. DEFORMABLE MODEL-TO-IMAGE REGISTRATION (MODULE 4)

The DRU-Net architecture of the "deformable model-to-image registration" module is illustrated in Figure 5.2. In this module, the fixed image (i.e., the intra-operative segmentation) and the moving image (i.e., the pre-operative projection), which have been previously aligned through the "affine model-to-image registration" module [10], are concatenated and fed into the DRU-Net.

The DRU-Net encoder consists of four residual blocks. Each residual block is followed by a 2×2 max-pooling layer to reduce the number of network parameters. Within each residual block, there are two convolutional layers with a kernel size of 3×3, followed by a ReLU activation layer. The number of filters used in each block is denoted by n and indicated in Figure 5.2.

In the DRU-Net decoder, each block consists of a 2×2 up-sampling layer followed by a residual block. Subsequently, a convolutional layer with 2 filters having a kernel size of 1×1 and a linear activation function is used, followed by a fully-connected layer with a hyperbolic activation function that produces output values within the range of

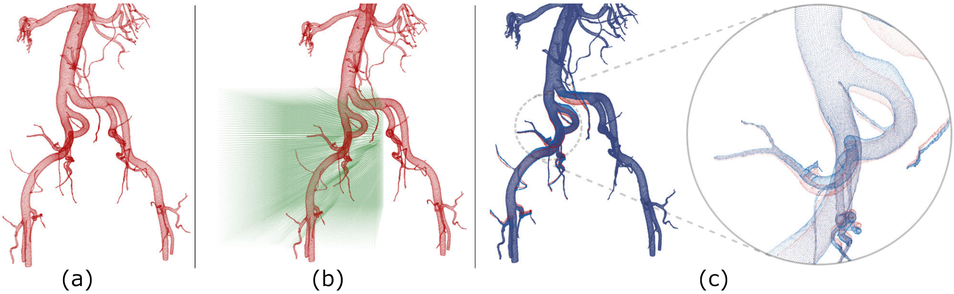

Figure 5.3: Workflow illustrating the application of predicted deformation fields on the 3D pre-operative mesh model. (a) The pre-operative mesh model (shown in red) serves as the base. (b) Evenly-distributed control points (depicted in green) are generated within the region of interest (ROI). (c) The predicted deformation fields are subsequently applied to the mesh model, resulting in a deformed mesh model (shown in blue).

$[-1,1]$. To ensure a meaningful range of deformation while preventing overfitting, these values are scaled by a factor h, which represents the maximum possible amplitude of the deformation field value [24, 25]. As a result, the output values are confined within the range of $[-h,h]$. The output of this fully-connected layer is a 2-channel image containing the deformation field components along the x and y axes. This deformation field is applied to the moving image and concatenated with the warped result, resulting in a single $256 \times 256 \times 3$ output. As shown in Figure 5.2, the DRU-Net generates a 3-channel image, consisting of a warped binary image and deformation field components along the x and y axes.

The model loss between the warped and fixed image is then calculated and utilized to update the neural network parameters during the subsequent training iterations. This iterative process allows the DRU-Net to optimize its performance and improve the accuracy of the deformable registration.

The network training utilizes an Adam optimizer [26] to minimize a customized loss function, which is a linear combination of two components:

$$\mathscr{L} = \alpha \mathscr{L}_A + \beta \mathscr{L}_B \tag{5.1}$$

Here, $\mathscr{L}$ represents the combined loss proposed in this work, while α and β are the weights assigned to each component. $\mathscr{L}_A$ corresponds to a customized similarity loss, and $\mathscr{L}_B$ refers to the customized Penalization of Deformations in Spare Space (PDSS). The following paragraphs present comprehensive explanations and definitions of these two loss components.

To improve upon the efficacy of the standard Dice Similarity Coefficient (DSC) [27], this study introduces the concept of Modified Dice Similarity Coefficient (MDSC). This approach involves partitioning both images into $N \times N$ subregions, thereby enhancing the performance of the traditional DSC metric in image similarity analysis. The formulation is given by:

$$\mathrm{MDSC} = \frac{2TP}{\sum_{i=1}^{N} \frac{a_i}{a_i+s} b_i + \frac{b_i}{b_i+s} a_i} \tag{5.2}$$

where True Positive (TP) represents the number of corresponding white pixels (vessels) in both images. a_i and b_i represent the number of white pixels in the ith subregion of the fixed and warped image, respectively, while s denotes a smoothing factor.

Compared to the traditional DSC, the improvement introduced in the denominator of MDSC reduces the dependence on vessel pixels that are absent in either the fixed and the warped images (where either a_i or b_i is equal to 0). This modification mitigates the adverse effects caused by incomplete vessel segmentation in fluoroscopy images, which has a substantial impact on the accuracy of the registration process. The loss component $\mathscr{L}_A$ in (5.1) is then defined as:

$$\mathscr{L}_A = 1 - \text{MDSC} \tag{5.3}$$

The loss component $\mathscr{L}_B$ is introduced to penalize deformations in sparse areas of the fixed image. To achieve this, both the fixed image and the deformation field in both x and y directions are divided into $N \times N$ subregions. $\mathscr{L}_B$ is then defined as follows:

$$\mathscr{L}_B = \text{PDSS} = \frac{1}{N^2} \sum_{i=1}^{N} \frac{\|1 - a_i\|}{k a_i + 1} \left(\frac{c_i + d_i}{2h} \right) \tag{5.4}$$

where c_i and d_i represent the maximum absolute values of the deformation field in the ith subregion along the x and y axes, respectively. The parameter k serves as an amplification factor.

The first part of the summation approaches 1 when the ith subregion of the fixed image is empty (i.e., $a_i = 0$) and approaches 0 otherwise. By doing so, it penalizes deformations in subregions of the moving image that do not correspond to any vessels in the fixed image.

5.2.3. 3D MODEL REGISTRATION (MODULE 5)

The process of the 3D model registration involves both 3D affine registration and 3D deformation reconstruction. The 3D affine registration [10], performed in Module 3 as shown in Figure 5.1, aligns the coordinate frames of the 3D model and the fixed image. Subsequently, the estimated deformation field obtained from the Module 4 is reconstructed onto the pre-operative 3D model (Figure 5.3a) using a FFD approach [23].

To discretize the 3D ROI in the model, an evenly-distributed grid of size $m_x \times m_y \times m_z$ is employed. Each voxel corresponds to a control point (Figure 5.3b) that applies a specific transformation in the three orthogonal axes based on its position. The number of control points m_x and m_y is set to be equal. The spacing between control points along the depth direction (z-axis) is set to be equal to the spacing in the other two directions.

Subsequently, the estimated deformation fields (obtained from Module 4) are applied to the control points. The deformation between adjacent control points is determined using non-linear cubic B-spline interpolation. It is assumed that the deformation field is consistent throughout the depth of the model, as the deformation information along the depth is not captured in fluoroscopy images. An example of the resulting 3D deformed model is illustrated in Figure 5.3c.

5.2.4. AUGMENTED REALITY VISUALIZATION (MODULE 6)

As shown in Figure 5.4, the 3D visualization interface of the deformed 3D model, along with the fluoroscopy image and deformation field, is developed using *Unity3D* under the

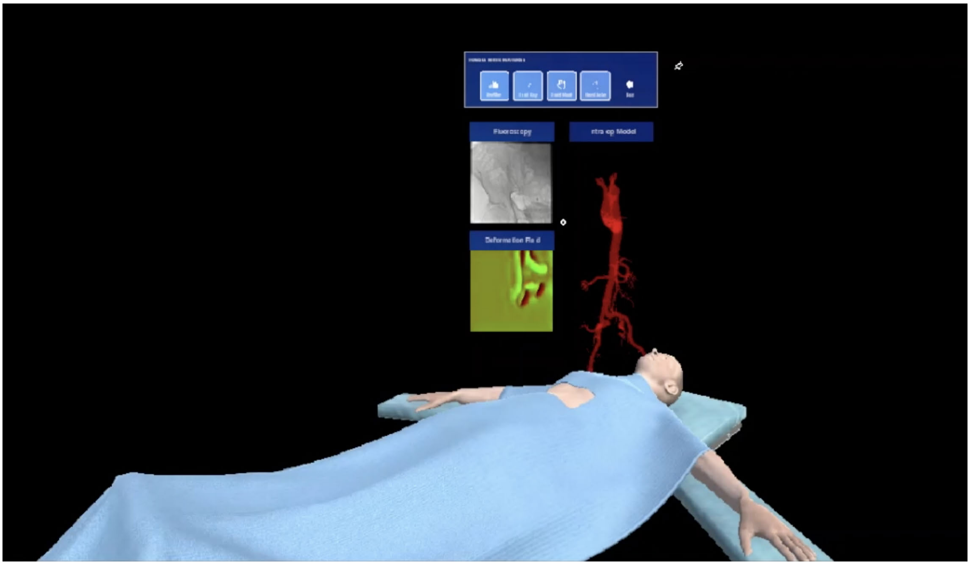

Figure 5.4: The 3D visualization interface, showcasing the fluoroscopy image, the deformation field, and the deformed 3D model.

support of Microsoft Mixed Reality Toolkit (MRTK) [28]. This interface application is deployed on the Microsoft HoloLens $2^{\circledR}$ AR device. Leveraging optical see-through display technology, digital elements are overlaid on real-world views with limited interaction.

5.3. EXPERIMENT AND VALIDATION

5.3.1. EXPERIMENTAL SETUP

The experimental setup for modules 1-3 remains consistent with the configuration described in [10].

DEFORMABLE MODEL-TO-IMAGE REGISTRATION

The DRU-Net was implemented in Python using the *Tensorflow* and *Keras* frameworks and trained on a NVIDIA GeForce RTX2080Ti GPU card.

The learning rate of the model was determined using *KerasTuner*, a scalable hyperparameter optimization framework for conducting hyperparameter search [29]. The search process involved sampling values of the learning rate within the commonly used range $[1e-5, 1e-2]$ on a logarithmic scale. The optimal learning rate was selected based on achieving the lowest loss after a number of iterations (e.g., 20 iterations). The best learning rate was found to be within the range $[1e-4, 5e-4]$. A batch size of 4 was chosen to strike a balance between gradient estimation precision and iteration time.

The weights in the loss function were set as $\alpha = 1$ and $\beta = 0.1$ to properly weigh the relative importance of image similarity and the penalization of spare space. The MDSC was computed using 16×16 subregions with $N = 16$ and a smoothing factor of $s = 1e-4$. The amplification factor k in the loss function was set to $1e6$, and $h = 15$ represented the maximum possible amplitude of the deformation field value.

3D MODEL REGISTRATION AND VISUALIZATION

The 3D model deformation is performed using the FFD approach, which is implemented utilizing the *PyGem* library [30].

The length of the ROI and the depth of the model in the corresponding volume were found to be similar across all patients. Consequently, when dealing with 256 × 256 images representing the estimated deformation field and $m_x = m_y = 256$, the number of control points surpassed the computational limitation of $1e6$, making precise deformations impractical. To address this constraint, the deformation field was downsampled to 64 × 64 using an averaging filter. This downsampling strategy reduced the number of control points to $m_x = m_y = 64$.

The 3D visualization interface is developed using *Unity3D* under the support of MRTK.

5.3.2. REGISTRATION ACCURACY VALIDATION

In order to validate the accuracy of registration in 3D, a dataset was generated since ground truth data for patients' intra-operative deformed mesh models was not available. This dataset was generated using a PBD simulator [31]. External forces were applied at three different locations on the left and right femoral arteries in the simulator, resulting in three distinct groups of images and mesh models. The three mentioned locations represent typical regions that experience deformations due to catheter-vessel contact [24, 25]. These groups comprised 64, 46, and 33 pairs of images and mesh models, respectively. Subsequently, a split of 7:2:1 was employed to assign each group to the training, validation, and testing datasets. The training dataset contained a total of 99 pairs of images and mesh models, while the validation and testing datasets consisted of 27 and 17 pairs, respectively.

During the optimization process, the hyperparameter framework determined that the optimal learning rate for the DRU-Net was $2e-4$. Additionally, the maximum possible amplitude of the deformation field value was set to $h = 60$. The remaining parameters remained consistent with the description provided in Sec. 5.3.1.

5.3.3. PERFORMANCE METRICS

REGISTRATION ACCURACY IN 2D

The performance metrics employed to assess the quality of the deformable registration results included the DSC (5.5), Precision (5.6), Recall (5.7), MDSC (5.2) and PDSS (5.4).

$$\text{DSC} = \frac{2TP}{2TP + FN + FP} \tag{5.5}$$

$$\text{Precision} = \frac{TP}{TP + FP} \tag{5.6}$$

$$\text{Recall} = \frac{TP}{TP + FN} \tag{5.7}$$

Here, TP represents the number of corresponding white pixels (vessels) in both images, False Positive (FP) represents the number of pixels that are white in the first image (warped image) but black (background) in the second (fixed image), and False Negative (FN) represents the number of pixels that are black in the first image but white in the second.

The first three metrics, namely DSC, Precision, and Recall, are commonly used in the field [32]. The DSC provides a comprehensive assessment of the registration performance by considering both FP and FN, while Recall and Precision offer insights into the predominant type of matching error. On the other hand, the MDSC and PDSS metrics were specifically introduced in this study to address the challenges associated with deformable registration in partial regions.

REGISTRATION ACCURACY IN 3D

To assess the accuracy of the 3D registration, the Mean Absolute Error (MAE) metric is employed. This metric measures the discrepancy between the vertex positions of the estimated mesh model and the ground truth positions of the deformed mesh model obtained from the simulator. The MAE values were computed for all vertices and for specific axes, denoted as e for overall MAE and e_x, e_y, and e_z for MAE along the x, y, and z axes, respectively.

$$e = \frac{\sum_{i=1}^{m} ||\boldsymbol{v}_i - \hat{\boldsymbol{v}}_i||}{m} \tag{5.8}$$

$$\begin{aligned} e_x &= \frac{\sum_{i=1}^{m} |(\boldsymbol{v}_i - \hat{\boldsymbol{v}}_i)\cdot(1,0,0)|}{m} \\ e_y &= \frac{\sum_{i=1}^{m} |(\boldsymbol{v}_i - \hat{\boldsymbol{v}}_i)\cdot(0,1,0)|}{m} \\ e_z &= \frac{\sum_{i=1}^{m} |(\boldsymbol{v}_i - \hat{\boldsymbol{v}}_i)\cdot(0,0,1)|}{m} \end{aligned} \tag{5.9}$$

Here, m represents the total number of vertices in the mesh model. In the context of the deformed mesh model, $\boldsymbol{v}_i$ denotes the actual position of the ith vertex, representing the ground truth. Conversely, $\hat{\boldsymbol{v}}_i$ signifies the position of the ith vertex in the estimated mesh model, illustrating the approximation of the vertex's location. Moreover, the MAE is calculated specifically for the vertices within the ROI, referred to as e_{ROI}. Additionally, the MAE is calculated along specific axes within the ROI: $e_{x-\mathrm{ROI}}$, $e_{y-\mathrm{ROI}}$, and $e_{z-\mathrm{ROI}}$, representing the MAE along the x, y, and z axes, respectively.

STATISTICAL SIGNIFICANCE

To assess the statistically significant differences between the method proposed in this study and the state-of-the-art approach developed by Hu *et al.* [33], the non-parametric Kruskal-Wallis test [34] is employed at a significance level of 0.05. In their work, Hu *et al.* [33] introduced a weakly-supervised CNN for multimodal image registration. The primary distinctions between this existing state-of-the-art CNN and the CNN proposed in this study lie in the unique design of the loss function and the form of deformation output. Specifically, the network proposed in this study generates a deformation field as its output, whereas the model presented by Hu *et al.* [33] employs a Dense Displacement Field (DDF) as its output mechanism.

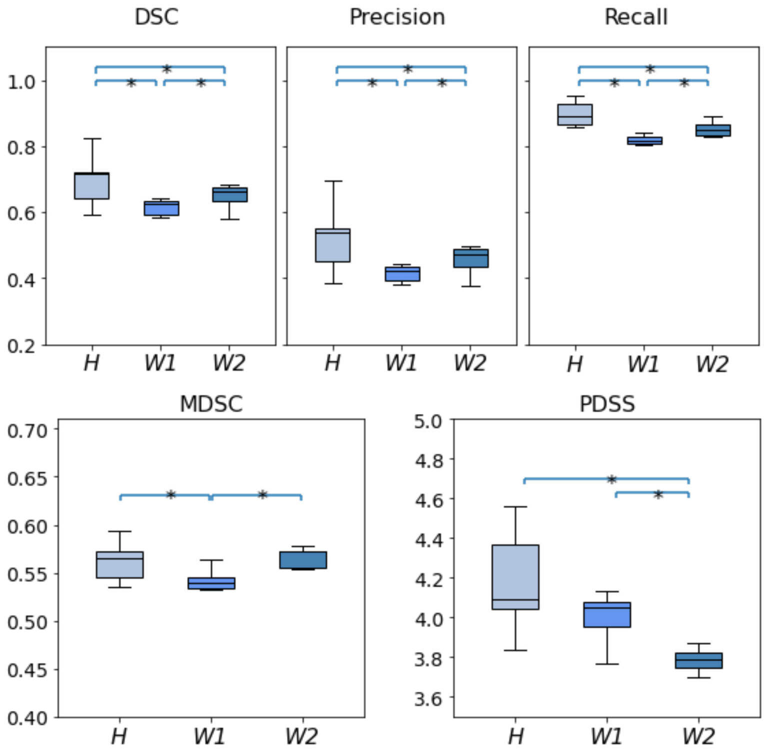

Figure 5.5: Boxplots of the testing data depicting the distribution of performance metrics including DSC, Precision, Recall, MDSC, and PDSS. The label *H* corresponds to the weakly-supervised CNN proposed by Hu *et al.* in 2018 [33]. The label *W1* represents the proposed deformable registration after the general training phase, while the label *W2* signifies the proposed deformable registration after the patient-specific retraining phase. Significance (*, $p < 0.05$) was determined using the Kruskal-Wallis test. A higher MDSC value indicates better performance, while a lower PDSS value indicates better performance.

5.4. RESULTS AND DISCUSSION

5.4.1. DEFORMABLE MODEL-TO-IMAGE REGISTRATION

Figure 5.5 presents the performance metrics of the testing data, including DSC, Precision, Recall, MDSC, and PDSS, following the deformable registration phase. The results are shown for three approaches: the state-of-the-art approach [33] (denoted as H), the DRU-Net model with general training only ($W1$), and the DRU-Net model with a patient-specific retraining phase ($W2$).

The testing results indicate that the retraining phase ($W2$) leads to a significant improvement across all performance metrics compared to the general training case. Specifically, the mean and standard deviation values of DSC increased from 0.61 ± 0.07 to 0.65 ± 0.06, Precision improved from 0.41 ± 0.08 to 0.46 ± 0.07, Recall increased from 0.76 ± 0.14 to 0.79 ± 0.13, MDSC improved from 0.52 ± 0.05 to 0.55 ± 0.04, and PDSS decreased from 4.01 ± 0.09 to 3.77 ± 0.09. These findings suggest that incorporating a patient-specific retraining phase using intra-operative images can effectively enhance

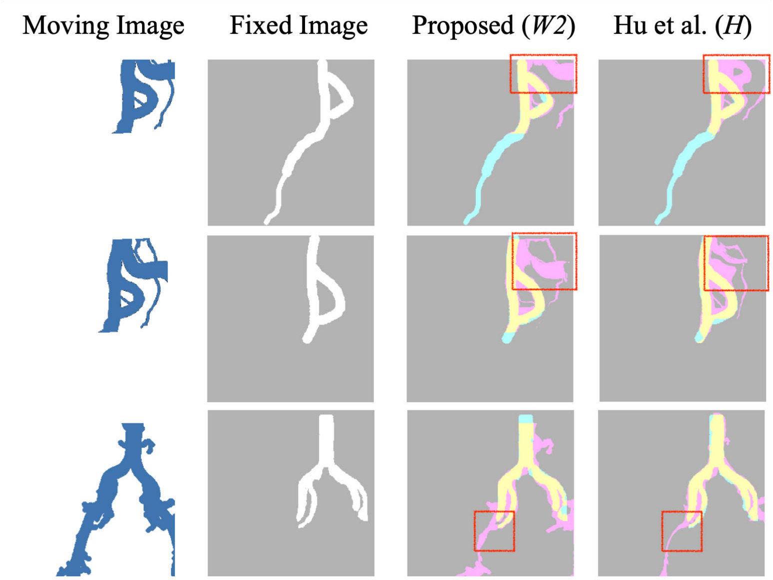

Figure 5.6: Examples of model-to-image registration results obtained using the method proposed by Hu *et al.* in 2018 [33] (*H*) and the DRU-Net retraining phase (*W*2). The last two columns display different elements of the confusion matrix between the fixed and warped images using distinct colors: yellow represents true positives (TP), gray represents true negatives (True Negative (TN)), cyan represents false negatives (FN), and magenta represents false positives (FP).

deformable model-to-image registration accuracy. It is noteworthy that the retraining process requires a relatively low number of epochs and minimal dataset extension, indicating the potential practicality of this technique in intra-operative applications. For instance, during the patient-specific retraining phase of the model, a training dataset comprising six images is utilized. The retraining involves 50 epochs, with each epoch taking approximately 4 s to complete. Consequently, this retraining phase can be accomplished in just a few minutes. This efficiency underscores the technique's potential for practical application within the same intervention session, offering a swift and adaptable solution for patient-specific requirements.

In this specific image registration scenario, Recall emerges as the most reliable metric among the conventional metrics (DSC, Precision, Recall) for evaluating registration accuracy. This is attributed to Recall's dependency solely on the number of TP and FN in the predicted image, considering that the fixed image typically represents a partial segmentation of the vessels visible in the moving image. The relatively lower Precision values obtained align with the expected outcome, indicating that the majority of prediction errors correspond to FP value.

In comparison to the state-of-the-art approach [33] (*H*), our proposed approach (*W*2) exhibits lower performance values in terms of DSC, Precision, and Recall. However, it is important to note that these metrics may not adequately capture the registration accuracy in the specific scenario characterized by vessels in the fixed image appearing in par-

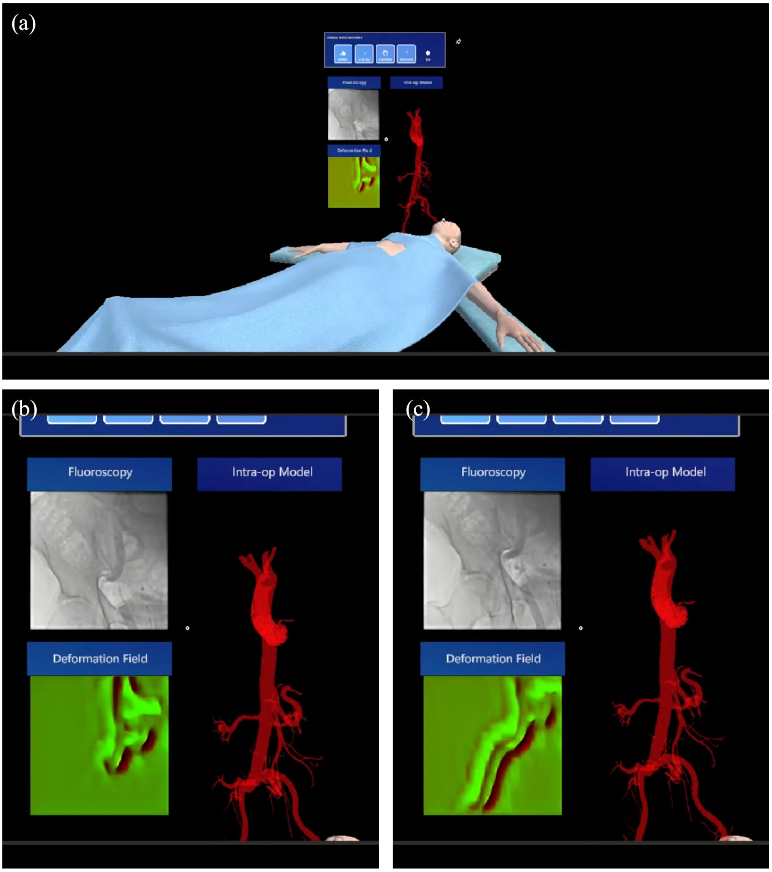

Figure 5.7: Examples of 3D model visualization at three different time stamps, showcasing the fluoroscopy image, the deformation field, and the deformed 3D model.

tial regions of the moving image only. Figure 5.6 showcases examples of deformable registration using both the state-of-the-art approach [33] (*H*) and our proposed approach (*W*2). Notably, our approach demonstrates improved performance in estimating deformations, particularly in regions where the vessels appear in the moving image but not in the fixed image (see the red boxes in Figure 5.6). It is worth mentioning that due to the low contrast media dose, the fixed image derived from fluoroscopy usually contains only partial vessel branches present in the moving image. This incomplete segmentation introduces challenges to the stability of the deformable registration network, resulting in deformation artifacts in areas of projected vessels that do not exist in the fixed image.

To provide a more comprehensive representation of registration accuracy, the performance metrics MDSC and PDSS are employed. As illustrated in Figure 5.5, the DRU-Net model (*W*2) did not exhibit a significant improvement in MDSC accuracy compared to the literature [33] (*H*). However, the DRU-Net model achieves a reduced penalization loss in terms of PDSS, with mean and standard deviation values of 3.77 ± 0.09 (com-

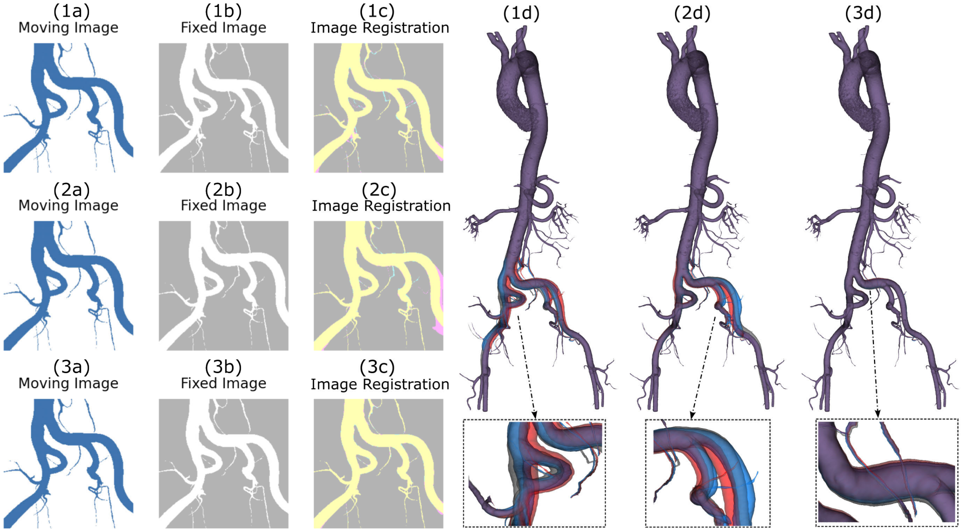

Figure 5.8: Examples of model-to-image registration results after deformable model-to-image registration (c) and 3D model registration and visualization (d). In the third column (1c-3c), different elements of the confusion matrix between the fixed and warped image are represented by different colors: yellow indicates true positives (TP), gray indicates true negatives (TN), cyan indicates false negatives (FN), and magenta indicates false positives (FP). In (1d-3d), red represents the pre-operative mesh model, blue represents the deformed mesh model predicted using the proposed approach, and gray represents the ground truth of the deformed mesh model.

pared to 4.19 ± 0.23). Despite the incorporation of the component $\mathcal{L}_B$ in the loss function, residual artifacts persist even after the retraining phase. Notably, these artifacts become more apparent in regions where the fixed image contains smaller vessel sections. As these deformation artifacts can potentially provide incorrect guidance, their suppression becomes crucial. Future work will address this challenge by introducing a post-processing step aimed at mitigating deformations outside the segmented vessel area and enhancing deformation smoothness.

5.4.2. 3D MODEL REGISTRATION AND VISUALIZATION

The deformed models provide improved accuracy and real-time representation of environmental changes during intra-operative procedures, benefiting both robotic systems and cardiologists. For a comprehensive demonstration of the 3D visualization, readers are referred to the accompanying video[1].

Figure 5.7 presents examples of the 3D model visualization at three distinct time stamps. The visualization includes fluoroscopy images, estimated deformation fields obtained from the DRU-Net, and the corresponding deformed 3D models. Consequently, the model-to-image registration facilitates 3D visualization, enhancing visual guidance during procedures.

---

[1] `https://youtu.be/3YbdejVkgzk`

Table 5.3: Performance metrics on the dataset obtained from the simulator.

Performance Metrics	Training	Validation	Testing
No. Images	99	27	17
DSC	0.98 ± 0.01	0.98 ± 0.01	0.97 ± 0.01
Precision	0.96 ± 0.02	0.96 ± 0.02	0.95 ± 0.02
Recall	0.98 ± 0.01	0.98 ± 0.01	0.98 ± 0.01
e [mm]	0.34 ± 0.26	0.33 ± 0.26	0.39 ± 0.26
e_x [mm]	0.22 ± 0.20	0.22 ± 0.21	0.26 ± 0.21
e_y [mm]	0.17 ± 0.12	0.17 ± 0.12	0.19 ± 0.12
e_z [mm]	0.08 ± 0.05	0.08 ± 0.05	0.09 ± 0.05
e_{ROI} [mm]	1.30 ± 1.01	1.30 ± 1.03	1.51 ± 1.02
$e_{x-\mathrm{ROI}}$ [mm]	0.85 ± 0.81	0.84 ± 0.82	0.99 ± 0.84
$e_{y-\mathrm{ROI}}$ [mm]	0.69 ± 0.52	0.68 ± 0.54	0.79 ± 0.54
$e_{z-\mathrm{ROI}}$ [mm]	0.24 ± 0.15	0.24 ± 0.15	0.27 ± 0.14

5.4.3. REGISTRATION ACCURACY VALIDATION

Table 5.3 presents the results of the model-to-image registration performed on the dataset obtained from the simulator [31]. The registration accuracy in 2D exceeds 0.9, indicating excellent performance. The mean 3D registration error for all vertices in the testing dataset is 0.39 mm, while for vertices within the ROI, it is 1.51 mm. The mean 3D registration error observed within the ROI is notably higher compared to the average registration error across the entire dataset. This discrepancy can be attributed to the fact that the ROI is subject to a greater degree of deformations compared to regions that are more distant or less affected by such changes. The majority of the error arises from the x-y plane rather than the z-axis, indicating that our assumption of uniform deformation along the depth direction is reasonable. Figure 5.8 showcases examples of model-to-image registration results. The pre-operative mesh model (depicted in red) is transformed into an intra-operative mesh model (shown in blue) using the predicted deformation field obtained from our proposed DRU-Net approach. The similarity between the predicted deformed mesh model and the ground truth (represented in gray) confirms the feasibility and accuracy of the model-to-image registration. For a comprehensive recording of the 3D visualization, please refer to the accompanying video[2].

In this study, the accuracy of the registration process is validated by applying a force near the femoral arteries in the simulator. This method effectively evaluates the precision of the registration under specific simulated conditions. However, this validation does not encompass the registration accuracy when considering deformations attributed to physiological factors such as heartbeat and pulsation. Future work could extend this validation process by incorporating these physiological factors into the simulator as described in [31]. This advancement would enable a more comprehensive assessment of the registration accuracy, particularly under the varying conditions that mimic the realistic physiological environment of heartbeat and pulsation.

---

[2] `https://youtu.be/2QFrwmTKIQs`

5.5. CONCLUSION

In this study, a deformable model-to-image registration framework is proposed based on deep learning for augmented reality-guided endovascular interventions. The proposed framework encompasses several key components: (i) autonomous vessel segmentation of intra-operative fluoroscopy images through a DRU-Net; (ii) affine model-to-image registration, achieved by employing a CNN to align the segmented images with the pre-operative 3D model reconstructed from CTA scans; (iii) deformable model-to-image registration, accomplished by employing a DRU-Net model to predict and reconstruct deformations from 2D images onto the pre-operative 3D model; and (iv) an immersive visualization of intra-operative 3D models using augmented reality. A comprehensive evaluation of registration accuracy is provided through the introduction of a customized loss function and performance metrics, namely MDSC and PDSS.

This framework has the potential to assist clinicians during procedures by providing augmented reality visualization of patient-specific intra-operative vascular models. Our results demonstrate improved accuracy and real-time representation of vascular changes compared to existing literature. The proposed DRU-Net approach achieved a reduced PDSS value of 3.77 ± 0.09 (compared to 4.19 ± 0.23 in the literature). Furthermore, the incorporation of a patient-specific retraining phase using intra-operative images effectively enhanced deformable model-to-image registration accuracy.

To validate the registration accuracy in 3D, a dataset was generated using a simulator. The mean 3D registration error for all vertices in the testing dataset was 0.39 mm, while for vertices within the ROI, it was 1.51 mm. The similarity between the predicted deformed mesh model and the ground truth further confirmed the feasibility and accuracy of the model-to-image registration approach.

Future work entails expanding the training dataset to enhance the robustness of the registration model, implementing post-processing techniques to address residual artifact suppression, and conducting end-user evaluations in the operating room. These endeavors will contribute to further advancements and practical application of the proposed framework in clinical settings.

BIBLIOGRAPHY

[1] Ameya Pore, Zhen Li, Diego Dall'Alba, Albert Hernansanz, Elena De Momi, Arianna Menciassi, Alicia Casals Gelpí, Jenny Dankelman, Paolo Fiorini, and Emmanuel Vander Poorten. "Autonomous Navigation for Robot-Assisted Intraluminal and Endovascular Procedures: A Systematic Review". In: *IEEE Transactions on Robotics* 39.4 (2023), pp. 2529–2548. DOI: `10.1109/TRO.2023.3269384`.

[2] Luigi Biasco, Enrico Ferrari, Giovanni Pedrazzini, Francesco Faletra, Tiziano Moccetti, Francesco Petracca, and Marco Moccetti. "Access sites for TAVI: patient selection criteria, technical aspects, and outcomes". In: *Frontiers in cardiovascular medicine* 5 (2018), p. 88. DOI: `10.3389/fcvm.2018.00088`.

[3] Sharan R Ravigopal, Timothy A Brumfiel, and Jaydev P Desai. "Automated Motion Control of the COAST Robotic Guidewire under Fluoroscopic Guidance". In: *2021 International Symposium on Medical Robotics (ISMR)*. IEEE. 2021, pp. 1–7. DOI: `10.1109/ISMR48346.2021.9661508`.

[4] Mohammad Hasan Dad Ansari, Beatriz Farola Barata, Fabian Trauzettel, Zhen Li, Di Wu, Diego DallÁlba, Gianni Borghesan, Mouloud Ourak, Veronica Iacovacci, Selene Tognarelli, Jenny Dankelman, Elena De Momi, Paul Breedveld, Paolo Fiorini, Jos Vander Sloten, Arianna Menciassi, and Emmanuel Vander Poorten. "Proof-of-Concept Medical Robotic Platform for Endovascular Catheterization". In: *Proceedings of the 11th Conference on New Technologies for Computer and Robot Assisted Surgery (CRAS)*. 2022, pp. 66–67. Available online: `https://atlas-itn.eu/wp-content/uploads/2022/05/CRAS2022_ATLAS_C3.pdf`.

[5] Martin Glöckler, Julia Halbfaβ, Andreas Koch, Stephan Achenbach, and Sven Dittrich. "Multimodality 3D-roadmap for cardiovascular interventions in congenital heart disease—A single-center, retrospective analysis of 78 cases". In: *Catheterization and Cardiovascular Interventions* 82.3 (2013), pp. 436–442. DOI: `10.1002/ccd.24646`.

[6] Daniel Toth, Shun Miao, Tanja Kurzendorfer, Christopher A Rinaldi, Rui Liao, Tommaso Mansi, Kawal Rhode, and Peter Mountney. "3D/2D model-to-image registration by imitation learning for cardiac procedures". In: *International journal of computer assisted radiology and surgery* 13.8 (2018), pp. 1141–1149. DOI: `10.1007/s11548-018-1774-y`.

[7] Christoff Heunis, Jakub Sikorski, and Sarthak Misra. "Flexible instruments for endovascular interventions: improved magnetic steering, actuation, and image-guided surgical instruments". In: *IEEE robotics & automation magazine* 25.3 (2018), pp. 71–82. DOI: `10.1109/MRA.2017.2787784`.

[8] Christian Butter, Hidehiro Kaneko, Grit Tambor, Masahiko Hara, Michael Neuss, and Frank Hoelschermann. "Clinical utility of intraprocedural three-dimensional integrated image guided transcatheter aortic valve implantation using novel automated computed tomography software: A single-center preliminary experience". In: *Catheterization and Cardiovascular Interventions* 93.4 (2019), pp. 722–728. DOI: `10.1002/ccd.27920`.

[9] Liang Zhao, Stamatia Giannarou, Su-Lin Lee, and Guang-Zhong Yang. "SCEM+: Real-Time Robust Simultaneous Catheter and Environment Modeling for Endovascular Navigation". In: *IEEE Robotics and Automation Letters* 1.2 (2016), pp. 961–968. DOI: `10.1109/LRA.2016.2524984`.

[10] Zhen Li, Maria Elisabetta Mancini, Giovanni Monizzi, Daniele Andreini, Giancarlo Ferrigno, Jenny Dankelman, and Elena De Momi. "Model-to-Image Registration via Deep Learning towards Image-Guided Endovascular Interventions". In: *2021 International Symposium on Medical Robotics (ISMR)*. 2021, pp. 1–6. DOI: `10.1109/ISMR48346.2021.9661511`.

[11] Yanhao Zhang, Liang Zhao, and Shoudong Huang. "Aortic 3D deformation reconstruction using 2D x-ray fluoroscopy and 3D pre-operative data for endovascular interventions". In: *2020 IEEE International Conference on Robotics and Automation (ICRA)*. IEEE. 2020, pp. 2393–2399. DOI: `10.1109/ICRA40945.2020.9197410`.

[12] Jian-Qing Zheng, Xiao-Yun Zhou, Celia Riga, and Guang-Zhong Yang. "Towards 3D Path Planning from a Single 2D Fluoroscopic Image for Robot Assisted Fenestrated Endovascular Aortic Repair". In: *2019 International Conference on Robotics and Automation (ICRA)*. 2019, pp. 8747–8753. DOI: `10.1109/ICRA.2019.8793918`.

[13] Grant Haskins, Uwe Kruger, and Pingkun Yan. "Deep learning in medical image registration: a survey". In: *Machine Vision and Applications* 31.1 (2020), pp. 1–18. DOI: `10.1007/s00138-020-01060-x`.

[14] Shaoya Guan, Cai Meng, Yi Xie, Qi Wang, Kai Sun, and Tianmiao Wang. "Deformable cardiovascular image registration via multi-channel convolutional neural network". In: *IEEE Access* 7 (2019), pp. 17524–17534. DOI: `10.1109/ACCESS.2019.2894943`.

[15] Lucio Tommaso De Paolis and Valerio De Luca. "Augmented visualization with depth perception cues to improve the surgeon's performance in minimally invasive surgery". In: *Medical & biological engineering & computing* 57.5 (2019), pp. 995–1013. DOI: `10.1007/s11517-018-1929-6`.

[16] Rafa Rahman, Matthew E Wood, Long Qian, Carrie L Price, Alex A Johnson, and Greg M Osgood. "Head-mounted display use in surgery: a systematic review". In: *Surgical innovation* 27.1 (2020), pp. 88–100. DOI: `10.1177/1553350619871787`.

[17] Swathi Chidambaram, Vito Stifano, Michelle Demetres, Mariano Teyssandier, Maria Chiara Palumbo, Alberto Redaelli, Alessandro Olivi, Michael LJ Apuzzo, and Susan C Pannullo. "Applications of augmented reality in the neurosurgical operating room: A systematic review of the literature". In: *Journal of Clinical Neuroscience* 91 (2021), pp. 43–61. DOI: `10.1016/j.jocn.2021.06.032`.

[18] Verónica García-Vázquez, Felix Von Haxthausen, Sonja Jäckle, Christian Schumann, Ivo Kuhlemann, Juljan Bouchagiar, Anna-Catharina Höfer, Florian Matysiak, Gereon Hüttmann, Jan Peter Goltz, et al. "Navigation and visualisation with HoloLens in endovascular aortic repair". In: *Innovative surgical sciences* 3.3 (2018), pp. 167–177. DOI: `10.1515/iss-2018-2001`.

[19] Hisham Iqbal, Fabio Tatti, and Ferdinando Rodriguez y Baena. "Augmented reality in robotic assisted orthopaedic surgery: A pilot study". In: *Journal of Biomedical Informatics* 120 (2021), p. 103841. DOI: `10.1016/j.jbi.2021.103841`.

[20] Long Qian, Anton Deguet, and Peter Kazanzides. "ARssist: augmented reality on a head-mounted display for the first assistant in robotic surgery". In: *Healthcare technology letters* 5.5 (2018), pp. 194–200. DOI: `10.1049/htl.2018.5065`.

[21] Long Qian, Chengzhi Song, Yiwei Jiang, Qi Luo, Xin Ma, Philip Waiyan Chiu, Zheng Li, and Peter Kazanzides. "FlexiVision: Teleporting the surgeon's eyes via robotic flexible endoscope and head-mounted display". In: *2020 IEEE/RSJ International Conference on Intelligent Robots and Systems (IROS)*. IEEE. 2020, pp. 3281–3287. DOI: `10.1109/IROS45743.2020.9340716`.

[22] Philipp Blanke, Jonathan R Weir-McCall, Stephan Achenbach, Victoria Delgado, Jörg Hausleiter, Hasan Jilaihawi, Mohamed Marwan, Bjarne L Nørgaard, Niccolo Piazza, Paul Schoenhagen, et al. "Computed tomography imaging in the context of transcatheter aortic valve implantation (TAVI)/transcatheter aortic valve replacement (TAVR) an expert consensus document of the Society of Cardiovascular Computed Tomography". In: *JACC: Cardiovascular Imaging* 12.1 (2019), pp. 1–24. DOI: `10.1016/j.jcmg.2018.12.003`.

[23] D. Rueckert, L.I. Sonoda, C. Hayes, D.L.G. Hill, M.O. Leach, and D.J. Hawkes. "Nonrigid registration using free-form deformations: application to breast MR images". In: *IEEE Transactions on Medical Imaging* 18.8 (1999), pp. 712–721. DOI: `10.1109/42.796284`.

[24] Giasemi Koutouzi, Marcus Pfister, Katharina Breininger, Mikael Hellström, Håkan Roos, and Mårten Falkenberg. "Iliac artery deformation during EVAR". In: *Vascular* 27.5 (2019), pp. 511–517. DOI: `10.1177/1708538119840565`.

[25] Laura Cercenelli, Barbara Bortolani, Guido Tiberi, Chiara Mascoli, Ivan Corazza, Mauro Gargiulo, and Emanuela Marcelli. "Characterization of vessel deformations during EVAR: a preliminary retrospective analysis to improve fidelity of endovascular simulators". In: *Journal of Surgical Education* 75.4 (2018), pp. 1096–1105. DOI: `10.1016/j.jsurg.2017.10.013`.

[26] Trishul Chilimbi, Yutaka Suzue, Johnson Apacible, and Karthik Kalyanaraman. "Project adam: Building an efficient and scalable deep learning training system". In: *11th {USENIX} Symposium on Operating Systems Design and Implementation ({OSDI} 14)*. 2014, pp. 571–582. Available online: `https://www.usenix.org/system/files/conference/osdi14/osdi14-paper-chilimbi.pdf`.

[27] Lee R Dice. "Measures of the amount of ecologic association between species". In: *Ecology* 26.3 (1945), pp. 297–302. DOI: `10.2307/1932409`.

[28] Microsoft. *Mixed Reality Toolkit - Unity*. 2021. URL: `https://github.com/Microsoft/MixedRealityToolkit-Unity`.

[29] Navin Kumar Manaswi. "Understanding and working with Keras". In: *Deep Learning with Applications Using Python*. Springer, 2018, pp. 31–43. DOI: `10.1007/978-1-4842-3516-4_2`.

[30] Marco Tezzele, Nicola Demo, Andrea Mola, and Gianluigi Rozza. "PyGeM: python geometrical morphing". In: *Software Impacts* 7 (2021), p. 100047. DOI: `10.1016/j.simpa.2020.100047`.

[31] Zhen Li, Enrico Manzionna, Giovanni Monizzi, Angelo Mastrangelo, Maria Elisabetta Mancini, Daniele Andreini, Jenny Dankelman, and Elena De Momi. "Position-based dynamics simulator of vessel deformations for path planning in robotic endovascular catheterization". In: *Medical Engineering & Physics* 110 (2022), p. 103920. DOI: `10.1016/j.medengphy.2022.103920`.

[32] Aarno Oskar Vuola, Saad Ullah Akram, and Juho Kannala. "Mask-RCNN and U-net ensembled for nuclei segmentation". In: *2019 IEEE 16th international symposium on biomedical imaging (ISBI 2019)*. IEEE. 2019, pp. 208–212. DOI: `10.1109/ISBI.2019.8759574`.

[33] Yipeng Hu, Marc Modat, Eli Gibson, Wenqi Li, Nooshin Ghavami, Ester Bonmati, Guotai Wang, Steven Bandula, Caroline M Moore, Mark Emberton, et al. "Weakly-supervised convolutional neural networks for multimodal image registration". In: *Medical image analysis* 49 (2018), pp. 1–13. DOI: `10.1016/j.media.2018.07.002`.

[34] Patrick E McKight and Julius Najab. "Kruskal-wallis test". In: *The corsini encyclopedia of psychology* (2010), pp. 1–1. DOI: `10.1002/9780470479216.corpsy0491`.

III

PATH PLANNING IN DEFORMABLE ENVIRONMENTS

6

ROBUST PATH PLANNING VIA LEARNING FROM DEMONSTRATIONS FOR ROBOTIC CATHETERS IN DEFORMABLE ENVIRONMENTS

This chapter proposes a robust path planner via a learning from demonstrations method, named Curriculum Generative Adversarial Imitation Learning (C-GAIL). This path planning framework takes into account the interaction between steerable catheters and vessel walls and the deformable property of vessels. In-silico comparative experiments show that the proposed network achieves smaller targeting errors, and a higher success rate, compared to a state-of-the-art approach based on GAIL. The in-vitro validation experiments demonstrate that the path generated by the proposed C-GAIL path planner aligns better with the actual steering capability of the pneumatic artificial muscle-driven catheter utilized in this study. Therefore, the proposed approach can provide enhanced support to the user in navigating the catheter towards the target with greater precision, in contrast to the conventional centerline-following technique. The targeting and tracking errors are 1.26±0.55mm and 5.18±3.48mm, respectively. The proposed path planning framework exhibits superior performance in managing uncertainty associated with vessel deformation, thereby resulting in lower tracking errors.

This chapter can be found in part from:
Zhen Li, Chiara Lambranzi, Di Wu, Alice Segato, Federico De Marco, Emmanuel Vander Poorten, Jenny Dankelman, and Elena De Momi. "Robust Path Planning via Learning from Demonstrations for Robotic Catheters in Deformable Environments". 2023. (Under Review)
Di Wu*, **Zhen Li***, Mohammad Hasan Dad Ansari, Xuan Thao Ha, Mouloud Ourak, Jenny Dankelman, Arianna Menciassi, Elena De Momi, and Emmanuel Vander Poorten. "Comparative Analysis of Interactive Modalities for Intuitive Endovascular Interventions". 2023. (Under Review. Di Wu and Zhen Li contributed equally to this manuscript. Corresponding author: Zhen Li.)

6.1. INTRODUCTION

Endovascular procedures are a rapidly emerging field in medicine. The number of patients treated has constantly increased over the past few decades [1]. These procedures increase patient comfort, reduce risks, and improve outcomes compared to traditional open surgery. However, navigation through narrow, fragile, and deformable vessels, using traditional non-steerable catheters and guidewires, requires considerable skill and experience [2]. Steerable catheters and navigation guidance could potentially lower the skill that would be required for percutaneous treatment [3]. Commercial robotic platforms can attest to the robot-assisted trend, such as CorPath™ GRX (Corindus, Waltham, USA), Sensei™ X and Magellan (J&J robotics, New Brunswick, USA), Amigo™ (Catheter Robotics Inc. Budd Lake, USA), R-One™ (Robocath, Rouen, France) and Niobe™ (Stereotaxis, St. Louis, USA). In the last decades, different research groups have focused their efforts on the development of steerable catheters [4, 5, 6, 7]. For example, a proof-of-concept medical robotic platform, composed of a multi-lumen catheter shaft and magnetically actuated microcatheter, was developed in [7]. Limited steering capability underscores the need for reliable path planning [8]. However, the complex interaction between the steerable catheter and vessel walls and the deformable property of the vessels makes reliable and real-time path planning a hard problem.

This work presents a robust and accurate path planning framework, designed to enhance risk management. This framework effectively mitigates the impact of vessel deformation while satisfying robot constraints. It achieves this by employing a method that keeps the catheter tip away from the vessel wall, thereby minimizing potential risks and reducing tracking errors. This strategic approach is pivotal in ensuring safer and more accurate navigational outcomes. The main contributions are:

- proposing a reliable path planning approach, named C-GAIL, to deliver the optimal path planning performance while satisfying the given robotic catheter constraints. The curriculum learning module of C-GAIL enables progressive training in a complex environment;
- presenting a path planning framework takes into account the deformable property of the environment and the dynamic movement of the target;
- validating the proposed path planner in an *in-vitro* environment using teleoperation control strategy. These experiments demonstrate the algorithm's feasibility in generating suitable paths that align with the actual steering capability of the catheter.

6.2. RELATED WORK

Over the last decade, several path planning methods for steerable/non-steerable catheters or guidewires have been proposed to assist clinicians. Table 6.1 summarizes the state-of-the-art from 2011 to 2022, in terms of path planning methodology, type of medical instrument used, type of environment (presence of dynamic changes), and type of validation (*in-silico*, *in-vitro*, *ex-vivo*, *in-vivo*). In the following a very brief description of the main types of planners is given.

Table 6.1: Overview of state-of-the-art path planning methods for endovascular catheterization (From 2011 to 2022). Key: NB - Node-Based Methods; SB - Sampling-Based Methods; OB - Optimization-Based Methods; LB - Learning-Based Methods.

Reference	**Method**	**Algorithm**	**Instrument**	**Environment**	**Validation**
[9] Wang 2011	NB	Centerline-based tree	Shaped catheter	Rigid	*in-vitro*
[10] Zheng 2018	NB	Centerline-based tree	- (Not specified)	Deformable	*in-vitro*
[11] Huang 2011	NB	DFS	Guidewire	Rigid	*in-silico*
[12] Qian 2019, [13] Cho 2021, [14] Schegg 2022	NB	Dijkstra	Guidewire	Rigid	*in-vitro*
[15, 16] Ravigopal 2022	NB	Modified hybrid A*	Steerable guidewire	Deformable	*ex-vivo*
[17] Fagogenis 2019	NB	Wall-following	Concentric tube robot	Deformable	*in-vivo*
[18], [19], [20] Fauser 2019	SB	bi-RRT	Catheter / Steerable guidewire	Rigid	*in-silico*
[21] Guo 2021	SB	RRT	Catheter	Rigid	*in-silico*
[22] Gao 2015	OB	ACO	Catheter	Rigid	*in-silico*
[23] Qi 2019	OB	Optimal IK	Steerable catheter	Rigid	*in-vitro*
[24] Li 2021	OB	GA	Steerable catheter	Rigid	*in-silico*
[25], [26] Rafii-Tari 2014	LB	GMM, HMM	Shaped catheter, preloaded guidewire	Rigid	*in-vitro*
[27], [28], [29] Chi 2020	LB	DMPs, GMMs, GAIL	Shaped catheter, preloaded guidewire	Deformable	*in-vitro*
[30] Zhao 2022	LB	GAN	Guidewire	Rigid	*in-vitro*
[31] Tibebu 2014, [32] You 2019	LB	Q-learning, DQN	Steerable catheter	Rigid	*in-vitro*
[33] Behr 2019, [34] Karstensen 2020, [35] Kweon 2021	LB	DQN, DDPG	Shaped guidewire	Rigid	*in-vitro*
[36] Meng 2021	LB	A3C	Guidewire	Rigid	*in-silico*
[37] Karstensen 2022	LB	DDPG	Shaped guidewire	Deformable	*ex-vivo*
Proposed	LB	C-GAIL	Steerable catheter	Deformable	*in-vitro*

6.2.1. NODE-BASED (NB) METHODS

Node-based algorithms use an information structure to represent the environment map. Studies [9] and [10] extracted the vessel centerline and built an exploration tree along the centerline. The aim of this method is to keep the tip of the instrument away from the walls. Nevertheless, path exploration inside the information structure is not mentioned in those studies. Graph search strategies such as DFS algorithm [11], Dijkstra algorithm [12, 13, 14] and A* algorithm [15, 16] were employed to generate a path solution in a tubular environment with multi-branches. For movement in the cardiac chamber, a wall-following strategy employing haptic vision was developed in [17] by Fagogenis *et al.* to keep a certain distance from the heart wall.

6.2.2. SAMPLING-BASED (SB) METHODS

Sampling-based methods randomly sample in the robot's configuration space or workspace to generate new tree vertices. Then collision-free vertices are connected as tree edges. Fauser *et al.* [18, 20, 19] introduced a RRT-connect method for instruments that follow curvature constrained trajectories in vena cava or aorta. The study in [21] implemented an improved RRT algorithm for cerebrovascular interventions. The expansion direction of the random tree is a compromise between the new randomly sampled node and the target. This strategy can improve the convergence speed of the algorithm. However, their work did not take into account any kinematic constraints governing catheter movement.

6.2.3. OPTIMIZATION-BASED (OB) METHODS

Path planning can be formulated as an optimization problem and solved by numerical solvers. Gao *et al.* [22] proposed an improved ACO algorithm to plan an optimal path that also accounted for factors such as catheter diameter, vascular length, diameter, curvature and torsion. Nevertheless, the high computational time with an average value of 12.32s makes it infeasible in real-time scenarios. Qi *et al.* [23] formulated the path planning as an optimization problem under the IK modeling of continuum robots. However, the optimization problem is solved locally without considering long-term cumulative costs. Li *et al.* [24] proposed a fast path planning approach via a local GA optimization. The approach is able to account for constraints on the catheter curvature, but the optimization algorithm is based on vessel centerlines that are sensitive to deformations of the anatomical model.

6.2.4. LEARNING-BASED (LB) METHODS

Learning-based methods use statistical tools and machine learning algorithms for path planning. Rafii-Tari *et al.* [25, 26] and Chi *et al.* [27, 28, 29] proposed LfD approaches to optimize trajectories or learn motion primitives using expert demonstrations. Zhao *et al.* proposed a GAN framework for real-time path planning and evaluated it in 2D-DSA images [30]. The work in [32, 33, 34, 31, 35, 36, 37] developed RL approaches to predict a sequence of actions to reach a target. LfD methods based on GAIL were adapted into other medical scenarios [38, 39] because of their ability to compromise between learning the distribution and ensuring the generalization of trajectories.

6.2.5. LIMITATIONS

Current approaches lack planning capabilities that actually take into account the deformable nature of the environment, even while those studies were verified in a soft environment [10, 17, 27, 28, 29, 37, 16]. Moreover, most of the studies that looked at deformable environments were actually developed for passive, non-steerable instruments [10, 27, 28, 29, 37]. The wall-following algorithm [17] was only tested on a short path along the inner heart-wall. This approach could be considered efficient if there are few feasible routes to reach the target. However, in scenarios where there are multiple feasible routes, the solution provided by a wall-following algorithm cannot ensure optimality and may cause the catheter to enter other branches along the vessel wall. This algorithm has limited application scenarios. For navigation along vessels, wall-following is not advisable as it could cause the catheter to come into excessive contact with fragile tissue, plaque or calcium that should actually be avoided.

In summary, there is a need for a reliable path planner elaborated in this work that takes into account the deformable nature of the environment and the kinematics of steerable catheters. The work is built up as follows. Section 6.3 introduces the modeling and path planning methods. Section 6.4 presents an *in-silico* and *in-vitro* experimental setup, followed by experimental results in Sec. 6.5. Conclusions and future directions are summarized in Sec. 6.7.

6.3. MATERIALS AND METHODS

6.3.1. MOVING AGENT

The tip of the catheter is considered as the moving agent. The movement of the catheter is fully determined by the tip under the assumption of Follow-The-Leader (FTL) deployment [3]. While this assumption may not seem very realistic for a catheter with a single bendable segment, it will be shown that it leads to reasonable results.

A fixed coordinate frame $\mathscr{F}_A$ is attached to the tip of the catheter as shown in Fig-

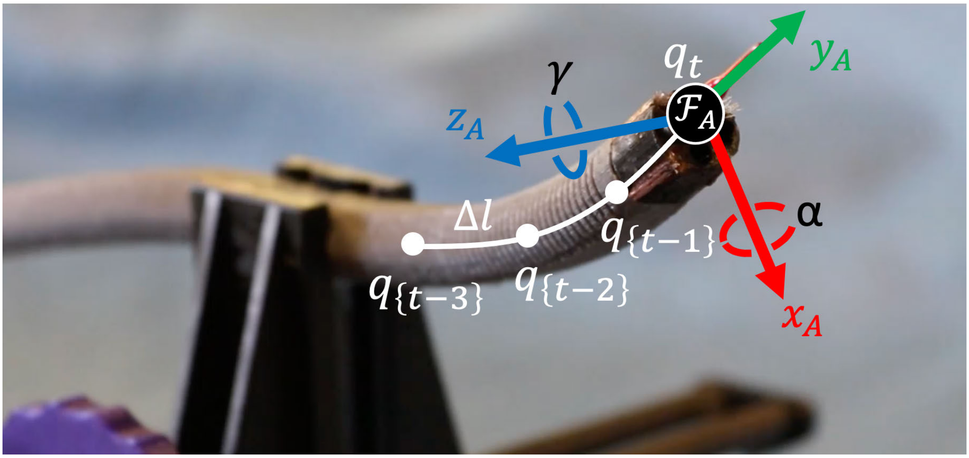

Figure 6.1: Parameterization of a robotic catheter agent: the catheter tip has configuration $\boldsymbol{q_t}$ at time t. The agent can perform an insertion movement Δ_l along the y_A axis and can bend with angle α about the x_A axis and with angle γ about the z_A axis, respectively, in the tip frame $\mathscr{F}_A$. The catheter segments following the tip adopt the previous configurations sequentially.

ure 6.1. The agent can perform an insertion movement Δ_l along the y_A axis and can bend with angle α about the x_A axis and with angle γ about the z_A axis, respectively. The pose of the agent is determined and updated at each time step by the 3-dimensional continuous action space $\mathscr{A} = [\alpha, \gamma, \Delta_l]$. The pose is defined by the tip's position $\boldsymbol{p_t} = [x, y, z]$ and orientation $\boldsymbol{r_t} = [\alpha, 0, \gamma]$ in a global frame $\mathscr{F}_0$. Using a transformation matrix, the agent configuration $\boldsymbol{q_t}$ can be defined by its pose as below, where the superscript T means transpose.

$$\boldsymbol{q_t} = \begin{bmatrix} \boldsymbol{R}(\alpha, 0, \gamma) & [x, y, z]^T \\ \boldsymbol{0}^T & 1 \end{bmatrix} \tag{6.1}$$

The geometric constraints of the catheter, such as its outer diameter and the length of the distal segment L, along with the kinematic constraints, such as the maximum bending angle θ_{max} and the maximum insertion speed, are considered in the agent's motion. θ^t_{max} is the maximum bending angle the catheter can bend at time t, given an insertion Δ_l. The bending angle is within the range of $[-\theta^t_{max}, \theta^t_{max}]$. This range further depends on the insertion speed v_t and time interval Δ_t because $\Delta_l = v_t \Delta_t$.

$$\theta^t_{max} = \frac{\theta_{max}\Delta_l}{L} \tag{6.2}$$

6.3.2. DYNAMIC ENVIRONMENT

An effective planner should address the level of uncertainty that is present in this problem. Due to the deformable nature of vessels, pre-planned paths will deviate from the reality. Rigidly following such outdated paths may lead to intense contacts with the fragile anatomy. A realistic and auto-adaptive simulator to predict vessels' global deformation induced by the catheter's contact and cyclic heartbeat motion was proposed in our previous work [40, 41]. The vessel modeling is based on a PBD approach. It discretizes an object into a particle system composed of particles. Then it computes the system's time evolution by directly updating particle positions, subject to a set of equality and inequality constraints. The deformable property was calibrated using a stress-strain curve which appropriately depicts the biomechanics properties.

In this work, for the construction of the 3D dynamic environment (see Figure 6.2), let us define:

- the "configuration space" C_{space} as the set of all the possible agent configurations $\boldsymbol{q_t}$;
- the "obstacle space" $C_{obst} \subset C_{space}$ that is the space occupied by the vessel wall that limits the area in which the catheter can move;
- the "free space" $C_{free} \subset C_{space}$ that is the set of all possible agent configurations $\boldsymbol{q_t}$ within the aorta lumen without collisions with other objects;
- the "centerline space" $C_{centerline}$ that is the shortest path computed via the Voronoi Diagram from the descending aorta to the left and right coronaries;
- the "target space" $C_{target} \subset C_{space}$ that is the volume where the target configuration $\boldsymbol{q_g}$ can locate. Once the delivery catheter reaches the target space, a microcatheter can be inserted from a channel of the delivery catheter [7]. $\boldsymbol{q_g}$ changes randomly at every learning episode within C_{target}. $\boldsymbol{q_g}$ is linked to a moving particle of the PBD system to cooperate with deformations;
- the agent start configuration $\boldsymbol{q_0}$ that is located in the descending aorta.

6.3.3. PATH PLANNING

The path planning problem can be described as: the agent has to find an admissible set of configurations $Q_t = \{\boldsymbol{q_0}, \ldots, \boldsymbol{q_g}\}$ to move from a start position $\boldsymbol{p_0} \in \boldsymbol{q_0}$ to a target position $\boldsymbol{p_g} \in \boldsymbol{q_g}$. The target position is reached when the distance between the agent and the target is smaller than a distance threshold ϵ, in our case set to 5mm.

The state of the agent consists of its pose, that can be changed through the actions of rotation and insertion $\mathscr{A} = [\alpha, \gamma, \Delta_l]$. In training, the agent learns to maximize the reward function by taking actions according to its policy τ, expressed in the paragraph *Reward Function* and by observing its interaction with the environment, described in the subsequent paragraph *Observations*.

REWARD FUNCTION

The reward function $R(\tau) = r_t$ associated with each time step t is designed to optimize the path according to a combination of multiple criteria: the number of steps, the number of collisions, reaching the target position, passing through the centerline waypoints, bending angle. The reward r_t consists of two main parts: r_{end}, a reward added at the end of a learning episode; r_{in}, a relatively small reward added at each step during a learning episode. The reward r_t is expressed in (6.3)-(6.5).

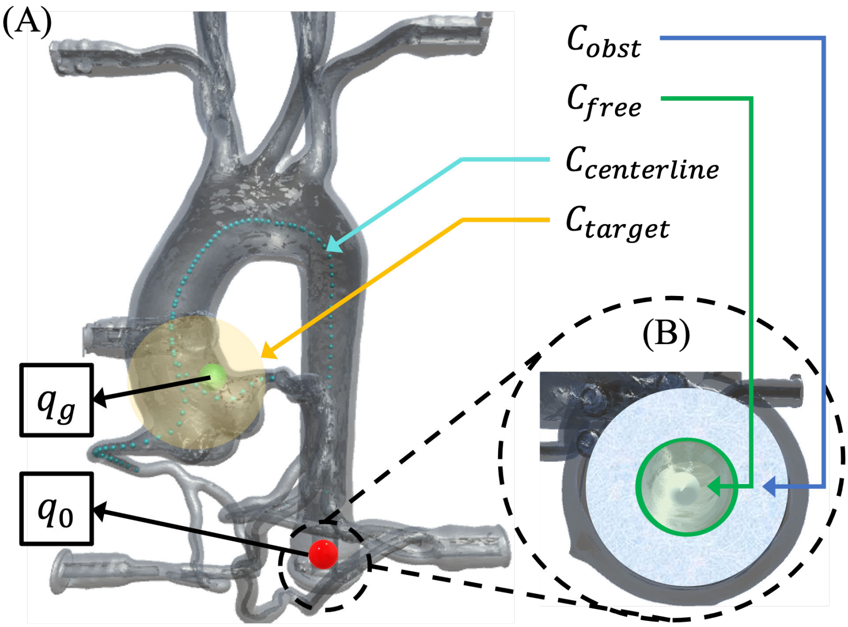

Figure 6.2: The environment is represented by an aortic anatomy, the obstacle space C_{obst}, the free space C_{free}, the centerline space $C_{centerline}$, and the target space C_{target}. The catheter moves from the start configuration $\boldsymbol{q_0}$ and proceeds to move to reach the target configuration $\boldsymbol{q_g}$. (A) Top view on the aortic model. (B) Cross-sectional view of the open lumen of the descending aorta.

$$r_t = r_{end} + r_{in} \tag{6.3}$$

$$r_{end} = \begin{cases} r_{obst} & \text{if} \quad \boldsymbol{q_t} \in C_{obst} \\ r_{exit} & \text{if} \quad \boldsymbol{q_t} \notin C_{free} \text{ and } \boldsymbol{q_t} \notin C_{obst} \\ r_{target} & \text{if} \quad ||\boldsymbol{p_t} - \boldsymbol{p_g}|| < \epsilon \end{cases} \tag{6.4}$$

$$r_{in} = r_{step} + r_{centerline} + r_{bending} \tag{6.5}$$

- r_{obst} is a negative reward that is given if a collision between the catheter tip and vessel walls is detected. This study only takes that collision into account because it has a higher risk during navigation. Conversely, detecting contact between the catheter body and the vessel walls may yield misleading or superfluous data. This is particularly relevant in scenarios where the catheter body maintains contact with the vessel walls, a phenomenon often necessitated by gravitational forces or constraints in the available workspace. An episode terminates when a non-minor collision occurs;

- r_{exit} is a negative reward when the agent tries to exit from the open lumen down the descending aorta;

- r_{target} is a positive reward given to the agent when it reaches the target;

- r_{step} is a negative reward given at each time step. It is set to keep the total number of steps of the trajectory as small as possible;
- $r_{centerline}$ is a positive reward if the agent reaches a waypoint in $C_{centerline}$;
- $r_{bending}$ is a positive reward that is given when the bending action is bigger than a threshold. This reward was introduced to overcome the tendency of the network to avoid producing actions near the catheter's maximum bending angle. To pass tortuous areas, the maximal bending range is often needed to be able to pass. This reward will not promote bending beyond the maximum bending angle, as such excessive bending is prevented by limitations on the configuration space.

The values of the reward function parameters obtained with an empirical method are summarized in Table 6.2. All rewards are set within the interval of [-1,1]. The minimum value of "-1" is assigned to prohibited behaviors such as violent collisions with the vessel walls. The maximum value of "1" is assigned to reaching the target, which is the agent's task. The other rewards are chosen based on their frequency. For instance, since r_{step} occurs very often, if it is not small enough, it can lead to a large cumulative reward. Similarly, the bending reward also has the potential to lead to a large cumulative reward. In contrast, the number of centerline points is relatively small, with only around 100 points, and not all of them are reachable if the catheter constraints are met. Hence, this positive reward is set slightly larger.

OBSERVATIONS

At every step, the agent collects observations o_t, which are composed of:

- the agent configuration $\boldsymbol{q_t}$;
- the normalized distance from the agent to the target $u = \frac{||\boldsymbol{p_g} - \boldsymbol{p_t}||}{d_{max}}$, where d_{max} is the maximum distance between the agent and the target when $\boldsymbol{q_t} \in C_{free}$;
- the direction from the agent to the target $\boldsymbol{v} = \boldsymbol{p_g} - \boldsymbol{p_t}$;
- a set of raycast observations o_{ray}. Each raycast detects the presence of the aortic wall along its direction within the ray length. In this research, a collection of raycasts, constituting a part of a sphere, is utilized. Specifically, this arrangement spans a range of 60 degrees in alignment with the heading direction.

Table 6.2: Values of the reward function parameters

Reward	**Value**	**Reward**	**Value**
r_{obst}	-1	r_{step}	-1e-5
r_{exit}	-1	$r_{centerline}$	+0.05
r_{target}	+1	$r_{bending}$	+1e-5

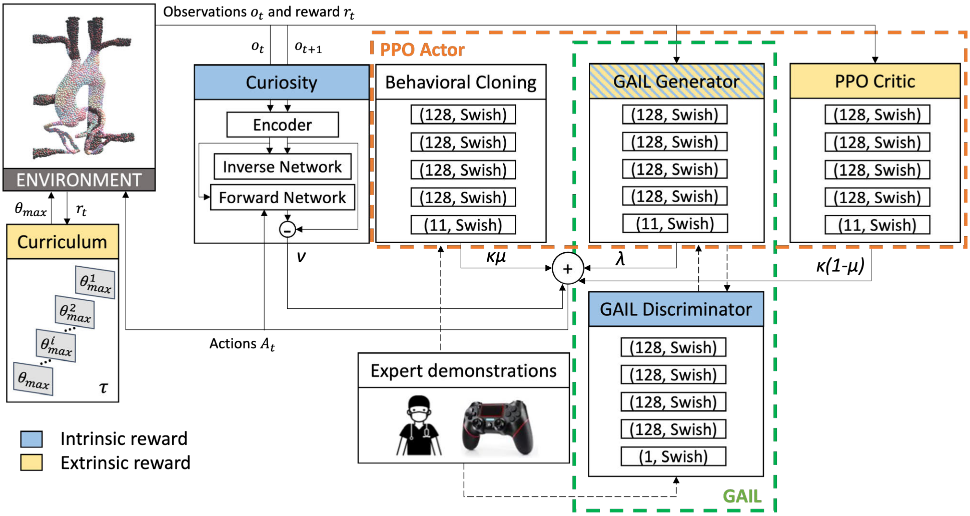

Figure 6.3: The proposed C-GAIL network architecture. The extrinsic reward signal considers the reward given by interacting with the environment, such as curriculum and PPO modules. The intrinsic reward has a policy that considers other factors, and it is defined inside the learning algorithm: for GAIL about the similarity of the path with respect to the expert demonstrations, for curiosity about the difference between the predicted and the actual path.

C-GAIL NETWORK

The new network proposed in this work, named C-GAIL network, is built around the combination of the principles of LfD and RL (see Figure 6.3). The LfD component is realized through Behavioral Cloning (BC) and GAIL networks. The Proximal Policy Optimization (PPO) network has two parts: the actor network provides an action given the observation; the critic network that evaluates the actor network using the extrinsic reward and suggests modification according to a gradient ascent policy. The actor network updates its actions according to three policies: the BC policy, PPO policy, and the GAIL generator policy. The curiosity module [42] acts as an intrinsic reward signal that enables the agent to explore its environment in novel states to help escape local minima of the policy function. The curiosity module contains an inverse and forward network. The inverse network predicts the action between observations, while the forward network predicts the next encoded observation. The difference between the predicted and actual encoded observations is defined as the loss of the forward network. Therefore, through curiosity-driven exploration, the agent can predict the outcome of its actions and acquire skills that may be valuable in the future. The curriculum learning module acts on the environment by progressively adding complexity during the training [43]. The curriculum learning module optimizes the bending angle while respecting the reachable bending range of the catheter. Specifically, in curriculum learning, the learning progress is measured through the reward function and once the agent performance improves, θ_{max} is decreased for the next level of learning. Finally, the agent is able to try actions in different reachable bending ranges and obtain globally optimal paths.

The proposed network can be represented as a set of modules with weights, that define the contribution of each module to the loss function. These modules interact with the environment and with each other. The goal is to come up with an optimal combination of the strengths of the different modules such that a performance is achieved that exceeds those of the offered demonstrations. The training is based on the linear combination of the respective RL and LfD losses:

$$\mathscr{L} = \kappa(1-\mu)\mathscr{L}_{PPO} + \lambda\mathscr{L}_{GAIL} + \kappa\mu\mathscr{L}_{BC} + \nu\mathscr{L}_{curiosity} \tag{6.6}$$

where $\mathscr{L}_{PPO}$ is the PPO critic network loss (see its definition in [44]), $\mathscr{L}_{GAIL}$ is the GAIL loss [45], $\mathscr{L}_{BC}$ is the BC loss [46], $\mathscr{L}_{curiosity}$ is the curiosity loss [42]. The weight μ indicates the degree to which the influence of BC is prioritized over the policy relative to PPO, with a higher weight indicating a higher learning rate of imitation from demonstrations and a lower weight indicating more operations attempting to maximize reward rather than imitating. The following weights were found empirically to work well: $\kappa = 0.2$, $\lambda = 0.8$, $\mu = 0.7$, $\nu = 0.02$. The GAIL is given the highest weight because the method combines two paradigms and reward types, intrinsic and extrinsic.

6.3.4. CLINICAL WORKFLOW FOR THE PROPOSED PATH PLANNER

Regarding the clinical translation of this work, the anticipated clinical workflow is designed as follows.

- Firstly, a 3D mesh model is reconstructed from the pre-operative CTA images of a specific patient using the *AW server* (GE Healthcare). Based on this 3D model, a patient-specific deformable environment is built using the PBD simulator [40].

- Then, the proposed C-GAIL network is trained using patient-specific demonstrations provided by experts. This network model can be trained from scratch for this specific patient, or retrained from a previous network model with a slightly different anatomy. This network training step may last around six hours in the PBD simulator without the involvement of expert clinicians.

- Given the desired target configuration, the proposed C-GAIL path planner gives a set of configurations to move from a starting position to the target and outputs an optimal path for the catheter.

- (optional) A patient-specific phantom is manufactured, and clinicians can teleoperate the robotic catheter to perform *in-vitro* experiments. The C-GAIL path is rendered through a GUI, serving as path guidance for the clinicians. This enables clinicians to acquire experience prior to the actual interventions, thereby reducing the likelihood of encountering unforeseen situations.

- For *in-vivo*, *ex-vivo*, or clinical practice, the C-GAIL path is rendered through a GUI and serves as path guidance for the clinicians. The clinicians can teleoperate the robotic catheter to reach the clinical target site by following the C-GAIL path.

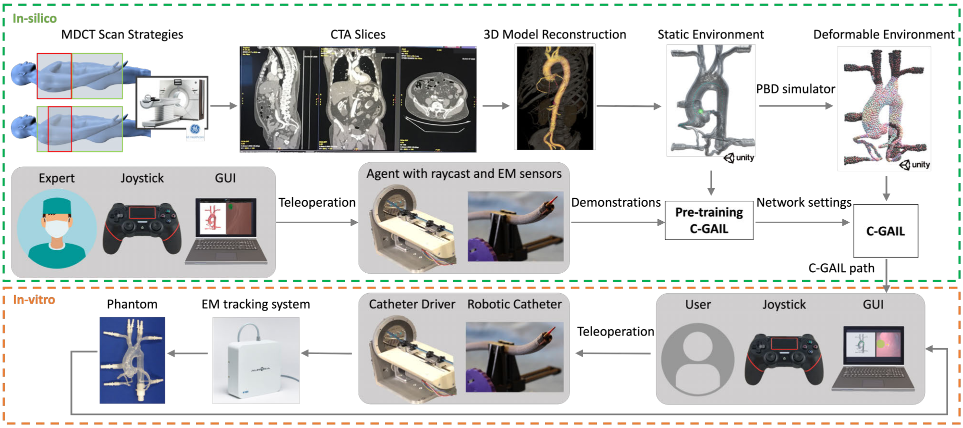

Figure 6.4: Workflow for simulation and *in-vitro* user study. First, a 3D model is reconstructed from CTA images for a specific patient, and a deformable environment is built. Next, based on expert demonstrations, the C-GAIL network is trained to provide an optimal path. This path is then rendered through a GUI for the *in-vitro* experiments and serves as path guidance for users.

6.4. EXPERIMENTAL SETUP

The proposed workflow for the simulation and *in-vitro* user study is illustrated in Figure 6.4. Firstly, a 3D mesh model is reconstructed from the CTA images of a specific patient, and a deformable environment is built using the PBD approach [40]. Then, the proposed C-GAIL network is trained using demonstrations provided by experts, which outputs an optimal path for the catheter. The C-GAIL network utilizes expert demonstrations to learn and transfer expert experience, which can provide path references for non-expert users and even autonomous catheters.

In addition to evaluating the path planning algorithm based on C-GAIL, this work also includes control experiments (path following experiments) to verify the feasibility of executing the planned path. The *in-vitro* experiments used human-in-the-loop teleoperation control to guide the catheter along the planned path. It is worth noting that while control strategies are not the focus of this work, they were merely included in the experiments to evaluate the feasibility and performance of the path planner. Teleoperation is more commonly used and easier to implement in practice, making it the method of choice for the *in-vitro* experiments. It is important to note that any control algorithm could theoretically be used to execute the path planned in this work.

6.4.1. *In-silico* PATH PLANNING SETUP

HARDWARE SPECIFICATION

Experiments are carried out on a computer equipped with an Intel(R) Core(TM) i9-9900KF CPU @3.60GHz 3.60 GHz processor and 32.0 GB RAM, with an NVIDIA GeForce RTX2080Ti GPU card.

Table 6.3: Training parameters for C-GAIL and GAIL.

Parameter	**Value**	**Parameter**	**Value**
PPO beta	5.0e-4	PPO gamma	0.99
max steps	5.0e5	GAIL gamma	0.99
batch size	1024	buffer size	10240

All parameters are defined in the Unity ML-Agents Toolkit [49].

EXPERIMENTAL PROTOCOL

The purpose of the *in-silico* experiments is to validate that, given the curvature constraints of the robotic catheter, the paths obtained by the proposed C-GAIL network have better performance than the state-of-the-art GAIL approach in a static environment and are also capable to operate in a complex dynamic environment.

Training and testing were conducted in a single aortic model. For the training, 70 demonstrations were recorded using a joystick by one expert user, who performed catheter navigation through vessels in the aortic model for a Percutaneous Coronary Intervention (PCI). The number of experiments for comparison was set to 100. Different start configurations in the descending aorta and possible target positions were chosen to make the training more generally valid. There are three possible start configurations distributed within 5.3cm along the descending aorta. There are five target positions distributed in a spherical space with a radius of 3cm near the coronaries and the vessel walls. Although having diverse configurations in the training data might hinder convergence, it could actually enhance the robustness and generalizability of the network model [47].

The C-GAIL network training was carried out in two phases: pre-training in a rigid, computationally less heavy environment, where the tuning of the network parameter settings is performed; re-training in a deformable environment, starting with the previously tuned network settings. Pre-training helps reduce the time required to obtain network settings with empirical parameters and compare the differences in agent behavior under different settings. The training parameters for the C-GAIL is presented in Table 6.3. The work from Chi *et al.* [29] is used as a reference to compare with. To keep consistency in comparison, the same training parameters are set for the state-of-the-art GAIL. The GAIL network architecture of [29] is adopted with minor modifications: each layer has 64 units and a Swish activation function [48].

6.4.2. *In-vitro* VALIDATION SETUP

HARDWARE SPECIFICATION

Experiments were performed in a transparent, deformable silicone aortic phantom (T-S-N-002, Elastrat Sarl, Geneva, Switzerland). The robotic catheter is fabricated out of Nitinol using metal laser cutting technology and is actuated by four integrated Pneumatic Artificial Muscles (PAMs) [50]. The outer diameter of the catheter is 7mm, and the length is 900mm. The distal Nitinol segment is 75mm long and includes a 50mm long 2 DOF steerable distal segment. The maximum bending angle is 90°. An EM sensor (Northern Digital Inc., Waterloo, Canada) is embedded at the tip of the catheter to track its pose. The robotic catheter driver system is described in [51]. The sleeve-based catheter driver

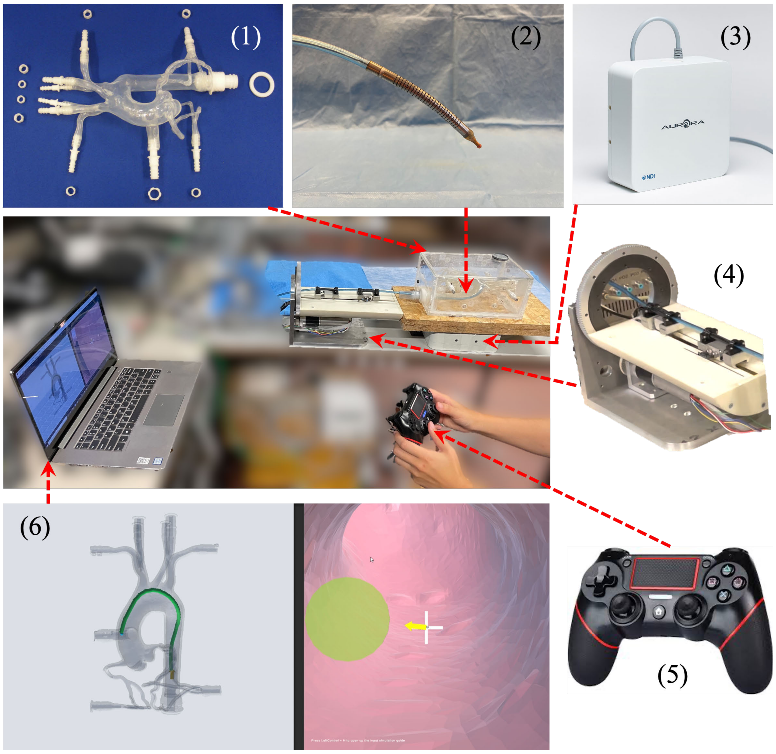

Figure 6.5: *In-vitro* experimental setup to validate the proposed path planning approach: (1) silicone aortic phantom; (2) robotic catheter; (3) Aurora EM field generator; (4) sleeve-based catheter driver; (5) wireless PlayStation 4 (PS4) controller; (6) the GUI as visual feedback.

has two pneumatically actuated grippers that grasp the catheter alternately and insert the catheter in a relay fashion. The maximum insertion (and retraction) speed is set as 5mm/s. The teleoperated catheter insertion and bending are realized through velocity control of the catheter driver and pressure control of the PAMs, respectively, using a wireless PlayStation 4 (PS4) controller. The path planning is visualized by a GUI, which includes an external projected view showing the aorta, path, and pose of the catheter tip, and an internal view showing the next waypoint and suggested bend direction. The *in-vitro* experimental setup, including the abovementioned devices, is depicted in Figure 6.5.

EXPERIMENTAL PROTOCOL

The objective of the *in-vitro* experiments is to validate whether the path obtained from the proposed C-GAIL path planner is more compatible with the actual steering capability of the catheter. Therefore, it can also be verified whether this path can better help the user steer the catheter accurately to the target.

For the *in-vitro* comparison with C-GAIL, the traditional centerline-following approach was chosen. The centerline path is widely used in interventions [52, 53], whereas

GAIL approach (which was served as a comparison in the *in-silico* experiments) has not yet been validated in clinical practice. Moreover, both GAIL and C-GAIL are RL approaches, which have limited interpretability. Therefore, it may be suggested to use traditional approaches in parallel with learning-based approaches in order to provide a more transparent and explainable analysis. By comparing C-GAIL with the traditional centerline approach, a more interpretable comparison can be achieved.

User-involved control experiments were carried out. In each trial, the user teleoperates with the robotic catheter, tries to pass through each waypoint, and finally reaches the target. The maximum operation time is set to 3 minutes. If the maximum operation time is exceeded and the target is still not reached, the experiment will be forcibly stopped and be regarded as a failure. Setting this stopping criterion can avoid the following two cases: 1) The user rushes to finish the experiment without considering the performance; 2) The user tries excessively to get better performance while the procedure is very time-consuming.

The user's performance was compared in two scenarios: with the C-GAIL assistance and centerline assistance. The waypoints from $C_{centerline}$ were utilized in the centerline-following approach. The C-GAIL network was trained using different targets and obtained a path to reach an unseen target (that was not used during training). To largely eliminate the impact of the user's learning curve, the user is required to be pre-trained. Only when the learning curve converges to a plateau can we assume that the user has stable catheter manipulation abilities. The user pre-training experiments are repeated ten times. After that, control experiments with the same C-GAIL path are conducted ten times. Similarly, the pre-training experiments with the centerline and the control experiments with the same centerline are repeated ten times each. The experiments with the C-GAIL path are first performed to eliminate experience learnt from the other scenario.

6.4.3. PERFORMANCE METRICS

The following criteria were chosen to quantify the performance of *in-silico* and *in-vitro* experimental results. The statistically significant difference between the proposed method and others is evaluated via the Kruskal-Wallis test in this work, with a significance level of 0.05.

SUCCESS RATE (δ)

Success rate represents the percentage of successes among the total number of attempts. A trial is deemed successful if the robotic catheter reaches the target within the given time, which is set as 3 minutes in these experiments.

$$\delta = n_s / n \tag{6.7}$$

where n_s is the number of successes to reach the target within a given time, and n is the number of attempts.

TIMESTEPS (T_s)

For *in-silico* experiments, at each time step, the agent receives observations, takes an action according to its policy and receives rewards. T_s is defined as the number of time steps moving from the start configuration to the target.

$$T_s = N_g - N_0 + 1 \tag{6.8}$$

where N_0 and N_g are the first and last time step, respectively.

DURATION (T)

Duration is the length of time a single experiment lasts from start to stop. An experiment stops when the target or the maximum duration has been reached.

$$T = t_g - t_0 \tag{6.9}$$

where t_0 and t_g are the first and last timestamp, respectively.

TRACKING ERROR (T_r)

Tracking error refers to the average deviation between the actual trajectory $\boldsymbol{p_j}$ ($j = 1, ...k$ with $t = t_0$ when $j = 1$, and $t = t_g$ when $j = k$) and desired trajectory $\boldsymbol{p_i^d}$ ($i = 1, ...m$). For each point $\boldsymbol{p_j}$ on the actual trajectory, the shortest distance to the desired trajectory is identified and treated as the deviation for that individual point. The tracking error is computed as the mean error of all these individual points. This criterion is used to evaluate the path following capability.

$$T_r = \frac{1}{k} \sum_{j=1}^{k} (\min_{\mathbf{i}} ||\boldsymbol{p_i^d} - \boldsymbol{p_j}||) \tag{6.10}$$

TARGETING ERROR (T_a)

Targeting error is calculated by searching the entire trajectory and determining the shortest distance between the trajectory $\boldsymbol{p_j}$ and the target $\boldsymbol{q_g}$. This metric serves as a criterion for evaluating the accuracy of reaching the target.

$$T_a = \min_{\mathbf{j}} ||\boldsymbol{q_g} - \boldsymbol{p_j}|| \tag{6.11}$$

6.5. RESULTS AND DISCUSSION

6.5.1. *In-silico* PATH PLANNING

The performance comparison of the proposed C-GAIL and the state-of-the-art GAIL [29] in a static environment is presented in Figure 6.6. The number of experiments for comparison is set to 100, and results are reported regardless of whether the target was successfully reached. Figure 6.6A shows an example of trajectories obtained by these two approaches. The C-GAIL approach generates paths with smaller targeting errors (see Figure 6.6B). An ablation study of the C-GAIL is also presented, investigating its performance when $\mu = 0$, $\lambda = 0$, or $\nu = 0$. The results indicate that BC, GAIL and curiosity modules are all critical for accurate target reaching. However, compared to GAIL, C-GAIL requires more timesteps to reach the target (see Figure 6.6C). This indicates that either the path is longer or there are more samples taken along the path to achieve the same level of path length. Furthermore, the robustness of the proposed network is verified by the success rate of the C-GAIL network, that is 66%, compared to that of the GAIL

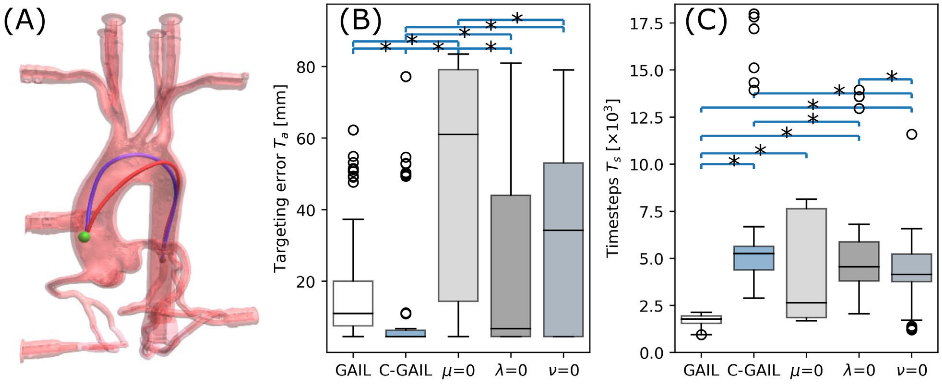

Figure 6.6: *In-silico* performance comparison between the proposed C-GAIL network (purple) and the state-of-the-art GAIL network [29] (red), with respect to (A) example of trajectories, (B) targeting error T_a, and (C) timesteps T_s. An ablation study of the C-GAIL is presented when $\mu = 0$, $\lambda = 0$ or $\nu = 0$. ($*, p < 0.05$ using Kruskal-Wallis test)

network [29] which is only 16%. The duration is affected by a large number of failures that often cause early termination of the experiment. A common failure is that the path planning tends to stop due to non-minor collision with the aortic arch and are therefore unsuccessful attempts. Minor collisions that cause slight deformation within reasonable stress ranges were considered harmless [54].

The agent was then trained using pre-trained weights from the static environment in a dynamic environment, where deformations are caused by contact with the catheter and the heartbeat motion. Figure 6.7A demonstrates the ability of real-time planning in a complex dynamic environment with deformable vessels and a moving target. The top zoom-in view shows that the paths of pre-trained $\boldsymbol{q}_{pre}$ and intraoperatively trained $\boldsymbol{q}_{intra}$ are initially close and then separate in the aortic arch, where the degree of deformation is greater. The bottom zoom-in view shows the change from the initial target position $\boldsymbol{q_g}_{pre}$ to the intraoperative target position $\boldsymbol{q_g}_{intra}$. Figure 6.7B-C present performance comparisons in static and dynamic environments. The timesteps are much more in the deformable environment. This is due to the fact that there are more possibilities when interacting with a deformable environment than with a static one. Due to the greater complexity of navigation and low success rate, targeting error is larger and more widely distributed than in the static environment. The success rate of 17% is relatively low but indicates that it is possible to find a feasible path in a constrained environment, compared to the success rate of 0% for the GAIL network [29] in the dynamic environment. A common failure is the inability to reach the moving targets with a small threshold of 5mm. Including this distance threshold to reach a target in the curriculum module would improve network performance, such as success rate. This would be investigated at a later stage. The limited bending capability of robotic catheters and the presence of moving targets in deformable environments led to a reduced success rate within a limited number of timesteps. Despite the relatively low success rate of C-GAIL, it has outperformed the state-of-the-art approach.

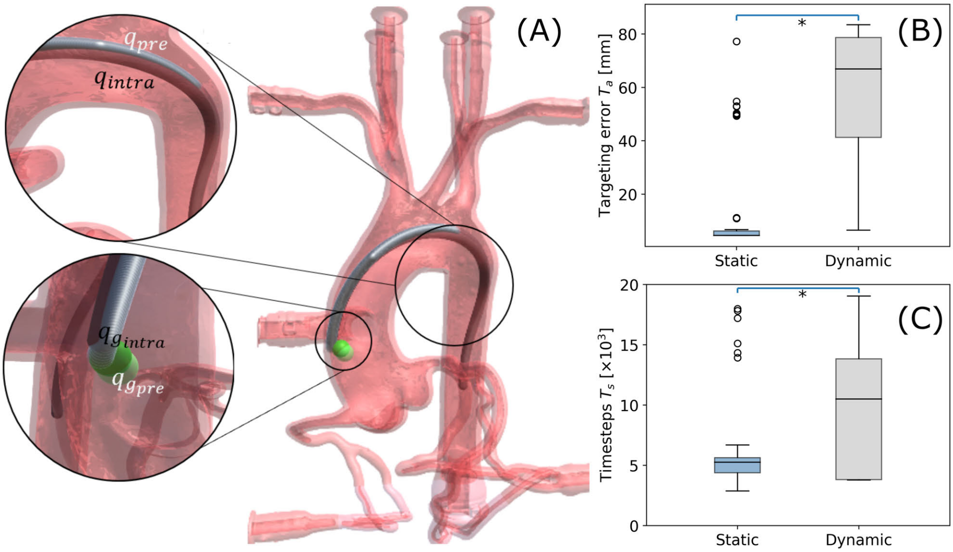

Figure 6.7: *In-silico* performance of the proposed C-GAIL network in static and dynamic environments: (A) The intra-operative adaptation of the pre-operative path q_{pre} when the environment is deformable and the target moves; (B) Targeting error T_a and (C) Timesteps T_s in static and dynamic environments. ($*, p < 0.05$ using Kruskal-Wallis test)

6.5.2. *In-vitro* VALIDATION

To essentially eliminate the impact of the user's learning curve, the user is required to be pre-trained. For example, the learning curve of the targeting error by following the C-GAIL path decreased from 3.6 to ~2mm in ten trials. The user can achieve a targeting error of 0.23mm in the later stage. Since the learning curve converges to a plateau, it can be concluded that the user has stable catheter manipulation ability. A video is made available showing example experiments of following the C-GAIL path and the centerline[1].

The performance comparison between the C-GAIL path and the centerline is shown in Figure 6.8. The C-GAIL path leads to a smaller tracking error of 5.18±3.48mm. It confirms that C-GAIL leads to a path that can be followed better by the robotic catheter. Furthermore, the C-GAIL path also shows a smaller targeting error of 1.26±0.55mm (Figure 6.8B). Following the C-GAIL path takes a longer time than following the centerline. This is interpretable given that since the user learned that the centerline waypoints could not be reached anyway when passing the aortic arch, the user kept inserting the catheter at the maximum bending angle and spent less effort following the centerline. While in the other scenario, the user realized that (s)he could follow the C-GAIL path waypoints. Therefore, it takes a longer time than following the centerline. Two of the ten experiments with the C-GAIL path took longer because the user made a retraction motion in order to re-reach the target more accurately. Both the C-GAIL path and centerline following experiments had a 100% success rate.

---

[1] https://youtu.be/GhBi_xHTMFw

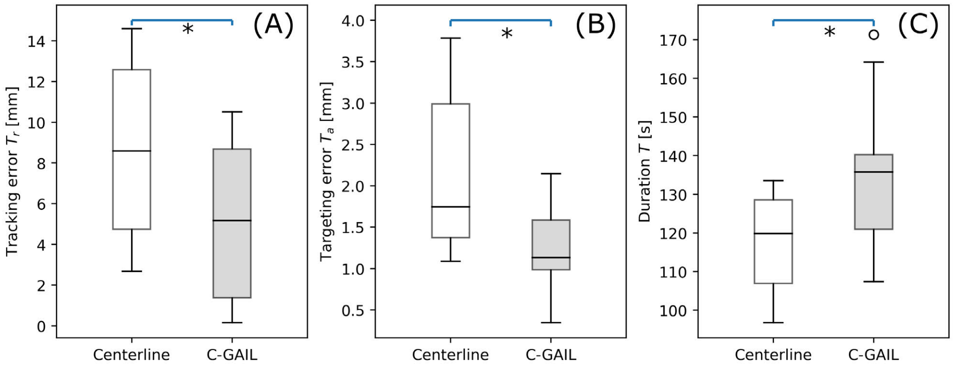

Figure 6.8: *In-vitro* performance comparison between C-GAIL path and centerline, with respect to (A) tracking error T_r, (B) targeting error T_a, and (C) duration T. ($*$, $p < 0.05$ using Kruskal-Wallis test)

Figure 6.9 presents a representative graphical comparison of actual trajectories and path guidance in two scenarios: following the C-GAIL path and following the centerline. The trajectories of the catheter tip following the C-GAIL path are more stable and smoother, with a curvature of $3.1 \pm 26.6 \text{mm}^{-1}$, compared to a curvature of $3.5 \pm 38.9 \text{mm}^{-1}$ when following the centerline. In the other scenario, the catheter tip can follow the centerline well at the beginning. However, the trajectory then moves away from the centerline as the catheter passes through the aortic arch due to the limited bending capability.

6.5.3. GENERALIZATION

To further generalize the proposed path planning framework, *in-silico* experiments were conducted in a different aortic anatomy (Materialise NV, Leuven, Belgium). 70 demonstrations were recorded, and 100 testing trials were performed. The success rate of the proposed C-GAIL network was 79% when $\epsilon = 10$. Other performance values with respect to targeting error and timesteps are summarized in Table 6.4. Representative paths obtained by the C-GAIL approach are shown in Figure 6.10. These results indicate the robustness and feasibility of applying the proposed path planning framework in anatomies with different geometries.

This work employs an EM sensor to measure the tip pose, which has been validated in a phantom study. EM sensor has demonstrated its efficacy also in *in-vivo* environments [55, 56] considering its small size (<1mm in diameter and <10mm in length) and bio-compatibility. Furthermore, other sensors, such as Fiber Bragg Gratings (FBG) sensor, as well as imaging modalities, can also be utilized to obtain catheter tip pose. In certain specific cases (e.g., free space), the catheter tip pose can also be obtained with a sensorless approach, e.g., an accurate forward kinematic model if control variables are provided [50]. One limitation of this study is that there was no intra-operative environment reconstruction for the *in-vitro* experiments. Instead, a simulated deformable model was utilized to predict intra-operative deformations. In clinical settings, real-time vessel reconstruction from IVUS or Optical Coherence Tomography (OCT) images would be suitable for providing raycast observations elaborated in this work.

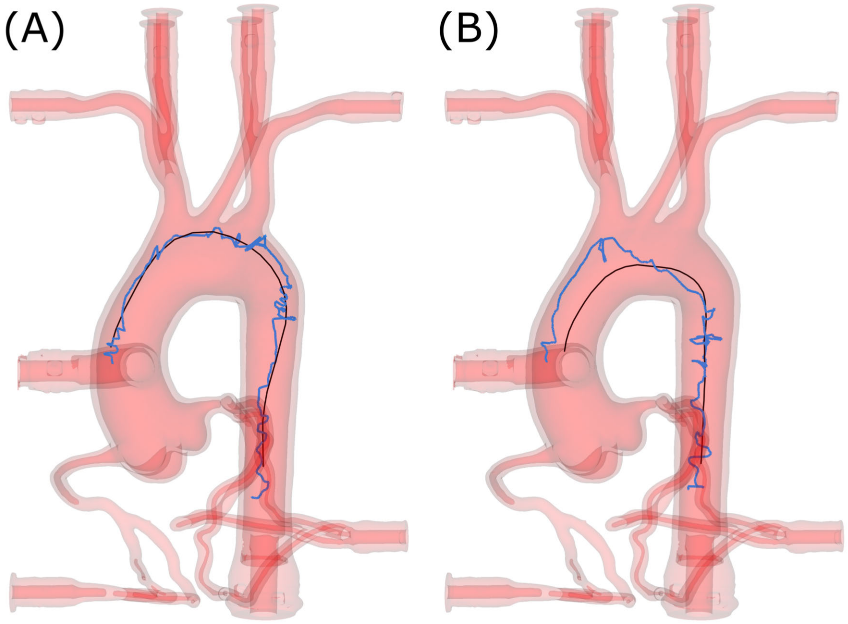

Figure 6.9: Representative *in-vitro* trajectories (blue) and path guidance (black) using: (A) C-GAIL path, and (B) centerline.

Table 6.4: In-silico performance of the proposed C-GAIL network in a different aortic anatomy.

T_a (mm)					T_s ($\times 10^3$)					δ
25th	median	75th	mean	std	25th	median	75th	mean	std	(%)
6.58	6.84	8.57	17.98	23.51	9.41	10.22	11.59	9.71	2.78	79

6.6. EXTENDED STUDY

Given the proposed path planner as navigation guidance for robotic catheters, three interactive control modalities have been designed for steering these catheters. Our study focuses on the application of these modalities in human-in-the-loop robot-assisted cardiac catheterization. The interactive modalities include a gaming joystick, a standard 2D monitor, and an AR HMD. Specifically, the Microsoft HoloLens 2® is utilized as an advanced AR headset for 3D visualization. To evaluate the effectiveness of these modalities, an *in-vitro* user study was conducted, comparing three interactive modes: 1) Mode JM - a joystick with a standard 2D monitor, 2) Mode JH - a joystick with a HoloLens providing 3D visualization, and 3) Mode HH - a HoloLens serving as both the control and visualization device. Figure 6.11 illustrates the control schematic for human-in-the-loop catheter navigation with visual feedback. Users can interact with either the joystick or the HoloLens to generate control commands, while receiving 3D visual feedback from the HoloLens or 2D visual feedback from a standard 2D screen.

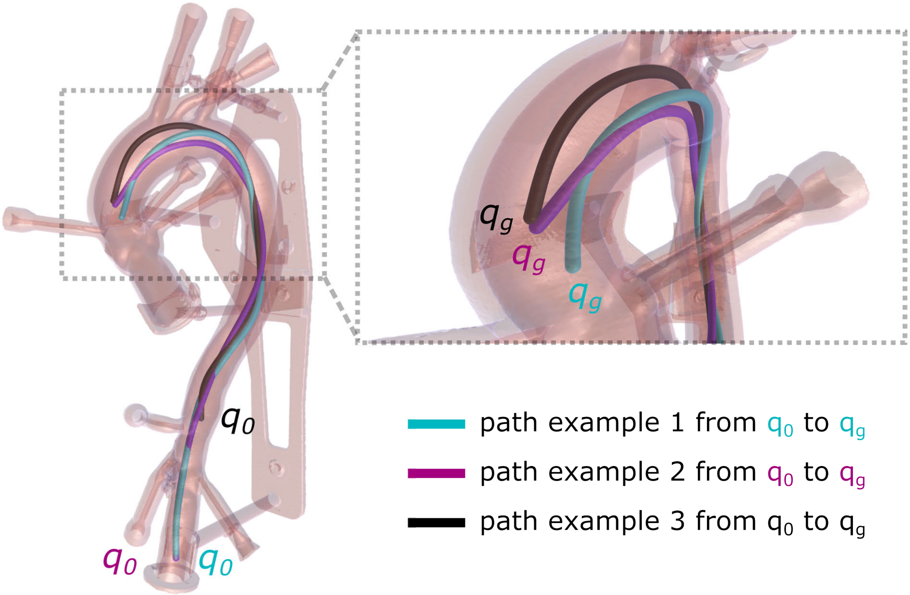

Figure 6.10: Examples of *in-silico* C-GAIL paths in a different aortic anatomy (Materialise NV, Leuven, Belgium).

The functionalities of the different thumbsticks and buttons are depicted in Figure 6.12a. Using a joystick driver library in ROS, the bending angle of the left thumbstick is read as a float value ranging from 0 to 1, while the button toggles between two distinct values: 0 and 1. Users can control the bending in the 2-DoFs by directly mapping the bending angle of the left thumbstick (ϕ, θ) to the pressure applied to the PAMs (p_ϕ, p_θ), namely $p_\phi \propto \phi$, $p_\theta \propto \theta$. The right thumbstick is utilized to adjust the speed of the catheter driver for insertion/retraction motion. The catheter driver is operated using velocity control. The thumbstick's bending angle r is mapped to the translation speed of the catheter driver v, namely $v \propto r$. The maximum translational speed is set at 5 mm/s. The PS (Δ) and OPTIONS (X) buttons on the right side (as shown in Figure 6.12a) are used to switch between insertion and retraction modes. This choice of selecting forward and backward motion commands rather than mapping the joystick's bi-directional motion to forward and backward motion helps prevent the catheter driver from continuously switching between forward and backward motion, making it a more deliberate and controlled choice by the user. The thumbstick is equipped with an automatic return mechanism similar to a spring, which may cause input fluctuations around 0 when abruptly released. Consequently, the catheter driver may rapidly alternate between forward and backward movements within a short duration. This approach is adopted as an alternative to implementing a deadzone where the catheter driver's speed defaults to zero.

Figure 6.12b depicts the user interface design of the HoloLens when utilized as a control input device. Users can interact with virtual buttons or sliders displayed by the

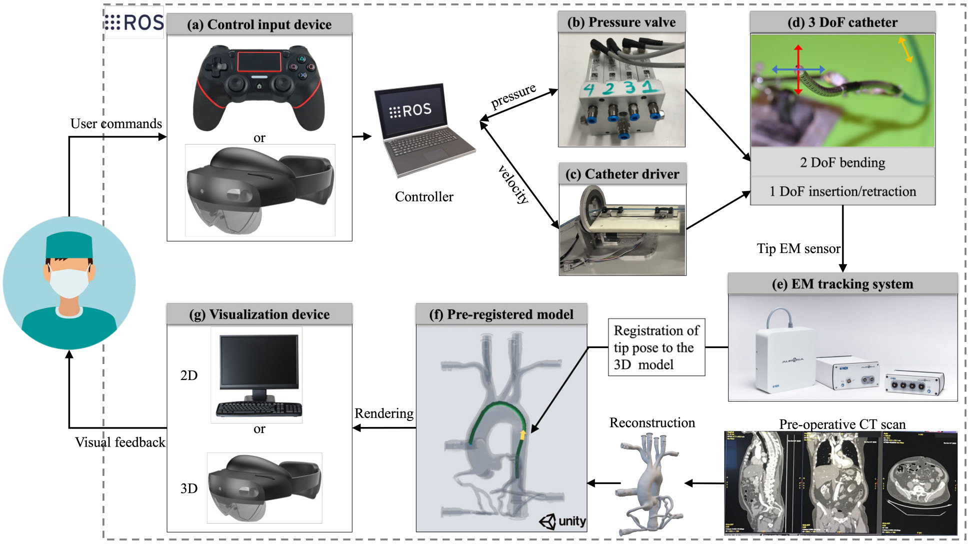

Figure 6.11: The schematic of our advanced human-in-the-loop vessel navigation system, which incorporates multiple interactive modalities. The system includes the following components: (a) a gaming joystick or an HMD serving as control devices; (b) a pneumatic valve with four output ports that receives control commands from ROS; (c) the catheter driver, which operates through velocity control to regulate the insertion and retraction of the catheter; (d) the PAM-driven catheter, featuring a 2-DoF mechanism and a 50 mm active bendable segment; (e) an EM tracking system that localizes the catheter tip, and its pose is registered to the mesh frame of the 3D reconstructed model; (f) a virtual 3D aortic model reconstructed using high-resolution CT images, along with the guidance path and the catheter tip pose registered and rendered within this virtual model frame; (g) visual feedback provided to users, either through a standard monitor displaying a 2D view or via a HoloLens headset offering a 3D view.

HoloLens, similar to how they would interact with physical objects, to send control commands for steering the catheter. The position of the slider r controls a speed v for the catheter driver. To ensure safety, an emergency button has been incorporated, enabling users to quickly halt the translational movement of the catheter in case of an emergency. The blue control panel is located on the right side, while the green sphere can be manipulated within this 2D plane. The sphere's coordinates are measured and proportionally converted into pressures. These pressures are then transmitted to the Pneumatic Artificial Muscles (PAMs) in two orthogonal directions, referred to as p_ϕ and p_θ. Users have the flexibility to reposition various holographic components within the HoloLens view by grasping and dragging them, allowing for customization of the layout based on their comfort and preference. Furthermore, users can activate a hand-ray feature, commonly found in HoloLens, which extends from their palm towards the holographic object. This feature enables interaction with holographic objects that are situated beyond their physical reach.

Control commands generated by either the joystick or the HoloLens are processed by the PC and subsequently transmitted to the pressure valves responsible for adjusting the catheter's bending, as well as to the catheter driver responsible for managing its translational movement, as depicted in Figure 6.12c. This systematic procedure enables precise

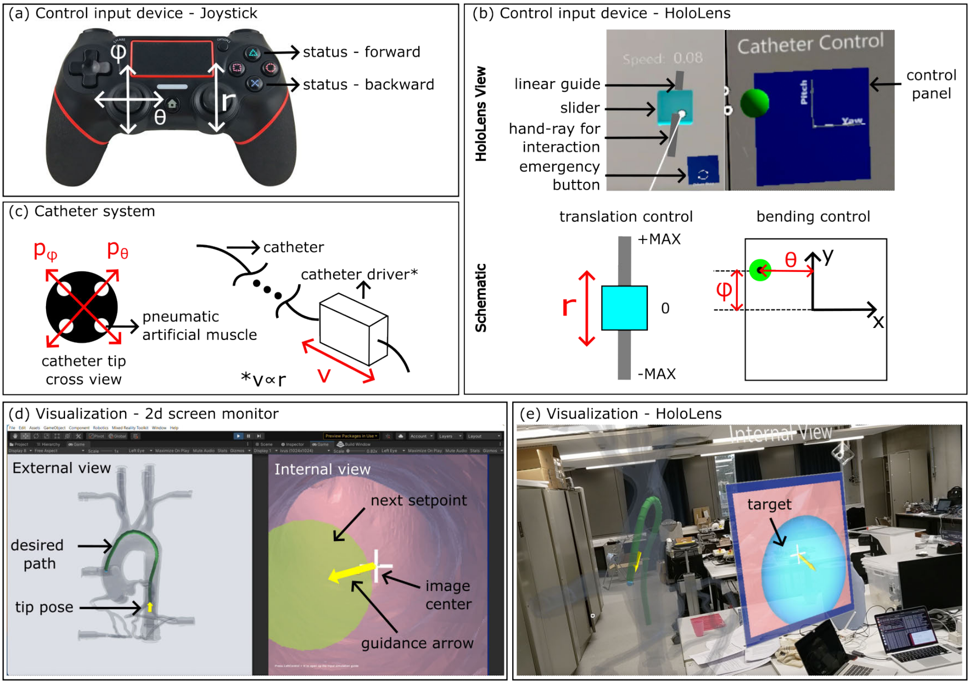

Figure 6.12: User interfaces for input devices and visual feedback: (a) a gaming joystick is provided as a control input device, allowing users to manipulate the system; (b) a HoloLens headset serves as an alternative control input device, equipped with hand gesture recognition capabilities for intuitive interaction; (c) a schematic illustration depicts the three mapping relationships corresponding to the 3-DoF of the catheter system; (d) 2D visualization is achieved using a standard monitor, providing users with a two-dimensional representation of the system and its feedback; (e) 3D visualization is facilitated through the use of the HoloLens, enabling users to view holograms from different perspectives by physically moving around in real-world space.

control over all 3-DoFs of the robotic catheter.

The visualizations for both the standard 2D monitor and the HoloLens can be observed in Figure 6.12d and Figure 6.12e, respectively, with each displaying similar user interface designs. The user interface is divided into two main sections: an external view on the left and an internal view on the right. The external view provides users with a comprehensive perspective of the aorta, featuring a prominent green line indicating the desired path to be followed and a yellow arrow denoting the current position of the catheter tip. The internal view offers an immersive inside-the-vessel view, resembling angioscopy, and showcases several discrete green spheres that represent the setpoints along the path. Specifically, there are 26 green spheres corresponding to the 26 setpoints generated by the C-GAIL path planning algorithm [57]. To provide guidance, a yellow arrow is included to indicate the direction and magnitude of the required bending of the catheter tip from its current position. The white cross represents the center of the field of view, while a blue sphere represents the final target located at the end of the path that users aim to reach with utmost accuracy.

It is important to mention that the internal view, as presented in this study, is not

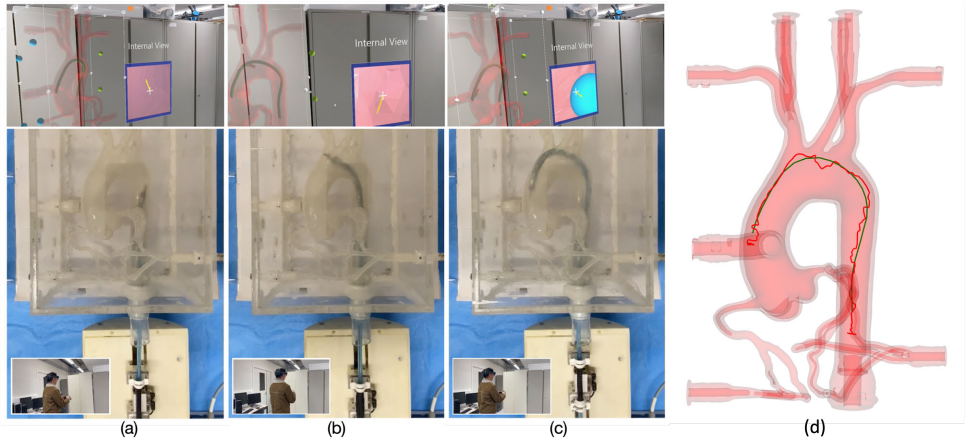

(a) (b) (c) (d)

Figure 6.13: The experimental procedure with the robotic catheter at three different locations when steering using Mode JH: a) descending aorta; b) aortic arch; c) aortic root; d) the recorded trajectory of a single trial.

currently utilized in clinical practice. Instead, it serves as an innovative and novel feature aimed at improving navigation capabilities within the vessels. The internal view images are obtained by utilizing a virtual camera in the Unity3D software. The camera's position and orientation are constantly synchronized with the pose of the catheter tip, providing the operator with a first-person perspective of the procedure.

The experimental procedure consisted of three distinct stages, as depicted in Figure 6.13. In Figure 6.13a, the catheter is positioned within the descending aorta, and the internal view displays an arrow pointing towards the upper left. This indicates to the user that the catheter should begin bending in that direction to follow the optimal path and navigate through the aortic arch. Moving on to Figure 6.13b, it can be observed that the catheter is nearing the end of the aortic arch, with the guidance arrow now pointing towards the bottom left, signifying the need for increased bending. Finally, Figure 6.13c demonstrates the successful arrival of the catheter at the aortic root, as evident in the corresponding view from the HoloLens, where the blue target is almost reached. An arrow pointing towards the bottom-right direction suggests that by gently bending the catheter in this direction, the target can be precisely achieved. Additionally, Figure 6.13d showcases an example of a recorded trajectory from a single trial.

A total of 15 participants, all between the ages of 20 and 35 and possessing an educational background in engineering, took part in the user study conducted. Based on the analysis of the obtained results from the user study, the use of a joystick for steering and a HoloLens for visual feedback (Mode JH) scored the best on all the subjective metrics except for mental demand. The Mode JH outperformed the other modalities also concerning the objective metrics showing a median tracking error of 4.72 mm, a median targeting error of 1.01 mm, a median duration of 82.34 s, and a median natural logarithm of dimensionless squared jerk of 40.38 in the conducted *in-vitro* study. Mode JH showed 8.5%, 4.7%, 6.5%, and 3.9% improvements over Mode JM and 1.5%, 33.6%, 34.9%, and 8.1% over Mode HH, respectively. More detailed information regarding the experimental protocol and the results of the comparative analysis can be found in the study [58].

The results of the study confirm the viability and effectiveness of employing the proposed path planning technique as a reliable guidance tool across different interactive modalities. This study conclusively highlights the practicality of using HoloLens for enhanced 3D visualization in catheterization. Additionally, it demonstrates the superiority of the joystick in catheter teleoperation, offering user-friendliness, responsiveness, and portability advantages.

6.7. CONCLUSION

This study set out to design a robust path planning approach respecting the kinematics of robotic catheters and real-time changes in deformable cluttered environments. The insights gained from this study add to the rapidly expanding field of autonomous navigation of robotic catheters. The findings of this study suggest that the proposed path planner can effectively handle the uncertainty present in vessel deformation. A further clinical study involving real-time vessel reconstruction will be carried out.

BIBLIOGRAPHY

[1] Andras P Durko, Ruben L Osnabrugge, Nicolas M Van Mieghem, Milan Milojevic, Darren Mylotte, Vuyisile T Nkomo, and A Pieter Kappetein. “Annual number of candidates for transcatheter aortic valve implantation per country: current estimates and future projections”. In: *European heart journal* 39.28 (2018), pp. 2635–2642. DOI: `10.1093/eurheartj/ehy107`.

[2] Rajesh Aggarwal, Stephen A Black, JR Hance, A Darzi, and NJW Cheshire. “Virtual reality simulation training can improve inexperienced surgeons’ endovascular skills”. In: *European journal of vascular and endovascular surgery* 31.6 (2006), pp. 588–593. DOI: `10.1016/j.ejvs.2005.11.009`.

[3] Costanza Culmone, Semih Fatih Yikilmaz, Fabian Trauzettel, and Paul Breedveld. “Follow-The-Leader Mechanisms in Medical Devices: A Review on Scientific and Patent Literature”. In: *IEEE Reviews in Biomedical Engineering* (2021). DOI: `10.1109/RBME.2021.3113395`.

[4] Tomas da Veiga, James H Chandler, Peter Lloyd, Giovanni Pittiglio, Nathan J Wilkinson, Ali K Hoshiar, Russell A Harris, and Pietro Valdastri. “Challenges of continuum robots in clinical context: A review”. In: *Progress in Biomedical Engineering* 2.3 (2020). DOI: `10.1088/2516-1091/ab9f41`.

[5] Awaz Ali, Tamas Szili-Torok, Marco Stijnen, Paul Breedveld, and Dimitra Dodou. “First expert evaluation of a new steerable catheter in an isolated beating heart”. In: *Cardiovascular Engineering and Technology* 11 (2020), pp. 769–782. DOI: `10.1007/s13239-020-00499-3`.

[6] Namrata Nayar, Seokhwan Jeong, and Jaydev P. Desai. “Design and Control of 5-DoF Robotically Steerable Catheter for the Delivery of the Mitral Valve Implant”. In: *2021 IEEE International Conference on Robotics and Automation (ICRA)*. 2021, pp. 12268–12274. DOI: `10.1109/ICRA48506.2021.9561146`.

[7] Mohammad Hasan Dad Ansari, Beatriz Farola Barata, Fabian Trauzettel, Zhen Li, Di Wu, Diego DallÁlba, Gianni Borghesan, Mouloud Ourak, Veronica Iacovacci, Selene Tognarelli, Jenny Dankelman, Elena De Momi, Paul Breedveld, Paolo Fiorini, Jos Vander Sloten, Arianna Menciassi, and Emmanuel Vander Poorten. “Proof-of-Concept Medical Robotic Platform for Endovascular Catheterization”. In: *Proceedings of the 11th Conference on New Technologies for Computer and Robot Assisted Surgery (CRAS)*. 2022, pp. 66–67. Available online: `https://atlas-itn.eu/wp-content/uploads/2022/05/CRAS2022_ATLAS_C3.pdf`.

[8] Alberto Favaro, Alice Segato, Federico Muretti, and Elena De Momi. “An Evolutionary-Optimized Surgical Path Planner for a Programmable Bevel-Tip Needle”. In: *IEEE Transactions on Robotics* 37.4 (2021), pp. 1039–1050. DOI: `10.1109/TRO.2020.3043692`.

[9] Junchen Wang, Takashi Ohya, Hongen Liao, Ichiro Sakuma, Tianmiao Wang, Iwai Tohnai, and Toshinori Iwai. “Intravascular catheter navigation using path planning and virtual visual feedback for oral cancer treatment”. In: *The International Journal of Medical Robotics and Computer Assisted Surgery* 7.2 (2011), pp. 214–224. DOI: `10.1002/rcs.392`.

[10] Jian-Qing Zheng, Xiao-Yun Zhou, Celia Riga, and Guang-Zhong Yang. “Towards 3d path planning from a single 2d fluoroscopic image for robot assisted fenestrated endovascular aortic repair”. In: *International Conference on Robotics and Automation (ICRA)*. IEEE. 2019, pp. 8747–8753. DOI: `10.1109/ICRA.2019.8793918`.

[11] Dongjin Huang, Wen Tang, Youdong Ding, Taoruan Wan, and Yimin Chen. “An Interactive 3D Preoperative Planning and Training System for Minimally Invasive Vascular Surgery”. In: *2011 12th International Conference on Computer-Aided Design and Computer Graphics*. 2011, pp. 443–449. DOI: `10.1109/CAD/Graphics.2011.40`.

[12] Hanxin Qian, Xiaofeng Lin, Zonghan Wu, Quan Zeng, Chichi Li, Yi Pang, Cheng Wang, and Shoujun Zhou. “Towards Rebuild The Interventionist’s Intra-Operative Natural Behavior: A Fully Sensorized Endovascular Robotic System Design”. In: *2019 International Conference on Medical Imaging Physics and Engineering (ICMIPE)*. 2019, pp. 1–7. DOI: `10.1109/ICMIPE47306.2019.9098198`.

[13] Yongjun Cho, Jae-Hyeon Park, Jaesoon Choi, and Dong Eui Chang. “Image processing based autonomous guidewire navigation in percutaneous coronary intervention”. In: *2021 IEEE International Conference on Consumer Electronics-Asia (ICCE-Asia)*. IEEE. 2021, pp. 1–6. DOI: `10.1109/ICCE-Asia53811.2021.9641975`.

[14] Pierre Schegg, Jérémie Dequidt, Eulalie Coevoet, Edouard Leurent, Rémi Sabatier, Philippe Preux, and Christian Duriez. “Automated Planning for Robotic Guidewire Navigation in the Coronary Arteries”. In: *2022 IEEE 5th International Conference on Soft Robotics (RoboSoft)*. IEEE. 2022, pp. 239–246. DOI: `10.1109/RoboSoft54090.2022.9762096`.

[15] Sharan R Ravigopal, Timothy A Brumfiel, and Jaydev P Desai. “Automated Motion Control of the COAST Robotic Guidewire under Fluoroscopic Guidance”. In: *2021 International Symposium on Medical Robotics (ISMR)*. IEEE. 2021, pp. 1–7. DOI: `10.1109/ISMR48346.2021.9661508`.

[16] Sharan R Ravigopal, Timothy A Brumfiel, Achraj Sarma, and Jaydev P Desai. “Fluoroscopic Image-Based 3-D Environment Reconstruction and Automated Path Planning for a Robotically Steerable Guidewire”. In: *IEEE Robotics and Automation Letters* 7.4 (2022), pp. 11918–11925. DOI: `10.1109/LRA.2022.3207568`.

[17] G Fagogenis, M Mencattelli, Z Machaidze, B Rosa, K Price, F Wu, V Weixler, M Saeed, JE Mayer, and PE Dupont. “Autonomous robotic intracardiac catheter navigation using haptic vision”. In: *Science robotics* 4.29 (2019). DOI: `10.1126/scirobotics.aaw1977`.

[18] Johannes Fauser, Igor Stenin, Julia Kristin, Thomas Klenzner, Jörg Schipper, Dieter Fellner, and Anirban Mukhopadhyay. “Generalized trajectory planning for nonlinear interventions”. In: *OR 2.0 Context-Aware Operating Theaters, Computer Assisted Robotic Endoscopy, Clinical Image-Based Procedures, and Skin Image Analysis*. Springer, 2018, pp. 46–53. DOI: `10.1007/978-3-030-01201-4_6`.

[19] Johannes Fauser, Romol Chadda, Yannik Goergen, Markus Hessinger, Paul Motzki, Igor Stenin, Julia Kristin, Thomas Klenzner, Jörg Schipper, Stefan Seelecke, et al. “Planning for flexible surgical robots via Bézier spline translation”. In: *IEEE Robotics and Automation Letters* 4.4 (2019), pp. 3270–3277. DOI: `10.1109/LRA.2019.2926221`.

[20] Johannes Fauser, Igor Stenin, Julia Kristin, Thomas Klenzner, Jörg Schipper, and Anirban Mukhopadhyay. “Optimizing clearance of bézier spline trajectories for minimally-invasive surgery”. In: *International Conference on Medical Image Computing and Computer-Assisted Intervention*. Springer. 2019, pp. 20–28. DOI: `10.1007/978-3-030-32254-0_3`.

[21] Jian Guo, Yue Sun, and Shuxiang Guo. “A Training System for Vascular Interventional Surgeons based on Local Path Planning”. In: *2021 IEEE International Conference on Mechatronics and Automation (ICMA)*. IEEE. 2021, pp. 1328–1333. DOI: `10.1109/ICMA52036.2021.9512808`.

[22] Ming-ke Gao, Yi-min Chen, Quan Liu, Chen Huang, Ze-yu Li, and Dian-hua Zhang. “Three-dimensional path planning and guidance of leg vascular based on improved ant colony algorithm in augmented reality”. In: *Journal of medical systems* 39.11 (2015), p. 133. DOI: `10.1007/s10916-015-0315-2`.

[23] Fei Qi, Feng Ju, Dongming Bai, Yaoyao Wang, and Bai Chen. “Kinematic analysis and navigation method of a cable-driven continuum robot used for minimally invasive surgery”. In: *The International Journal of Medical Robotics and Computer Assisted Surgery* (2019), e2007. DOI: `10.1002/rcs.2007`.

[24] Zhen Li, Jenny Dankelman, and Elena De Momi. “Path planning for endovascular catheterization under curvature constraints via two-phase searching approach”. In: *International Journal of Computer Assisted Radiology and Surgery* 16.4 (2021), pp. 619–627. DOI: `10.1007/s11548-021-02328-x`.

[25] Hedyeh Rafii-Tari, Jindong Liu, Su-Lin Lee, Colin Bicknell, and Guang-Zhong Yang. “Learning-Based Modeling of Endovascular Navigation for Collaborative Robotic Catheterization”. In: *Advanced Information Systems Engineering*. Springer Berlin Heidelberg, 2013, pp. 369–377. DOI: `10.1007/978-3-642-40763-5_46`.

[26] Hedyeh Rafii-Tari, Jindong Liu, Christopher J Payne, Colin Bicknell, and Guang-Zhong Yang. “Hierarchical HMM based learning of navigation primitives for cooperative robotic endovascular catheterization”. In: *International Conference on Medical Image Computing and Computer-Assisted Intervention*. Springer. 2014, pp. 496–503. DOI: `10.1007/978-3-319-10404-1_62`.

[27] Wenqiang Chi, Jindong Liu, Mohamed EMK Abdelaziz, Giulio Dagnino, Celia Riga, Colin Bicknell, and Guang-Zhong Yang. “Trajectory Optimization of Robot-Assisted Endovascular Catheterization with Reinforcement Learning”. In: *IEEE/RSJ International Conference on Intelligent Robots and Systems (IROS)*. IEEE, Oct. 2018. DOI: `10.1109/IROS.2018.8593421`.

[28] Wenqiang Chi, Jindong Liu, Hedyeh Rafii-Tari, Celia Riga, Colin Bicknell, and Guang-Zhong Yang. “Learning-based endovascular navigation through the use of non-rigid registration for collaborative robotic catheterization”. In: *International Journal of Computer Assisted Radiology and Surgery* 13.6 (Apr. 2018), pp. 855–864. DOI: `10.1007/s11548-018-1743-5`.

[29] Wenqiang Chi, Giulio Dagnino, Trevor Kwok, Anh Nguyen, Dennis Kundrat, Mohamed E. M. K. Abdelaziz, Celia Riga, Colin Bicknell, and Guang-Zhong Yang. “Collaborative robot-assisted endovascular catheterization with generative adversarial imitation learning”. In: *IEEE International Conference on Robotics and Automation (ICRA)*. IEEE, June 2020. DOI: `10.1109/ICRA40945.2020.9196912`.

[30] Yan Zhao, Yuxin Wang, Jianhua Zhang, Xinke Liu, Youxiang Li, Shuxiang Guo, Xu Yang, and Shunming Hong. “Surgical GAN: Towards Real-time Path Planning for Passive Flexible Tools in Endovascular Surgeries”. In: *Neurocomputing* (2022). DOI: `10.1016/j.neucom.2022.05.044`.

[31] Abraham Temesgen Tibebu, Bingbin Yu, Yohannes Kassahun, Emmanuel Vander Poorten, and Phuong Toan Tran. “Towards autonomous robotic catheter navigation using reinforcement learning”. In: *4th Joint Workshop on New Technologies for Computer/Robot Assisted Surgery*. 2014, pp. 163–166. Available online: `https://lirias.kuleuven.be/1748447?limo=0`.

[32] Hyeonseok You, EunKyung Bae, Youngjin Moon, Jihoon Kweon, and Jaesoon Choi. “Automatic control of cardiac ablation catheter with deep reinforcement learning method”. In: *Journal of Mechanical Science and Technology* 33.11 (2019), pp. 5415–5423. DOI: `10.1007/s12206-019-1036-0`.

[33] Tobias Behr, Tim Philipp Pusch, Marius Siegfarth, Dominik Hüsener, Tobias Mörschel, and Lennart Karstensen. “Deep Reinforcement Learning for the Navigation of Neurovascular Catheters”. In: *Current Directions in Biomedical Engineering* 5.1 (2019), pp. 5–8. DOI: `10.1515/cdbme-2019-0002`.

[34] Lennart Karstensen, Tobias Behr, Tim Philipp Pusch, Franziska Mathis-Ullrich, and Jan Stallkamp. “Autonomous guidewire navigation in a two dimensional vascular phantom”. In: *Current Directions in Biomedical Engineering* 6.1 (2020). DOI: `10.1515/cdbme-2020-0007`.

[35] Jihoon Kweon, Kyunghwan Kim, Chaehyuk Lee, Hwi Kwon, Jinwoo Park, Kyoseok Song, Young In Kim, Jeeone Park, Inwook Back, Jae-Hyung Roh, et al. “Deep reinforcement learning for guidewire navigation in coronary artery phantom”. In: *IEEE Access* 9 (2021), pp. 166409–166422. DOI: `10.1109/ACCESS.2021.3135277`.

[36] Fanxu Meng, Shuxiang Guo, Wei Zhou, and Zhengyang Chen. “Evaluation of a Reinforcement Learning Algorithm for Vascular Intervention Surgery”. In: *2021 IEEE International Conference on Mechatronics and Automation (ICMA)*. IEEE. 2021, pp. 1033–1037. DOI: `10.1109/ICMA52036.2021.9512675`.

[37] Lennart Karstensen, Jacqueline Ritter, Johannes Hatzl, Torben Pätz, Jens Langejürgen, Christian Uhl, and Franziska Mathis-Ullrich. “Learning-based autonomous vascular guidewire navigation without human demonstration in the venous system of a porcine liver”. In: *International Journal of Computer Assisted Radiology and Surgery* (2022), pp. 1–8. DOI: `10.1007/s11548-022-02646-8`.

[38] Ameya Pore, Eleonora Tagliabue, Marco Piccinelli, Diego Dall’Alba, Alicia Casals, and Paolo Fiorini. “Learning from demonstrations for autonomous soft-tissue retraction”. In: *2021 International Symposium on Medical Robotics (ISMR)*. IEEE. 2021, pp. 1–7. DOI: `10.1109/ISMR48346.2021.9661514`.

[39] Alice Segato, Marco Di Marzo, Sara Zucchelli, Stefano Galvan, Riccardo Secoli, and Elena De Momi. “Inverse reinforcement learning intra-operative path planning for steerable needle”. In: *IEEE Transactions on Biomedical Engineering* 69.6 (2021), pp. 1995–2005. DOI: `10.1109/TBME.2021.3133075`.

[40] Zhen Li, Enrico Manzionna, Giovanni Monizzi, Angelo Mastrangelo, Maria Elisabetta Mancini, Daniele Andreini, Jenny Dankelman, and Elena De Momi. “Position-based dynamics simulator of vessel deformations for path planning in robotic endovascular catheterization”. In: *Medical Engineering & Physics* 110 (2022), p. 103920. DOI: `10.1016/j.medengphy.2022.103920`.

[41] Zhen Li, Enrico Manzionna, Giovanni Monizzi, Angelo Mastrangelo, Maria Elisabetta Mancini, Daniele Andreini, Jenny Dankelman, and Elena De Momi. “Simulation of Deformable Vasculature for Robot-assisted Endovascular Catheterization”. In: *Proceedings of the 33rd Conference of the International Society for Medical Innovation and Technology (iSMIT)*. 2022. Available online: `https://atlas-itn.eu/wp-content/uploads/2022/10/SMIT_-poster_Zhen.pdf`.

[42] Deepak Pathak, Pulkit Agrawal, Alexei A. Efros, and Trevor Darrell. “Curiosity-driven Exploration by Self-supervised Prediction”. In: *Proceedings of the 34th International Conference on Machine Learning*. Ed. by Doina Precup and Yee Whye Teh. Vol. 70. Proceedings of Machine Learning Research. PMLR, Aug. 2017, pp. 2778–2787. URL: `https://proceedings.mlr.press/v70/pathak17a.html`.

[43] Sanmit Narvekar, Jivko Sinapov, Matteo Leonetti, and Peter Stone. “Source task creation for curriculum learning”. In: *Proceedings of the 2016 international conference on autonomous agents & multiagent systems*. 2016, pp. 566–574. URL: `https://www.cs.utexas.edu/~sanmit/papers/AAMAS16-Narvekar.pdf`.

[44] John Schulman, Filip Wolski, Prafulla Dhariwal, Alec Radford, and Oleg Klimov. “Proximal policy optimization algorithms”. In: *arXiv preprint arXiv:1707.06347* (2017). URL: `https://arxiv.org/abs/1707.06347`.

[45] Jonathan Ho and Stefano Ermon. “Generative Adversarial Imitation Learning”. In: *Advances in Neural Information Processing Systems*. Ed. by D. Lee, M. Sugiyama, U. Luxburg, I. Guyon, and R. Garnett. Vol. 29. Curran Associates, Inc., 2016. URL: `https://proceedings.neurips.cc/paper_files/paper/2016/file/cc7e2b878868cbae992d1fb743995d8f-Paper.pdf`.

[46] Faraz Torabi, Garrett Warnell, and Peter Stone. “Behavioral cloning from observation”. In: *arXiv preprint arXiv:1805.01954* (2018). URL: `https://arxiv.org/abs/1805.01954`.

[47] Wendong Xiao, Liang Yuan, Li He, Teng Ran, Jianbo Zhang, and Jianping Cui. “Multigoal Visual Navigation With Collision Avoidance via Deep Reinforcement Learning”. In: *IEEE Transactions on Instrumentation and Measurement* 71 (2022), pp. 1–9. DOI: `10.1109/TIM.2022.3158384`.

[48] Prajit Ramachandran, Barret Zoph, and Quoc V Le. “Searching for activation functions”. In: *arXiv preprint arXiv:1710.05941* (2017). URL: `https://arxiv.org/abs/1710.05941`.

[49] Arthur Juliani, Vincent-Pierre Berges, Ervin Teng, Andrew Cohen, Jonathan Harper, Chris Elion, Chris Goy, Yuan Gao, Hunter Henry, Marwan Mattar, et al. “Unity: A general platform for intelligent agents”. In: *arXiv preprint arXiv:1809.02627* (2018). URL: `https://arxiv.org/abs/1809.02627`.

[50] Di Wu, Yao Zhang, Mouloud Ourak, Kenan Niu, Jenny Dankelman, and Emmanuel Vander Poorten. “Hysteresis modeling of robotic catheters based on long short-term memory network for improved environment reconstruction”. In: *IEEE Robotics and Automation Letters* 6.2 (2021), pp. 2106–2113. DOI: `10.1109/LRA.2021.3061069`.

[51] Omar Al-Ahmad, Mouloud Ourak, Johan Vlekken, and Emmanuel Vander Poorten. “Force Control With a Novel Robotic Catheterization System Based on Braided Sleeve Grippers”. In: *IEEE Transactions on Medical Robotics and Bionics* (2023), pp. 1–1. DOI: `10.1109/TMRB.2023.3291026`.

[52] J. Sobocinski, H. Chenorhokian, B. Maurel, M. Midulla, A. Hertault, M. Le Roux, R. Azzaoui, and S. Haulon. “The Benefits of EVAR Planning Using a 3D Workstation”. In: *European Journal of Vascular and Endovascular Surgery* 46.4 (2013), pp. 418–423. ISSN: 1078-5884. DOI: `10.1016/j.ejvs.2013.07.018`.

[53] Steve Ramcharitar, Mark S Patterson, Robert Jan Van Geuns, Carlos Van Meighem, and Patrick W Serruys. “Technology insight: magnetic navigation in coronary interventions”. In: *Nature Clinical Practice Cardiovascular Medicine* 5.3 (2008), pp. 148–156. DOI: `10.1038/ncpcardio1095`.

[54] Xiufen Ye, Jianguo Zhang, Peng Li, Tian Wang, and Shuxiang Guo. “A fast and stable vascular deformation scheme for interventional surgery training system”. In: *Biomedical engineering online* 15.1 (2016), pp. 1–14. DOI: `10.1186/s12938-016-0148-3`.

[55] M. Ourak, S. De Buck, X. T. Ha, O. Al-Ahmad, K. Bamps, J. Ector, and E. Vander Poorten. “Fusion of Biplane Fluoroscopy With Fiber Bragg Grating for 3D Catheter Shape Reconstruction”. In: *IEEE Robotics and Automation Letters* 6.4 (2021), pp. 6505–6512. DOI: `10.1109/LRA.2021.3094238`.

[56] Xuan Thao Ha, Mouloud Ourak, Omar Al-Ahmad, Di Wu, Gianni Borghesan, Arianna Menciassi, and Emmanuel Vander Poorten. “Robust Catheter Tracking by Fusing Electromagnetic Tracking, Fiber Bragg Grating and Sparse Fluoroscopic Images”. In: *IEEE Sensors Journal* 21.20 (2021), pp. 23422–23434. DOI: `10.1109/JSEN.2021.3107036`.

[57] Zhen Li, Chiara Lambranzi, Di Wu, Alice Segato, Federico De Marco, Emmanuel Vander Poorten, Jenny Dankelman, and Elena De Momi. “Robust Path Planning via Learning from Demonstrations for Robotic Catheters in Deformable Environments”. 2023. (Under Review).

[58] Di Wu, Zhen Li, Mohammad Hasan Dad Ansari, Xuan Thao Ha, Mouloud Ourak, Jenny Dankelman, Arianna Menciassi, Elena De Momi, and Emmanuel Vander Poorten. “Comparative Analysis of Interactive Modalities for Intuitive Endovascular Interventions”. 2023. (Under Review).

IV

DISCUSSION AND CONCLUSION

7

DISCUSSION AND CONCLUSION

There will come a time when you believe everything is finished.
Yet that will be the beginning.

Louis L'Amour

The best way to predict the future is to create it.

Peter Drucker

In conclusion, this dissertation has explored and advanced the field of path planning for robotic catheters in tortuous and deformable environments. The last chapter consolidates all findings and provides a comprehensive summary of the key contributions made throughout this research. Additionally, a comprehensive evaluation of this work in relation to the existing literature is provided, accompanied by an acknowledgment of the inherent limitations. Furthermore, a comprehensive exploration of the prevailing challenges that persist in this domain is presented, offering valuable insights and recommendations for future research endeavors. Presenting these findings in an academic context aims to foster further scholarly inquiry and contribute to the ongoing development of this dynamic field of study.

7.1. CONTRIBUTIONS AND LIMITATIONS

This dissertation contributes to the development of safe, accurate, and efficient path planning techniques for robotic catheters. This research focused on offering a realistic and dynamic environment for path planning, and designed path planning algorithm accounting for the deformable property of the vessels and the limited steering capability of catheters. In detail, the main findings and contributions of this thesis in accordance with the sub-objectives presented in Chapter 1 are summarized as follows.

Path planning incorporating the limited steering capability of catheters (O1)
In Chapter 2, a comprehensive systematic review of path planning techniques in intraluminal and endovascular interventions was conducted. The limitations of existing path planning methods are identified, and recommendations for improving the robustness of these algorithms are proposed.

In Chapter 3, a novel path planning approach called BFS-GA was proposed, which effectively adheres to the robot curvature constraint while keeping the catheter's path as close to the centerlines as possible. The proposed BFS-GA path planner is capable of swiftly calculating obstacle-free trajectories that conform to the patient's vasculature, while incorporating the inherent limitations of the catheter such as maximum curvature. The presented work is suited for clinical procedures demanding satisfying curvature constraints while optimizing specified criteria. It is also applicable for curvature-constrained robots in narrow passages.

The proposed path planner has undergone comprehensive evaluation and validation using diverse datasets, encompassing various anatomical models such as the coronary artery, aorta, femoral artery, and peripheral arterial system, etc. Comparative analysis against conventional sampling-based path planning methods reveals the superior efficiency and performance of the proposed BFS-GA approach. Specifically, the proposed method exhibits notable advantages, including reduced computation time, shorter path length, increased distance from vascular walls, diminished path curvature, and elevated success rates.

Nevertheless, it is important to acknowledge that the effectiveness of the proposed path planner is contingent upon the accuracy of the anatomical centerlines, which can be influenced by deformations within the anatomical model. Consequently, the computational cost and precision of the anatomical centerline extraction process significantly impact the performance of the path planner. A comparison with other alternative optimization algorithms would be interesting to investigate. Additionally, the use of the GA as the chosen optimization approach for the local planner raises considerations regarding its advantages and disadvantages. Notably, alternative optimization algorithms such as PSO and ACO offer potential alternatives worth exploring through comparative analysis. Undertaking such investigations would provide valuable insights into the selection of the most suitable optimization algorithm for the local planner.

Auto-adaptive simulator accurately predicting the deformation of vessels (O2)
In Chapter 4, a realistic, auto-adaptive, and visually plausible simulator was designed. This simulator can accurately predict the global deformation of vessels induced by the

contact of a robotic catheter and cyclic motion corresponding to the heartbeat. Compared with the literature, some novel properties of the proposed simulator are highlighted, such as a simulated movement of the vessels caused by the heartbeat and an autonomous calibration of PBD parameters using the PSO algorithm. Compared with the literature, this simulator has an error of 0.23±0.13% for deformation and 0.30±0.85mm for the aortic root displacement. *In-vitro* experiments show an error of 1.35±1.38mm for deformation prediction. The reported results of *in-vitro* validation show that this simulator framework can be applied to different datasets and represents a good surrogate for the modelization of deformation. The proposed workflow implements the modeling and simulation of intervention devices and a deformable aorta that could create a dynamic environment for intra-operative path planning and control in robotic endovascular catheterization.

However, it should be noted that the induced deformation of vessels resulting from the cyclic motion of the heartbeat has yet to be empirically validated through *in-vitro* experiments. The inclusion of an experimental setup featuring a phantom incorporating a pump to mimic the motion of the heartbeat would significantly enhance the credibility of this study. Furthermore, to attain a simulation environment that closely resembles real-world scenarios, it is crucial to incorporate the modeling and simulation of robotic catheters with a steerable tip and flexible shaft body. Currently, the simulation only considers the steerable tip, overlooking the force transmission loss occurring between the proximal and distal ends of the shaft body. Since the interaction between the shaft and vessels directly impacts the pose of the steerable tip of the catheter, delving into the intricate modeling of robotic catheters will undoubtedly bolster the simulator's performance.

Deformable model reconstruction from intra-operative medical images (O3)

In Chapter 5, a deformable model-to-image registration framework was proposed based on deep learning for augmented reality-guided endovascular interventions. The proposed framework encompasses several key components: (i) autonomous vessel segmentation of intra-operative fluoroscopy images through a DRU-Net; (ii) affine model-to-image registration, achieved by employing a CNN to align the segmented images with the pre-operative 3D model reconstructed from CTA scans; (iii) deformable model-to-image registration, accomplished by employing a DRU-Net model to predict and reconstruct deformations from 2D images onto the pre-operative 3D model; and (iv) an immersive visualization of intra-operative 3D models using augmented reality. To provide a comprehensive evaluation of registration accuracy, a customized loss function and performance metrics (i.e., MDSC and PDSS) were introduced. This framework has the potential to assist clinicians during procedures by providing augmented reality visualization of patient-specific intra-operative vascular models.

Compared to the literature, this framework can effectively handle tissue deformations in a weakly-supervised manner and accurately reconstruct deformations from 2D to 3D space. The DRU-Net model achieves a notable reduction in penalization loss, as evidenced by the improved PDSS scores with mean and standard deviation values of 3.77 ± 0.09 (compared to 4.19 ± 0.23). However, despite the incorporation of the $\mathscr{L}_B$ component in the loss function, residual artifacts persist even after the retraining phase. Notably, these artifacts become more pronounced in regions where the fixed image contains smaller vessel sections, posing a concern as they can potentially provide incorrect guidance. It is therefore imperative to address this challenge by introducing a post-processing step that targets the suppression of deformations outside the segmented vessel area and enhances deformation smoothness.

To evaluate the accuracy of the 3D registration, the discrepancy between the predicted and ground truth mesh models, obtained from the aforementioned simulator, was quantified. Within the ROI, the mean 3D registration error for vertices was measured to be 1.51 mm. However, it is important to note that the accuracy of the 3D registration has not yet been validated using patient-specific image datasets due to the lack of ground truth, specifically intra-operative mesh models. This presents an opportunity for future research to explore and validate the accuracy of the proposed 3D registration approach using such datasets, which would further strengthen the findings of this study.

Robust path planning algorithm incorporating deformable environments (O4)
In Chapter 6, an enhanced path planner named C-GAIL is proposed, tailored for steerable catheters. This planner ensures higher precision and robustness by accounting for both the deformable properties of vessels and the catheter's steering capabilities. The robustness of the proposed network is verified by the success rate of the C-GAIL network, which is 17%-66%, compared to that of the GAIL network in literature, which is only 0%-16%. This framework can reduce the uncertainty in vessel deformation, thereby minimizing tracking errors. One of the contributions is validating the proposed path planner in an *in-vitro* environment using a teleoperation control strategy. These experiments demonstrate the algorithm's feasibility in generating suitable paths that align with the actual steering capability of the catheter. Compared with the traditional centerline-following approach, the proposed C-GAIL path planner leads to a smaller tracking error of 5.18±3.48mm and a smaller targeting error of 1.26±0.55mm.

One limitation of this study is the absence of intra-operative environment reconstruction for the *in-vitro* experiments. Instead, a simulated deformable model was employed to predict intra-operative deformations. In real clinical scenarios, the utilization of real-time vessel reconstruction from IVUS or OCT images would be more appropriate for generating raycast observations as elaborated in this work. This would enhance the fidelity and relevance of the findings to actual clinical practice. Future research could incorporate such real-time imaging techniques to validate the proposed framework in a more realistic and clinically relevant environment.

Our extended work [1] presents an in-depth exploration of interactive modalities in teleoperation, utilizing the path guidance derived from the robust path planner C-GAIL mentioned earlier. The findings from this user study hold the potential to improve current cardiac catheterization procedures by introducing an innovative clinical workflow. In this approach, physicians remotely maneuver the catheter using a joystick while wearing a HoloLens, under the path guidance obtained through the C-GAIL path planner.

Nevertheless, one limitation of this study is the limited number of studies conducted thus far. Given the delicate and complex structure of vessels, intuitive catheter steering becomes crucial in these applications. Therefore, it would be valuable to conduct an increased number of trials per user and engage a broader range of participants in future research.

7.2. RECOMMENDATIONS FOR FUTURE RESEARCH

The subsequent sections delve into the prominent unresolved challenges in path planning for robotic catheters, outline directions for future research, and explore potential extensions of the studies conducted in this dissertation.

Efficient centerline extraction approaches

As illustrated in the systematic review [2], a significant portion of existing literature on path planning for intraluminal and endovascular interventions relies on anatomical centerlines. These centerlines serve as a common basis for path guidance in interventions [3, 4]. However, the accuracy of anatomical centerlines is susceptible to deformations in the anatomical model. Incorporating centerline extraction methods into real-time intra-operative procedures necessitates addressing the challenges of reducing computation time and efficiently generating closed mesh models (such as the models required in the VMTK library [5]).

Adaptive path planning algorithms

Chapter 6 showcases the potential for generalizing the proposed path planning method. *In-silico* experiments were conducted using two different aortic anatomies. However, exploring an easier and more adaptable approach for the current network model to be applied to new, unseen anatomy models would be of interest.

In addition, it would be highly valuable to conduct a clinical study that involves intra-operative path planning accompanied by real-time vessel reconstruction using imaging modalities such as through IVUS [6] or OCT [7]. These intraoperative imaging techniques, including IVUS and OCT, offer the advantage of direct observation and visualization capabilities [6, 8, 7]. By combining the information obtained from IVUS and EM sensors, intravascular vessel reconstruction can be achieved [9, 6]. Leveraging real-time vessel reconstruction enables the effective achievement of precise and reliable path re-planning for continuum robots during intra-operative procedures.

Simulation of respiration motion

Chapter 4 presents an auto-adaptive simulator designed to accurately predict vessel deformations caused by the contact of a robotic catheter and cyclic heartbeat motion. While the heartbeat motion is considered, it is important to note that the respiratory motion can also contribute to vessel deformations [10]. According to findings in [10], the spatial variation in the respiratory displacement of the coronary arteries suggests that the heart's breathing motion is more complex than a simple 3D translation. For a dataset of 10 patients, the maximum 3D displacement of the right coronary artery ostium during a respiratory cycle is reported as 5.0±1.3 mm [10]. By simulating the impact of respiratory motion on vessel deformations, the realism and accuracy of the simulator can be enhanced.

Design of intuitive haptic feedback

The GUI of the simulator proposed in Chapter 4 provides visual feedback indicating the collision force when the device tip collides with the vessel wall. However, considering the conventional clinical workflow and reducing the visual burden of users, incorporating haptic feedback, such as utilizing joystick vibrations [11], would potentially provide a more intuitive experience for users.

Improvements of deformable registration

In Chapter 5, a deformable image registration framework is introduced to extract the vessel deformations from intra-operative 2D images and reconstruct those deformations on the pre-operative 3D model. To enhance the robustness of the registration model, future work involves expanding the training dataset and implementing post-processing techniques to suppress residual artifacts. Additionally, conducting end-user evaluations in the operating room is an important step. These efforts will contribute to the continued advancement and practical implementation of this framework in clinical settings.

Research beyond the scope of this thesis

Proprioception and Shape-sensing: To achieve precise and reliable path planning for robotic catheters, it is crucial to have accurate and real-time shape-sensing capabilities. However, accurately modeling the shape of these robots presents challenges due to factors such as friction, backlash, the deformable nature of the lumen or vessels, and collisions with the anatomy [12]. In recent years, sensor-based shape reconstruction techniques have emerged as promising solutions for interventional devices, utilizing sensors such as Fiber Bragg Grating (FBG) and Electromagnetic (EM) sensors [12, 13, 14, 15, 16]. Both FBG and EM-enabled techniques offer advantages such as real-time shape estimation, short response time, compact size, biocompatibility, non-toxicity, and high sensitivity. By attaching multiple sensors along the length of the continuum robot, the robot's position can be tracked, and axial strain can be measured. However, FBG sensors exhibit limitations in high-strain conditions, while EM sensors are susceptible to electromagnetic interference [13]. Therefore, a sensor-fusion approach that combines FBG, EM sensors, and sparse fluoroscopic images has the potential to enhance the accuracy of 3D catheter shape reconstruction [16].

Catheter design: Steerable catheters designed for endovascular procedures are developed using various technologies. For example, pneumatic-driven or magnetic-driven systems have been utilized in different instruments [17, 18, 19]. Soft robotics systems are emerged as a promising paradigm, offering the potential for multi-steering capabilities and stress-less interventions in narrow passageways. To enhance the bending capability of steerable catheters, novel designs for catheter actuation or the use of soft materials can be explored as potential solutions.

BIBLIOGRAPHY

[1] Di Wu, Zhen Li, Mohammad Hasan Dad Ansari, Xuan Thao Ha, Mouloud Ourak, Jenny Dankelman, Arianna Menciassi, Elena De Momi, and Emmanuel Vander Poorten. “Comparative Analysis of Interactive Modalities for Intuitive Endovascular Interventions”. 2023. (Under Review).

[2] Ameya Pore, Zhen Li, Diego Dall’Alba, Albert Hernansanz, Elena De Momi, Arianna Menciassi, Alicia Casals Gelpí, Jenny Dankelman, Paolo Fiorini, and Emmanuel Vander Poorten. “Autonomous Navigation for Robot-Assisted Intraluminal and Endovascular Procedures: A Systematic Review”. In: *IEEE Transactions on Robotics* 39.4 (2023), pp. 2529–2548. DOI: `10.1109/TRO.2023.3269384`.

[3] J. Sobocinski, H. Chenorhokian, B. Maurel, M. Midulla, A. Hertault, M. Le Roux, R. Azzaoui, and S. Haulon. “The Benefits of EVAR Planning Using a 3D Workstation”. In: *European Journal of Vascular and Endovascular Surgery* 46.4 (2013), pp. 418–423. ISSN: 1078-5884. DOI: `10.1016/j.ejvs.2013.07.018`.

[4] Steve Ramcharitar, Mark S Patterson, Robert Jan Van Geuns, Carlos Van Meighem, and Patrick W Serruys. “Technology insight: magnetic navigation in coronary interventions”. In: *Nature Clinical Practice Cardiovascular Medicine* 5.3 (2008), pp. 148–156. DOI: `10.1038/ncpcardio1095`.

[5] Luca Antiga, Bogdan Ene-Iordache, and Andrea Remuzzi. “Computational geometry for patient-specific reconstruction and meshing of blood vessels from MR and CT angiography”. In: *IEEE transactions on medical imaging* 22.5 (2003), pp. 674–684. DOI: `10.1109/TMI.2003.812261`.

[6] Beatriz Farola Barata, Phuong Toan Tran, Gianni Borghesan, Keir McCutcheon, Diego Dall’Alba, Paolo Fiorini, Jos Vander Sloten, and Emmanuel Vander Poorten. “IVUS-Based Local Vessel Estimation for Robotic Intravascular Navigation”. In: *IEEE Robotics and Automation Letters* 6.4 (2021), pp. 8102–8109. DOI: `10.1109/LRA.2021.3102307`.

[7] Guiqiu Liao, Oscar Caravaca-Mora, Benoit Rosa, Philippe Zanne, Diego Dall’Alba, Paolo Fiorini, Michel de Mathelin, Florent Nageotte, and Michalina J Gora. “Distortion and Instability Compensation with Deep Learning for Rotational Scanning Endoscopic Optical Coherence Tomography”. In: *Medical Image Analysis* (Jan. 1, 2022), p. 102355. DOI: `https://doi.org/10.1016/j.media.2022.102355`.

[8] Natalia Zulina, Oscar Caravaca, Guiqiu Liao, Sara Gravelyn, Morgane Schmitt, Keshia Badu, Lucile Heroin, and Michalina J Gora. “Colon phantoms with cancer lesions for endoscopic characterization with optical coherence tomography”. In: *Biomedical optics express* 12.2 (2021), pp. 955–968.

[9] Chaoyang Shi, Carlos Tercero, Xianliang Wu, Seiichi Ikeda, Kimihiro Komori, Kiyohito Yamamoto, Fumihito Arai, and Toshio Fukuda. “Real-time in vitro intravascular reconstruction and navigation for endovascular aortic stent grafting”. In: *The International Journal of Medical Robotics and Computer Assisted Surgery* 12.4 (2016), pp. 648–657. DOI: `10.1002/rcs.1736`.

[10] Guy Shechter, Jon R Resar, and Elliot R McVeigh. “Displacement and velocity of the coronary arteries: cardiac and respiratory motion”. In: *IEEE transactions on medical imaging* 25.3 (2006), pp. 369–375. DOI: `10.1109/TMI.2005.862752`.

[11] Pavel Zikmund, Miroslav Macik, Lukas Dubnicky, and Michaela Horpatzska. “Comparison of Joystick guidance methods”. In: *2019 10th IEEE International Conference on Cognitive Infocommunications (CogInfoCom)*. IEEE. 2019, pp. 265–270. DOI: `10.1109/CogInfoCom47531.2019.9089978`.

[12] Chaoyang Shi, Xiongbiao Luo, Peng Qi, Tianliang Li, Shuang Song, Zoran Najdovski, Toshio Fukuda, and Hongliang Ren. “Shape sensing techniques for continuum robots in minimally invasive surgery: A survey”. In: *IEEE Transactions on Biomedical Engineering* 64.8 (2016), pp. 1665–1678.

[13] Sujit Kumar Sahu, Canberk Sozer, Benoit Rosa, Izadyar Tamadon, Pierre Renaud, and Arianna Menciassi. “Shape reconstruction processes for interventional application devices: State of the art, progress, and future directions”. In: *Frontiers in Robotics and AI* 8 (2021), p. 758411.

[14] Xuan Thao Ha, Mouloud Ourak, Omar Al-Ahmad, Di Wu, Gianni Borghesan, Arianna Menciassi, and Emmanuel Vander Poorten. “Robust Catheter Tracking by Fusing Electromagnetic Tracking, Fiber Bragg Grating and Sparse Fluoroscopic Images”. In: *IEEE Sensors Journal* 21.20 (2021), pp. 23422–23434. DOI: `10.1109/JSEN.2021.3107036`.

[15] Xuan Thao Ha, Di Wu, Chun-Feng Lai, Mouloud Ourak, Gianni Borghesan, Arianna Menciassi, and Emmanuel Vander Poorten. “Contact Localization of Continuum and Flexible Robot Using Data-driven Approach”. In: *IEEE Robotics and Automation Letters* (2022).

[16] Xuan Thao Ha, Di Wu, Mouloud Ourak, Gianni Borghesan, Jenny Dankelman, Arianna Menciassi, and Emmanuel Vander Poorten. “Shape Sensing of Flexible Robots Based on Deep Learning”. In: *IEEE Transactions on Robotics* (2022).

[17] Yoshinori Inoue and Koji Ikuta. “Hydraulic driven active catheters with optical bending sensor”. In: *2016 IEEE 29th international conference on micro electro mechanical systems (MEMS)*. IEEE. 2016, pp. 383–386. DOI: `10.1109/MEMSYS.2016.7421641`.

[18] Sungwoong Jeon, Ali Kafash Hoshiar, Kangho Kim, Seungmin Lee, Eunhee Kim, Sunkey Lee, Jin-young Kim, Bradley J Nelson, Hyo-Jeong Cha, Byung-Ju Yi, and Hongsoo Choi. “A magnetically controlled soft microrobot steering a guidewire in a three-dimensional phantom vascular network”. In: *Soft robotics* 6.1 (2019), pp. 54–68. DOI: `10.1089/soro.2018.0019`.

[19] Tomas da Veiga, James H Chandler, Peter Lloyd, Giovanni Pittiglio, Nathan J Wilkinson, Ali K Hoshiar, Russell A Harris, and Pietro Valdastri. "Challenges of continuum robots in clinical context: A review". In: *Progress in Biomedical Engineering* 2.3 (2020). DOI: `10.1088/2516-1091/ab9f41`.

ACRONYMS

2D	two-dimensional.
3D	three-dimensional.
ACO	Ant Colony Optimization.
AFT	Adaptive Fractal Trees.
AHFT	Adaptive Hermite Fractal Tree.
AR	Augmented Reality.
BC	Behavioral Cloning.
BFS	Breadth First Search.
C-GAIL	Curriculum Generative Adversarial Imitation Learning.
CBS	Centerline-based Structure.
CCM	Centro Cardiologico Monzino.
CNN	Convolutional Neural Network.
CT	Computed Tomography.
CTA	Computed Tomography Angiography.
CTRs	Concentric Tube Robots.
DDF	Dense Displacement Field.
DFS	Depth First Search.
DMPs	Dynamical Movement Primitives.
DNN	Deep Neural Network.
DoFs	Degrees-of-Freedom.
DQN	Deep Q-Network.
DRL	Deep Reinforcement Learning.
DRU-Net	Deep Residual U-Net.
DSA	Digital Subtraction Angiography.
DSC	Dice Similarity Coefficient.
ECG	Electrocardiogram.
EM	Electromagnetic.
EVAR	Endovascular Aortic Repair.
FBG	Fiber Bragg Gratings.
FEM	Finite-Element Method.
FFD	Free Form Deformation.

FN	False Negative.
FoV	Field-of-View.
FP	False Positive.
FTL	Follow-The-Leader.
GA	Genetic Algorithm.
GAIL	Generative Adversarial Imitation Learning.
GAN	Generative Adversarial Network.
GMM	Gaussian Mixture Model.
GPUs	Graphics Processing Units.
GUI	Graphical User Interface.
HMD	Head-Mounted Display.
HMMs	Hidden Markov models.
IK	Inverse Kinematics.
IPEI	Intraluminal Procedures and Endovascular Interventions.
IVUS	IntraVascular UltraSound.
L-BFGS	Limited-memory Broyden-Fletcher-Goldfarb-Shanno.
LfD	Learning from Demonstrations.
LoA	Level of Autonomy.
LPA*	Lifelong Planning A*.
LSTM	Long Short Term Memory.
MCNN	Multi-Channel Convolutional Neural Network.
MDCT	Multidetector Computed Tomography.
MDSC	Modified Dice Similarity Coefficient.
MRI	Magnetic Resonance Imaging.
MRTK	Microsoft Mixed Reality Toolkit.
MSM	Mass-Spring Model.
OCT	Optical Coherence Tomography.
PAMs	Pneumatic Artificial Muscles.
PBD	Position-Based Dynamics.
PCI	Percutaneous Coronary Intervention.
PDSS	Penalization of Deformations in Spare Space.
PPO	Proximal Policy Optimization.
PRM	Probabilistic RoadMap.
PRM*	Probabilistic RoadMap*.
PSO	Particle Swarm Optimization.
RL	Reinforcement Learning.
RMSE	Root Mean Square Error.

ROI	Region of Interest.
RRG	Rapidly-exploring Random Graph.
RRM	Rapidly-exploring RoadMap.
RRT	Rapidly-exploring Random Tree.
RRT-connect	bi-directional RRT (or bi-RRT).
SARSA	State-Action-Reward-State-Action.
SVD	Singular Value Decomposition.
TAVI	Transcatheter Aortic Valve Implantation.
TN	True Negative.
TP	True Positive.
VMTK	Vascular Modeling Toolkit.

ACKNOWLEDGEMENTS

I would like to express my gratitude to the predecessors who have made significant contributions in the field of medical robotics.

I am sincerely thankful to the individuals and institutions that have shown kindness and provided assistance throughout my doctoral journey.

May the field of medical robotics continue to thrive and benefit humanity.

LIST OF PUBLICATIONS

JOURNAL ARTICLES

6. Di Wu*, **Zhen Li***, Mohammad Hasan Dad Ansari, Xuan Thao Ha, Mouloud Ourak, Jenny Dankelman, Arianna Menciassi, Elena De Momi, and Emmanuel Vander Poorten. "Comparative Analysis of Interactive Modalities for Intuitive Endovascular Interventions". 2023. (Under Review. Di Wu and Zhen Li contributed equally to this manuscript. Corresponding author: Zhen Li.)

5. **Zhen Li**, Chiara Lambranzi, Di Wu, Alice Segato, Federico De Marco, Emmanuel Vander Poorten, Jenny Dankelman, and Elena De Momi. "Robust Path Planning via Learning from Demonstrations for Robotic Catheters in Deformable Environments". 2023. (Under Review)

4. **Zhen Li**, Letizia Contini, Alessandro Ippoliti, Elena Bastianelli, Federico De Marco, Jenny Dankelman, and Elena De Momi. "Deformable Model-to-Image Registration towards Augmented Reality-Guided Endovascular Interventions". 2023. (Under Review)

3. Ameya Pore*, **Zhen Li***, Diego Dall'Alba, Albert Hernansanz, Elena De Momi, Arianna Menciassi, Alicia Casals Gelpí, Jenny Dankelman, Paolo Fiorini, and Emmanuel Vander Poorten. "Autonomous Navigation for Robot-Assisted Intraluminal and Endovascular Procedures: A Systematic Review". In: *IEEE Transactions on Robotics* 39.4 (2023), pp. 2529–2548. DOI: 10.1109/TRO.2023.3269384. (Ameya Pore and Zhen Li contributed equally to this manuscript. Corresponding author: Zhen Li.)

2. **Zhen Li**, Enrico Manzionna, Giovanni Monizzi, Angelo Mastrangelo, Maria Elisabetta Mancini, Daniele Andreini, Jenny Dankelman, and Elena De Momi. "Position-based dynamics simulator of vessel deformations for path planning in robotic endovascular catheterization". In: *Medical Engineering & Physics* 110 (2022), p. 103920. DOI: 10.1016/j.medengphy.2022.103920

1. **Zhen Li**, Jenny Dankelman, and Elena De Momi. "Path planning for endovascular catheterization under curvature constraints via two-phase searching approach". In: *International Journal of Computer Assisted Radiology and Surgery* 16.4 (2021), pp. 619–627. DOI: 10.1007/s11548-021-02328-x

CONFERENCE PAPERS

6. Mohammad Hasan Dad Ansari*, Beatriz Farola Barata*, Fabian Trauzettel*, **Zhen Li***, Di Wu*, Diego DallÁlba, Gianni Borghesan, Mouloud Ourak, Veronica Iacovacci, Selene Tognarelli, Jenny Dankelman, Elena De Momi, Paul Breedveld, Paolo Fiorini, Jos Vander Sloten, Arianna Menciassi, and Emmanuel Vander Poorten. "Proof-of-Concept Medical Robotic Platform for Endovascular Catheterization". In: *Proceedings of the 11th Conference on New Technologies for Computer and Robot Assisted Surgery (CRAS)*. 2022, pp. 66–67. (*Authors contributed equally.)

5. **Zhen Li**, Enrico Manzionna, Giovanni Monizzi, Angelo Mastrangelo, Maria Elisabetta Mancini, Daniele Andreini, Jenny Dankelman, and Elena De Momi. “Simulation of Deformable Vasculature for Robot-assisted Endovascular Catheterization”. In: *Proceedings of the 33rd Conference of the International Society for Medical Innovation and Technology (iSMIT)*. 2022. Available online: `https://atlas-itn.eu/wp-content/uploads/2022/10/SMIT_-poster_Zhen.pdf`
4. **Zhen Li**, Maria Elisabetta Mancini, Giovanni Monizzi, Daniele Andreini, Giancarlo Ferrigno, Jenny Dankelman, and Elena De Momi. “Model-to-Image Registration via Deep Learning towards Image-Guided Endovascular Interventions”. In: *2021 International Symposium on Medical Robotics (ISMR)*. 2021, pp. 1–6. DOI: `10.1109/ISMR48346.2021.9661511`
3. **Zhen Li**, Enrico Manzionna, Giovanni Monizzi, Angelo Mastrangelo, Daniele Andreini, Jenny Dankelman, and Elena De Momi. “Development of a virtual simulator for endovascular catheterization training”. In: *Poster presentation at the 13th Hamlyn Symposium on Medical Robotics (HSMR)*. 2021. Available online: `https://re.public.polimi.it/bitstream/11311/1206853/1/Hamlyn-poster-Li.pdf`
2. **Zhen Li**, Pagliari Andrea, Pasini Nicolò, Vittorio Zaccaria Pasolini, Chiara Quartana, Jenny Dankelman, and Elena De Momi. “Continuous-curvature path planning for endovascular catheterization”. In: *Proceedings of the 10th Conference on New Technologies for Computer and Robot Assisted Surgery (CRAS)*. 2020, pp. 18–19. Available online: `https://re.public.polimi.it/bitstream/11311/1148212/1/ZhenLi_CRAS2020_Extended_Abstract_revised.pdf`
1. **Zhen Li**, Alice Segato, Alberto Favaro, Jenny Dankelman, and Elena De Momi. “A Heuristic-Sliding-Window-based RRT Path Planning for Endovascular Catheterization”. In: *Proceedings of the 7th Congress of the National Group of Bioengineering (GNB)*. Pàtron editore. 2020. Available online: `https://atlas-itn.eu/wp-content/uploads/2020/12/GNB2020_ZhenLi.pdf`

CURRICULUM VITÆ

Zhen Li (Graduate Student Member, IEEE) was born in Henan, China, in 1995. She obtained her B.Eng degree in Intelligent Science and Technology from Nankai University, China, in 2017. Continuing her academic journey, she pursued dual M.Sc. degrees in European Master on Advanced Robotics (EMARO+) at Warsaw University of Technology, Poland, and Ecole Centrale de Nantes, France, between 2017 and 2019. Her master's thesis project was dedicated to the design and control of a variable aerial cable-towed system, conducted under the guidance of Prof. Stéphane Caro, Prof. Chriette Abdelhamid, and Dr. Julian Erskine.

In November 2019, Zhen began a dual degree PhD program as an Early Stage Researcher (ESR) within the MSCA ATLAS project, funded by the European Union Innovative Training Network. For her doctoral research, she is affiliated with the NearLab at Politecnico di Milano, Italy, under the supervision of Prof. Elena De Momi, and is also a member of the MISIT Lab at TU Delft, the Netherlands, guided by Prof. Jenny Dankelman.